A Numerical and Experimental Investigation of Flow Induced Noise In Hydraulic Counterbalance Valves

by

Mutasim Elsheikh

A dissertation submitted in partial fulfillment
of the requirements for the degree of
Doctor of Philosophy
Department of Mechanical Engineering
College of Engineering
University of South Florida

Co-Major Professor: Jose L. F. Porteiro, Ph.D.
Co-Major Professor: Steven T. Weber, Ph.D.
Rajiv Dubey, Ph.D.
Richard Gilbert, Ph.D.
Craig Lusk, Ph.D.
Kandethody M. Ramachandran, Ph.D.

Date of Approval:
June 23, 2015

Keywords: Steady State, Unsteady State Analysis, Fluid Flow,
Mass Flow Rate, High Pressure, Low Pressure

DEDICATION

To my mother, Azeeza, Thank you for everything that you have done, for all of your love and support. To my wife, Haifa, and our lovely Kids, Azeeza, Magdi and Rawan. To my Dear brother Magdi and his family, And specially in memory of my father, Mohamed Sarour.

To My Advisors Professor. Jose Porteiro and Dr. Steven Weber, Thank you for your enormous tolerance and guidance, without your guidance and persistent help, this dissertation would not have been materialized.

ACKNOWLEDGMENTS

I wish to express my gratitude and sincere thanks for those who were directly or indirectly support and guide me to master this successful work.

I would like to thank Mr. Bernard Batson for all he has done for me, his help and support gave me the necessary confidence to overcome my education problems. I would also like to thank Sun Hydraulics (Sarasota, FL). I also want to express my gratitude to Alfred P. Sloan Foundation Minority PhD (MPHD) program and Florida Education Fund's McKnight Dissertation Fellowship Program NSF S-STEM award DUE #0807023 for their generous support.

My sincere appreciation is offered to Professors Rajiv Dubey, Craig Lusk, Richard Gilbert and Kandethody M. Ramachandran for being my committee members, and Professor Susana Lai-Yuen for been my defense chair, I am grateful for their constant support and help.

Special Thanks to Catherine Button for her guidance and valuable support. In addition, I sincerely thank my colleague Solomon Kang for his help Richard Gilbert and Kandethody M. Ramachandran for being my committee members, and Professor Susana Lai-Yuen for been my defense chair, I am grateful for their constant support and help.

Last but not least, I would like to thank Yaricet Ruiz and Judith Chiang for their help.

TABLE OF CONTENTS

LIST OF TABLES

LIST OF FIGURES

ABSTRACT

The main objective of this study is to explore the complex fluid flow phenomena that result in the generation of a high frequency noise in counterbalance valves through an experimental and numerical investigation of the flow. Once the influence of the different components involved in noise generation is established, a secondary objective is the introduction of design modifications that eliminate the undesired effect without altering the operation envelope or the performance of the valve.

A hydraulic test bench was used to carry out an experimental investigation of the noise generation process. A computer based data acquisition system was used to record pressure fluctuations, flowrates and hydraulic oil temperatures in a production valve under a variety of operational conditions. Extensive experimental measurements and numerical modeling lead to the hypothesis that noise generation is the result of an acoustic resonance triggered by shear layer instability at the valve inlet. The pressure gradients developed when the shear layer entrains the stagnant fluid in the valve main cavity cause the layer to become unstable and oscillate. The oscillation frequency will depend on a great number of factors such as valve geometry, pressure and velocity gradients and the density and viscosity of the fluid. It is postulated that the observed noise is generated when this frequency matches one of the resonant frequencies of the valve cavity.

The proposed mechanism is theoretically poorly understood and well beyond simplified analysis, its accurate numerical simulation is computational very intensive requiring sophisticated CFD codes. The numerical investigation was carried out using STAR–CCM+, a commercially available CFD code featuring 3-D capabilities and sophisticated turbulence modeling. Streamline, pressure, velocity-vector and velocity-scalar plots were obtained for several valve configurations using steady and unsteady state flow simulations.

An experimental and numerical analysis of an alternative valve geometry was carried out. Experimental results demonstrated a greatly reduced instability range. The numerical analysis of the unsteady behavior of the shear-layer streamlines for both valves yielded results that were compatible with the experimental work.

The results of this investigation promise a great positive impact on the design of this type of hydraulic valves.

CHAPTER 1: INTRODUCTION

1.1. Background

The study of fluid-power systems is the study of the characteristics and uses of liquids and gases in the conversion, control, and transmission of power. Pneumatics and hydraulics are applications of fluid power. Pneumatics uses compressed air while hydraulics uses incompressible liquid media such as oil or water. Actuators and control systems are mechanical devices often found in hydraulic systems. Although mankind has used hydraulic power in the form of water wheels for centuries, the study of hydraulics started in the late seventeenth century, when French philosopher Blaise Pascal (1623 - 1662) discovered that liquids cannot be compressed. He stated that pressure exerted in a confined incompressible fluid is transmitted equally in all directions. Pascal’s law is the main reference for all hydraulics science. Using Pascal’s law, engineers have been successful in designing hydraulic components such as pumps, control valves, and actuators. Later, Joseph Bramah (1748 - 1814) invented the hydraulic press. The hydraulic press was based on Pascal's law, it consists of two cylinders and two pistons with different cross-sectional areas. Bramah stated that when a force is applied on the small piston, it will produce a large force on the larger piston. He proved that the difference between the two forces increased with the difference in the area of the two pistons.

Modern fluid power was born in the early twentieth century with the replacement of some electrical systems with hydraulic systems. There are three main types of hydraulic-system components: pumps, control valves, and actuators. The most common types of pumps are gear, vane, and piston pumps. The function of these pumps is to convert mechanical energy into pressure. The actuators use a source of energy, hydraulic-fluid pressure, or pneumatic pressure, and convert that energy into motion as in brakes, hydraulic cylinders, and hydraulic motors. Actuators can operate efficiently at varying speeds, unlike motors, which prefer to operate at constant speed. Actuators can be reversed instantly while in motion without damage. In addition, actuators can be stopped and immediately restarted. The function of a valve is to direct or control fluid flow by opening, closing, or partly interrupting flow in hydraulic lines.

The most common types of valves include counterbalance, check, directional, pressure reduction, proportional, flow-divider, rotary, and pressure-relief valves. Hydraulics are used where power density must be optimized. Examples of applications of hydraulic systems are commonplace. A man lift is a machine used for lifting or lowering loads and to provide access to inaccessible high areas, and is widely used in places such as factories, hotels, and airports. A utility lift truck is a mechanical device used in factories to carry and move merchandise; they are used frequently by utility companies. A straddle crane is a heavy-duty machine used in port terminals for lifting, moving and stacking containers. Fire rescue trucks and mining equipment are additional examples of common machinery that use hydraulic systems.

Hydraulic systems have several advantages over other methods of transmitting power. First, they have more efficient and consistent work or power output and in general can transmit power more efficiently better than mechanical or electrical systems in a small space, this is particularly true when a high force or torque needs to be applied. Second, through the use of hydraulic or pneumatic cylinders, hydraulic systems can readily produce linear motion, while typical electrical systems require additional machinery to convert the rotational motion into linear motion. Third, hydraulic fluids operate very well in hot working environments. Finally, hydraulic systems also provide high power with very small weight and size [1].

1.2. Literature Review

Most studies of flow-generated noise are focused on the relationship between the frequency of the fluid fluctuations and that of the emitted sound. The frequency of an oscillating flow was first related to flow parameters by Strouhal who, as a result of quantitative observations, introduced the non-dimensional frequency, the Strouhal number. Lord Rayleigh related the Strouhal number to the Reynolds number. He published a masterful treatise (The Theory of Sound) [2] on acoustics that develops the mathematical physics of wave propagation and vibration. He developed the theory of vibrating systems by formulating approximation techniques to describe complex physical situations. These principles are still relevant to the modern field of acoustics. Among the pioneers of aeroacoustics was Sir James Lighthill [3], [4], who in 1955 derived a theory for the estimation of the intensity of the sound that radiates from turbulent flow. Lighthill first introduced the concept of the aeroacoustic analogy, which consists of replacing the actual flow field responsible for generating noise with an equivalent system of noise sources. The noise sources act on a uniform stagnant fluid that is governed by standard acoustic propagation equations. The aerodynamic characterization of the sources then becomes the main issue in noise prediction. Curle [5] extended the concepts that Lighthill developed to include the effect of flow body interaction on sound generation. Ffowcs Williams and Hawkings [6] extended the Lighthill analogy to account for arbitrary surface motion. This formulation was used for noise prediction in rotor blade aerodynamics, such as in the helicopter and turbine industries.

The focus of this literature review will be on the previous experimental and computational work in the flow characteristics of counterbalance valves, load control valves, and direct acting relief valves.

1.2.1. Computational Work

Fleming et al. [7] used a computational fluid dynamics (CFD) code to examine gas flow through a disk valve. The simulation was carried out to study how changing the values of the eddy kinematic viscosity (to determine the Reynolds stresses) in the turbulence model influenced the computed value of gas forces. The work concluded emphasizing computational techniques with turbulence models instead of investigating flows through different valves.

Guo and Nakano [8] used boundary element methods to investigate axial flow force compensation in spool valves. Pressure distributions were determined using a linear smoothing technique. The fluid used in the simulation was viscous and incompressible and the flow was steady. A recirculating bucket on the valve spool was modeled in two–dimensions. The Reynolds number of the flow in the simulation was 280. The results illustrated the ratio of the flow force caused by the momentum change in the jet to the force in the axial direction generated by the compensation bucket increases as the Reynolds number increased.

Ito, Takahashi, and Inoue [9] used a unique combination of numerical techniques to model the flow through a poppet valve to study the pressure distribution and flow forces on the valve body. A steady, laminar axisymmetric flow around the poppet valve was simulated. The simulated flows through a 45° conical poppet valve were of very low Reynolds numbers (200-300). Both experimental and numerical results were found in good agreement in the pressure distributions for Reynolds numbers less than 200, and they showed a large difference for Reynolds greater than 200.

Jahnston et al. and Vaughan et al. [10] used both experimental techniques and numerical simulations, in an extensive study the flow characteristics of a poppet valve. The CFD models were good trend predictors of flow patterns, but had limitations on determining exact values. This work provided an excellent description of the flow structure in poppet valves.

Nguyen–Schaefer et al. [11] studied the vibration induced by the internal flow of a ball seat valve in mobile hydraulics under various extreme flow conditions using both experimental techniques and CFD. The aim of the research was to prove that CFD was a good method to understand the flow and the dynamic features in the valve. The authors explained that to reduce the noise associated with these vibrations, it was necessary to gain a thorough understanding of the flow in this particular hydraulic component and of the dynamic characteristic of the hydraulic system. They concluded that the combined, method using CFD and direct measurements, suggests itself as a very suitable approach to gain more understanding not only of the flow processes in the valve but also of the causes for the instability of the valve closing body.

Francis and Betts [12] used an axisymmetric CFD model and experimental techniques to study the incompressible isothermal flow in a disc relief valve. The CFD simulation was used to investigate the fluid flow of an axisymmetric valve, and used the results to compare with the pressure distribution on the production valve disc. The oil-film technique was used to facilitate the simulation and to record the reattachment lengths of the detached shear layers. The results obtained allowed the identification of the flow regimes and flow characteristics of the valve as well as the transition between the separated flow patterns. Their investigation found that the CFD model results were a maximum of 30% higher than from the experimental results.

Weber, Rahman, and Porteiro [13], and [14] provide an extensive study of flow characteristics of counterbalance valve–induced noise using both experimental techniques (including flow visualization) and numerical modeling. The authors explain that the formation of the noise is due to shear layer instability. In order to eliminate the noise two approaches were attempted by the authors. The first approach was to insure that the flow remained attached and did not separate, the second approach was to disturb the free stream in such a manner that no coherent oscillations were produced. The unique combination of these two approaches eliminated the noise.

Borghi et al. [15] carried out a numerical analysis of the transient flow through a spool valve. They used laminar two-dimensional non-symmetric steady and transient flows to study the velocity and the pressure distribution in the tapered gap of the spool valve. The authors concluded that the relationship between the transient flow force and the time-rate-of change of the valve flow rate are proportional. They employed a CFD method for fully developed turbulent flow in the investigation rather than using the simpler two-dimensional momentum conservation theory. Their CFD results and experimental measurements did not agree well for the transient and the steady flow forces. They concluded that the CFD model was useful as a qualitative guideline and in explaining some hydraulic behaviors.

Wang, Chen, and Lu [16] used particle image velocimetry measurements to validate their computational technique predictions of axial flow forces in a spool valve. The authors used the k – Ɛ two-equation turbulence model, specifying the inlet velocity and the outlet pressure to define the flow. Their work proved that modifying the relative position of the oil port and the “buckets” can remarkably reduce the steady flow force. In addition to the numerical results from CFD analysis, they also employed the particle velocimetry technology to visualize the flow field experimentally. The visualized flow field indicated that a vortex developed with in the valve chamber.

Pennington, and Porteiro [17] used numerical simulation, experimental techniques, and flow visualization to develop guidelines for the design of direct-acting, differential area relief valves by studying the effects that changes in geometry of internal components have on valve performance. The numerical simulation of the relief valve proved to be in reasonable agreement with flow visualization and experimental results, these results were qualitative rather than quantitative. The solutions of steady and transient simulations of the fluid flow were in agreement with model prediction, the influence of the seat angle, exhaust hole diameter, and hole position on valve performance. The experimental investigation revealed how a number of component geometry variations influenced valve performance.

Weerachai et al. [18] investigated water flow characteristics past butterfly valves. The research presented a numerical simulation of the fluid flow through the valve using the available code CFD ANSYS FLUENT. The test was carried out when the valve was fully opened (at 0°) and then at 30°, 45°, 60° and 75,° at a water speed of 1, 2 and 3 m/s. Dynamics analysis was carried out for water speed of 1 m/s at angular velocities of 0.039 and 1.57 rad/s. The valve diameter was set for 150 mm and 300 mm to investigate the characteristic of the loss coefficient and torque behavior. The results showed that as the disk angle increased so did the torque and loss coefficient. Weerachai stated that the loss coefficient remained constant when the water speed increased, even though the torque increased. He concluded that at both angular speeds, the maximum torque occurred at 70°−80° in closing and 100°−110° in opening. An experiment was also carried out to verify the numerical results. Both experimental and numerical values agreed well for both loss coefficient and torque.

Zhang, S. and Manring, N [19] used numerical simulation, experimental techniques, and pressure wave generation to study the pressure transient flow-force for spool-type two-way valves.

Three types of flow forces were identified: pressure-difference-induced, viscous-shear-induced, and momentum-induced. Nondimensional analysis showed that among all steady flow forces the pressure-difference-induced flow force was largest, the viscous-shear-induced flow force was second largest and the momentum-induced flow force was the smallest. Trial tests on a hydraulic circuit showed that the sound wave phenomenon was very strong and there was a pressure gradient in the vertical direction. A two-way valve with longer valve length, stepped housing and larger clearance was investigated on a second experiment. The geometry modifications on the second experiment were made to reduce the energy that could be reflected at the ends and reduce the pressure gradient in the vertical direction. The usefulness of those modifications was proven experimentally.

Lisowski, Czyżycki, and Rajda [20] used three-dimensional CFD and experimental tests to investigate the flow force acting on the spool of a solenoid operated directional control valve in order to calculate the pressure and viscous forces associated with the flow. They explained that flow forces increase proportionally with the flow rate, which provide unstable operation of the valve and affect the balance of forces acting on the spool. In the proposed method, the surface affected by the forces associated with the flow through each path was defined and the values of the flow forces were determined. The force values obtained in the CFD simulations agreed well with those obtained on the test bench. In order to reduce flow forces additional internal channels were added in the valve body. The innovative solution of the valve allowed for a higher flow range of about 45% without any change of spring or solenoid.

1.2.2. Experimental Work

Tidor [21] used half of an axisymmetric two-dimensional glass model poppet valve for flow visualization. The maximum working pressure was limited to 45 psi, because of the use of glass for wall material. To observe the flow with bubbles, air was injected into the model with a 0.012 inch hypodermic needle. Several observations were noted by the author, the most important one is that the bubbles were possibly caused by cavitation occurring at low pressures.

Stone [22] conducted a series of tests to measure flow forces in poppet valves operating in hydraulic oil. Theoretical analysis was also conducted based upon the assumptions that the flow was steady and neglecting both viscous friction and gravity. The author found that the experimental results did not agree well with the predicted theoretical values because the viscous friction was ignored and the boundary layer was a large part of the flow at small valve openings. He also found that the flow forces were strongly influenced by the downstream configuration, the smaller the diameter of the downstream chamber, the higher the forces. A poppet configuration was designed and tested which virtually eliminated the flow forces.

Stone [23] extended his work by modifying the test apparatus and measuring the discharge coefficient and flow forces in poppet valves of various shapes. He used a mixture of Esso Univis 40 and J43 oils as working fluids in a pressure range of 500 and 2000 psi. The author observed that in some tests when oil passed into the valve it caused the poppet to oscillate at a frequency of 1300 Hz. Also, the release of air bubbles in the low-pressure region beneath the poppet was observed. Stone [24] developed a flow force compensated design. Hence, the articles are useful references for developing a flow force measurement tool and in trying to understand the effects that discharge coefficients have on the flow forces.

Kawakami, Oki [25], and [26] extended the previous work on the disc valves of Schrenk. They used the same apparatus, but the diameter ratio between the disc and the valve throat was larger. A series of experiments on valves were carried out with different diameter ratios. The authors did not mention cavitation but considering that the work was conducted with a relatively low head, cavitation could not have been much of an issue. One of the important conclusions of this work was that flow separation adds hysteresis and uncertainty to the measurements of flow with respect to valve opening.

Takenaka, Yamane, and Iwamizu [27] tested circular disc valves, presenting the relationship between lifting force and discharge coefficients. The results showed that viscosity has a large influence with small openings and that the influence rapidly decreases as the valve opens. They observed that the discharge coefficient is approximately in inverse relation to the valve thrust. They suggest that valve stability can be described through discharge coefficients instead of valve lift.

McCloy and McGuigan [28] studied the previous works of Schrenk, Tidor, and Stone. They used the results of their work to develop an understanding of how flow forces, discharge coefficient, Reynolds number, valve height, pressure drop, and flow rate interact and influence valve performance under both steady and non-steady flow conditions. They conducted a series of experiments with different sized downstream chambers that were either full of air or full of water. The flow forces were calculated using the pressures measured over the surface area of the poppet. They were affected by changes in flow patterns and size of the downstream chamber. It was determined that flow forces are strongly dependent upon the downstream chamber size. It was also demonstrated that the oscillations in pressure cause changes in the discharge coefficient. The authors concluded that the flow forces decrease as the chamber size decreases because of the presence of recirculating flow.

Takenaka et al. [29] used both theoretical and experimental techniques to analyze disc valves. The authors assumed a parabolic velocity profile at the seat. This is unusual, since most hydraulic systems operate in turbulent flow, particularly in the seat areas of the valves.

Experimental and numerical results did not agree very well. The disagreement increased when the ratio of disc diameter to valve throat diameter increased from 1.5 to 3.0. Takenaka et al. [30] tested flow control and relief valves, observing their static and dynamic characteristics. The flow between the valve and the valve seat was very complex. The pressure distribution over the valves surface and the lifting-force were calculated. The results showed the correlation between the lifting-force and the discharge coefficient. In addition, they concluded that the determination of the discharge coefficients is the most important factor in the valve design.

Urata [31] extended Takenaka's work. He studied flow forces in poppet style valves used both laminar and turbulent fluid flow. The author used dye injection flow visualization techniques to develop a qualitative understanding of how the flow behaves going through the valve opening. Two different liquids (oil and water) were used in the experiments. The validity of the results from the two–dimensional models was limited. The author stated that the theoretical and experimental results agreed well in the laminar and turbulent flow regimes with small deviations.

Feigel [32] experimented on the deflection of oil jets as a function of spool deflection in uncompensated valves. The aim of the research was to demonstrate that even in complex flows, flow force compensation could be applied. The study was qualitative and used an interactive process to develop an understanding of the flow patterns through the spool valves. He concluded that the number and size of the outlet holes influenced the flow patterns, finding more favorable results with a small number of larger holes than with a larger number of small holes. He noticed that the chamber created between the controlling edge and the exit hole influences the flow compensation with respect to the jet angle.

Ishii et al. [33] used flow visualization to study the flow in poppet valves. A fully three-dimensional steel valve was constructed as part of experimental apparatus. Two industrial fiber optic scopes were attached to two high-speed video cameras. Acrylic portholes were mounted in the test valve at 90° to each other for three-dimensional viewing. The working fluid was oil, the flow was not seeded but relied upon the air bubbles that naturally came out of solution as well as the bubbles formed from cavitation. The valve was a simple conical poppet that was used as a relief valve. The study examined the flow under steady and cavitating conditions. This configuration was unstable at low flow rates.

Tsukiji et al. [34], [35], and [36] investigated the cavitation of counterbalance valves using flow visualization. ISO 32 oil at a temperature of 40° ± 1° was the working fluid. The model was constructed from plastic by sectioning a full valve and installing a window in the area of interest. Geometry modifications were made to reduce cavitation and hence the noise. The experiments were conducted at Reynolds numbers of 2772, 2847, 3594, and 3478. The flow was photographed with a 35 mm camera using the naturally occurring bubbles of cavitation to seed the flow. Very good photographs of flow visualization through the valve model were obtained.

Guivier, Deplano, and Bertrand [37] validated a numerical three-dimensional fluid–structure interaction (FSI) model for a prosthetic aortic valve based on experimental particle image velocimetry (PIV) measurements. CFD analysis was used as the basis for the experiments. For validation of the numerical model, an experimental model was developed for both the hydrodynamic conditions and the geometrical one. The authors concluded that in both models the fluid-flow behaviour and the velocity fields were similar through the quantitative and qualitative comparisons methods. The investigation allowed for the confirmation of a fully coupled 3-D fluid-structure interaction (FSI) numerical model.

Wang, Chen, and Hsoao [38] studied the flow rectification performance of conical diffuser valves. The cell test performance of the diffuser was set-up. The diffuser angle and the actuation volume for different values of the high frequency of the fluid were studied in this research. The range of diffuser angles varied from 10° to 35°, with corresponding Roshko numbers from 25 to 300. The results showed that the taper angle and the Roshko number significantly affect the performance of the valve diffuser. The diffuser valve with diverging angle of 10° exhibited the best performance. The authors stated that the experimental results agreed well with their simulations. By setting the backpressure to zero, the authors attained maximum flow efficiency around 48%. At the same time, the author measured the time-dependent behavior of pressure inside the actuation chamber, they concluded that the amplitude pressure variations similar for Roshko number to those of the valving efficiency; and the large actuation pressures result in high rectification efficiencies. They obtained that the valve performance decreases for a large actuation volume, however the actuation pressure increases. In addition, the authors have explanation for this phenomenon.

Herakovic [39] presented a new way to reduce the flow force within a spool valve. His studied focused on how to change the jet angle by a proper design and shape of the valve piston. The valve piston has many pressure compensation grooves on its outer surface, and the shape of the piston is not perfectly cylindrical. The pressure compensation grooves are on the spool on this valve. The experimental results confirmed that these pressure compensation grooves are capable of changing the steady flow force greatly, and his new design was very effective for reducing the steady flow force.

1.3. Problem Description, Methods, and Goals of the Research

Counterbalance valves provide smooth positive control of overrunning loads, prevent load drifting caused by directional control valves, and protect a load from dropping. An overrunning load is one that has the tendency to cause the actuator to move faster than the supply fluid coming from the pump. This condition is undesirable because loss of control and cavitation may occur in the actuator. The counterbalance valve acts to restrict the fluid flow from the actuator and prevents cavitation at the inlet side of the actuator. The valve operates when the fluid enters the valve through six axial holes, and exits the valve through six radial holes locate on the valve periphery as shown in Figures 1.8. The fluid with high-pressure force acts on the piston area. Fluid also enters the spring chamber through a small hole in the piston, causing pressure on the back of the piston area. If the force from the oil coming from the directional valve is greater than the force generated by the preset of the bias spring, the piston will move inward towards the spring chamber. The poppet will move with piston until it reaches the tip of the adjust screw. The piston is free to continue moving inward while the poppet will be stopped. This causes a large pressure drop at the gap area (the area created between the piston and the poppet) causing under certain condition a loud high–frequency noise that can be described as a “squeal”. It is believed this noise is caused by the shear layer instability of the fluid flow generating an acoustic resonance on the valve cavity. This theory will be tested by experimental investigation, and numerical simulation. The experimental investigation of the flow instability will provide the data base for our numerical simulations.

Three–dimensional numerical simulation of the flow will be conducted with a commercially available computational fluid dynamics code (STAR–CCM+). STAR CCM+ uses the Reynolds-Averaged Navier-Stokes (RANS) equations to solve the momentum conservation equations that govern fluid flow.

The aim of the current work is to use numerical simulation (CFD), and experimental techniques to develop guidelines for the design of counterbalance valves by understanding the effects that the changes in geometry of the internal components have on valve performance. A hydraulic fluid flow test bench, shown in Figure 1.10, will be used for the experimental work. The redesign goals of this study are to eliminate the noise without impacting the operation performance of the valve. The piston and poppet geometry are the main two components of the valve to be studied in this redesign.

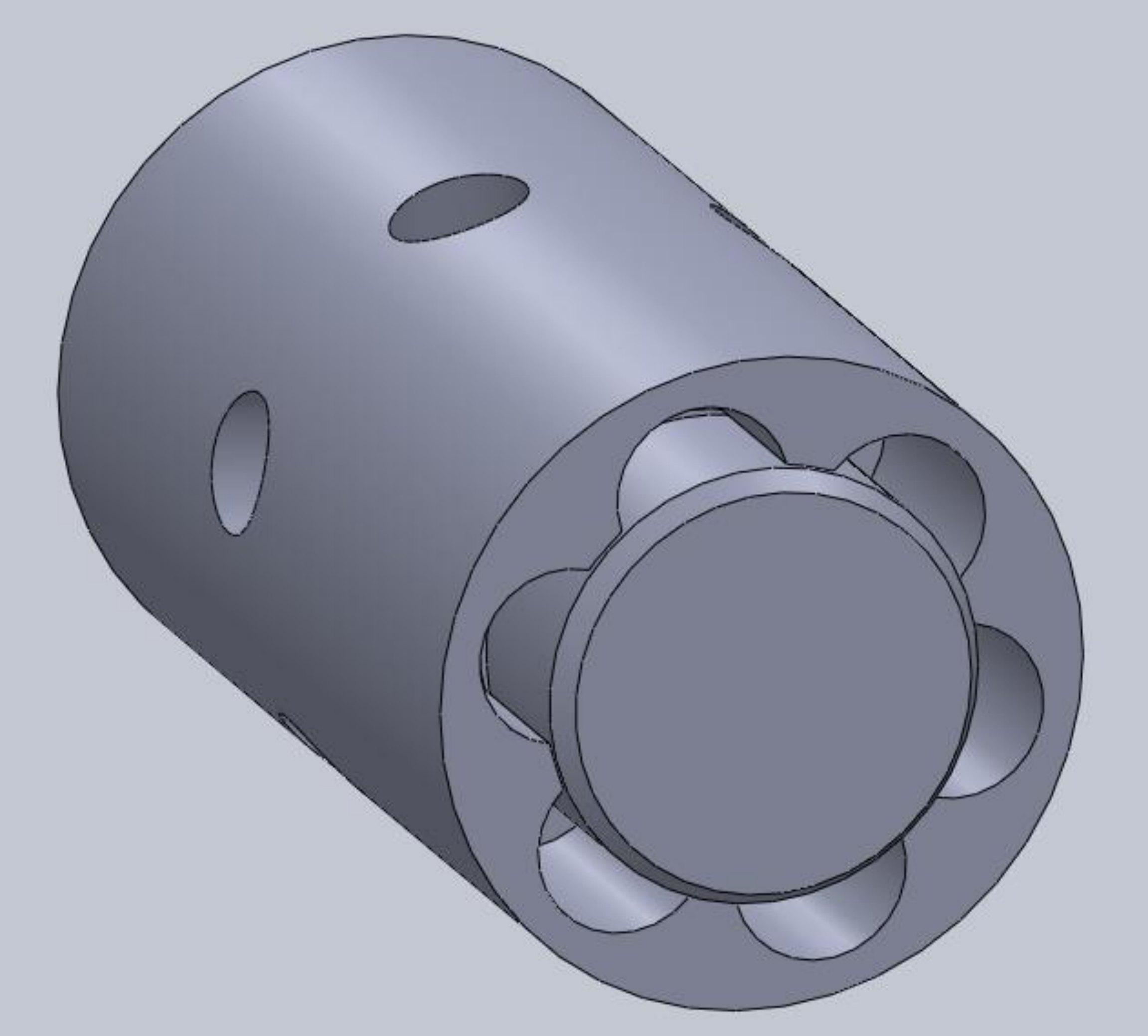

Figure 1.1. Assembly of counterbalance valve.

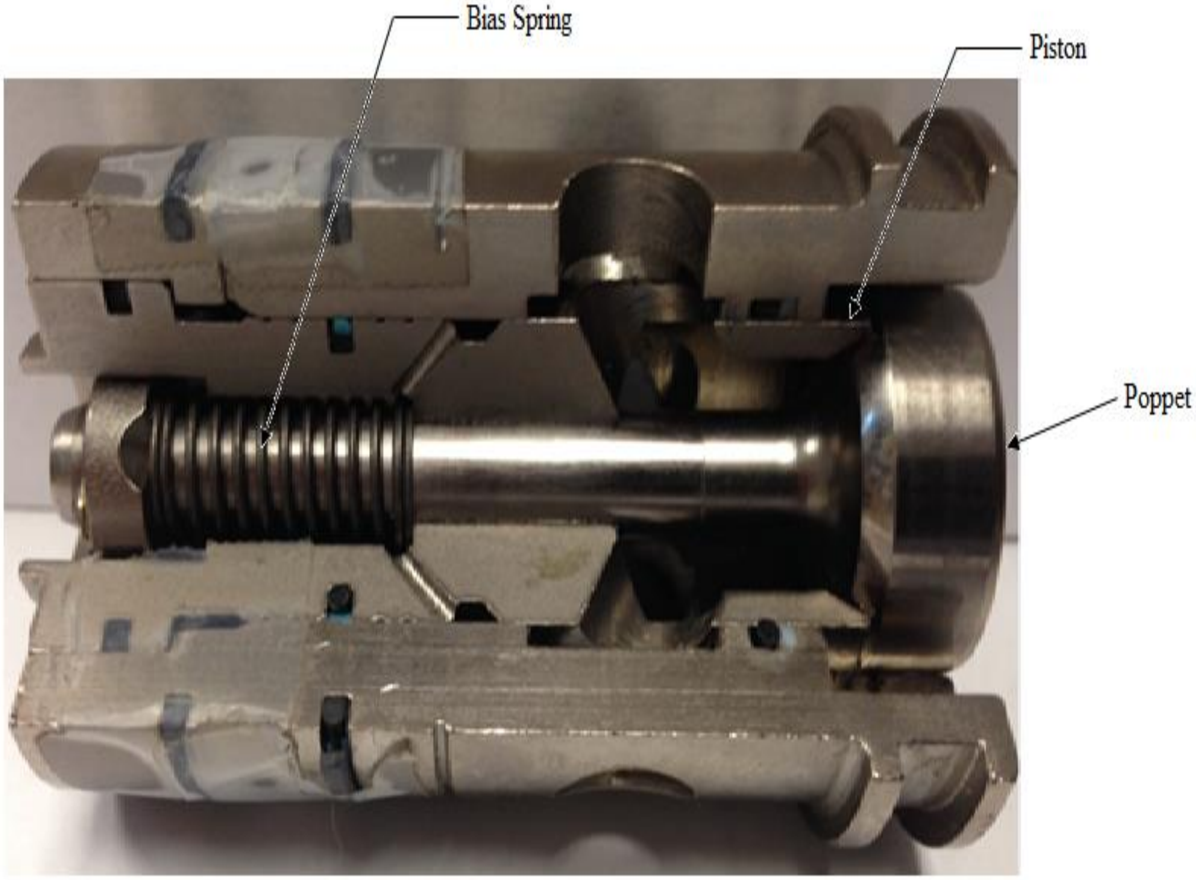

Figure 1.2. Cross section of counterbalance valve type A.

CHAPTER 2: NUMERICAL SIMULATION

2.1. Introduction

The fluid flow through the counterbalance valve was numerically simulated using the 3D–fluid dynamics code STAR – CCM+. STAR-CCM+ can be used in the simulation of compressible, incompressible, laminar and turbulent flows of both Newtonian and non-Newtonian fluids. STAR-CCM+ uses a finite-element technique to solve the equations of motion. The finite-element (FEM) technique finds approximate solutions to boundary value problems by discretizing the continuum into a number of simply shaped elements. The dependent variables velocity, pressure, and temperature are interpolated to a set of nodal points that define each finite element. Within each element, the velocity, pressure, and temperature fields are approximated in order to confirm the predicted rates of convergence of the finite element approximations. The resulting global set of algebraic equations are then solved after imposing the boundary conditions. The solution is a numerical integration of the partial differential equations obtained from the conservation laws.

2.2. Governing Equations, Boundary, and Initial Conditions

The governing equations of fluid flow are: conservation of mass, conservation of momentum, and conservation of energy. The conservation of mass equation (Continuity equation) is:

$$\frac{\partial \rho}{\partial t}+\frac{\partial}{\partial \vec{x}}(\rho \vec{V})=0 \qquad (2.1)$$

For incompressible fluids, the continuity equation reduces to:

$$\nabla \cdot \vec{V} = 0 \tag{2.2}$$

For an axisymmetric model in cylindrical coordinates, $\vec{r} = (r, \theta, z)$ $\vec{V} = (v_r, v_\theta, v_z)$ the equation 2.3 becomes:

$$\frac{1}{r}\frac{\partial}{\partial r}(rv_r) + \frac{1}{r}\frac{\partial}{\partial \theta}(v_\theta) + \frac{\partial}{\partial z}(v_z) = 0 \tag{2.3}$$

The conservation of momentum can be written as:

$$\rho\frac{\partial \vec{V}}{\partial t} = \rho\vec{g} - \nabla\vec{p} + \nabla.\vec{\tau} \tag{2.4}$$

For a Newtonian incompressible flow with constant viscosity the equation becomes:

$$\rho\frac{\partial \vec{V}}{\partial t} = \rho\vec{g} - \nabla\vec{p} + \mu\nabla^2.\vec{V} \tag{2.5}$$

which is a set of three partial differential equations, known as the Navier-Stokes equations, when external forces are assumed negligible, equation 2.5 becomes:

$$\rho\frac{\partial \vec{V}}{\partial t} = -\nabla\vec{p} + \mu\nabla^2.\vec{V} \tag{2.6}$$

For an axisymmetric problem in cylindrical coordinates, they can be written as:

$$\frac{\partial v_r}{\partial t} + (\vec{V}.\nabla)v_r - \frac{1}{r}v_\theta^2 = -\frac{1}{\rho}\frac{\partial p}{\partial r} + \upsilon(\nabla^2 v_r - \frac{v_r}{r^2} - \frac{2}{r^2}\frac{\partial v_\theta}{\partial \theta}) \tag{2.7}$$

$$\frac{\partial v_\theta}{\partial t} + (\vec{V}.\nabla)v_\theta - \frac{1}{r}v_r v_\theta = -\frac{1}{\rho r}\frac{\partial p}{\partial \theta} + \upsilon(\nabla^2 v_\theta - \frac{v_\theta}{r^2} - \frac{2}{r^2}\frac{\partial v_r}{\partial \theta}) \tag{2.8}$$

$$\frac{\partial v_z}{\partial t} + (\vec{V}.\nabla)v_z = -\frac{1}{\rho}\frac{\partial p}{\partial z} + \upsilon\nabla^2 v_z \tag{2.9}$$

where $\upsilon = \frac{1}{\mu}$ is the kinematic viscosity

The energy equation can be expressed as:

$$\rho\frac{d\bar{V}}{\partial t}+\rho(\bar{V}.\nabla.\bar{V})=\nabla.(k\nabla T)+\Phi \tag{2.10}$$

where Φ is the viscous dissipation function.

For flows without heat generation $du \approx C_v\, dT$ and C_v, μ, k, $\rho \approx$ const, the energy equation simplifies to:

$$\rho c_V\frac{dT}{dt}=k\nabla^2 T+\Phi \tag{2.11}$$

in cylindrical coordinates, this equation becomes:

$$\rho c_V\left[\frac{\partial T}{\partial t}+(V.\nabla)T\right]=k\nabla^2 T+\mu[2(\varepsilon_{rr}^2+\varepsilon_{\theta\theta}^2+\varepsilon_{zz}^2)+\varepsilon_{r\theta}^2+\varepsilon_{\theta z}^2+\varepsilon_{rz}^2] \tag{2.12}$$

$$\text{where}\quad \begin{aligned} \varepsilon_{rr}&=\frac{\partial v_r}{\partial r} & \varepsilon_{\theta\theta}&=\frac{1}{r}\left(\frac{\partial v_\theta}{\partial\theta}+v_r\right)\\ \varepsilon_{zz}&=\frac{\partial v_z}{\partial z} & \varepsilon_{\theta z}&=\frac{1}{r}\frac{\partial v_r}{\partial\theta}+\frac{\partial v_\theta}{\partial z}\\ \varepsilon_{rz}&=\frac{\partial v_r}{\partial z}+\frac{\partial v_z}{\partial r} & \varepsilon_{r\theta}&=\frac{1}{r}\left(\frac{\partial v_r}{\partial\theta}-v_\theta\right)+\frac{\partial v_\theta}{\partial r} \end{aligned} \tag{2.13}$$

The governing equations contain seven unknowns: density, three velocity scalars, pressure, internal energy, and temperature. If the fluid is assumed incompressible, body forces are assumed negligible, the fluid is viscous with Newtonian characteristics, and internal heat generation is assumed negligible, the seven unknowns are now reduced to five: temperature, three velocity scalars, and pressure.

The simulations were conducted as pressure-driven flows. In other words, an inlet and outlet pressure boundary conditions were imposed, and no inlet velocity boundary condition was prescribed. The fluid temperature was assumed to be known and was used to determine fluid properties. The no-slip condition on the walls was assumed. The fluid properties were assumed to be those of the Chevron AW 32 hydraulic oil at 40° C, $\mu = 33.6$ cSt, and $\rho = 0.864$ kg/m^3.

2.3. Turbulence Modeling

Turbulent flow is a highly complex phenomenon not easily characterized from a theoretical standpoint. There are, however, many aspects that are well established: turbulent is highly non-linear; three-dimensional, characterized by eddies; eddy break-down converts kinetic energy to heat by means of viscous dissipation. Accurate prediction of turbulent flow is key to calculate flow quantities such as pressure loss, drag, heat transfer, noise, etc. For most engineering analyses, the main interest is in the prediction of the mean (averaged) flow field. STAR-CCM+ uses three basic approaches to modeling turbulence, in increasing order of complexity they are: Reynolds Averaged Navier-Stokes (RANS), Detached Eddy Simulation (DES), and Large Eddy Simulation (LES).

The most commonly turbulence model used today is the kinetic energy (k-Ɛ) model, which is generally applicable to most flow types. Another popular model is the model k-Ɛ which is well suited for predicting flow separation. Reynolds Stress Transport Models (RSM) are more computationally intensive than k-Ɛ or k-Ɛ models. DES and LES solve the large turbulent scales directly providing a greater degree of accuracy but at a larger computational cost. Accurate modeling of the transition between laminar and turbulent flow is carried out by using the γ ρ θ (Gamma Re Theta) model for transition prediction. The transition variables are set by the user to provide accurate modeling of the transition process.

2.4. Numerical Stabilization Techniques

In order to solve for the flow field and pressure fluctuations inside the counterbalance valve, the equations governing the conservation of mass and momentum (2.1 – 2.7) were discretized using finite-element method techniques ([40], [41] and [42]). Numerical stability decreases as the time-step Δt is increased and special techniques such as upwinding and relaxation have to be used to numerically stabilize the iterative solvers. The particular numerical scheme used by the STAR – CCM+ solver also determines the solution accuracy. This is mainly because first order schemes neglect higher order gradients to enhance solver stabilization and convergence at the expense of accuracy. To achieve convergence in turbulent simulations using STAR CCM+, a second-order scheme must be used. This may require using a first-order scheme for a set number of iterations or time-steps before using a second order one. In transient simulations, the STAR – CCM+, in addition to first-order and second-order upwind, offers the following numerical schemes [43]:

- Central-Difference
- Blended Upwind/Central
- Hybrid Second-Order Upwind/Central
- Hybrid Second-Order Upwind/Bounded-Central

The simulation of the flow through the counterbalance valve made use of a hybrid second-order upwind scheme. This scheme employs a combination of relaxation strategies: explicit relaxation, implicit convection/diffusion-based relaxation, and implicit source-based relaxation.

The hybrid scheme automatically activates those portions of the relaxation schemes, as necessary, based on their influence in the source terms of the equations. This scheme speeds up convergence rates and minimizes the need for tuning relaxation factors. The hybrid relaxation factors for turbulent flows used in this work are shown in Table 2.1. The hybrid second-order upwind scheme seeks to achieve second-order accuracy and first-order stability. This is accomplished by linear combinations of first and second-order schemes. Relaxation slows down convergence to numerically stabilize the solution. Explicit and implicit schemes are also used, the explicit schemes are evaluated in terms of known quantities at the previous time step, while the implicit schemes are evaluated in terms of unknown quantities at the previous time step. The implicit scheme is appropriate when there are strong coupling requirements, physics-wise, between the solid and the fluid. The field exchange controller can be used to control the data exchange for the implicit scheme. The initial conditions used in this work are shown in Table 2.2.

Table 2.1. Hybrid relaxation factors for turbulent flows used in this work

Under-Relaxation factor	0.7
Pressure	0.3
k-Omega Turbulence Under-Relaxation factor	0.8
k-Omega Turbulent viscosity Under-Relaxation factor	1.0
Flex Cycle- Restriction tolerance	0.9
Flex Cycle- Prolongation tolerance	0.5

Table 2.2. Initial conditions of physics model used in the present simulation

Pressure	700 psi
Turbulence Intensity	0.01
Turbulent Velocity Scale	1.0 m/s
Turbulent Viscosity Ratio	10
Velocity $v\ (x, y, z)$	[0, 0, 0] m/s

2.5. Computational Procedure

Two difference designs of counterbalance valves, as shown in Figure 2.1 and 2.2 were used for the simulations. Three different gaps for each design (shown in Table 2.3) were considered.

The DES (Detached Eddy Simulation) technique with a hybrid approach was used. In the boundary layer, URANS (Unsteady Reynolds-Averaged Navier-Stokes) was used, while in the bulk domain LES (Large Eddy Simulation) was used. The complex valve geometry was discretized using a combination of polyhedral, prism layer, and surface meshes. A mesh with over 2,345,079 cells and 1,063,032 faces was created, three different views of this mesh are shown in Figure 2.3. A more detailed cross sectional view of the mesh for the boundary layer in the gap is shown in Figure 2.4. A mesh of ten prismatic layers was used along the walls. The parameters used to create the fluid mesh are shown in Table 2.4.

When modeling the boundary layer a “wall treatment” must be used. A “wall treatment” is a set of assumptions for modeling near-wall turbulence quantities such as shear stress, turbulent production and turbulent dissipation. The most common types of wall treatments are the high and low $y+$ treatments.

In the high $y+$ wall treatment, wall shear stress, turbulent production and turbulent dissipation are all derived from equilibrium turbulent boundary layer theory. It is assumed that the near-wall cells lie within the logarithmic region of the layer, and therefore the centroid of the cells attached to the wall should have a value of $y+ > 30$, where the dimensionless wall distance y^+, for a wall-bounded flow is defined as:

$$y^+ = \frac{uy}{v} \tag{2.14}$$

Here u is the velocity near the wall, y is the distance to the wall and v is the local kinematic viscosity of the fluid.

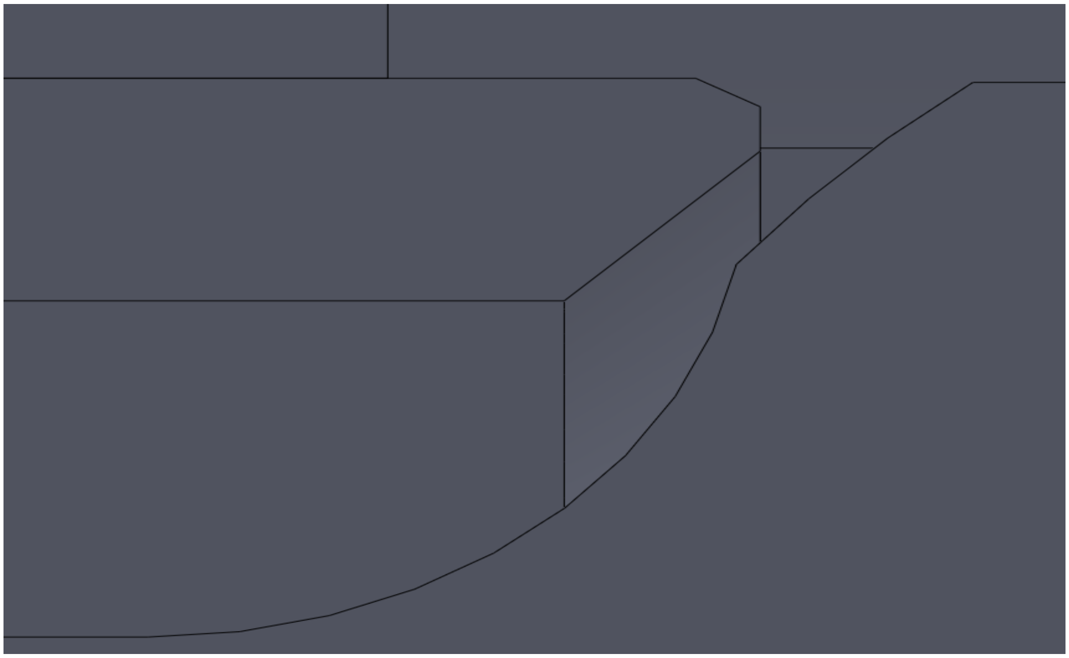

Figure 2.1. 3-D cross section of counterbalance of the type A valve.

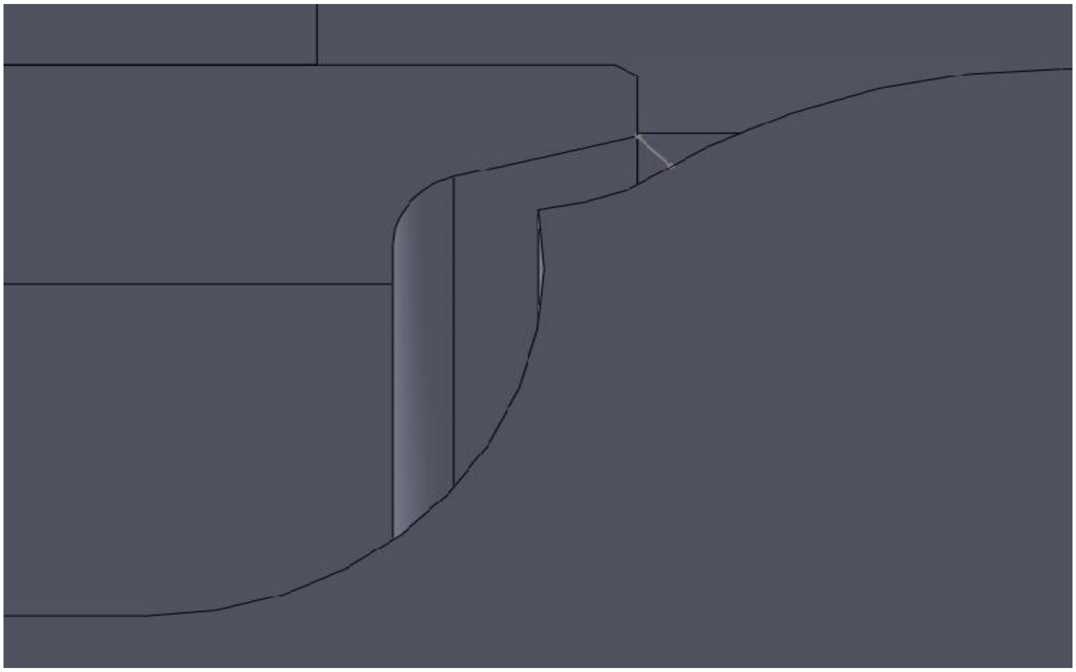

Figure 2.2. 3-D cross section of counterbalance of the type B valve.

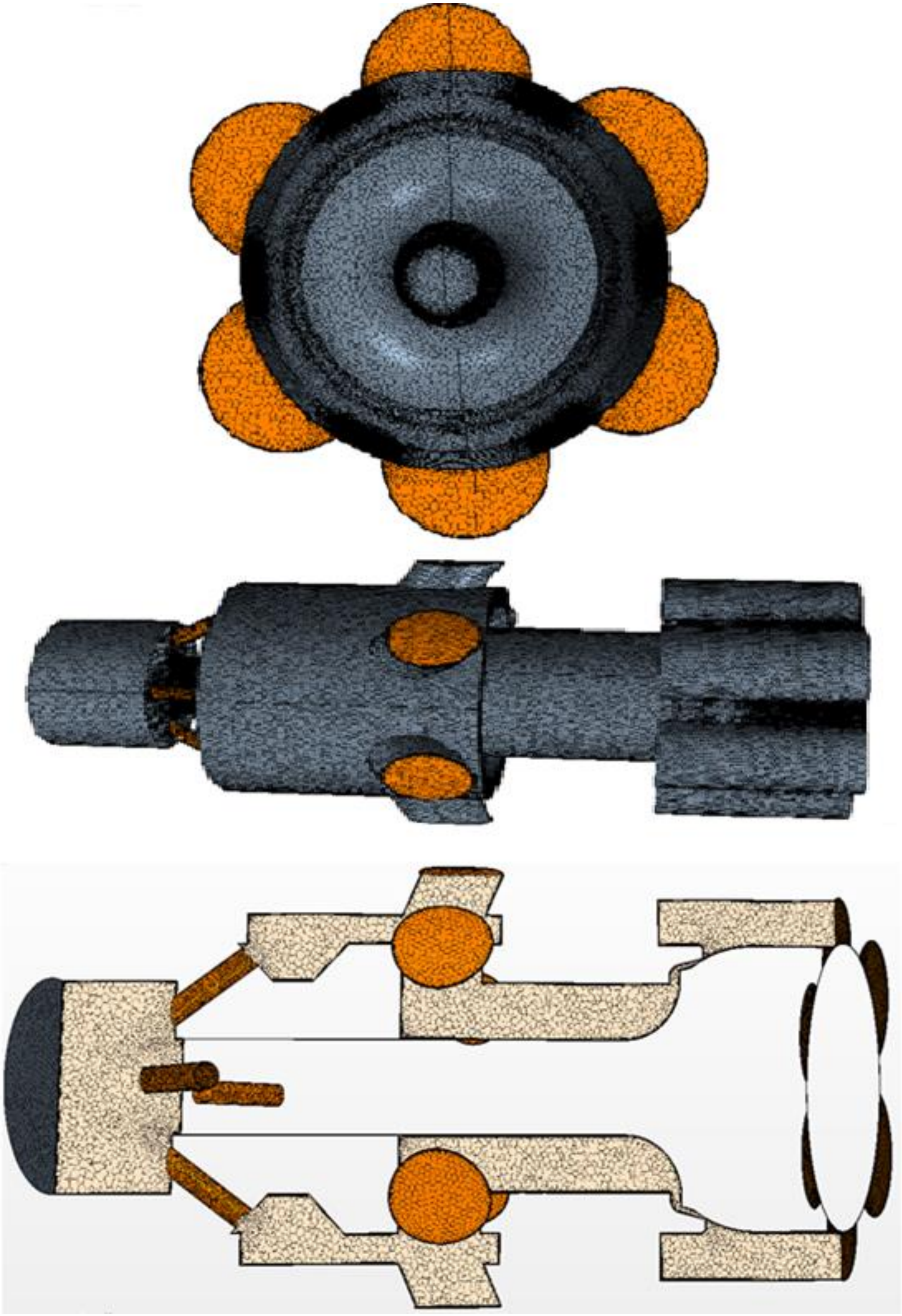

Figure 2.3. Axis-symmetric and cross-sectional views of the computational mesh.

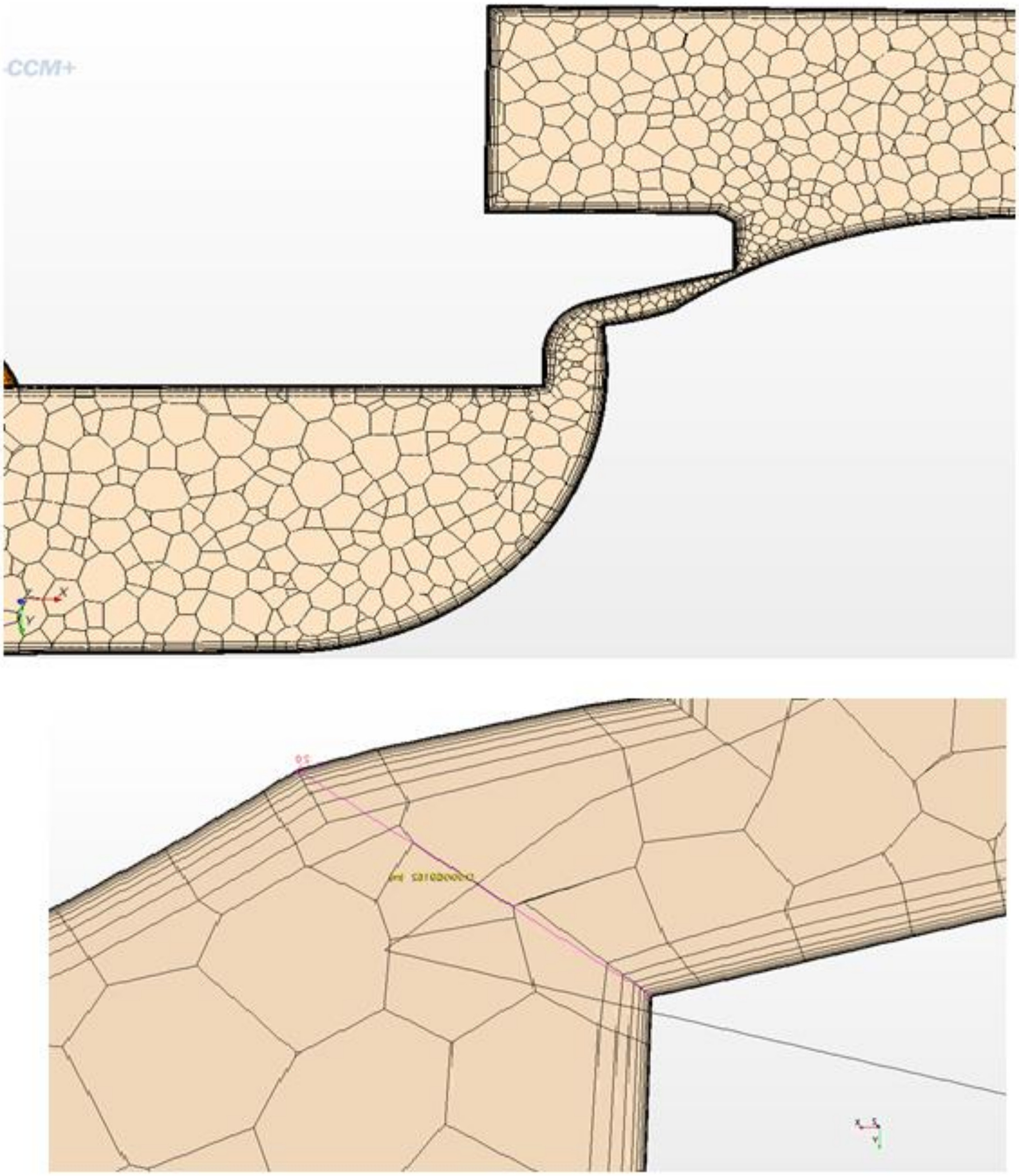

Figure 2.4. Cross sectional of computational mesh showing a detail of the boundary layer in the gap area.

Table 2.3. Gaps differences of the two design of counterbalance valves

Counterbalance type A	0.002 in	0.005 in	0.017 in
Counterbalance type B	0.002 in	0.005 in	0.017 in

Table 2.4. Initial conditions for simulation model used in the present simulation

Mesh base size	0.0003 m
Number of prism layers	10
Prism layer stretching	1.5
Prism layer thickness (Absolute size)	0.0003 m
Surface size (Maximum)	10 percent of base
Surface size (Minimum)	100 percent of base

The low $y+$ wall treatment assumes that the viscous sublayer is well resolved by the mesh, and thus wall laws are not needed. It is used when the entire mesh is fine enough for $y+$ to be approximately 1 or less. The all $y+$ wall treatment is a hybrid wall treatment that combines the high $y+$ wall treatment for coarse meshes and the low $y+$ wall treatment for fine meshes. It is designed to give results similar to the low $y+$ treatment as $y^+ \rightarrow 0$ and to the high-y+ treatment for $y^+ > 30$. It is also formulated to produce reasonable values for meshes of intermediate resolution, when the wall-cell centroid falls within the buffer region of the boundary layer, i.e. when $1 < y+ < 30$. The "All $y+$" method averages turbulence quantities (TQ) such as dissipation, production, stress tensor, etc.

The final value for a turbulence quantity (TQ) is calculated as:

$$\mathrm{TQ} = \mathrm{gTQ\_low} + (1 - \mathrm{g})\mathrm{TQ\_high} \tag{2.15}$$

where g is given by the following function:

$$g = \exp\left(-\frac{\mathrm{Re}_y}{11} \right) \tag{2.16}$$

here Re_y is the Reynolds number.

$$\mathrm{Re}_y = \frac{\sqrt{k}y}{\upsilon} \tag{2.17}$$

where y is the normal distance from the wall to the wall-cell centroid, υ is the kinematic viscosity, and *k* is the turbulent kinetic energy.

To obtain a transient simulation, a steady-state solution was used as the initial condition. The same mesh was used for both steady state and transient simulations. A typical steady-state simulation model required a 24 hours run to converge, and it carried out 400-iterations using over 800 megabytes of file space. The convergence of a steady-state simulation is based on the relative change in the solution between iterations. A tolerance of one tenth of one percent (0.001) between iterations was used on the values of the velocity (r and z components), pressure, turbulent kinetic energy, and turbulent dissipation. A typical steady-state simulation convergence graph can be seen in Figure 2.5.

A typical transient simulation model required 240 hours to achieve convergence using a one tenth of a millisecond time step and running for a total simulation time of eight hundredths of a second. A typical transient simulation convergence graph can be seen in Figure 2.6. The following simulation settings were used for all runs: axisymmetric geometry, incompressible Newtonian fluid, turbulent isothermal flow, anisotropic turbulence, eddy-viscosity turbulence model, hybrid upwinding and hybrid relaxation.

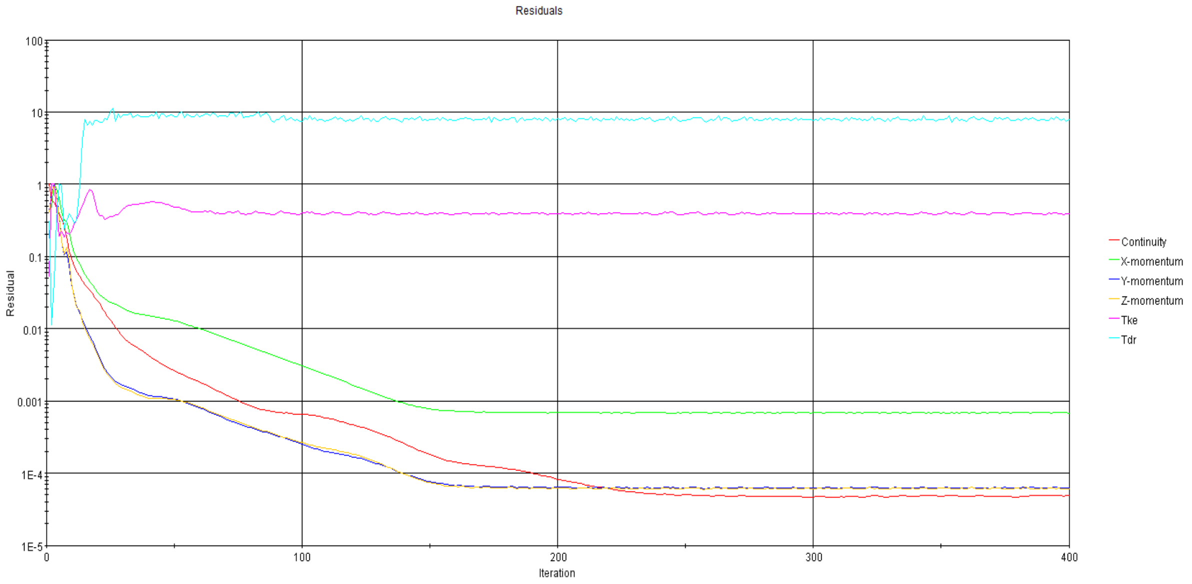

Figure 2.5. Typical STAR-CCM+ steady state convergence plot.

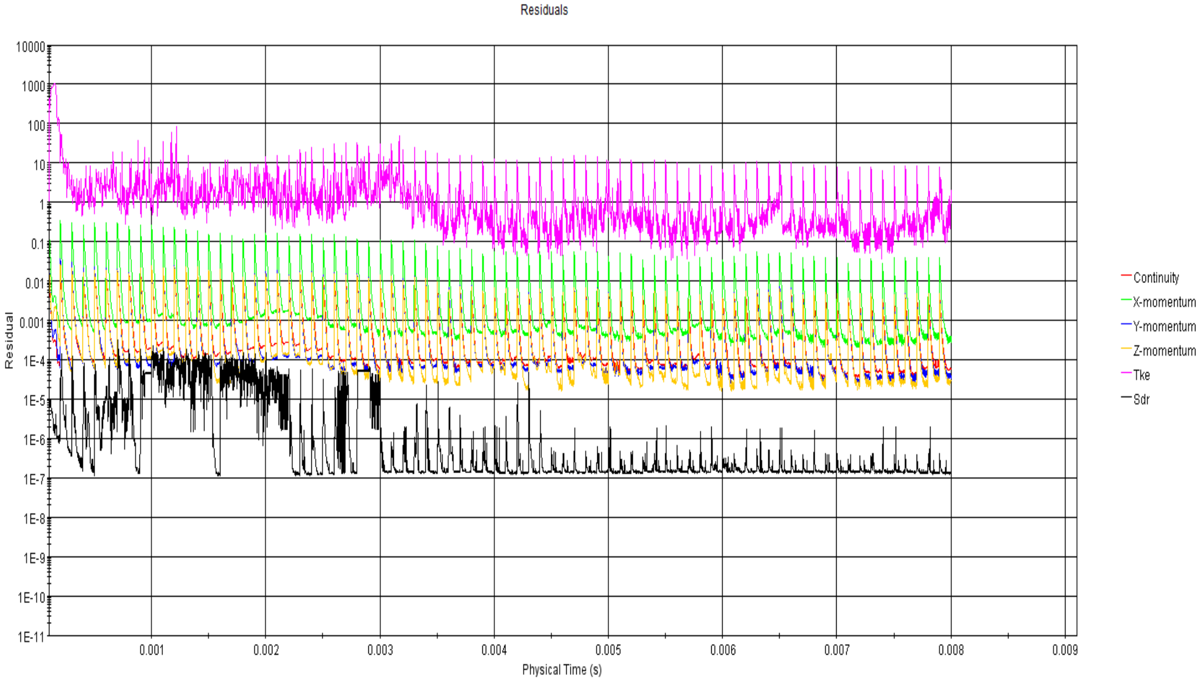

Figure 2.6. Typical STAR-CCM+ unsteady state convergence plot.

CHAPTER 3: EXPERIMENTAL INVESTIGATION

3.1. Introduction

A series of experiments were conducted to quantify the flow characteristics of the counterbalance valve through its operating pressure range. A hydraulic test bench instrumented to measure flow rate, temperature, and pressure using a computer based data acquisition system was used. A data acquisition program using LabVIEW-NI (2011-32-bit) was written to record the test results.

The main objective of the experimental studies was to explore design modifications that would eliminate the generation of the high frequency noise. A secondary objective was to identify the influence of the different components in noise generation.

The experimental procedure used in all of the tests and the operational details of the hydraulic test bench are discussed and explained in the following sections.

3.2. Experimental Apparatus

The main components of the hydraulic system used are: a test bench, a hydraulic power unit, a high voltage supply, and a data acquisition system. The test bench was certified operational after successful testing of *benchmark* valves.

3.2.1. Hydraulic Power Unit

The power unit provides high-pressure hydraulic oil for use by the test bench. The power unit is located 10 feet from the test bench, behind the electric control panel wall, affording the operator a measure of protection and reducing the noise level in the lab. It consists of a main reservoir, suction strainer, vane charge pump, heat exchanger, four-micron filter, three high-pressure three-stage gear pumps, and several check valves and pressure relief valves. Fifty-five gallons of Chevron AW 32 hydraulic oil are stored in the main reservoir. Two pictures of the hydraulic power unit and the hydraulic circuit are shown in Figures 3.2 and 3.3 respectively. Four electric motors power the unit. One is double ended and operates the charge pump and a gear pump, and two others power the remaining two gear pumps. The fourth motor powers the test bench reservoir return pump.

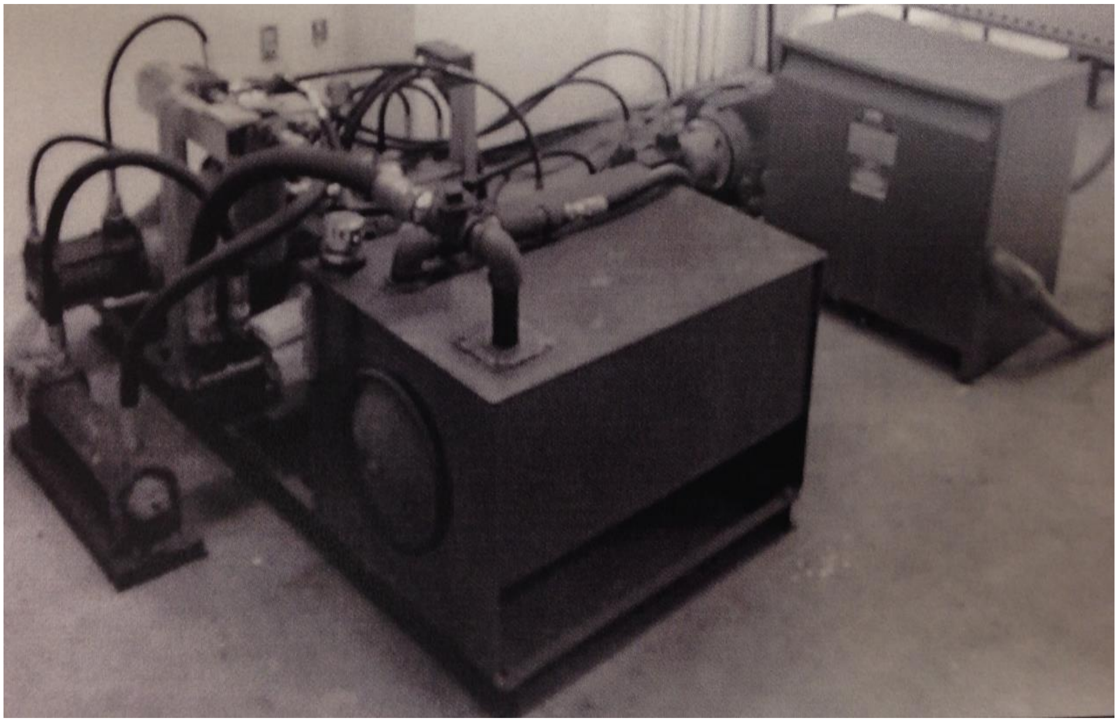

Figure 3.1. Hydraulic power unit, oil reservoir (front), 208/480 vac transformer (right), oil/water heat-exchanger (left), pumps (behind oil reservoir).

3.2.2. High Voltage Supply

The operation of this hydraulic system requires high voltage power. The high voltage supply powers the pump motors as shown in Figure 3.4. The building main electric panel is supplied three-phase power at 208 V. It feeds a single-phase breaker panel and a three-phase transformer. The transformer raises the voltage from 208 to 480 volts. This high voltage powers the three starters that control the charge and gear pump motors. The main electric panel also feeds power to the single-phase motor starter and the test bench. The motor starters, local disconnect and breaker panels are installed next to the test bench.

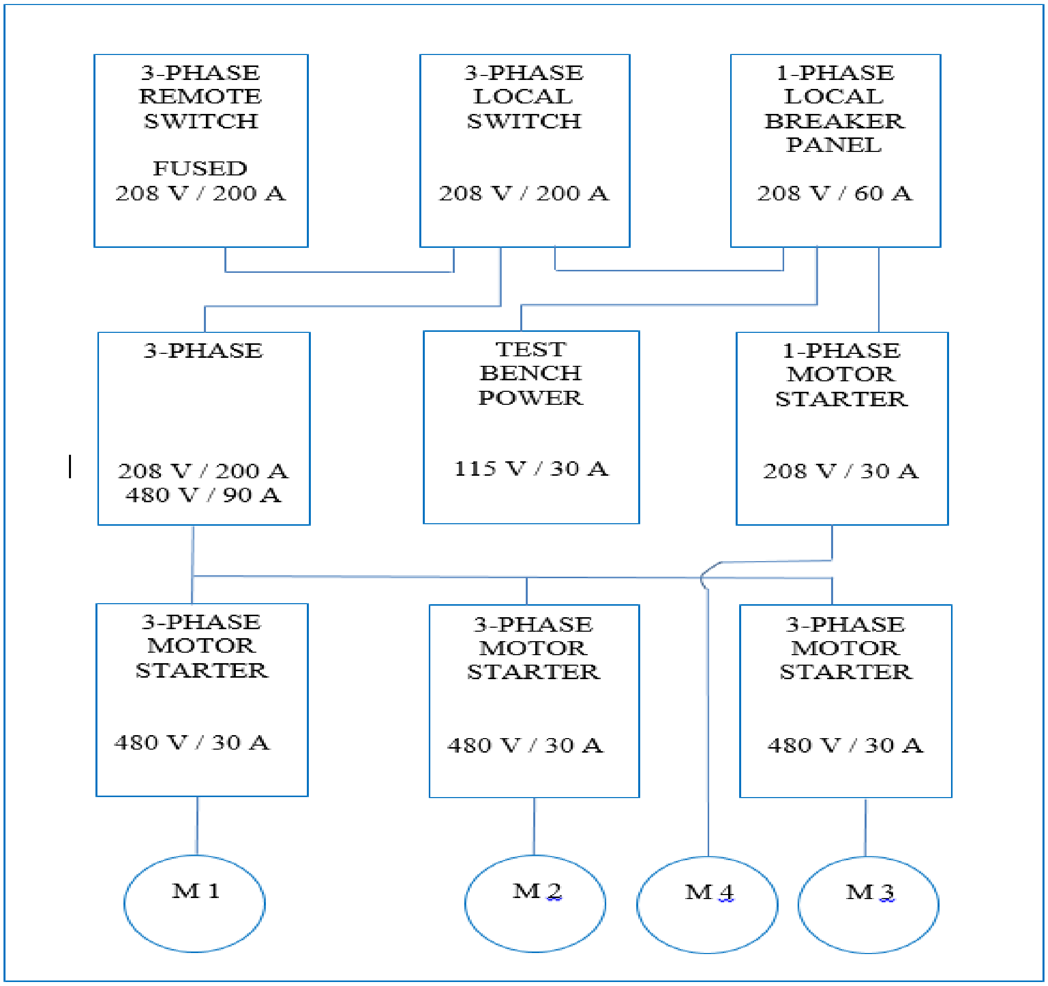

Figure 3.2. High voltage schematic.

3.2.3. Hydraulic Test Bench

The hydraulic test bench is the most important component of the hydraulic system. A picture is shown in Figure 1.10. It contains a fluid collection system that consists of a four-foot by five-foot steel basin set on steel supports, with high back and left side walls for mounting components and low front and right side walls for access. It has an integral sump with a total capacity of 40 gallons.

Oil is drawn from the main reservoir through a suction strainer with a vane pump. After filtering, the vane pump provides the three high-pressure pumps with positive charge oil. Any excess oil flows through a check valve and returns to the reservoir. Three pumps of a staged-gear design provide high-pressure oil to the rest of the circuit. The pumps are capable of delivering 24.6 lpm (6.5 gpm) each or a combined total of 73.8 lpm (19.5 gpm). The pumps can be run separately or all together. The inline check valves on the exhaust of the pumps prevent the pumps from motoring in reverse direction when not on use. The pumps are limited to a maximum of 275 bar (4000 psi) which is below the nameplate rating of 310 bar (4500 psi). Direct acting relief valves provide very quick operation and are less susceptible to contamination than pilot-operated relief valves. The outlet of the high-pressure pumps goes to a sequence valve that is set to open at 21 bar (300 psi) providing pilot-pressure for the logic circuit valves. This allows the motors turning the high-pressure pumps to start with a small load. The high-pressure oil is also directed to solenoid valves that apply the pilot-pressure to the controlling valves to create the desired flow path. Circuit operation is described in the truth presented in Figure 3.1. Solenoid S1 needs to be switched on to provide the oil flow path for “P” to “A”. The all ports blocked condition is only possible momentarily while the solenoid valves are shifting. This an important safety issue when working with high-pressure positive displacement pumps because high-pressure can be unexpectedly develop very quickly if the outlet is blocked. The pressure would then only be limited by the relief valves at the pumps. The oil flowing out of the “A” work port goes to the load side of the counterbalance valve being evaluated. The pressure at this port is controlled by a pilot-operated relief valve. A pilot-operated relief valve is used in this position instead of a direct-acting relief valve because they can be easily adjusted while subjected to high-pressure. Pilot-pressure for the counterbalance valve is developed by tapping the high-pressure oil ahead of the relief valve and plumbing it through a needle valve to a pressure-reducing valve. This reduced pressure is plumbed to the pilot port of the counterbalance valve. The needle valve was placed in series with the pressure-reducing valve so that the pilot flow could be shut off. Oil flowing out of the valve port of the counterbalance valve must flow through a relief valve before returning to the reservoir.

Again, a pilot-operated relief valve is used in this position so that it can be adjusted under pressure. This relief valve simulates the downstream flow restrictions that cause backpressure at the valve port. All of the oil form the control portion and test portion of the test stand is dumped into a basin for collection and pumped through a heat exchanger before going back to the reservoir.

3.2.4. Data Acquisition System

Data acquisition was carried out using a National Instruments PCI-MIO-16E-4 data acquisition card using LabVIEW (version 2011). The card is capable of a 500 KS/s single channel scanning rate, 250 KS/s stream-to-disk data rate at a 12-bit resolution for analog inputs. The card can be configured for sixteen single-ended or eight differential analog inputs. It can be used for input ranges from ±0.05 V to ±10 V, with a maximum resolution better than 5μV.

Two pressure transducers rated to 1000 and 5000 psia were used to measure the pressure at the valve inlet and outlet. The transducers generate an output voltage from 0 to 5 vdc, and their natural frequency is greater than 400 KHz. A National Instruments terminal box model SCB-68, interfaces the transducers with the data acquisition card.

A EG&G turbine flow meter was used to measure the fluid flow in the test circuit. The flow meter was calibrated for 33.6 cSt kinematic viscosity hydraulic oil for a range of 0 to 30 gpm and its output is corrected for temperature variations. It provides a linear output from 0 to 5 vdc.

Fluid temperature is measured at the outlet of the flow meter with a fine wire T type thermocouple. A schematic diagram of the data acquisition system wiring is shown in Figure 3.5.

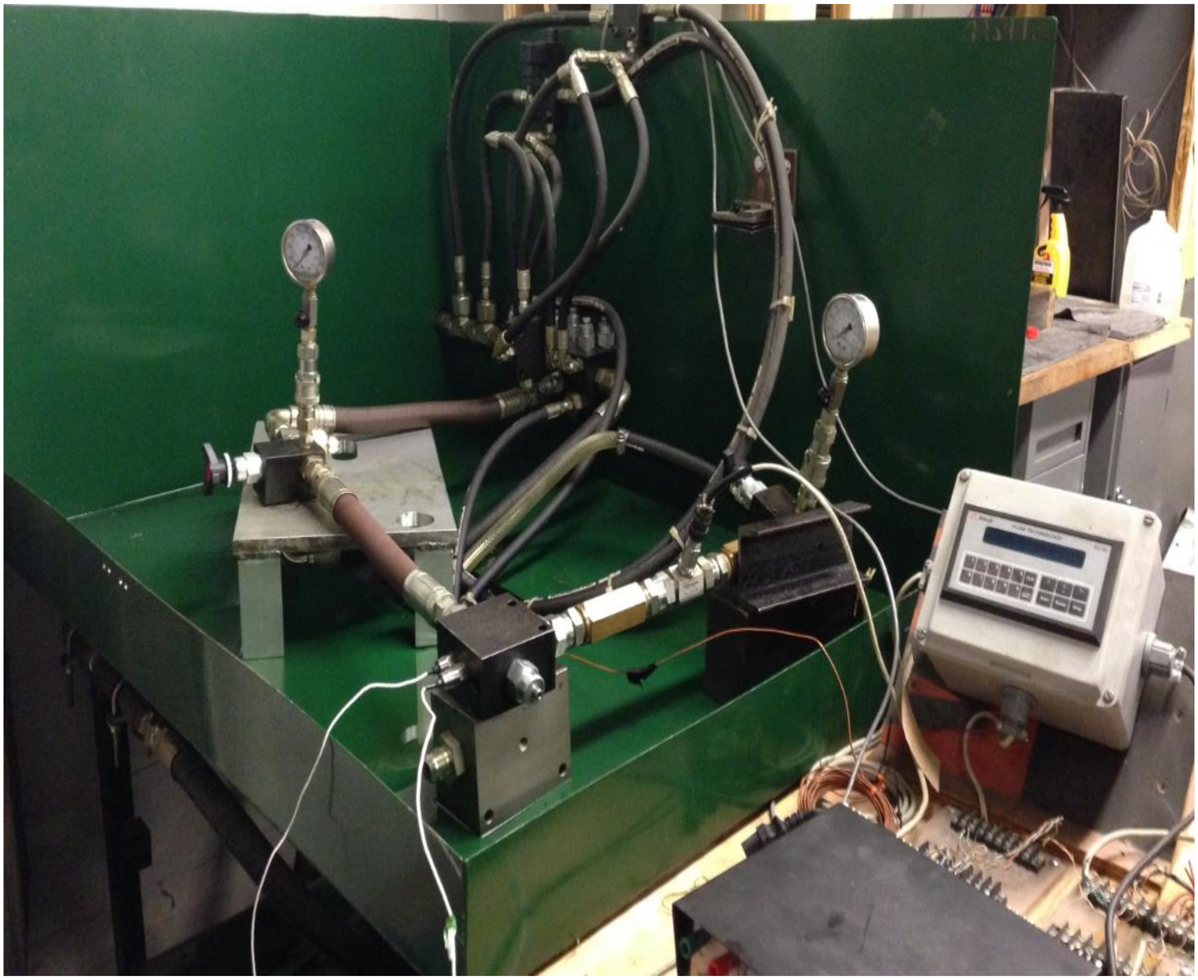

Figure 3.3. Test bench hydraulic test circuit.

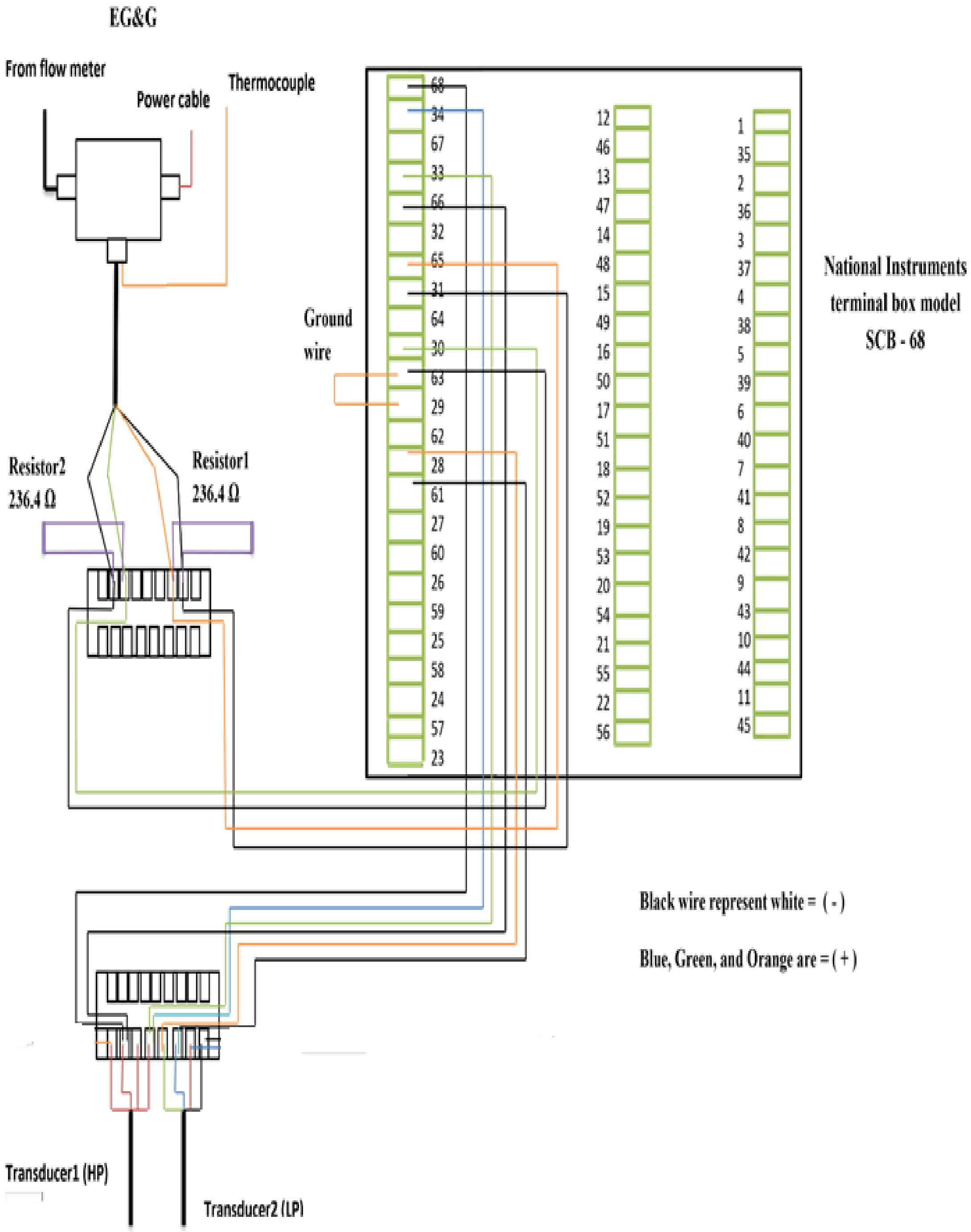

Figure 3.4. Schematic diagram of the data acquisition system.

3.3. Experimental Procedure

The experimental procedure varies with the pressure range of the test valves. The hydraulic system configuration depends on operating pressure range of the counterbalance valves. The pressure transducers were selected to match the maximum full flow pressure while the inlet pressure control (IPC) valve was selected to match the minimum cracking pressure of the test valves. The two pressure transducers have operating pressure ranges from zero to 1000 and zero 5000 psid. The three-inlet pressure control valves have operating pressure ranges from 25 to 400 psig, 25 to 800 psig, and 150 to 4500 psig. Installing the counterbalance valve completes the hydraulic circuit.

After the components were selected and installed, the system was started. Water supply to the oil-water heat exchanger was set to a 6 gpm flow rate. The charge pump and high-pressure pumps were started. The basin sump return pump was started and the divider manifold valves adjusted until the basin sump fluid level was steady at its operating level. The oil was circulated through the system until it warmed to approximately 40 $^{\circ}$C. Solenoid S1 was energized to activate oil flow through the test circuit, and the inlet pressure control valve was cycled to remove air from the test valve and lubricate its internal parts. The test valve was set into the manifold. The test bench was now ready to begin data acquisition. After recording all the data the system was shutting down.

CHAPTER 4: RESULTS AND DISCUSSION EXPERIMENTAL WORK

4.1. Introduction

An experimental investigation was conducted to determine the conditions under which the whistling noise was generated and to characterize the flow parameters present in that condition. Upstream and downstream dial pressure gages were used to measure average pressures upstream and downstream of the counterbalance valve and a temperature compensated flowmeter connected to the data acquisition system recorded the flowrates. Upstream and downstream pressures could be controlled though needle valves located just upstream of the upstream and downstream pressure gages. A pressure transducer with a natural frequency larger than 400 KHz installed at the valve outlet port was used to record the downstream pressure fluctuations.

Table 4.1. Geometry differences in counterbalance valves A and B

Description	**Type A**	**Type B**
Piston sleeve angle	45 °	14 °
Piston sleeve radius	0	0.0471 in
Poppet gap radius	0.2969 in	0.0971 in
Poppet Expansion radius	0.2969 in	0.1988 in

Both types of counterbalance valves (A and B), shown in Figures 4.1, and 4.2 were investigated. Table 4.1 shows some of the geometry differences between the two of valves. It was hoped that the modifications in type B would result in reduced noise generation when compared to type A.

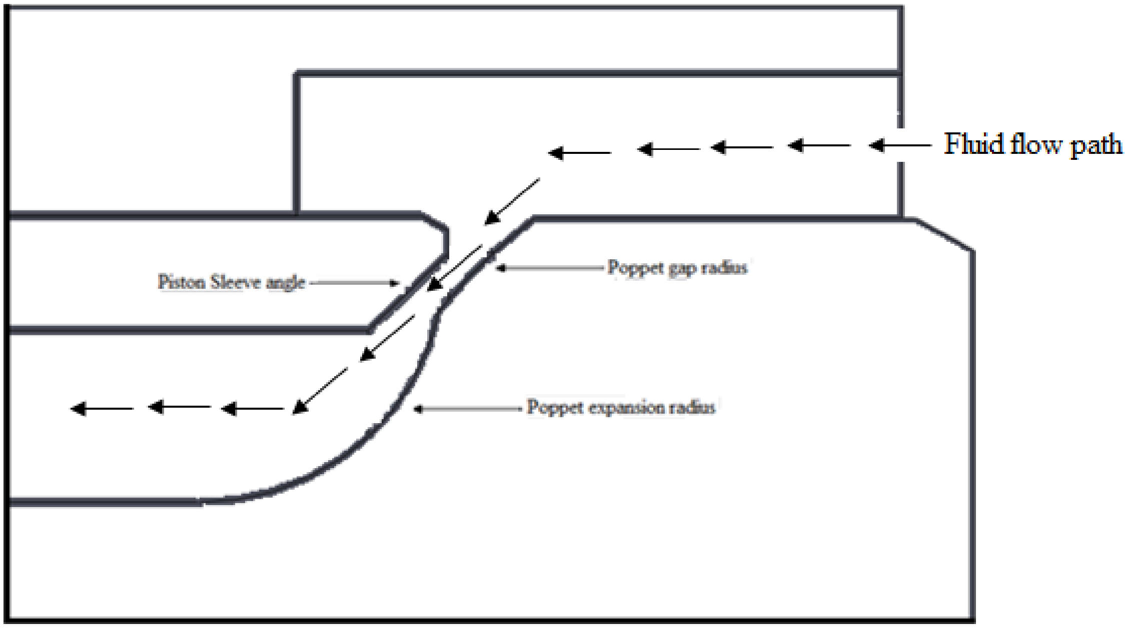

Figure 4.1. Piston and poppet geometry on counterbalance valve type A.

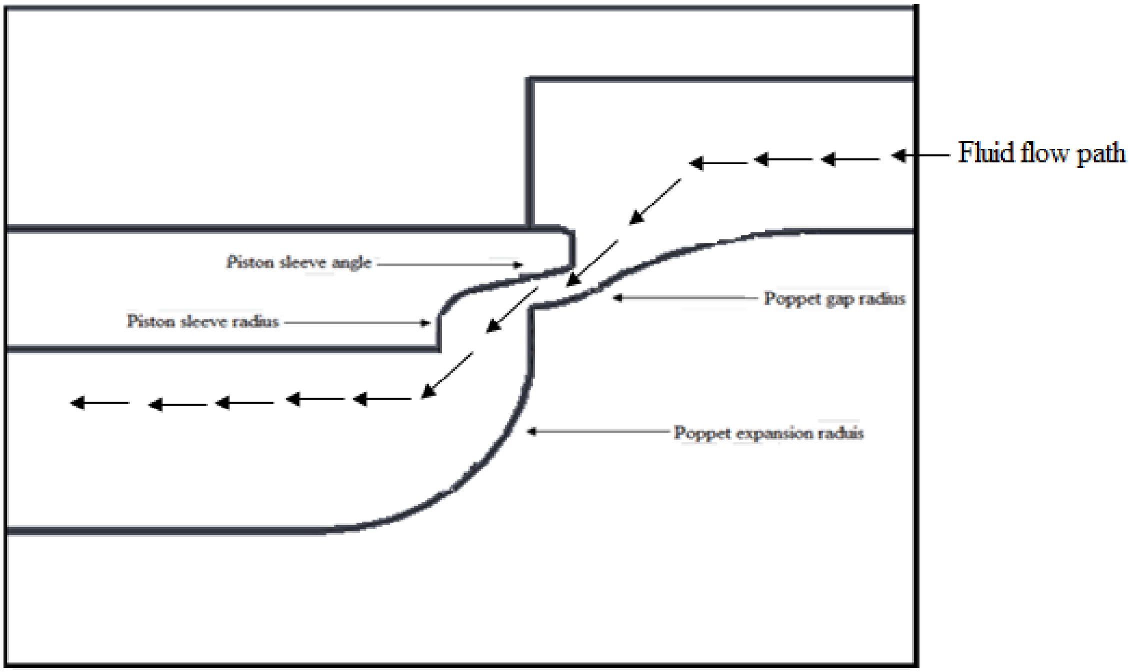

Figure 4.2. Piston and poppet modifications on counterbalance valve type B.

4.2. Experimental Procedure

A thorough investigation of the conditions required to generate the desired whistling sound in valve type A was conducted. Through trial an error it was determined that whistling can be generated in a great number of conditions. Once the downstream pressure was set, the upstream pressure can be changed in order to generate the desired effect or vice versa.

It is important to note that finding then instability associated with the noise generation strongly depends in the operational procedure used and not only on the operational conditions. In general, slow changes may result in an unstable condition generating the desired noise, while a rapid change in pressure may not. Once a whistling sound has been generated it is sometimes possible to maintain it through further increases in pressure. It is also important to note that valve behavior is subject to hysteresis and that oil temperature effects are significant. Typically different results are obtained when upstream pressure is increased as opposed as when it is decreased. As it was our purpose, through trial and error we became very proficient in noise generation, and, in this respect, our procedures may not be representative of normal valve operation.

4.3. Results

4.3.1. Results of the Type A Valve

As mentioned above, the desired whistling effect can be obtained through a great number of operational conditions. It was decided to characterize the flow by looking at its behavior for a fixed setting of the downstream needle valve (equivalent to an almost constant downstream pressure) from zero flow conditions to full flow. Once this was accomplished, tests were carried out at other downstream pressures in an effort to correlate the results.

A nominal initial back (downstream) pressure of 200 psi was set for our first trial. The valve opened at slightly below 300 psi upstream pressure and the pressure was slowly increased until it was fully opened at a pressure slightly below 2000 psi and a flowrate of 6.59 gpm. At this point the back pressure had risen to a value of 250 psi. Data was recorded at approximately 0.5 gpm intervals. Once full flow was achieved, upstream pressure was slowly decreased until the valve closed. Again, data was recorded at 0.5 gpm intervals at flowrates halfway between those of the upward run.

A medium amplitude whistle was first obtained at a flowrate of 2 gpm (Mode 1). It persisted until approximately 3 gpm. At this flowrate, it changed to large amplitude whistle and persisted until reached flow of 4 gpm. From this point, it decreased in intensity as the flowrate was increased and it disappeared at 6.2 gpm (Mode 2). As the upstream pressure was decreased from its full flow value, the Mode 2 amplitude whistle reappeared at approximately 6 gpm, transitioning at approximately at 3 gpm to a medium amplitude whistle Mode 1. At 1.8 gpm, small amplitude whistle with high frequency appeared (Mode 3), disappearing very quickly at 1.5 gpm.

An analysis of the downstream pressures shows that, even for the conditions in which no amplitude whistle is present, the downstream pressure fluctuations are significant. Figure 4.3 (1.04, 1.3 and 1.52 gpm) and Figure 4.4 (6.25 and 6.69 gpm) show the pressure traces for those conditions. In the first case, the oscillations are organized and increasing in amplitude with the flowrate, while in the second they are random with an amplitude of about 20 psi.

Pressure oscillations for modes 1 and 3 are shown in Figure 4.5. The oscillations are much larger (40 to 50 psi) and, except for the highest flowrate (2.75 gpm), quasi sinusoidal in nature. At 2.75 gpm the flow is close to transitioning to Mode 2. Mode 2 behavior is shown in Figure 4.6. Pressure oscillations are much larger, of the order of 200 psi, and show significant deviations from the sinusoidal behavior.

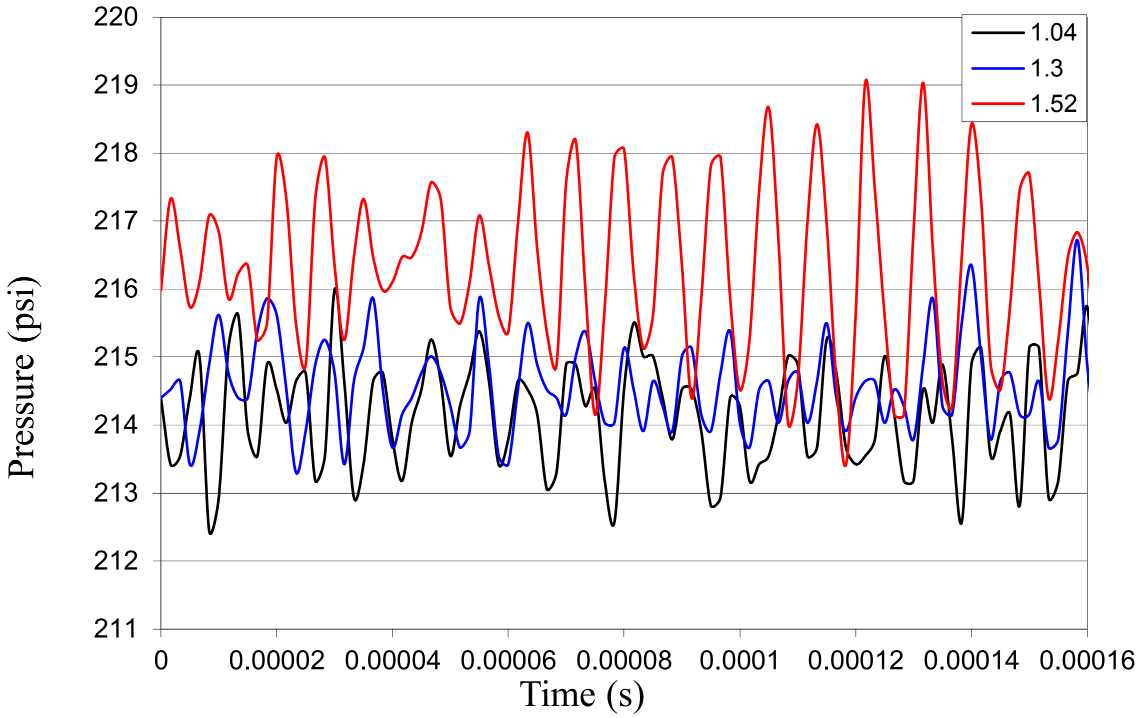

Figure 4.3. Type A valve downstream pressures at 1.04, 1.3 and 1.52 gpm.

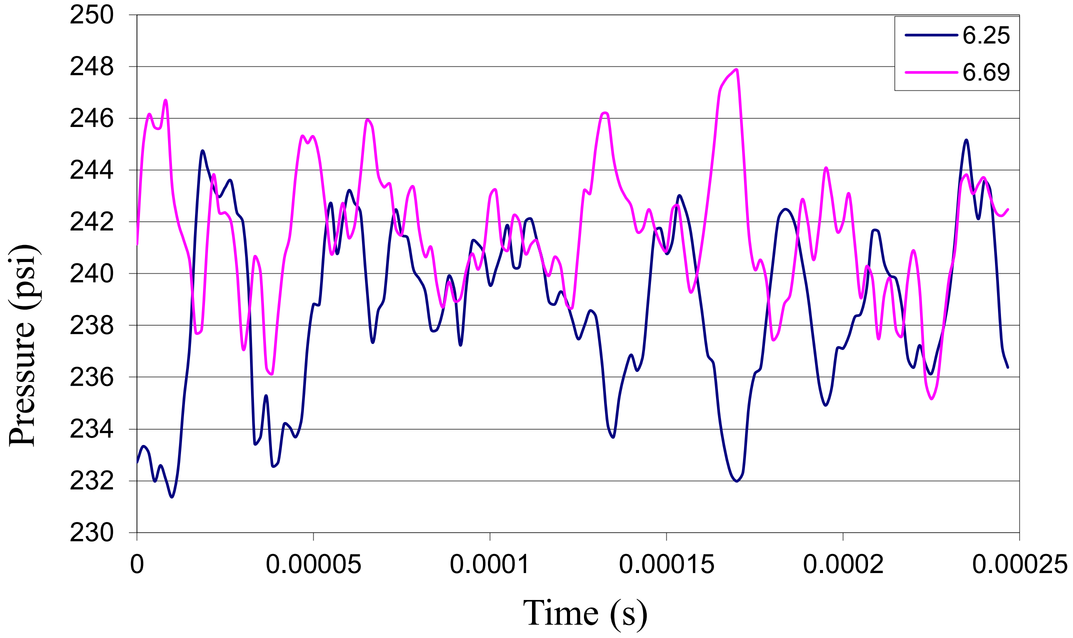

Figure 4.4. Type A valve downstream pressures at 6.25 and 6.69 gpm.

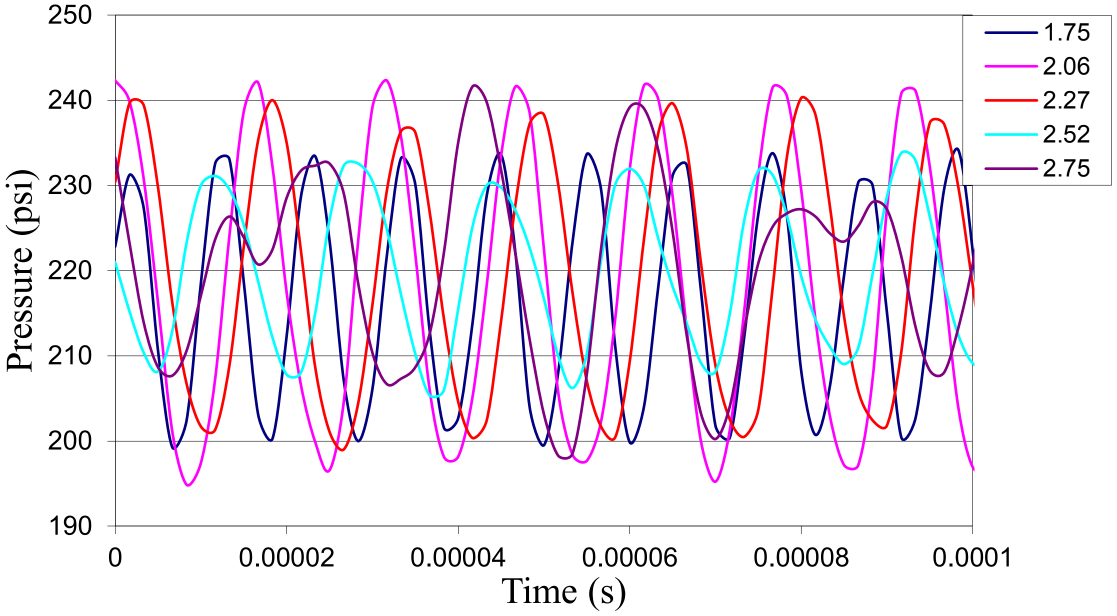

Figure 4.5. Type A valve downstream pressure oscillations for Modes 1 and 3.

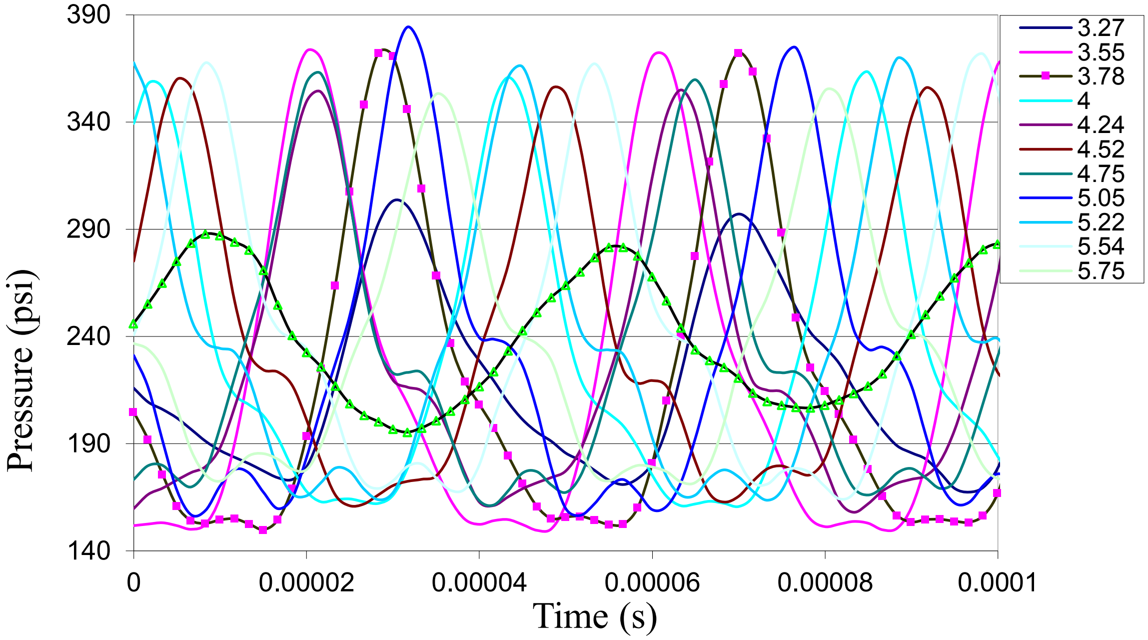

Figure 4.6. Type A valve pressure oscillations for Mode 2.

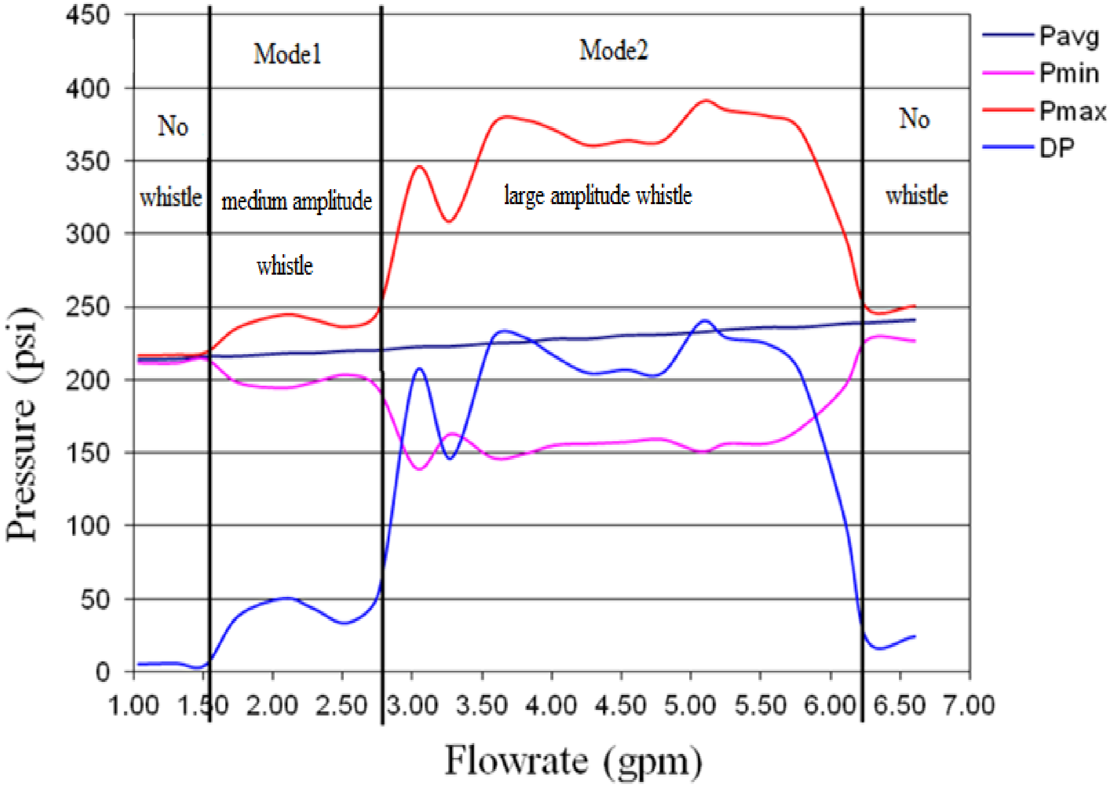

Figure 4.7. Type A valve maximum, minimum and average pressures as a function of flowrate.

A summary of these results is presented in Figure 4.7 that shows maximum, minimum and average pressures as well as pressure differential as a function of the flowrate. In it, the three regions are clearly identifiable: no amplitude and small pressure differentials (1-1.75, 6.25-6.75), modes 1 and 3 with pressure differentials of about 50 psi, (1.75-2.75) and Mode 2 with differential of 250 psi (2.75-6.25).

In order to capture the oscillation frequency, pressure data was collected at a 60,000 Hz. sampling rate and a Fast Fourier Transform (FFT) was used to extract the frequency information. A sample size of 1024 was used resulting in a frequency resolution of 58.59 Hz, which is acceptable for our purposes.

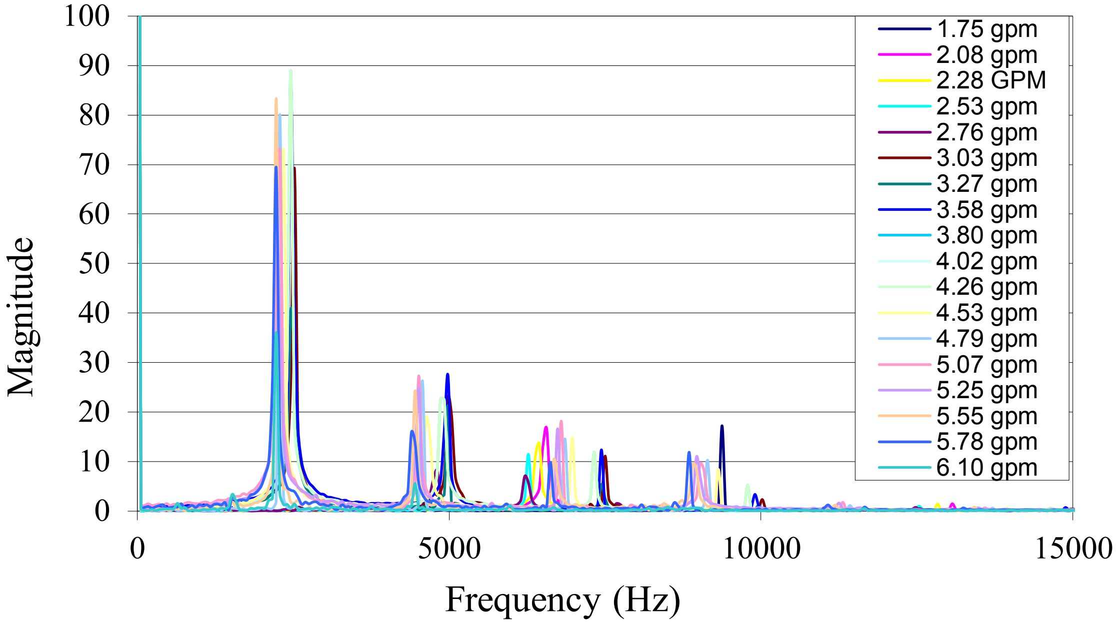

Figure 4.8. Type A valve frequency spectrum.

The result of this analysis is shown in Figure 4.8. As can be seen, 7 frequency clusters can be observed and there is no frequency information above 10000 Hz.

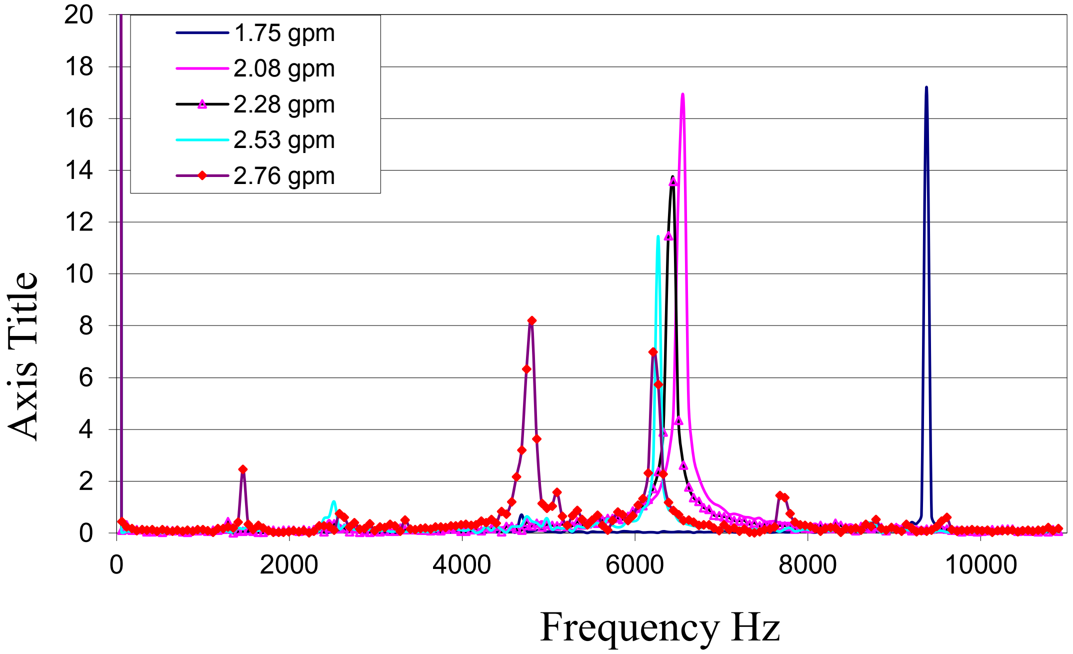

Figure 4.9. Type A valve frequency analysis of Modes 1 and 3.

A frequency analysis of Modes 1 and 3 is presented in Figure 4.9. The solitary peak at 9375 Hz corresponds to Mode 3, (1.75 gpm, going down) and the rest to Mode 1. Mode 1 frequencies cluster around 6300 Hz, the highest frequency being 6562 Hz at 2.08 gpm. Both frequency and amplitude decrease as the flowrate increases reaching a low value of 6269 Hz at 2.76 gpm. At this flowrate, the flow is close to transition to Mode 2 and two new peaks appear at 4804 and 1464 Hz, the one a 4804 Hz having a larger amplitude that the one at 6269 Hz.

Mode 2 results are presented in Figure 4.10. It shows a dominant frequency around 2460 Hz with lower magnitudes at twice and three times this value. The amplitude of the dominant frequency peaks at a flowrate of 4.26 gpm.

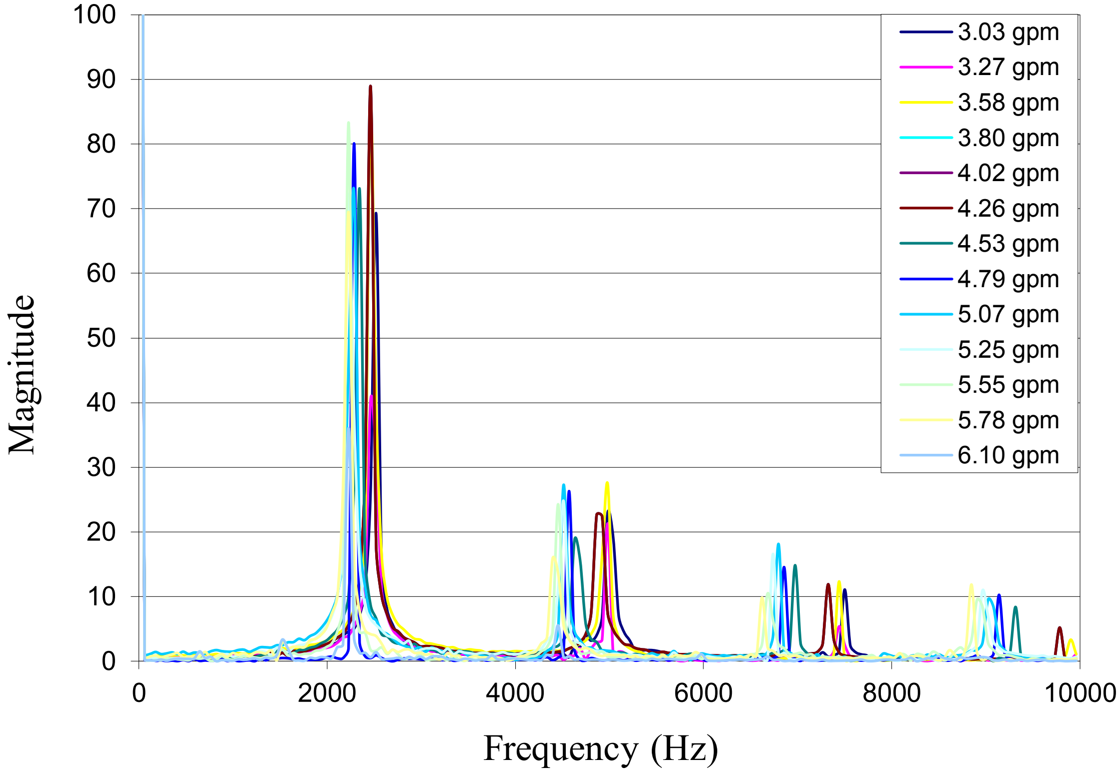

Figure 4.10. Type A valve frequency analysis of Mode 2.

To illustrate the influence of the downstream pressure, the behavior of the valve at nominal backpressures of 160, 260 and 300 psi is described below. For the 160 psi downstream pressure run, a small amplitude appeared at an upstream pressure of 1500 psi and a 1.82 gpm flowrate. At 260 psi downstream pressure, medium amplitude was found when the upstream pressure reached 2000 psi at 2.25 gpm. Increasing the backpressure to 300 psi resulted in a larger amplitude at an upstream pressure of 3000 psi and 4.69 gpm.

Pressure data was sampled at 30,000 Hz and, as before, an FFT was used to obtain the frequency information. The results are presented in Figure 4.11 and Figure 4.12. The downstream pressure fluctuations for all three runs are shown in Figure 4.11 showing quasi sinusoidal fluctuations for the two lowest flowrates and a more complex pattern for the highest one.

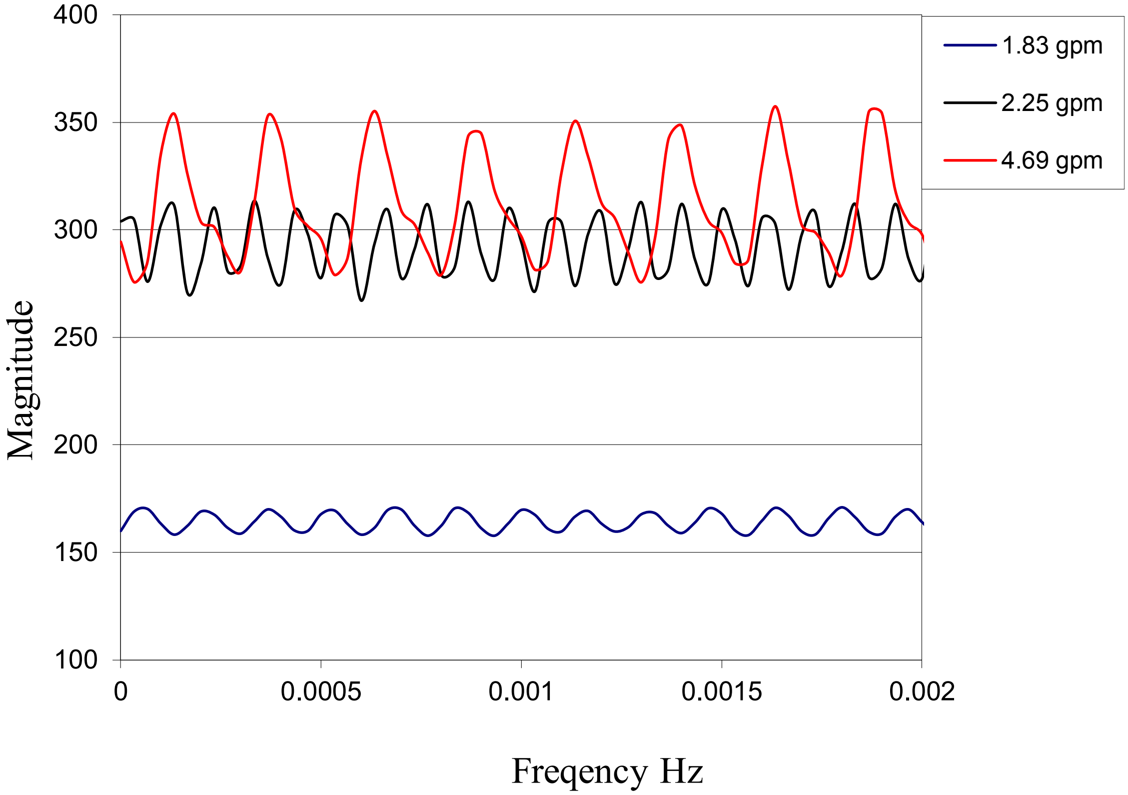

Figure 4.11. Type A valve downstream pressure fluctuations.

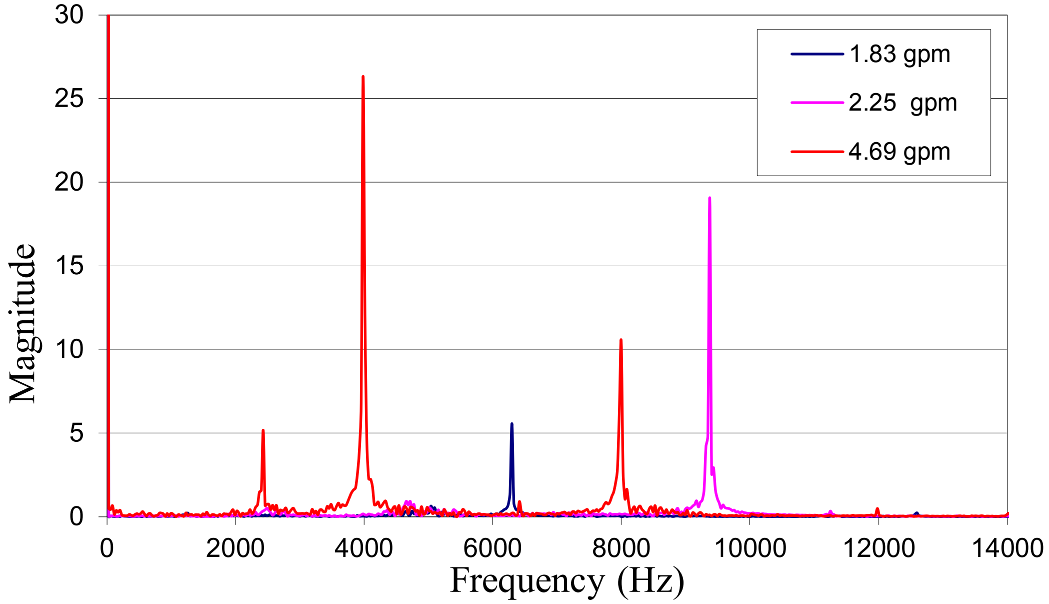

Figure 4.12. Type A valve FFT analysis at 1.83, 2.25, 4.69 gpm.

The FFT analysis results presented in Figure 4.12 confirm the pressure results. They show a single frequency for the 1.82 and 2.25 gpm flowrates, corresponding to modes 3 and 1, while the frequencies present at 4.69 gpm are suggestive of a Mode 1 to Mode 2 transition.

A summary of these results is presented in Table 4.2. The table includes a subjective description of the amplitude type and also indicates if it was obtained as pressures were increased (up) or decreased (down). Frequencies are listed according to their magnitude as determined by the FFT. It is interesting to note that as Mode 1 transitions to Mode 2, at 2.76 gpm; its dominant frequency is the 2nd dominant frequency of mode 2 and that the dominant frequency of the emerging Mode 2 is half that value. Lowering the backpressure to 160 psi also lowers the appearance of Mode 1 to 1.82 gpm, while raising it to 260 psi causes mode 3 to appear at the much higher flowrate of 2.25 gpm. The frequency spectrum at 4.46 gpm is interesting in that it appears to be transitional presenting a large signal at the Mode 2 dominating frequency. Summary of the results at down-stream pressure of 160, 260 and 300 psi are presented in Table 4.3.

Table 4.2. Summary of type A valve at 200-psi of down-stream pressure

gpm	**Up /Dwn**	**Whistle/mode**	**Frequency**			**P_{min}**	**P_{max}**	**ΔP**	**P_{avg}**
1.04	U	No				211	216	5	214
1.30	D	No				211	217	6	215
1.52	U	No				214	219	5	216
1.75	D	Small ampt-mode3	9375			197	236	38	216
2.08	U	Med ampt- mode1	6562			194	245	50	218
2.28	D	Med ampt- mode1	6386			197	242	44	219
2.53	U	Med ampt- mode1	6269			203	237	33	220
2.76	D	M-L ampt- mode1	4804	6269	1474	194	247	54	220
3.03	U	larger ampt- mode2	2519	4980	7500	139	345	206	223
3.27	D	larger ampt- mode2	2460	4980	7441	165	309	146	223
3.58	U	larger ampt- mode2	2460	4980	7441	146	375	229	225
3.80	D	larger ampt- mode2	2460	4980	7324	149	378	229	226

Table 4.2. (Continued)

4.02	U	larger ampt- mode2	2460	4980	7324	155	372	217	228
4.26	D	large ampt- mode2	2460	4980	7324	156	361	205	228
4.53	U	large ampt- mode2	2343	4628	6972	157	365	207	231
4.79	D	large ampt- mode2	2285	4570	6855	159	364	205	231
5.07	U	large ampt- mode2	2285	4511	6796	151	391	240	233
5.25	D	Med-L ampt- mode2	2226	4511	6738	156	385	229	234
5.55	U	Med-L ampt- mode2	2226	4453	6679	156	381	224	236
5.78	D	Med-L ampt- mode2	2226	4424	6621	166	372	205	236
6.10	U	Med ampt- mode2	2226	4453	1523	195	299	104	238
6.26	D	No				227	249	21	239
6.60	U	No				227	251	24	241

Table 4.3. Summary of type A valve at 160, 260 and 300 psi of down-stream pressure

gpm	Whistle	Frequency			P_{min}	P_{max}	ΔP	P_{avg}
1.82	Small ampt	6200			156	172	16	164
2.25	Med ampt	9320			266	318	52	292
4.69	Med-L ampt	3984	7998	2431	268	368	100	318

4.3.2. Results of the Type B Valve

Investigation of the type B valve was carried out following the experimental procedures used with type A. Type B, however, proved to be far more "whistle resistant" that type A and could only be made to whistle under a narrow set of test conditions.

A small amplitude corresponding to a frequency of 1113 Hz (with a very small peak at twice that frequency) was found at a much lower upstream pressure (900 psi) and flowrate (1.25 gpm) than for type A. This oscillation mode was not found in the type A valve. The three other instability test points take place at frequencies of 6269 and 6563 Hz (twice) which fall within the Mode 1 frequency range found in type A. The pressure plot for these instabilities is presented in Figure 4.13. For the Mode 1 type instability, the magnitude of the pressure oscillations ($\Delta P \approx 50$ psi) is similar to that of the type A valve. Only two modes can be found in the FFT plot shown in Figure 4.14. It clearly shows the low flow, low-pressure 1113 Hz component as well as the two other Mode 1 frequencies. The similarity of the Mode 1 component to that fond in the type A valve is remarkable once we eliminate from the latter the transitional frequencies corresponding to the 2.75 gpm data point. Table 4.4 summarizes the test results.

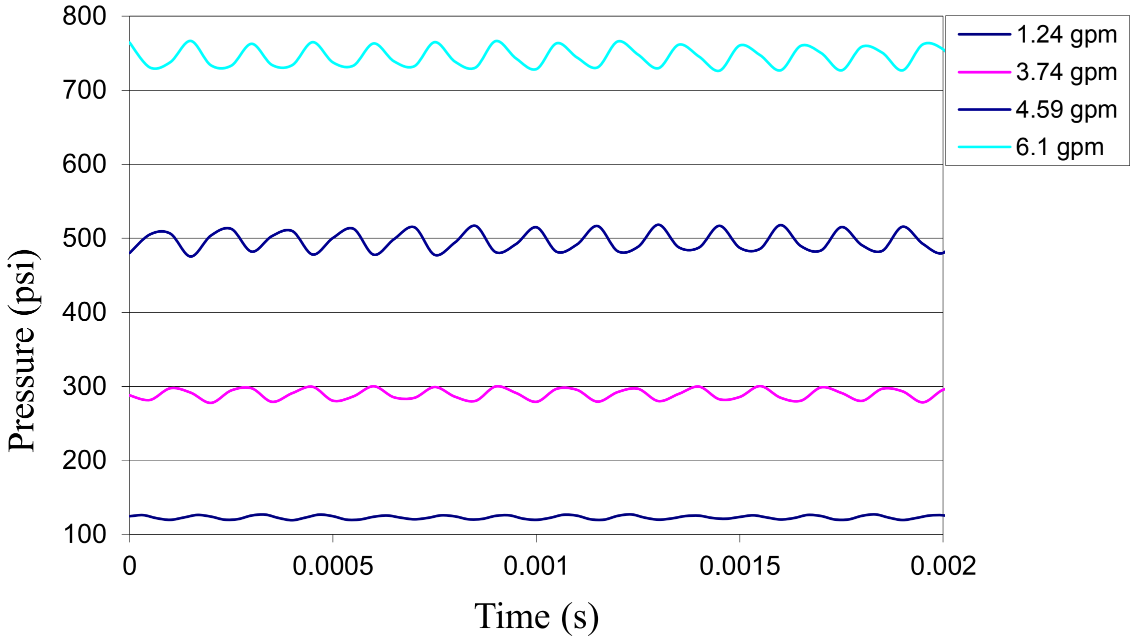

Figure 4.13. Type B valve downstream pressure fluctuations.

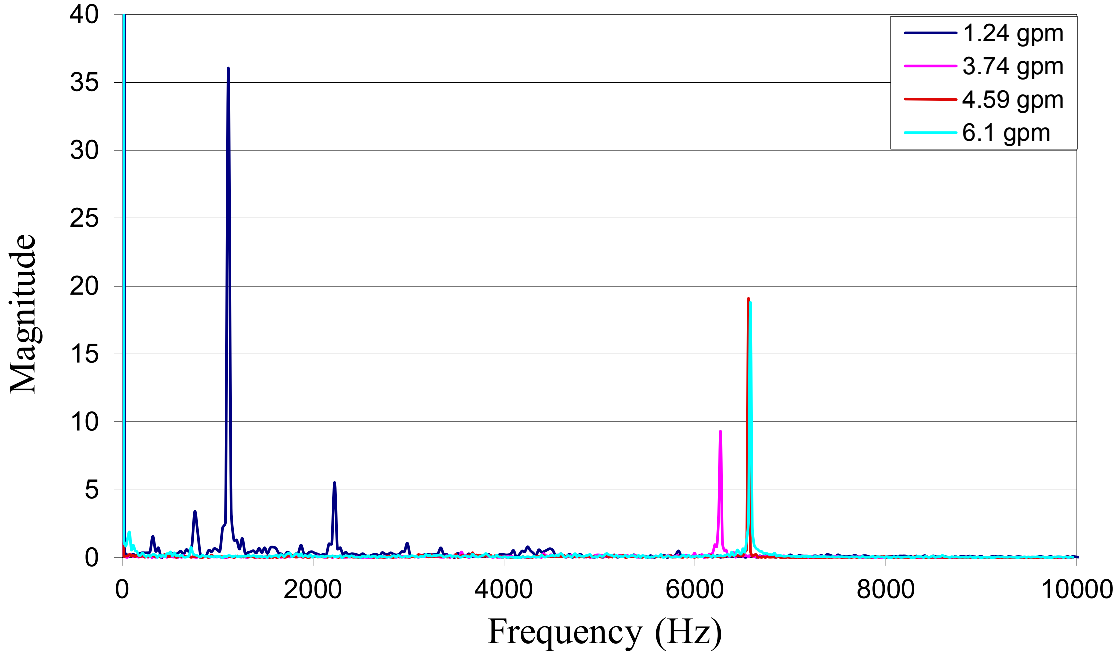

Figure 4.14. Type B valve FFT analysis at 1.24, 3.74, 4.59, 6.1 gpm.

Table 4.4. Summary of type B valve behavior

P_{upst}	**P_{dst}**	**gpm**	**Whistle**	**Frequency**		**P_{min}**	**P_{max}**	**ΔP**	**P_{avg}**
900	125	1.24	Small ampt	1113	2226	118	128	10	123
1800	300	3.74	Med-L ampt	6269		276	304	29	290
2600	500	4.58	large ampt	6563		475	518	43	497
3500	750	6.06	large ampt	6563		717	771	54	745

4.4. Summary and Conclusion

It is clear that the pressure fluctuations are a complex phenomenon resulting from the interaction of a number of parameters that are on the one hand not easily identifiable and on the other poorly understood. Noise can be generated through a large number of upstream/downstream pressure combinations. Oscillations occur at a fixed frequency or at a set of frequencies. It appears that once an oscillation mode has been excited the magnitude of the pressure oscillations remains constant within that mode, the oscillations being mode dependent rather that upstream pressure dependent.

The presence of the Mode 1 oscillation in both valves despite the radically different internal flows strongly points out to the fact that the oscillations are indeed a resonance phenomenon and therefore heavily dependent on the overall valve shape and dimensions. The fact that Mode 2, has been suppressed in the type B valve solely through internal flow modification is encouraging in the sense that it might be possible through further modifications to suppress Mode 1 as well.

The task of suppressing these undesirable oscillations, however, is complicated by the presence of multiple excitation frequencies, as it is likely that the appearance of any of them may trigger a much more complex instability.

CHAPTER 5: RESULTS AND DISCUSSION NUMERICAL WORK

5.1. Introduction

The modifications of the seat, piston, poppet, and the sleeve components of the counterbalance valves were numerically investigated in order to study their influence on noise elimination. The two types of counterbalance valves (A, and B), were used in order to compare the results with the experimental ones. The counterbalance valves are axis-symmetric, consequently the numerical simulation geometry is also axis-symmetric, as shown in Figures 2.3 and 2.4. The path of fluid for all figures is from right to left.

The STAR CCM+ code used the dimensionless wall distance from the wall $y+$ (law of the wall), in order to get the results near the wall. It is assumed that the near-wall cells lie within the logarithmic region of the boundary layer, therefore the centroid of the cells attached to the wall should have $y+ > 30$.

For both valves the viscous effects dominate the gap flow. For small gaps the boundary layers may fill the narrow opening.

The simulation of the oscillatory nature of the flow was the primary goal of this research, so we are smoothly interested in the unsteady state solutions. A fully converged steady state simulation must be obtained first to be used as the initial state for the unsteady solution, this will facilitate the convergence of the unsteady state solution. Without using steady state simulation, it is difficult to obtain an unsteady state solution. A summary of the geometry and test conditions is shown in Tables 5.1.

Table 5.1. Counterbalance valve parameters for both types (A, and B)

Parameters	Scale
Gap-1	0.002 in
Gap-2	0.005 in
Gap-3	0.017 in
Inlet-pressure	700 psi
Outlet-pressure	300 psi

5.2. Steady State Solutions

The steady-state simulation does not depend on time, and it will run to the maximum number of iterations specified in the simulation solver control. The steady-state simulation must be obtained first to be used as the initial state for the unsteady solution; this facilitated the convergence of the unsteady-state solution. The steady-state simulations needed 400-iterations to converge. The convergence of a steady-state simulation is based on the relative change in the solution values between iterations. For both valves streamline, pressure, velocity-vector and velocity-scalar plots were obtained for three different piston displacements (gaps) as shown in Table 2.3. The gap is defined as the minimum distance between piston and poppet as shown in Figure 4.1.

5.2.1. Counterbalance Valve Type A

The velocity-scalar, velocity-vector, pressure and streamline plots for all three gaps are presented in Figures 5.1 to 5.15. It can be seen from the velocity-scalar plots shown in Figures 5.1 to 5.3 that the velocity is low everywhere except on the gap areas and that the velocity increases as the gap increases. Maximum velocities of 46, 78 and 93 m/s can be noticed at gaps of 0.002, 0.005 and 0.017 inches respectively. For the small gap, the velocity at the expansion area is very low close to the piston wall and then increases slightly towards the poppet. For the second gap, the piston wall velocity is higher than for the small gap with a faster growth towards the poppet. Much higher velocities for the whole area can be seen for the large gap case.

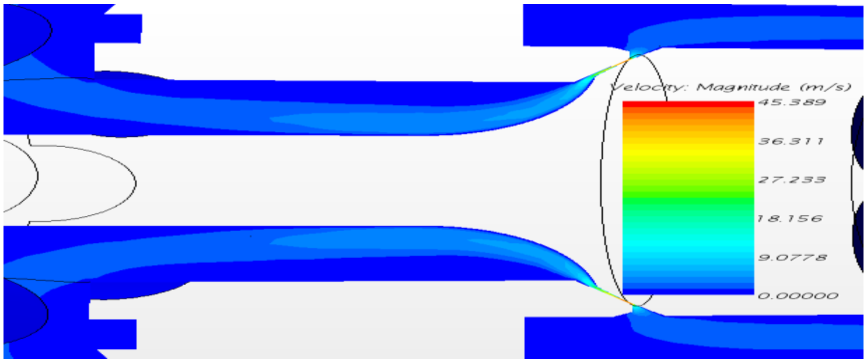

Figure 5.1. Steady state velocity scalar - type A- gap 0.002in.

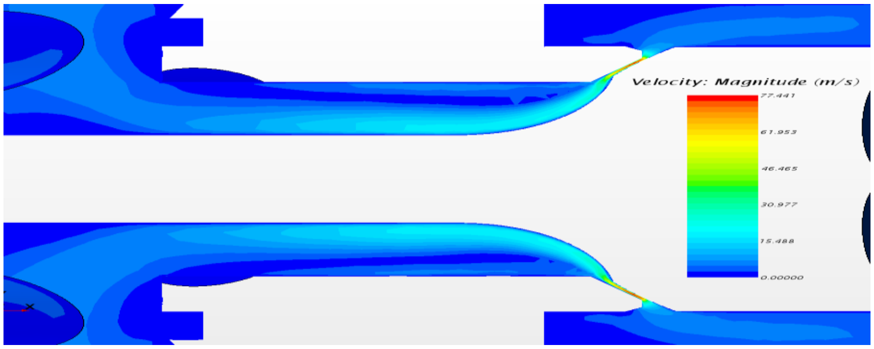

Figure 5.2. Steady state velocity scalar - type A- gap 0.005in.

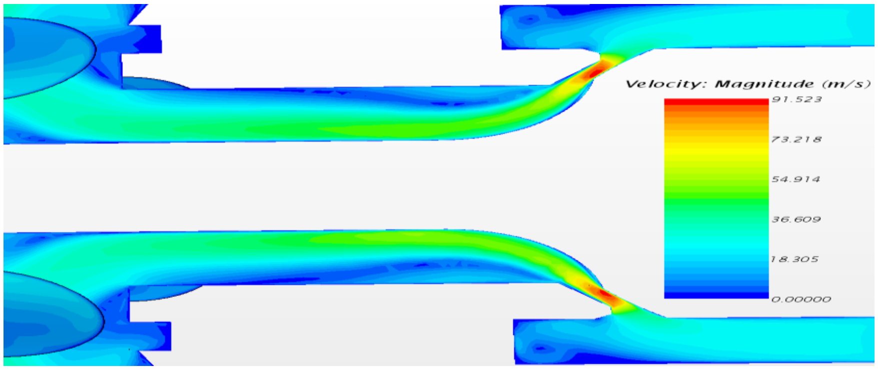

Figure 5.3. Steady state velocity scalar - type A- gap 0.017in.

The velocity-vector plots shown in Figures 5.4 to 5.6 confirm the results of the velocity-scalar plots showing low velocities dominant except on the gap areas. Recirculation areas can be seen at the dead-end areas of the fluid inlet (area above the gaps) and at the expansion areas, next to the throat, for all three gaps. The recirculation bubble in the expansion area forms close to the piston wall and grows smaller as the external velocity increases. For the smallest opening, the bubble is the largest and velocities the smallest, for the largest opening the bubble is much smaller and velocities much larger. The six different plots for the scalar and vector velocity are in agreement with the experiments of Porteiro et al. [13], and Weber et al. [14]. Animation of the velocity-vector plots for all three gaps showing the oscillatory nature of the flow through the valve can be seen on movies A-0.002in, A-0.005in and A-0.017in attached with this dissertation as (DVD). The videos clearly illustrate the fluid flow paths and recirculation bubbles. A small recirculation bubble can be seen above the gap inlet and a larger one at the gap outlet close to the piston wall. A non-recirculating fluid jet develops at the gap, passes between the recirculation bubble and the poppet, exiting at the left.

Flow-field pressure plots can be seen in Figures 5.7 to 5.9. All the numerical simulations were run with 700 psi upstream pressure and 300 psi downstream pressure. It can be seen that the pressure values before the gap are similar for the 0.002 and 0.005 inches plots. For the large gap, a noticeable pressure decrease can be observed before the gap. Pressure drops to 200 psi and stays constant through the gaps and at the expansion areas for gaps 0.002 and 0.005 inches. For the larger opening (0.017in) the pressure decreases in the gap to 250 psi and then increases to a constant pressure of 400 psi at the gap exit and the area of the expansion. The pressure drop across the gap decreases as the gap increases.

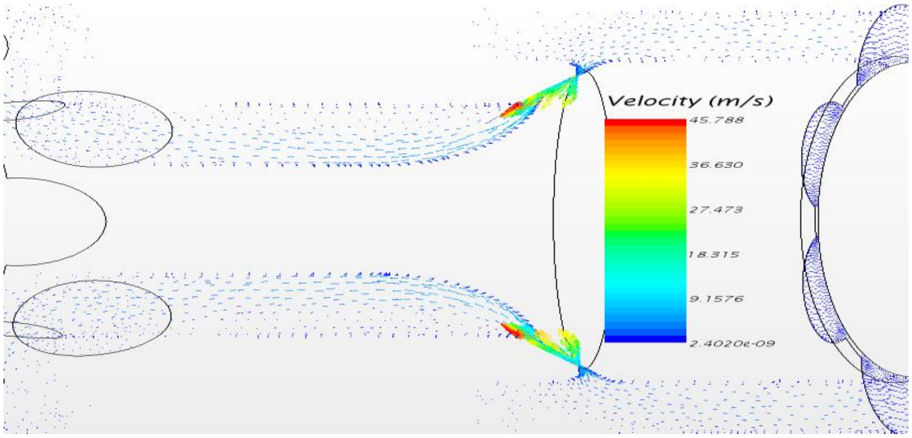

Figure 5.4. Steady state velocity vector - type A- gap 0.002in.

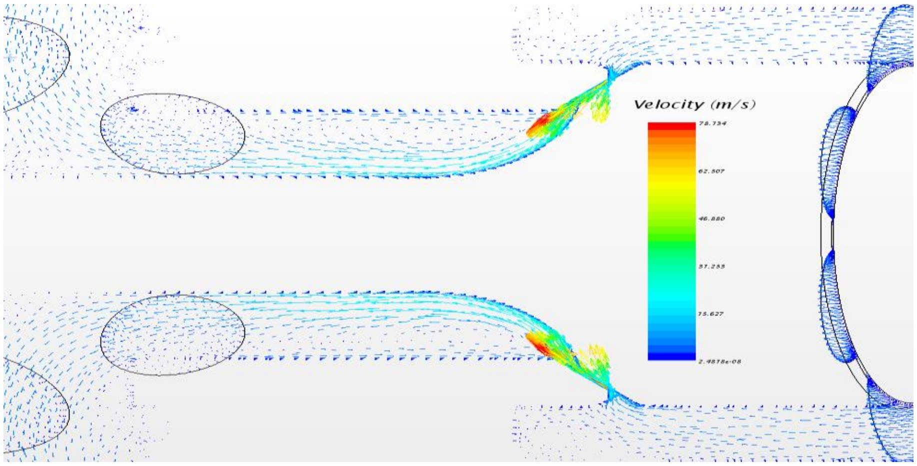

Figure 5.5. Steady state velocity vector - type A- gap 0.005in.

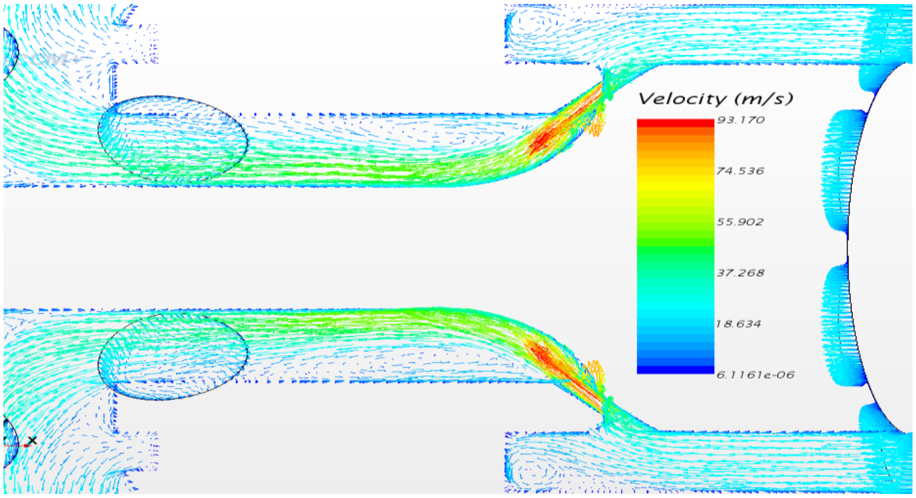

Figure 5.6. Steady state velocity vector - type A- gap 0.017in.

Figure 5.7. Steady state pressure scalar - type A- gap 0.002in.

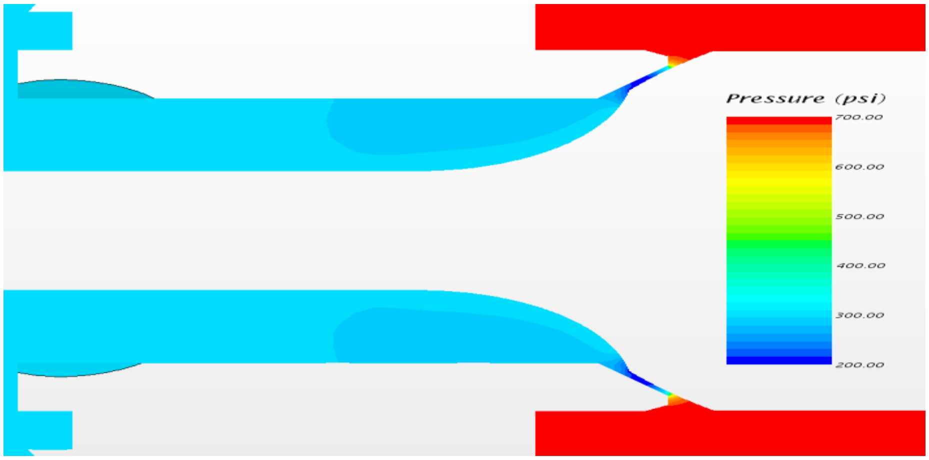

Figure 5.8. Steady state pressure scalar - type A- gap 0.005in.

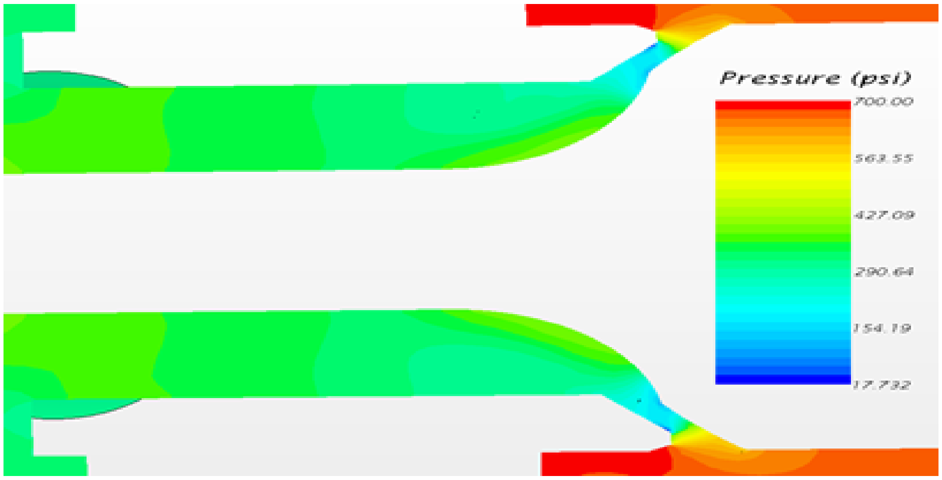

Figure 5.9. Steady state pressure scalar - type A- gap 0.017in.

Flow streamlines are shown in the Figures 5.10 to 5.15. Again, no recirculation bubbles can be seen close to the poppet wall in Figures 5.10 to 5.12. Figures 5.13 to 5.15 clearly show recirculation bubbles at the expansion areas next to the piston walls. The streamlines confirm the results of the velocity-scalar and velocity-vector plots showing that the recirculation region increases and elongates as the gap decreases. It can be seen that the bulk of the flow is carried by the hollow cylindrical jet that develops between the recirculating bubble and the poppet. The jet expands in order to carry the high flow rates as the gap increases. It passes through the gap, then between the recirculation bubble and the poppet and exits radially through the six exit holes.

The volumetric flow rate was calculated for each gap. The results show that 0.73, 2.39 and 12.98 gallons per minute for the 0.002, 0.005 and 0.017 gaps respectively. As expected the volumetric flow rate increases as the gap increases.

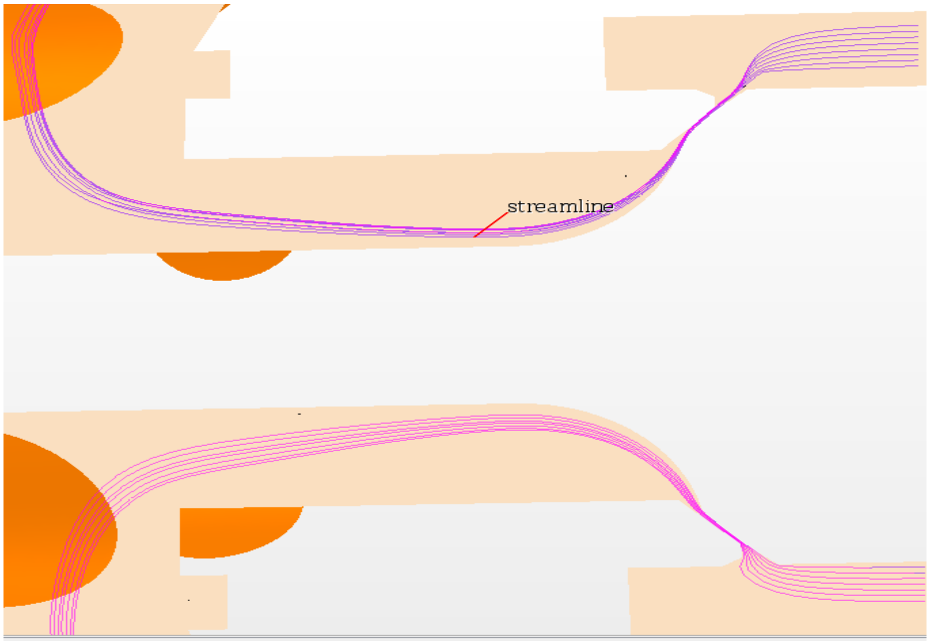

Figure 5.10. Steady state streamline plot for gap 0.002in, valve type A.

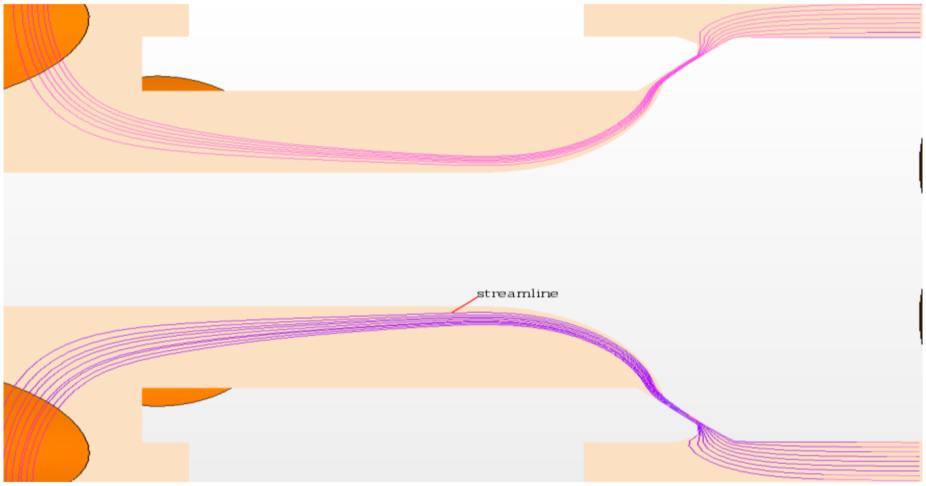

Figure 5.11. Steady state streamline plot for gap 0.005in, valve type A.

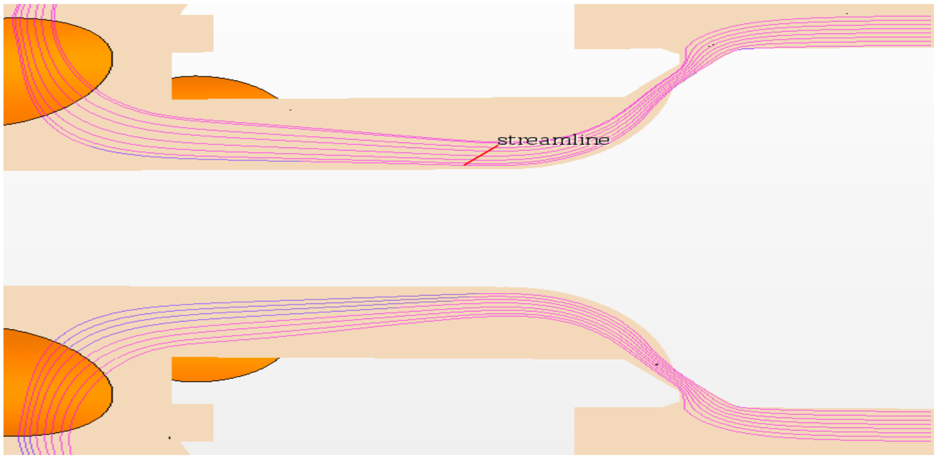

Figure 5.12. Steady state streamline plot for gap 0.017in, valve type A.

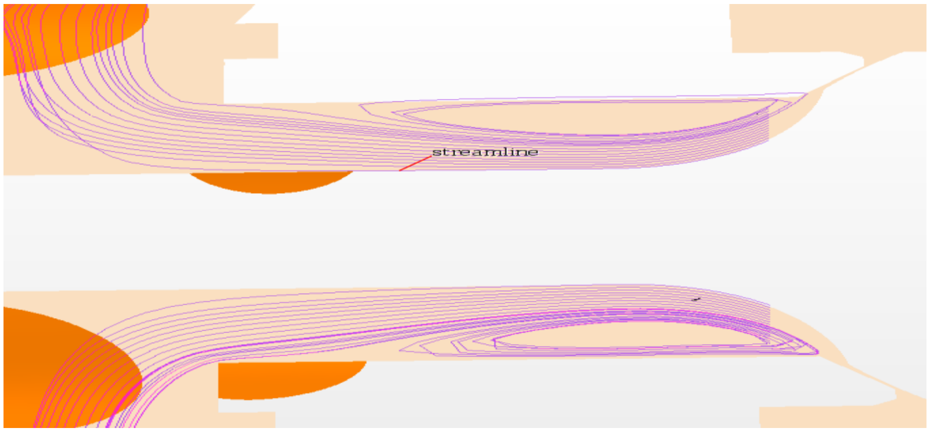

Figure 5.13. Steady state streamline plot at the expansion area, for gap 0.002in, valve type A.

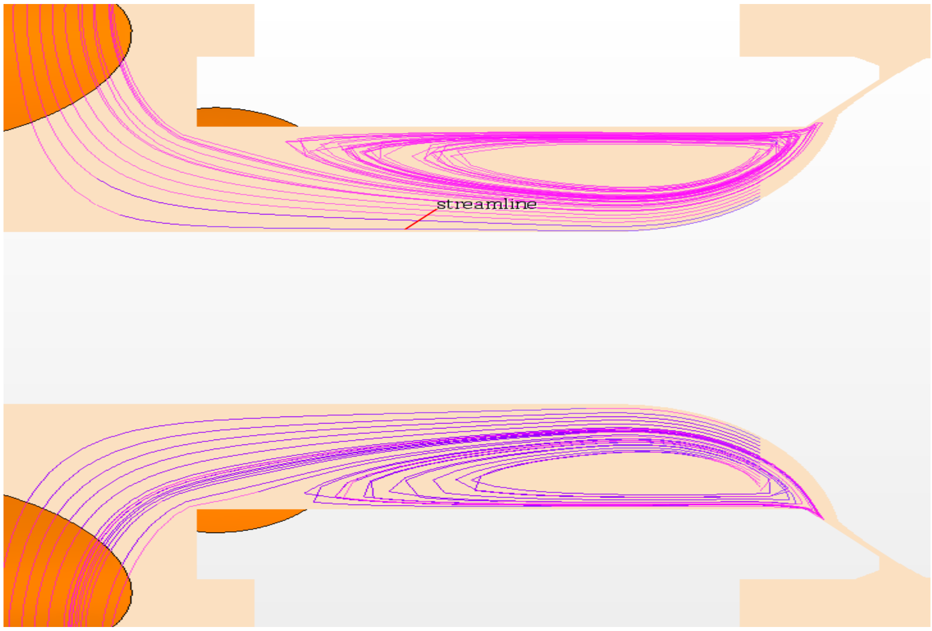

Figure 5.14. Steady state streamline plot at the expansion area, for gap 0.005in, valve type A.

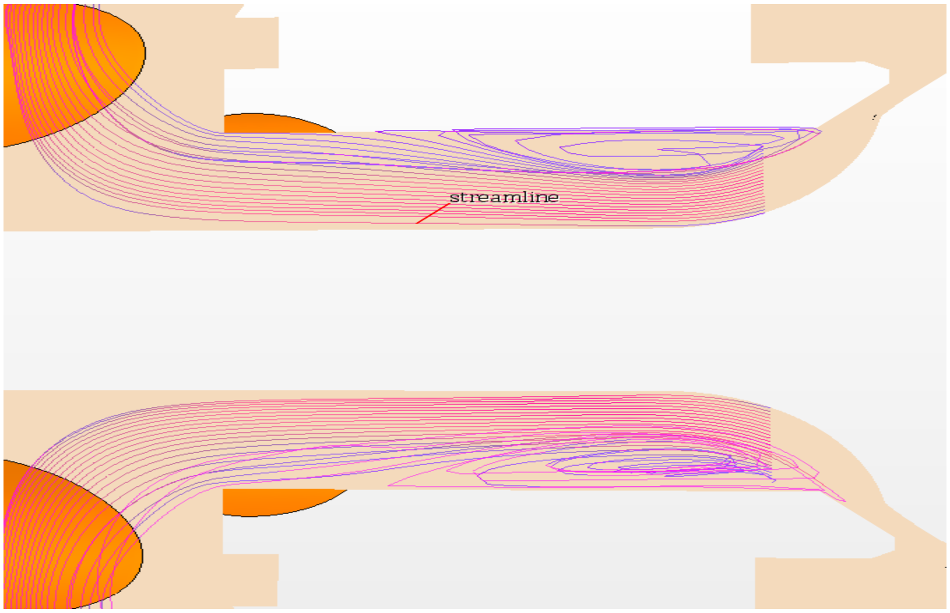

Figure 5.15. Steady state streamline plot at the expansion area, for gap 0.017in, valve type A.

5.2.2. Counterbalance Valve Type B

Figures 5.16 to 5.31 present the velocity (scalar and vector), pressure and streamline plots for the 0.002, 0.005 and 0.017in gaps. The velocity-scalar plots (Figures 5.16 to 5.18) show the same fluid flow behavior as valve type A for all gaps in that the velocity is low everywhere except on the gap areas. The velocity increases with the gap from the 0.002 to 0.005in gaps but it decreases for the 0.017in gap. For the 0.002in gap, the maximum velocity is 90 m/s, increasing to 94 m/s for the 0.005in gap and then decreasing to 74 m/s for the 0.017in gap. It can be seen however that the velocity at the expansion area for the larger gap is higher than the velocities at the other two.

The velocity-vector plots can be seen in Figures 5.19 to 5.21. They confirm the results of the velocity-scalar plots in that low velocities can be seen everywhere except at gap areas. Recirculation bubbles can be observed above the gap and at the expansion areas are similar to those of the type A valve. In addition, a small recirculation bubble can be observed for the 0.017in gap at the expansion area next to the jet exit. This recirculation zone partially blocks the flow at the gap and this explains why the maximum velocity for larger gap is lower than for the smaller and middle gaps. As in the type A valve, the recirculation bubbles grow smaller as the gap increases. Animation of the velocity vector plots for all three gaps showing the oscillatory nature of the flow through the valve can be seen on movies B-0.002in, B-0.005in and B-0.017in attached with this dissertation as (DVD). For all three gaps, a larger recirculation bubble can be seen at the gap outlet close to the piston wall, and a small one above the gap inlet. The B-0.017in DVD video clearly illustrates the small recirculation bubble at the gap. A non-recirculating fluid jet develops at the gap inlet, passes through the gap and between the recirculation bubble and the poppet, exiting at the left, as was the case for the type A valve.

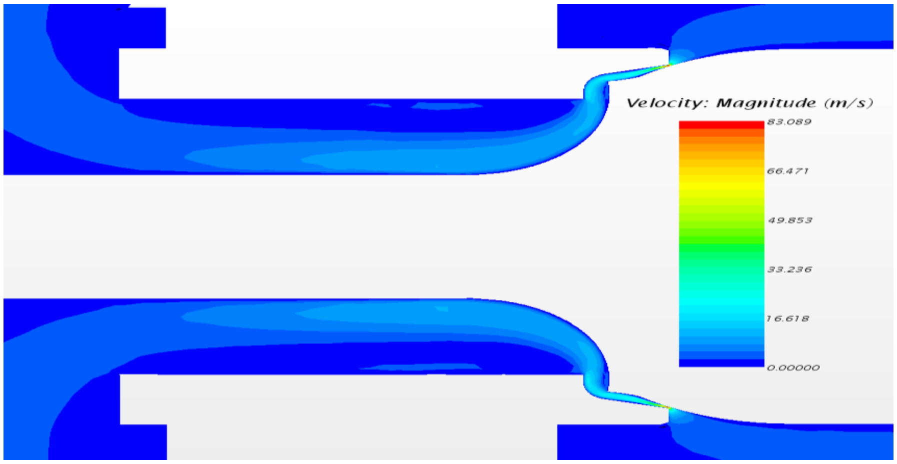

Figure 5.16. Steady state velocity scalar - type B- gap 0.002in.

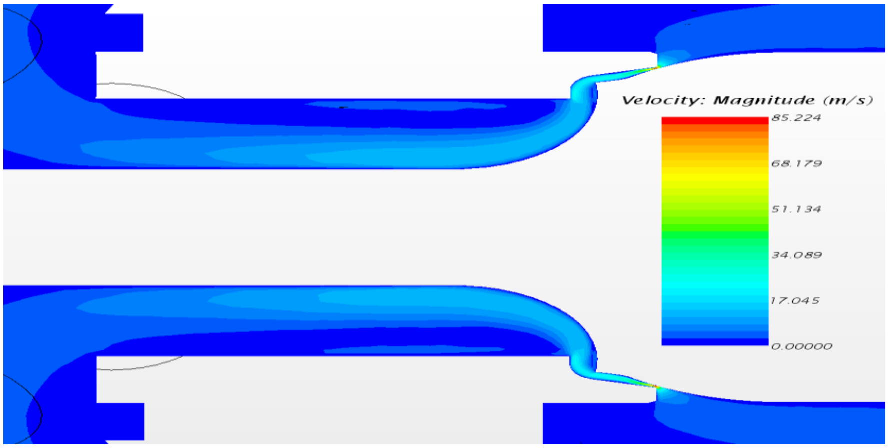

Figure 5.17. Steady state velocity scalar - type B- gap 0.005in.

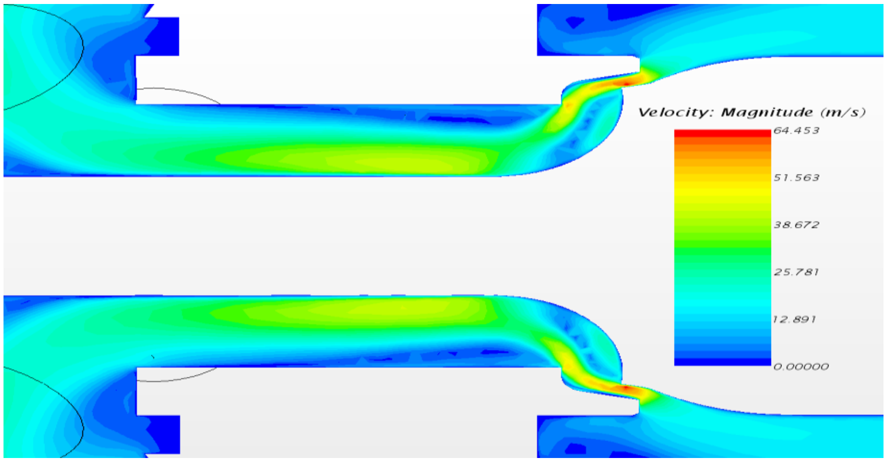

Figure 5.18. Steady state velocity scalar - type B- gap 0.017in.

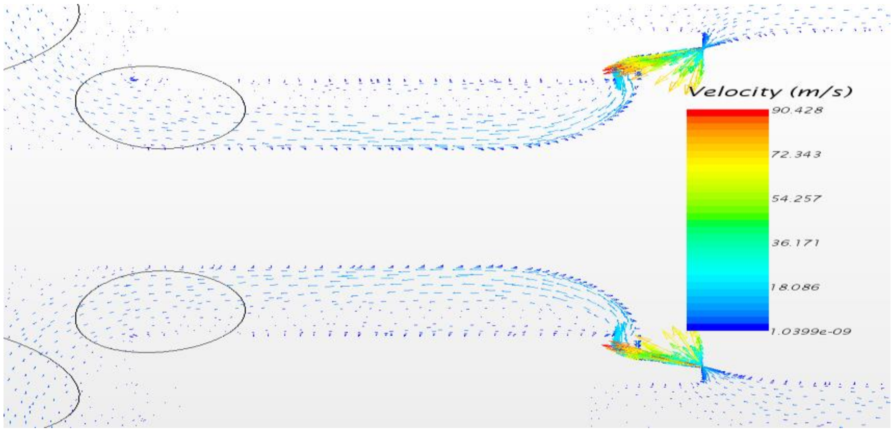

Figure 5.19. Steady state velocity vector - type B- gap 0.002in.

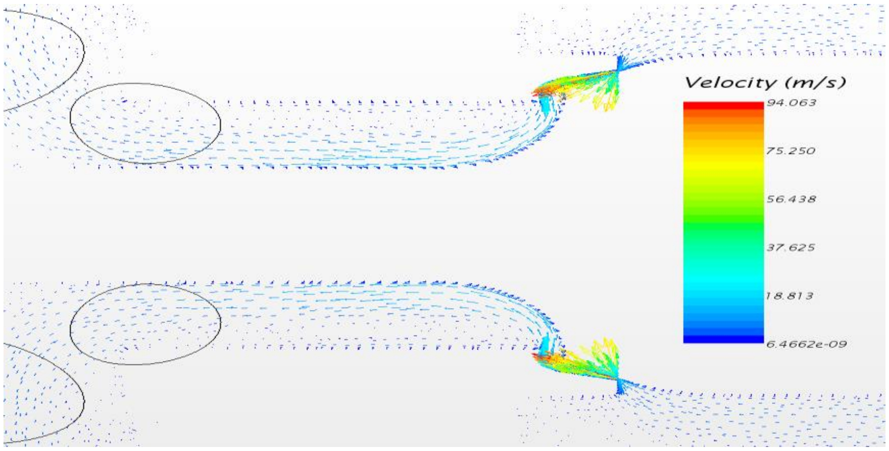

Figure 5.20. Steady state velocity vector - type B- gap 0.005in.

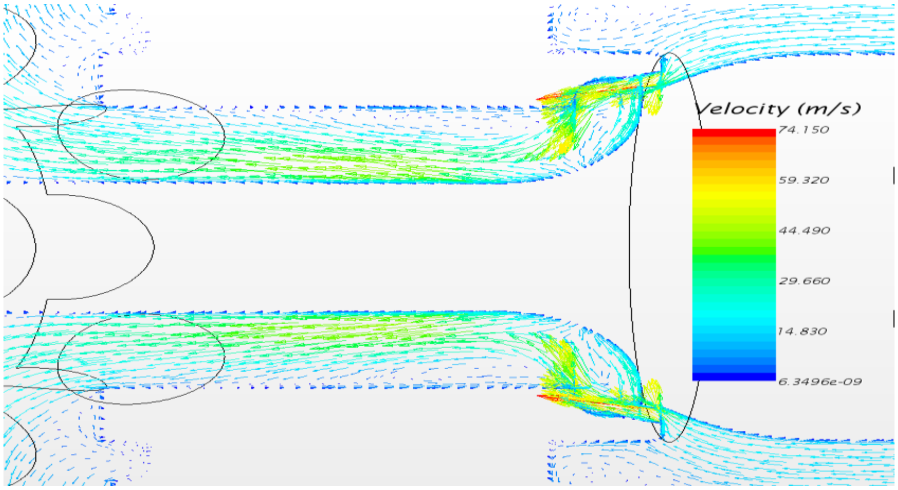

Figure 5.21. Steady state velocity vector - type B- gap 0.017in.

700-psi upstream and 300-psi downstream flow field pressure plots can be seen in Figures 5.22 to 5.24. For the 0.002in and 0.005in gaps, the plots are similar both before the gap and at the area of expansion. A clear pressure decrease can be seen before the gap for the larger opening. In the first two areas, the pressure drops to 250 psi and stays constant through the gap and at the expansion areas. Pressure profiles are quite different for the larger opening. Pressures of 450 psi can be observed on both piston and poppet in the gap area. A constant pressure of 300 psi can be observed at the rest of the expansion area.

Flow streamlines are shown in Figures 5.25 to 5.31. The results are similar to those found for the type A valve except for the appearance of the small recirculation bubble at the large opening that can be clearly observed in Figure 5.31. These plots are in agreement with velocity plots, showing the same recirculation regions.

For each gap of this valve the volumetric flow rate results was obtained. The results show the 0.002in has 1.60 gpm, 0.005in has 1.99 gpm and the 0.017in has 8.60 gpm. As was the case for the type A valve, the results show the volumetric flow rate increases as the gap increases.

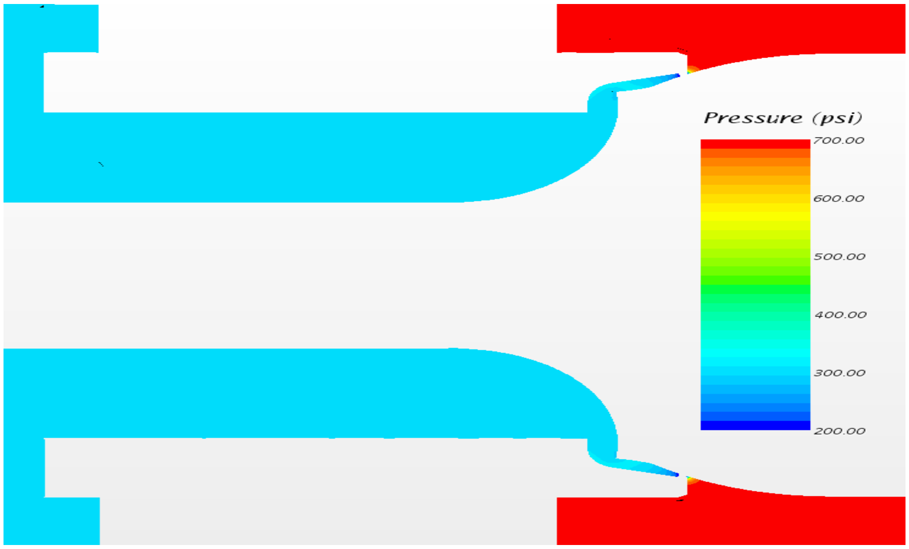

Figure 5.22. Steady state pressure scalar - type B- gap 0.002in.

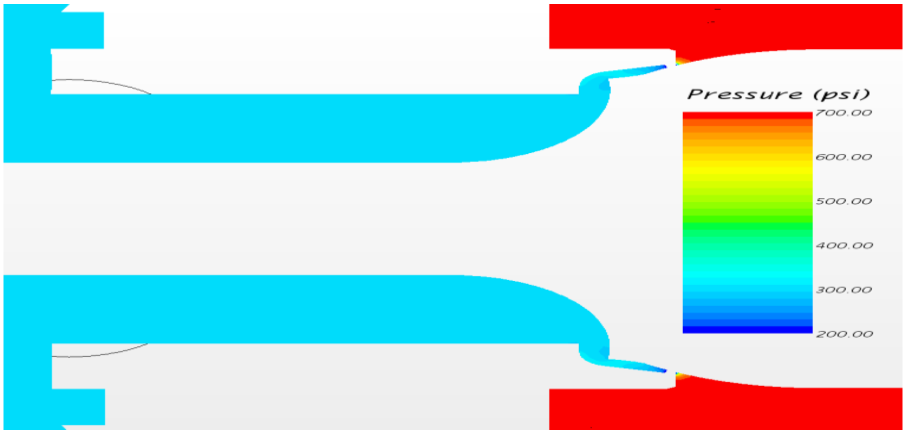

Figure 5.23. Steady state pressure scalar - type B- gap 0.005in.

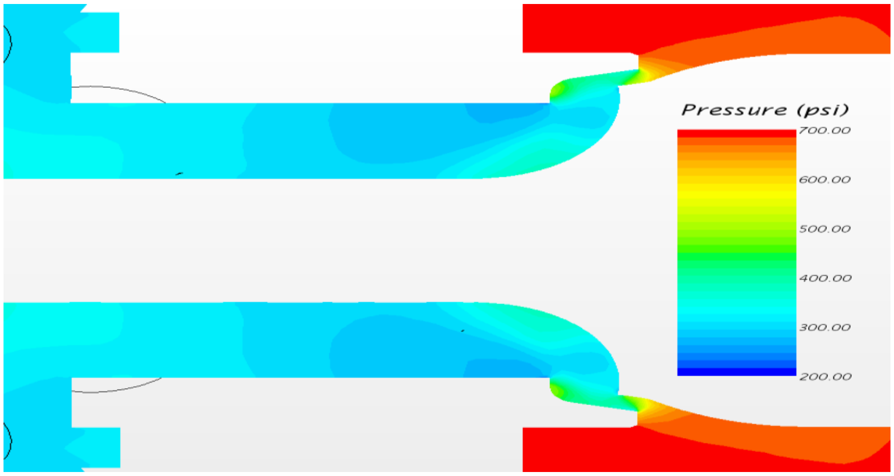

Figure 5.24. Steady state pressure scalar - type B- gap 0.017in.

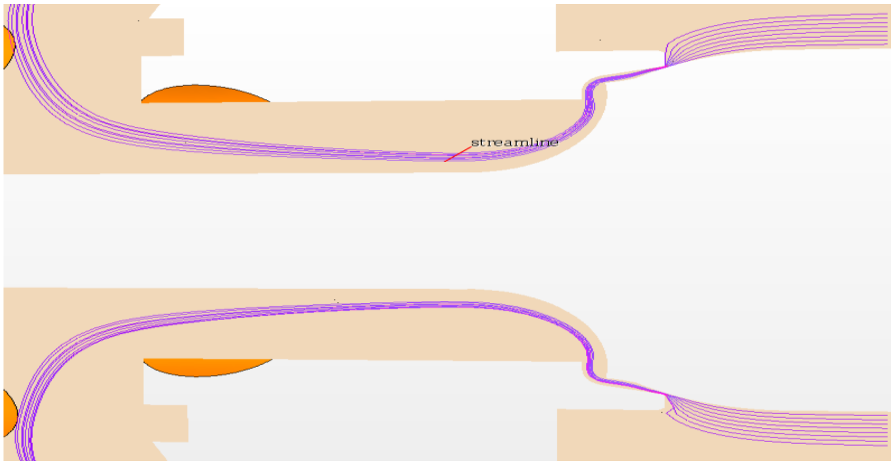

Figure 5.25. Steady state streamline plot for gap 0.002in, valve type B.

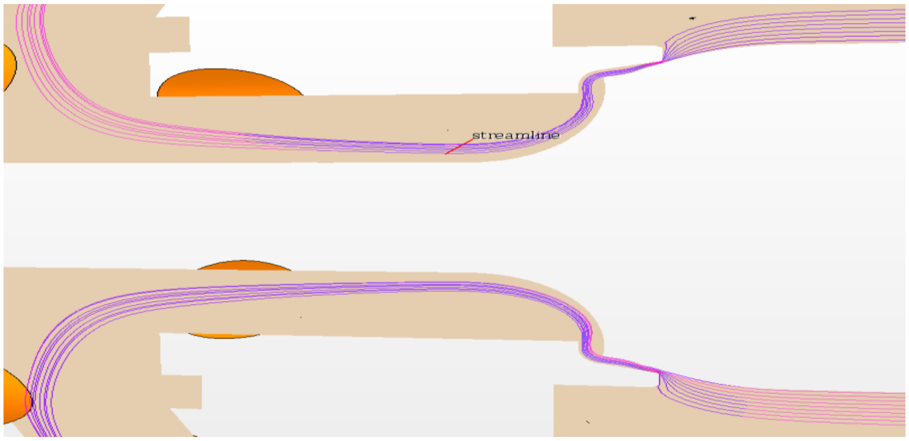

Figure 5.26. Steady state streamline plot for gap 0.005in, valve type B.

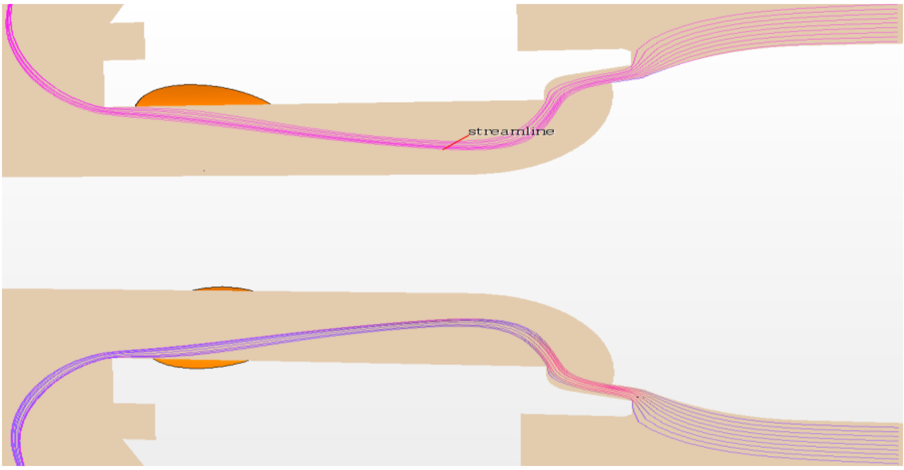

Figure 5.27. Steady state streamline plot for gap 0.017in, valve type B.

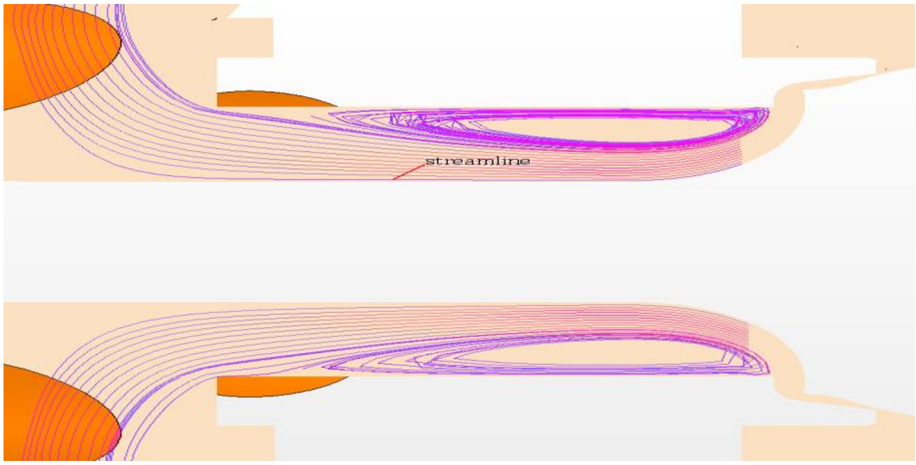

Figure 5.28. Steady state streamline plot at the expansion area, for gap 0.002in, valve type B.

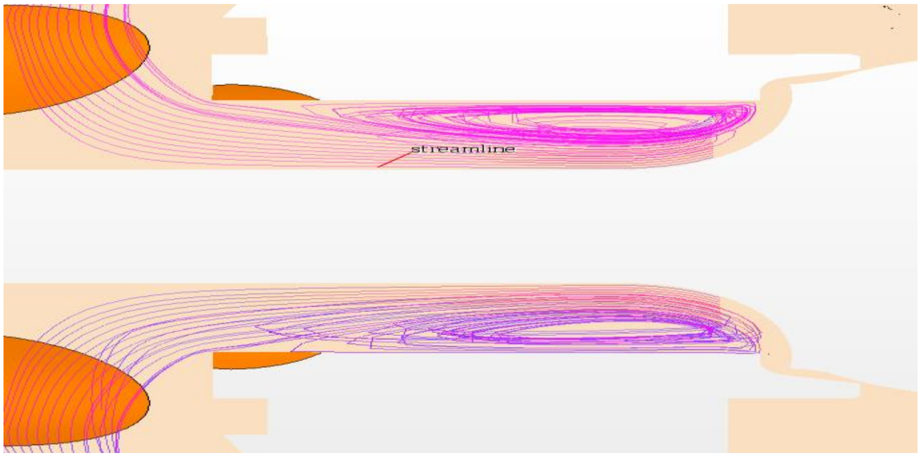

Figure 5.29. Steady state streamline plot at the expansion area, for gap 0.005in, valve type B.

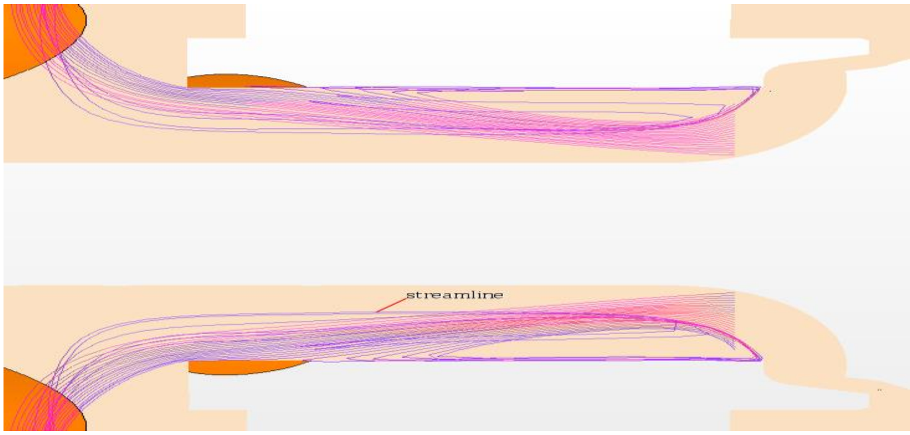

Figure 5.30. Steady state streamline plot at the expansion area, for gap 0.017in, valve type B.

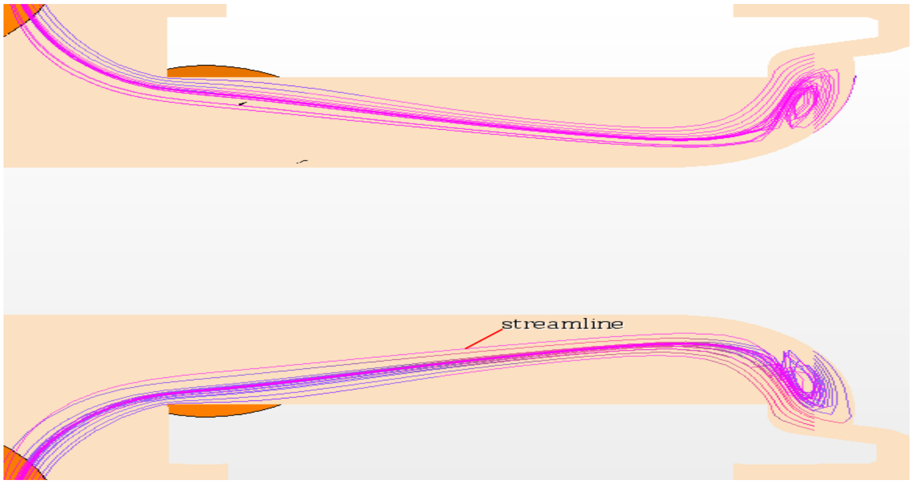

Figure 5.31. Steady state streamline plot at the expansion area, for gap 0.017in, showing recirculation at the jet exit, valve type B.

5.2.3. Steady State Summary

The steady state simulation work produced many useful results. For both valves (A and B) the fluid flow was characterized using velocity-scalar, velocity-vector, pressure-scalar and streamline plots, for gaps of 0.002, 0.005 and 0.017 inches. The results are very much similar on both valves, except for valve type B with a large gap. For both valves and for all three openings, the velocity scalar plots are in agreement in that the velocity low everywhere except at the gap area. The velocity increases proportionally with the gap increases from 0.002in to 0.005in. For the 0.017in gap, valve type A shows similar flow fields as those of the type B 0.002in and 0.005in gaps. The velocity increases as the gap increases while the type B valve shows a velocity decreases for the 0.017in gap.

The velocity-vector plots confirm the results of the velocity-scalar plots. No recirculation bubbles can be seen close to the poppet wall in both valves. For both valves, recirculation zones can be seen above the gap and the expansion areas. The recirculation bubble at the expansion area increases and elongates when the gap decreases. For the type B valve, a small recirculation bubble can be seen at the area of expansion next to the jet exit. The oscillatory nature of the fluid flow has been animated on movies for both valves under all opening conditions. The B-0.017in movie clearly illustrate the small recirculation bubble at the jet exit.

Boundary conditions of 700-psi upstream and 300-psi downstream were used for both valves. High pressure before the gap can be seen for both valves for the 0.002in and 0.005in gaps. A noticeable pressure decrease can be observed in the area for the two larger gaps. The results show that for both valves the pressure drop across the gap decreases as the gap increases.

Flow streamline plots are similar for both valves for all three gaps in that the recirculation can be observed at the expansion area except for the small recirculation bubble can be seen only at the large opening of valve type B. No recirculation bubbles can be seen close the poppet wall, except for valve B with a large opening. For both valves the streamlines confirm the results of the velocity-scalar and velocity-vector plots showing that the recirculation zone increases and elongates as the gap decreases.

For both valves, the volumetric flow rate increases with the gap. A summary for the maximum velocities and the volumetric flow rates for both valves can be seen in Table 5.2.

Table 5.2. Maximum velocities and volumetric flow rates of the steady-state solution for both valves (A, and B)

Gap type	Maximum Velocity m/s	Volumetric flow rate gpm
A-0.002	150	0.73
A-0.005	255	2.39
A-0.017	307	12.98
B-0.002	297	1.60
B-0.005	309	1.99
B-0.017	243	8.60

5.3. Unsteady State Solutions

In order to observe the time-dependent behavior of the flow field, unsteady flow simulations were run for both the type A and B valves. The unsteady state simulations were computationally very intensive with very high data storage demands. They typically required ten days of computing time to converge. Runs were made for the three different piston displacements used in the steady state simulations for both type of valves. As in the steady-state case, streamline, pressure, velocity-vector and velocity-scalar plots were obtained for both valves with same piston displacements (gaps). In additional, the oscillatory behavior of the streamlines of the shear-layer in the gap was investigated.

To verify convergence the simulations were ran for maximum physical times of 0.004 and 0.08 seconds, the latter time determined by the data storage limitations. For the 0.08 seconds runs, each gap simulation results in an output of 800 simulation files, with 1.31 gigabytes required for each file.

5.3.1. Counterbalance Valve Type A

The unsteady state velocity-scalar, velocity-vector, pressure and streamline plots for all three gaps presented in Figures 5.32 to 5.62 show no significant differences with respect to those of the steady-state simulations. Figures 5.32 to 5.37 present the velocity-scalar plots. The results show the velocity is low everywhere except on the gap areas and that the velocity increases as the gap increases. Maximum velocities of 46, 78 and 90 m/s can be observed at gaps of 0.002, 0.005 and 0.017 inches respectively. These values are the same as the steady-state ones except for the large gap which is slightly lower. At the expansion areas, low velocities can be seen close to the piston wall, increasing as they approach the poppet, for all three gaps. The velocity also increases at the expansion area when the gap increases.

Figures 5.38 to 5.43 present the velocity-vector plots. As for the steady state of type A valve the results confirm the velocity-scalar plots showing low velocities can be seen everywhere except on the gap areas. On the other hand, recirculation areas can be observed at the area above the gaps and at the expansion areas as appeared for the type A of valve of the steady state, for all three gaps. As in the steady-state, bubbles in the expansion area forms close to the piston wall and grow smaller as the external velocity increases, furthermore, the bubble decrease with the valve-opening while the velocities increase. Animation of the velocity-vector plots for all three gaps showing the oscillatory nature of the flow through the valve can be seen on movies A-0.002in-unst, A-0.005in-unst and A-0.017in-unst attached with this dissertation as (DVD). Again, the videos clearly illustrate a detailed fluid flow paths and recirculation bubbles close to the piston wall, poppet and the expansion area.

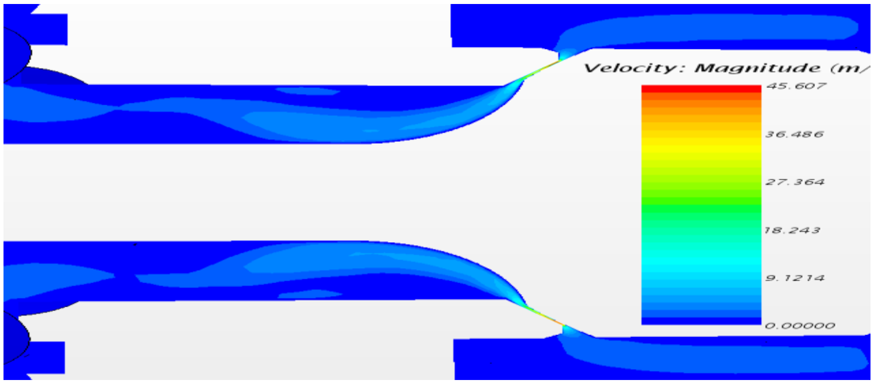

Figure 5.32. Unsteady state velocity scalar - type A- gap 0.002in, time-step 0.004S.

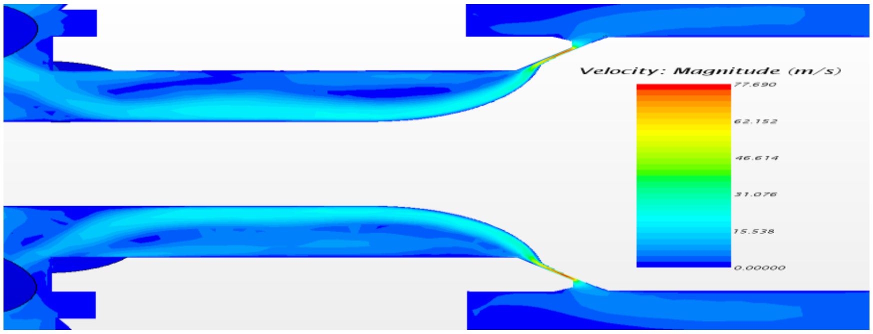

Figure 5.33. Unsteady state velocity scalar - type A- gap 0.005in, time-step 0.004S.

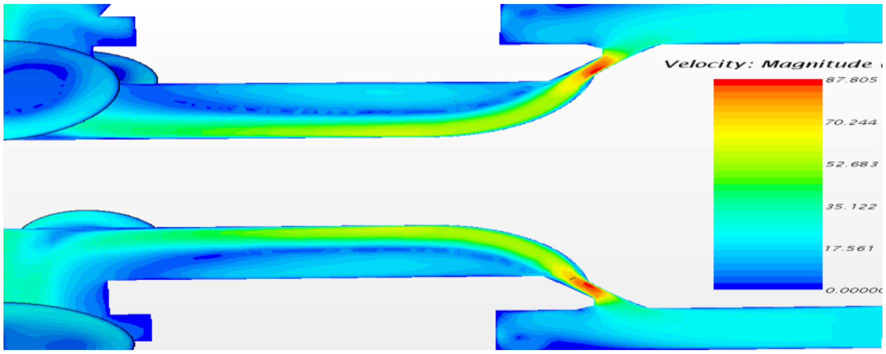

Figure 5.34. Unsteady state velocity scalar - type A- gap 0.017in, time-step 0.004S.

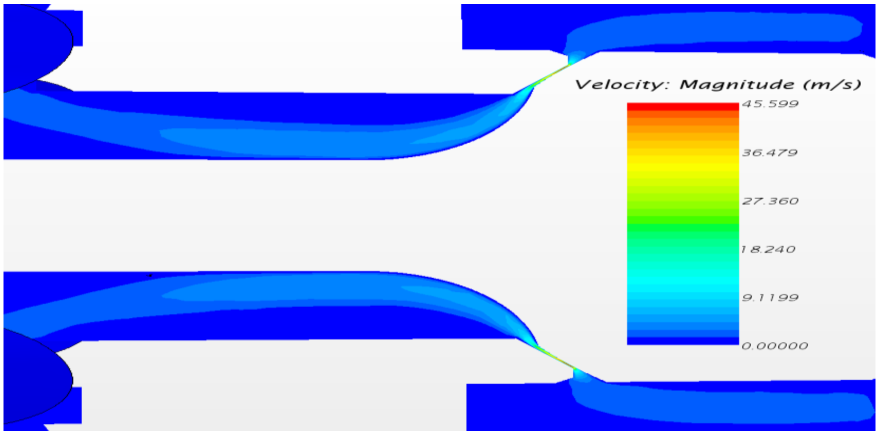

Figure 5.35. Unsteady state velocity scalar - type A- gap 0.002in, time-step 0.08S.

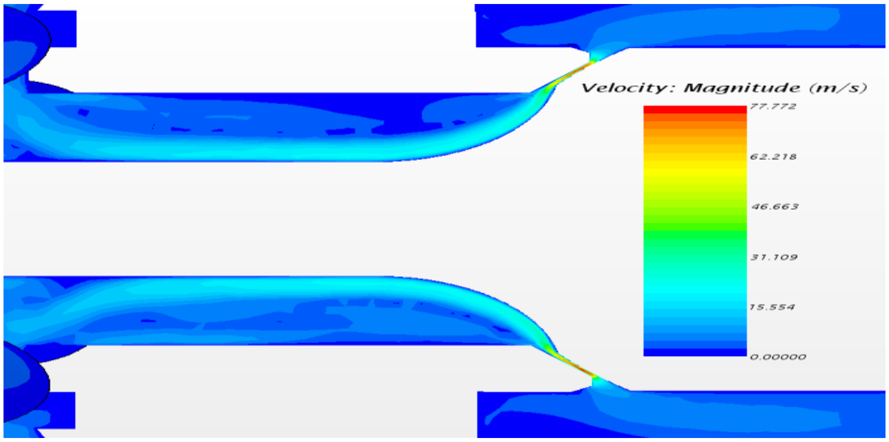

Figure 5.36. Unsteady state velocity scalar - type A- gap 0.005in, time-step 0.08S.

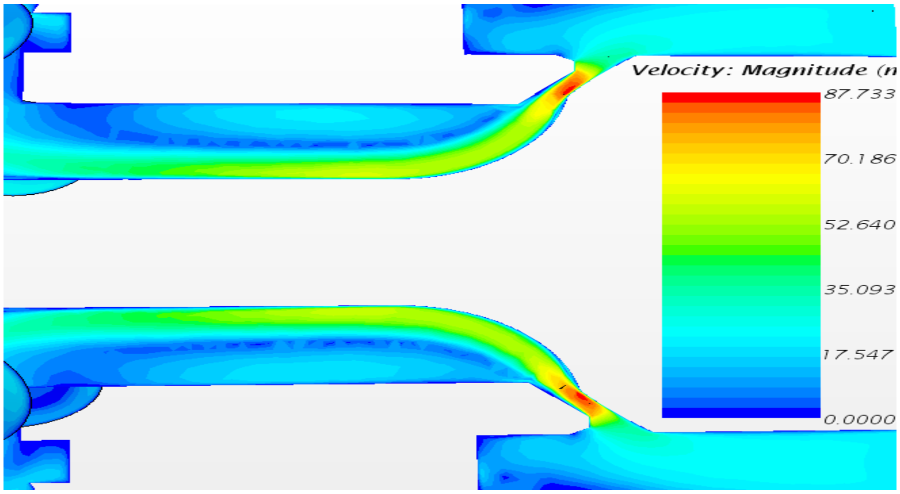

Figure 5.37. Unsteady state velocity scalar - type A- gap 0.017in, time-step 0.08S.

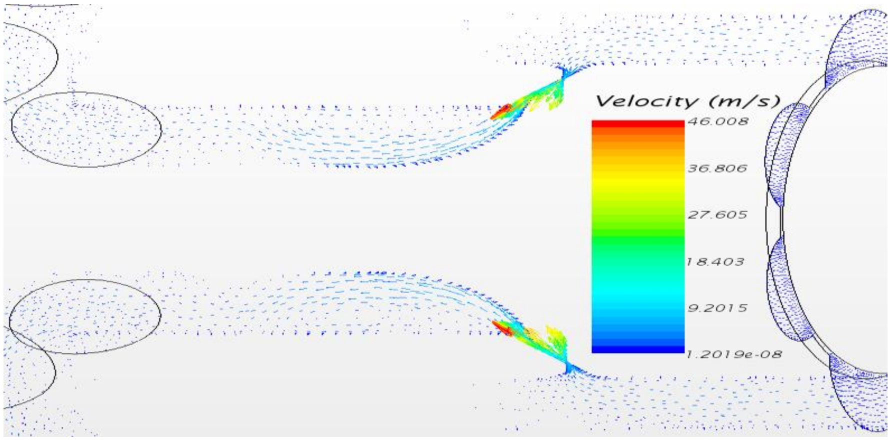

Figure 5.38. Unsteady state velocity vector - type A- gap 0.002in, time-step 0.004S.

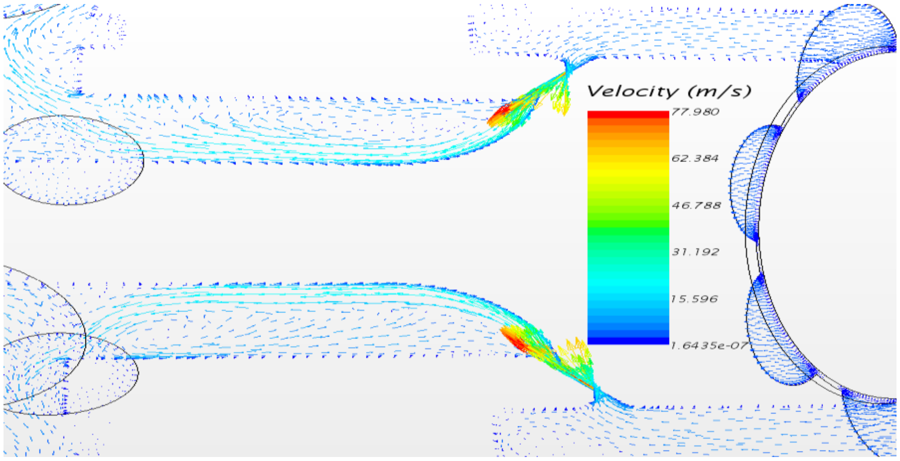

Figure 5.39. Unsteady state velocity vector - type A- gap 0.005in, time-step 0.004S.

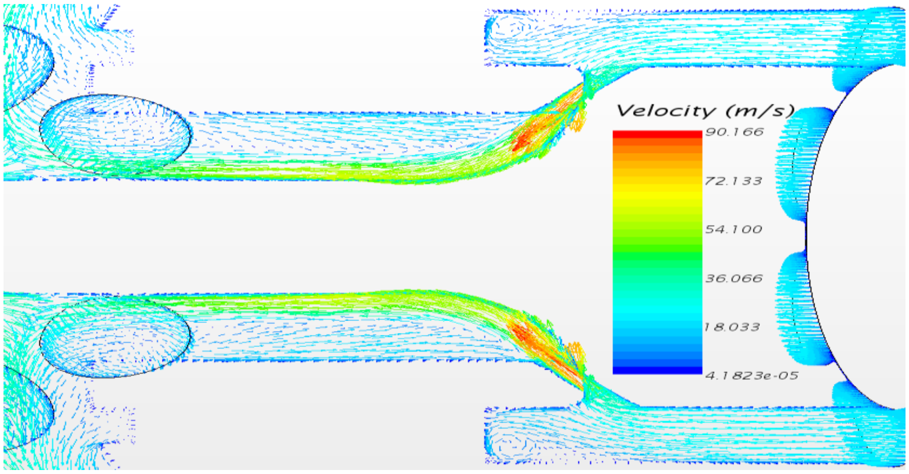

Figure 5.40. Unsteady state velocity vector - type A- gap 0.017in, time-step 0.004S.

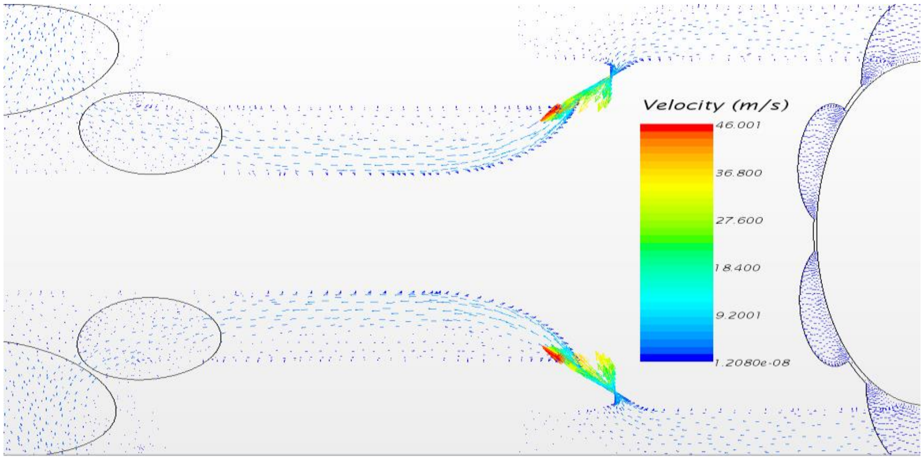

Figure 5.41. Unsteady state velocity vector - Type A- gap 0.002in, time-step 0.08S.

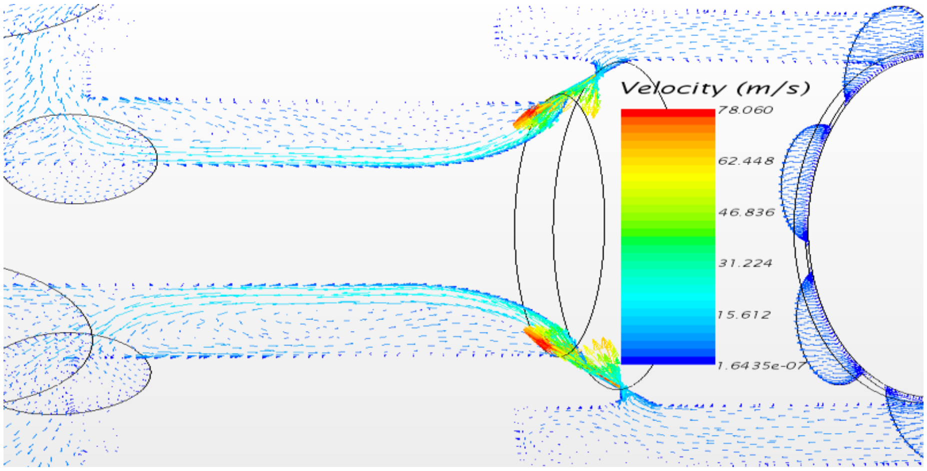

Figure 5.42. Unsteady state velocity vector - Type A- gap 0.005in, time-step 0.08S.

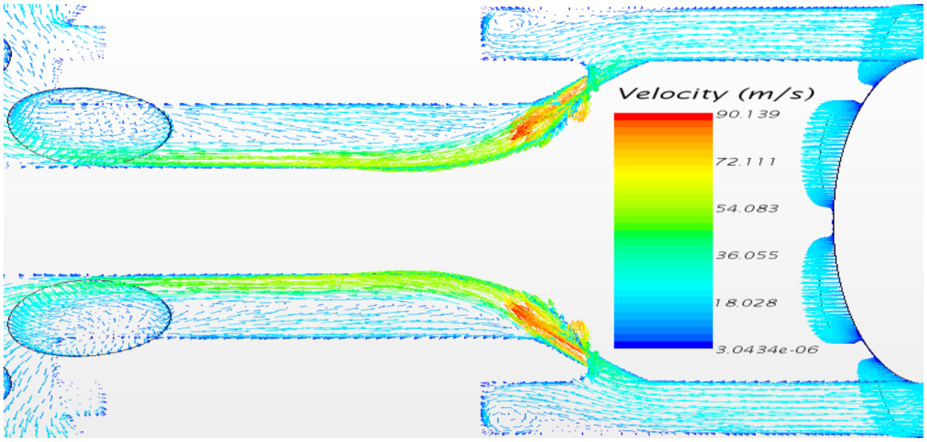

Figure 5.43. Unsteady state velocity vector - Type A- gap 0.017in, time-step 0.08S.

Flow field pressure plots can be seen in Figures 5.44 to 5.49. The boundary conditions are similar to those for type A valve of steady in that the numerical simulations were run with 700 psi upstream pressure and 300 psi downstream pressure. The results are very much the same for both steady-state and unsteady-state. Pressure values before the gap are similar for the 0.002 and 0.005 inches plots. A noticeable pressure decrease it can be observed before the gap for the 0.017in gap. Pressure drops to 278 psi and stays constant through the gaps and at the expansion areas for gaps 0.002. For gap (0.005in) pressure drops to 206 psi and then recovers to 310 psi at the expansion area. For the larger opening (0.017in) the pressure decreases in the gap to 90 psi and then increases to a constant pressure of 330 psi at the gap exit and the area of the expansion. The pressure drop across the gap decreases as the gap increases.

Flow streamlines are shown in the Figures 5.50 to 5.61. Figures 5.50 to 5.55 depict streamlines close to the poppet wall similar to those of the steady state case. While Figures 5.55 to 5.61 show recirculation bubbles at the expansion areas next to the piston walls. Again, the streamlines confirm the results of the scalar and velocity vector plots showing that the recirculation region increases and elongates as the gap decreases. Figures 0.005in and 0.017in show 3-D recirculation over the poppet area and 2-D recirculation at the plane section. The 3-D recirculation illustrate that for running with time-dependent and at high velocities, fluid flows randomly to different directions. This phenomenon proved the oscillatory nature of the fluid flow vary with change in velocities. The volumetric flow rate was calculated for each gap, the results show flows of 0.73, 2.92 and 14.99 gallons per minute for the 0.002, 0.005 and 0.017 gaps respectively. As for type A of the steady state case the volumetric flow rate increases as the gap increases.

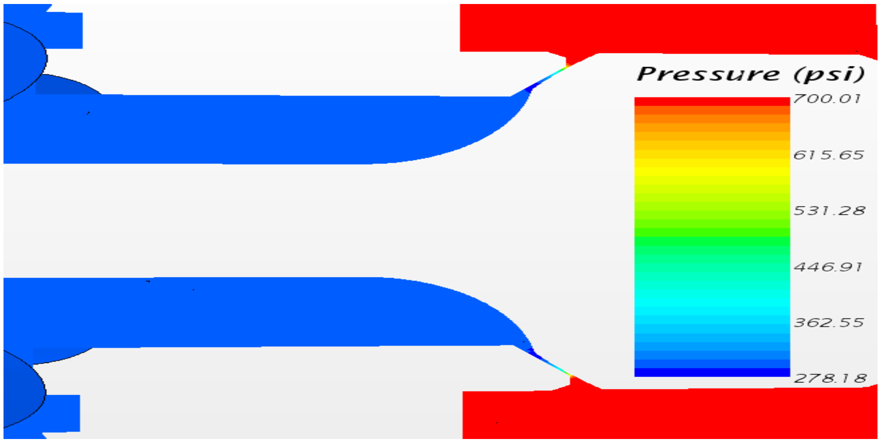

Figure 5.44. Unsteady state pressure scalar - type A- gap 0.002in, time-step 0.004S.

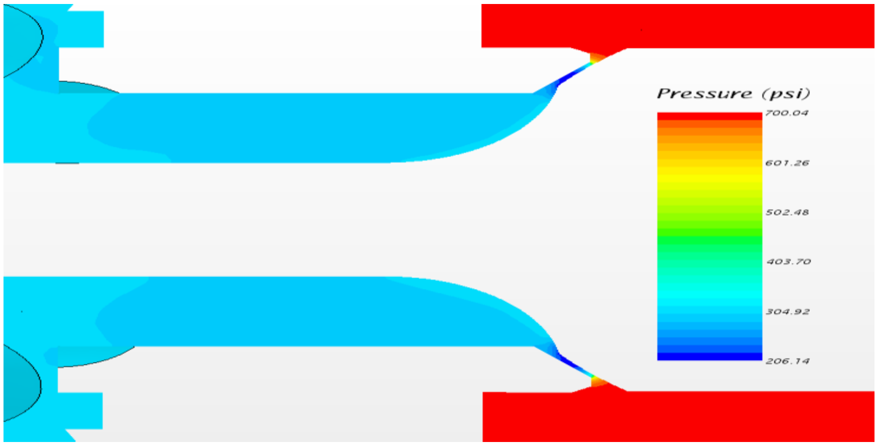

Figure 5.45. Unsteady state pressure scalar - type A- gap 0.005in, time-step 0.004S.

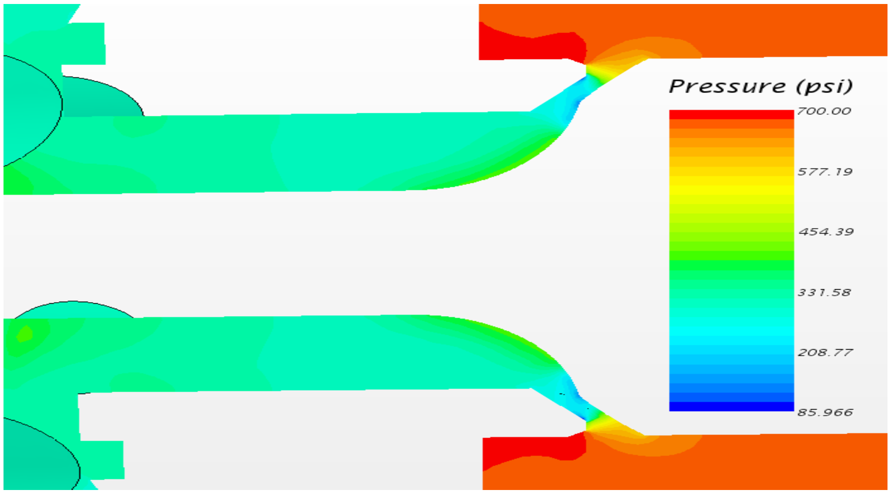

Figure 5.46. Unsteady state pressure scalar - type A- gap 0.017in, time-step 0.004S.

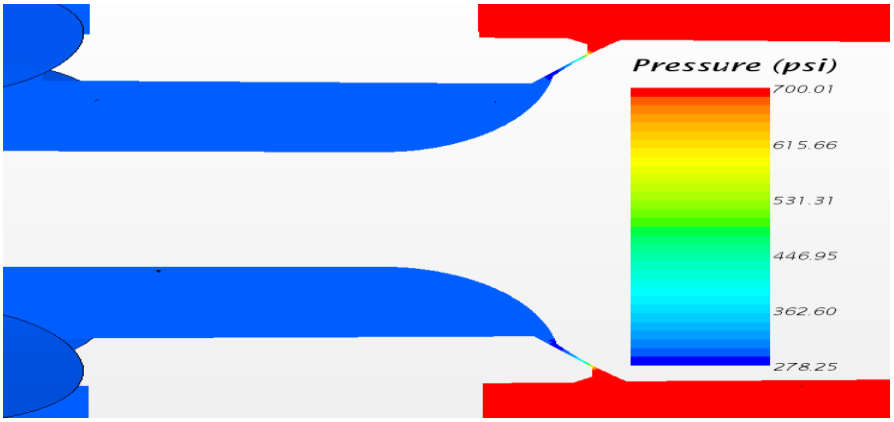

Figure 5.47. Unsteady state pressure scalar - type A- gap 0.002in, time-step 0.08S.

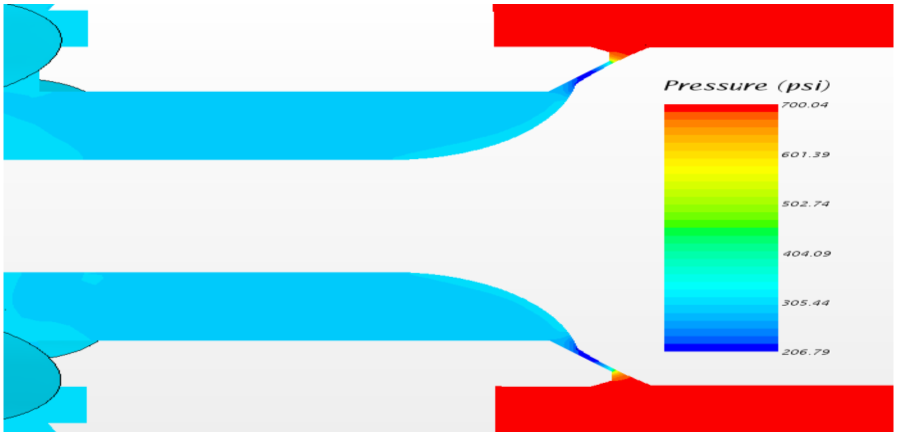

Figure 5.48. Unsteady state pressure scalar - type A- gap 0.005in, time-step 0.08S.

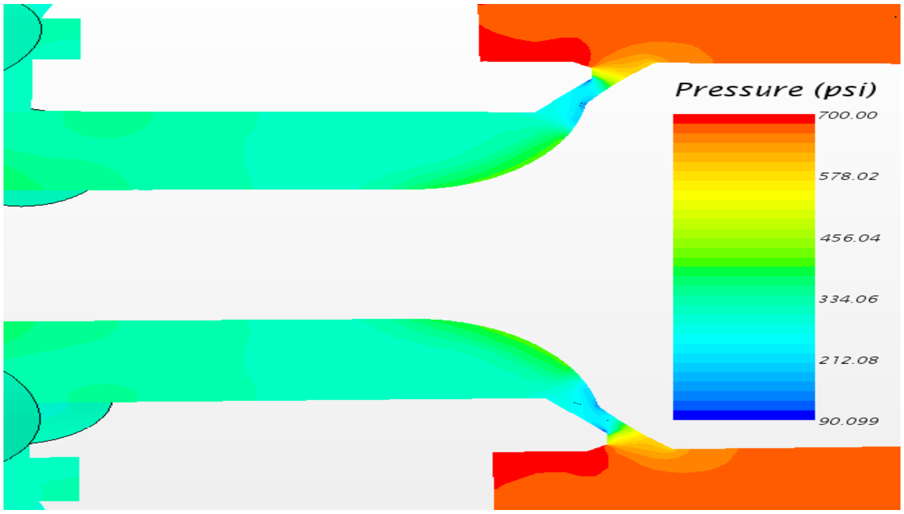

Figure 5.49. Unsteady state pressure scalar - type A- gap 0.017in, time-step 0.08S.

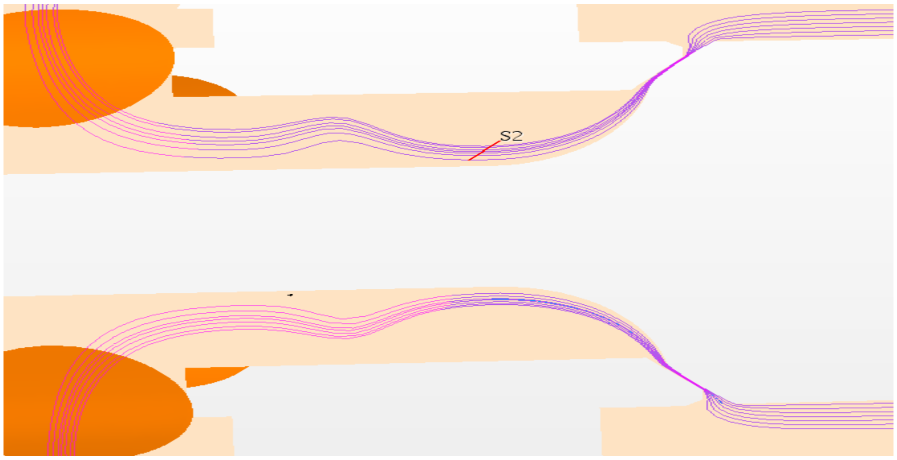

Figure 5.50. Unsteady state streamline plot for gap 0.002in, valve type A, time-step 0.004S.

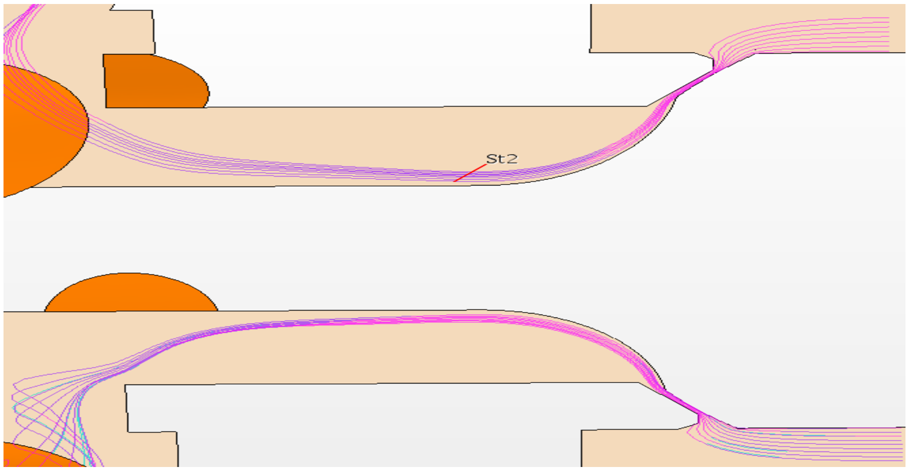

Figure 5.51. Unsteady state streamline plot for gap 0.005in, valve type A, time-step 0.004S.

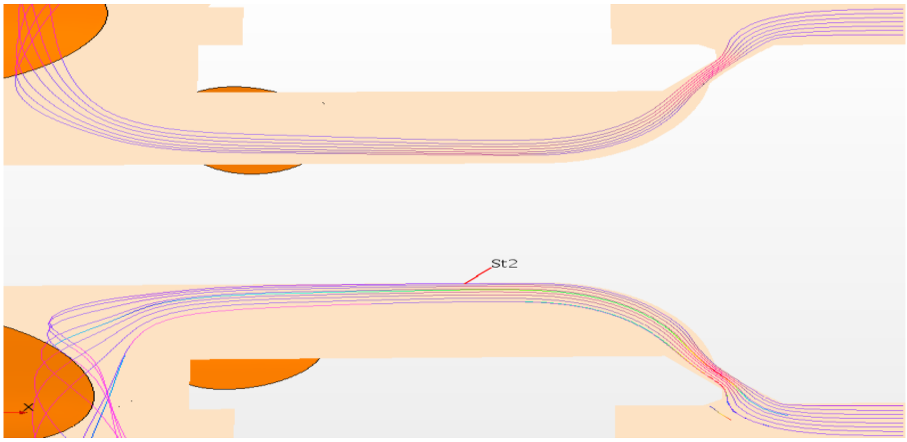

Figure 5.52. Unsteady state streamline plot for gap 0.017in, valve type A, time-step 0.004S.

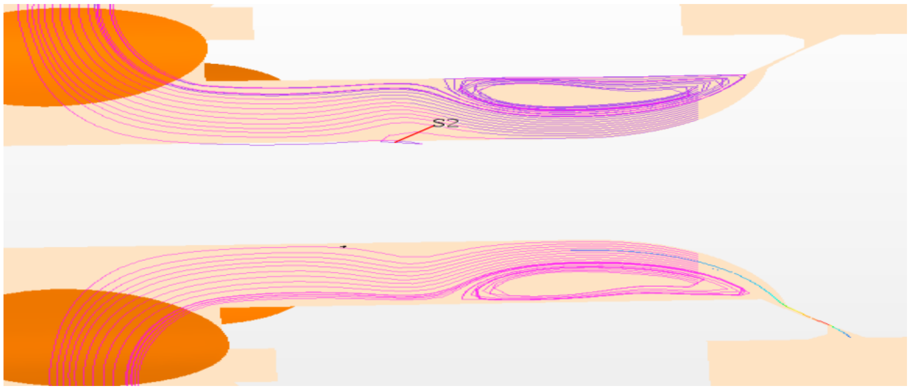

Figure 5.53. Unsteady state streamline plot at the expansion area, gap 0.002in, valve type A, time-step 0.004S.

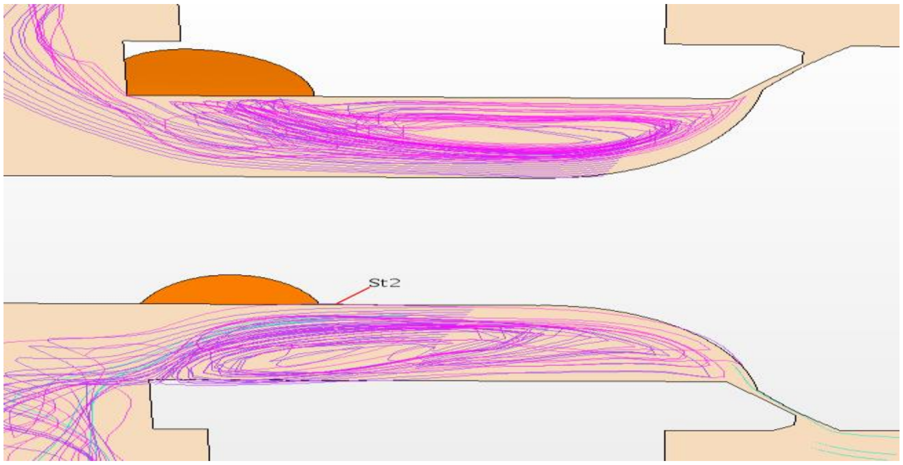

Figure 5.54. Unsteady state streamline plot at the expansion area, gap 0.005in, valve type A, time-step 0.004S.

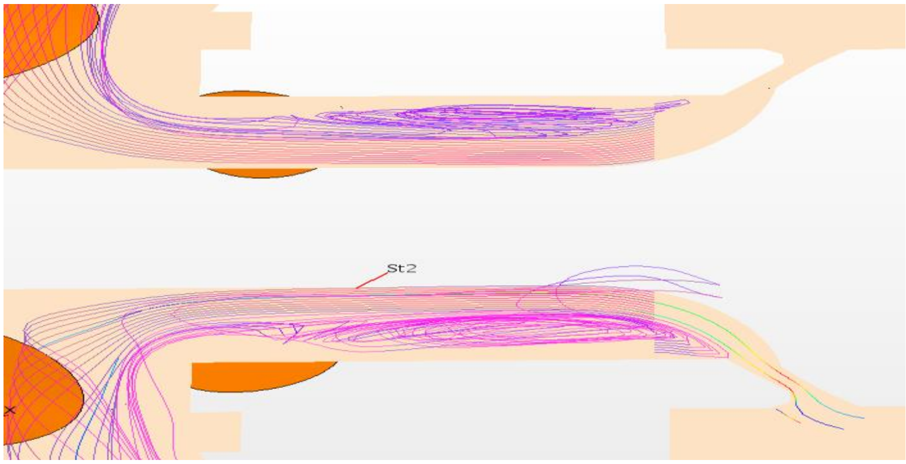

Figure 5.55. Unsteady state streamline plot at the expansion area, gap 0.017in, valve type A, time-step 0.004S.

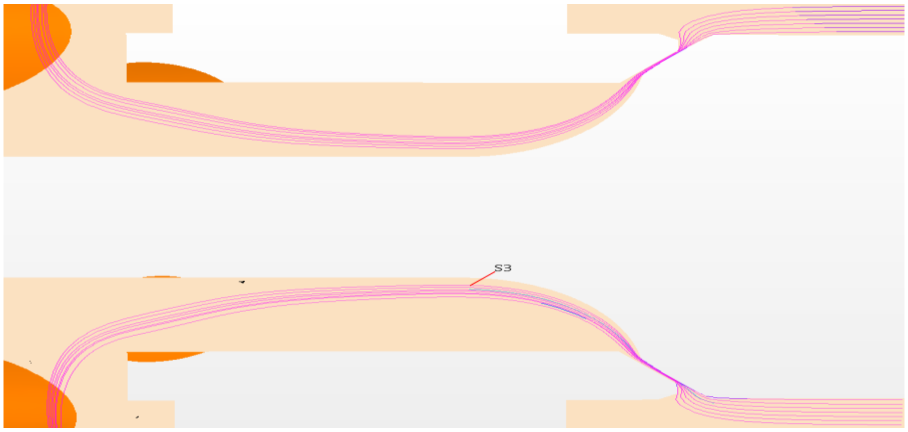

Figure 5.56. Unsteady state streamline plot for gap 0.002in, valve type A, time-step 0.08S.

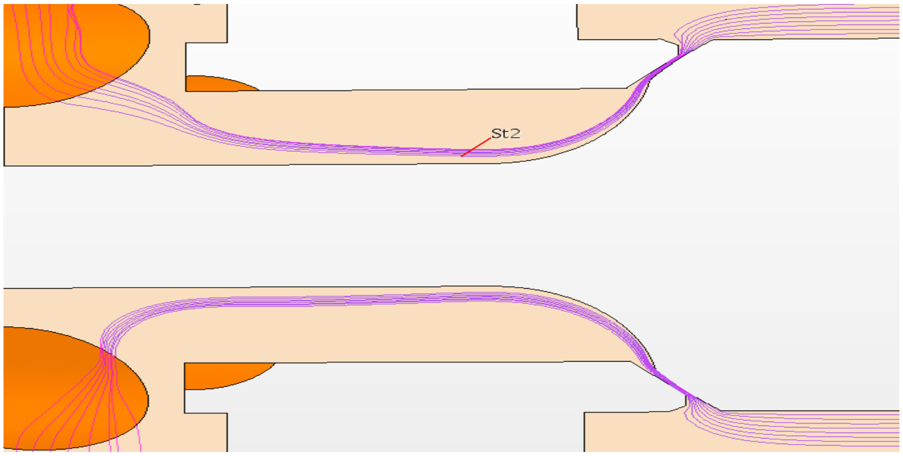

Figure 5.57. Unsteady state streamline plot for gap 0.005in, valve type A, time-step 0.08S.

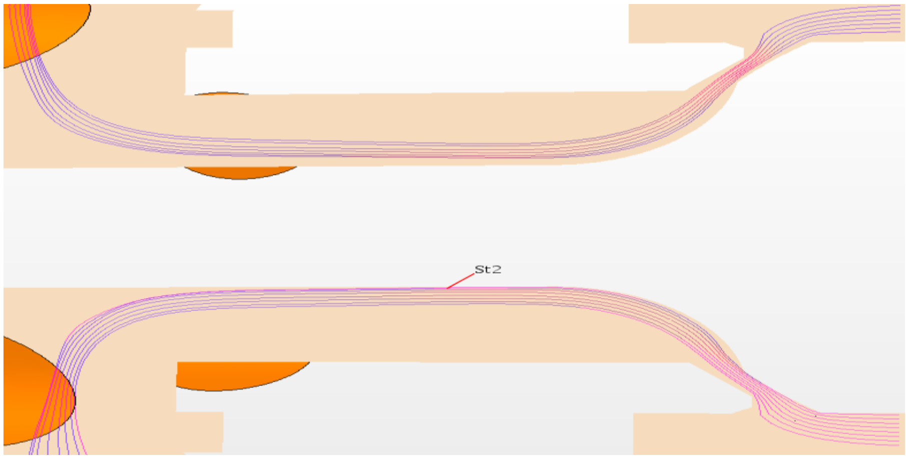

Figure 5.58. Unsteady state streamline plot for gap 0.017in, valve type A, time-step 0.08S.

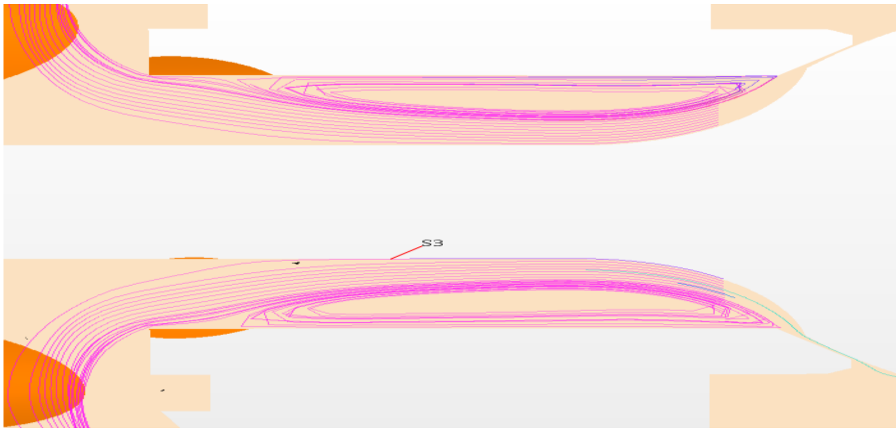

Figure 5.59. Unsteady state streamline plot at the expansion area, gap 0.002in, valve type A, time-step 0.08S.

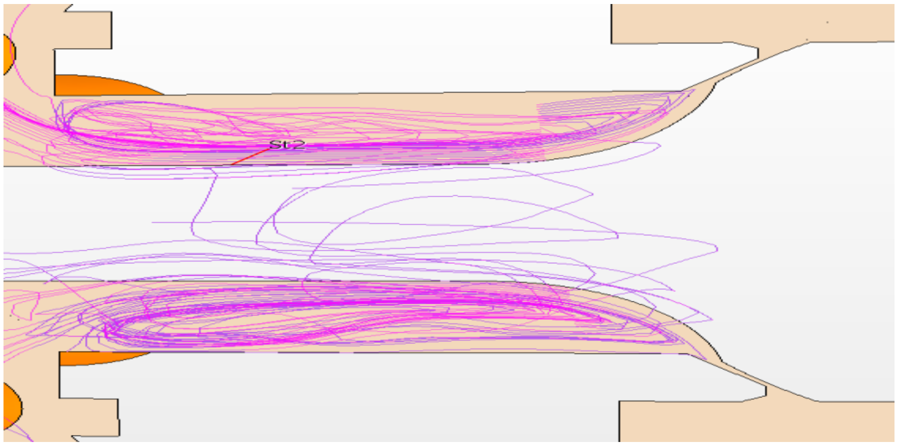

Figure 5.60. Unsteady state streamline plot at the expansion area, gap 0.005in, valve type A, time-step 0.08S.

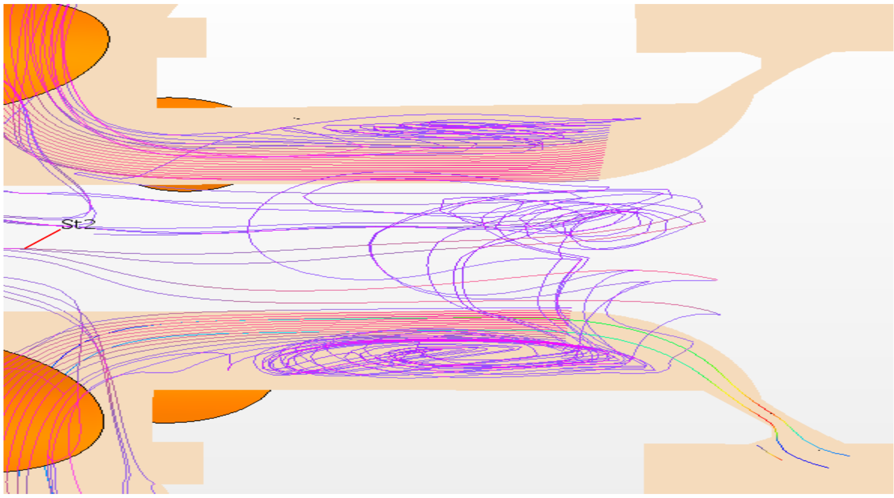

Figure 5.61. Unsteady state streamline plot at the expansion area, gap 0.017in, valve type A, time-step 0.08S.

5.3.2. Counterbalance Valve Type B

Numerical simulations of the turbulent flow through this type of valve for the same piston displacements were carried out to study the development of the unsteady-state flow. The velocity (scalar and vector), pressure and streamline plots obtained for the 0.002, 0.005 and 0.017in gaps are shown in Figures 5.62 to 5.93. As in the steady-state case, Figures 5.62 to 5.67 show that velocity is low everywhere except in the gap areas. The maximum velocity increases with the gap for the 0.002 and 0.005in gaps, but decreases for the 0.017in gap as in the steady-state case. For the 0.002in gap, the maximum velocity is 90.50 m/s, increasing to 136.98 m/s for the 0.005in gap and then decreasing to 120.22 m/s for the 0.017in gap. A larger velocity can be observed at the expansion area for the larger gap. The smallest two gaps show low velocity at the expansion areas.

The velocity-vector plots are presented in Figures 5.68 to 5.73. As in the type A valve, the plots confirm the results of the velocity-scalar plots in that low velocities are dominant except at gap areas. Again, recirculation bubbles can be noticed above the gap and at the expansion areas are similar to those of the type A valve. The resulting recirculating zones matching those observed in the steady-state case. The 0.017in gap plot shows a small recirculation bubble at the expansion area next to the jet exit. Similar to that of the steady-state case. As in the steady state, the recirculation zone partially blocks the flow at the gap and this explains why the maximum velocity for larger gap is lower than for the smaller and middle gaps. The recirculation bubbles grow smaller as the gap increases as for the type A valve, but their size appears to be larger and the velocities lower than the steady state case. In general, the recirculating flow appears to be weaker in the unsteady state case.

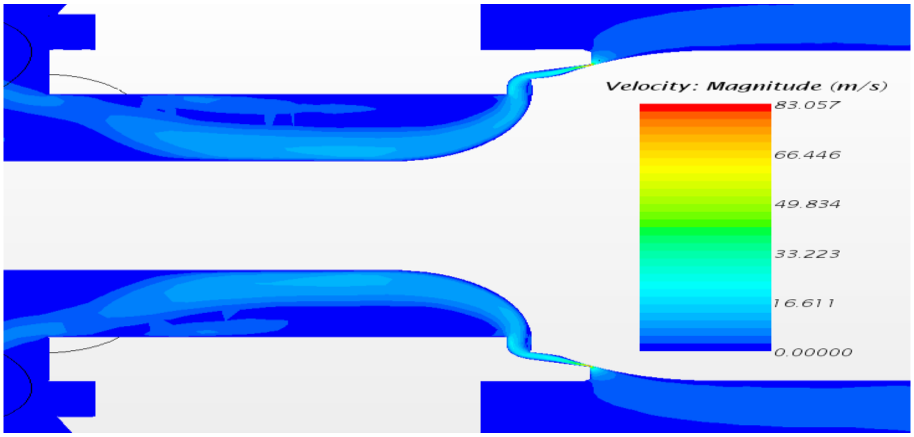

Figure 5.62. Unsteady state velocity scalar - type B- gap 0.002in, time-step 0.004S.

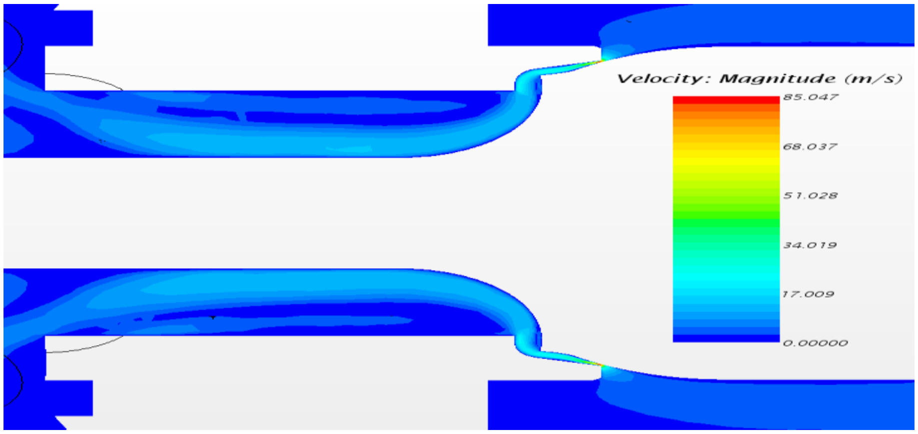

Figure 5.63. Unsteady state velocity scalar - type B- gap 0.005in, time-step 0.004S.

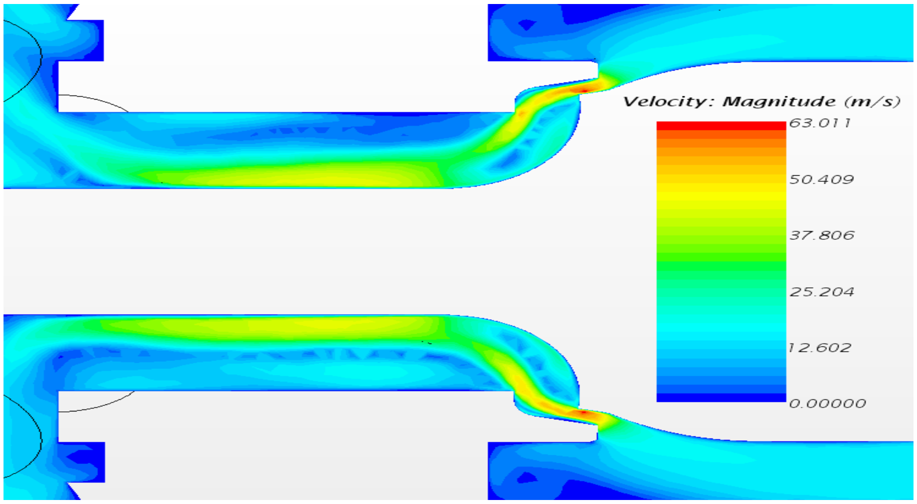

Figure 5.64. Unsteady state velocity scalar - type B- gap 0.017in, time-step 0.004S.

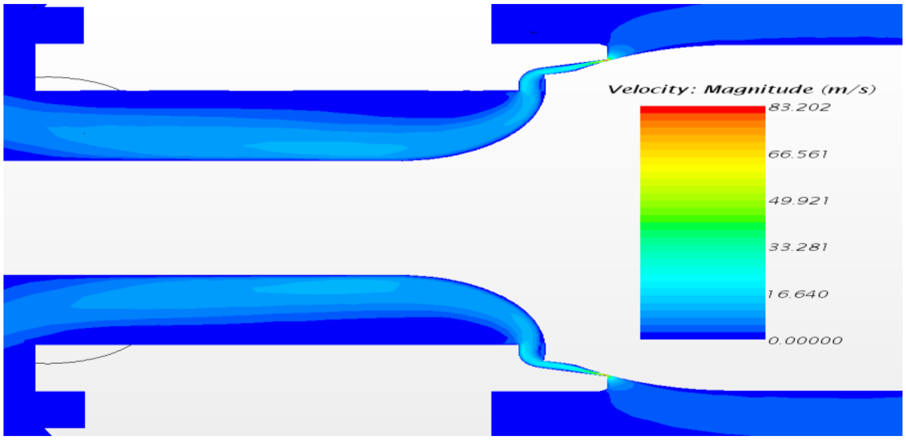

Figure 5.65. Unsteady state velocity scalar - type B- gap 0.002in, time-step 0.08S.

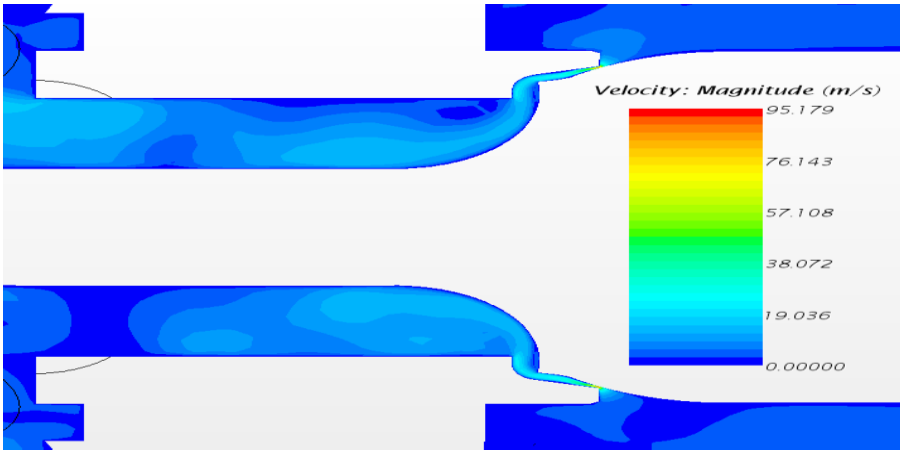

Figure 5.66. Unsteady state velocity scalar - type B- gap 0.005in, time-step 0.08S.

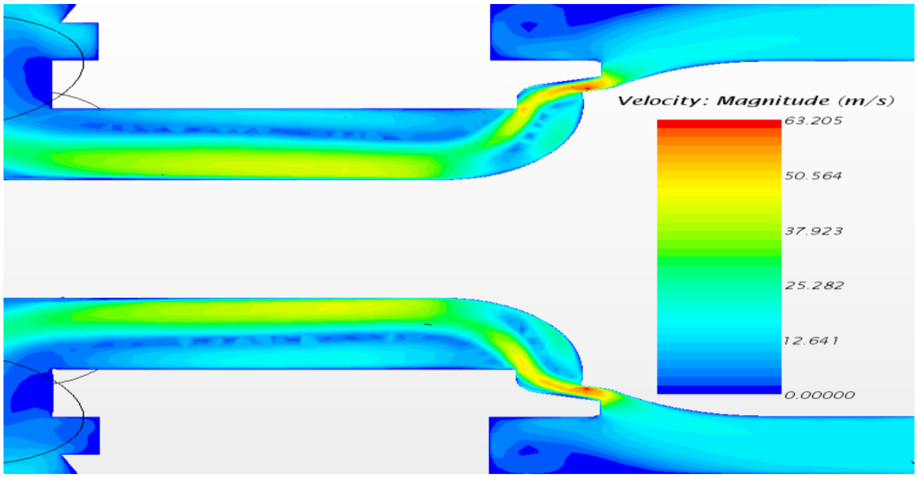

Figure 5.67. Unsteady state velocity scalar - type B- gap 0.017in, time-step 0.08S.

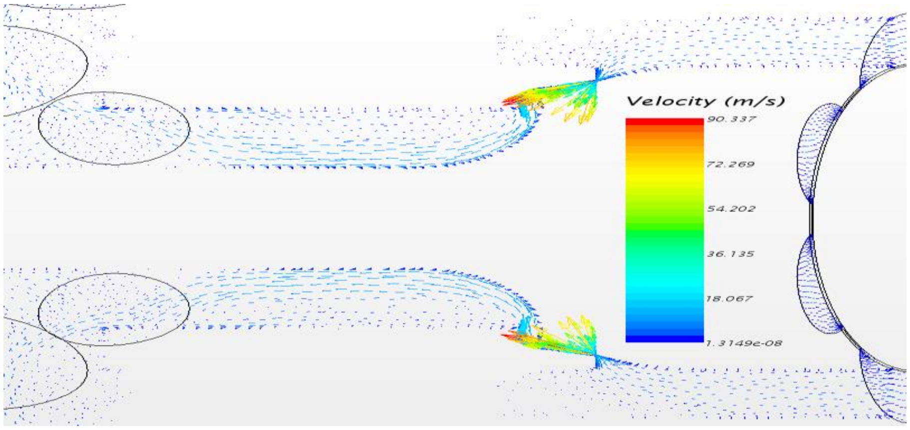

Figure 5.68. Unsteady state velocity vector - type B- gap 0.002in, time-step 0.004S.

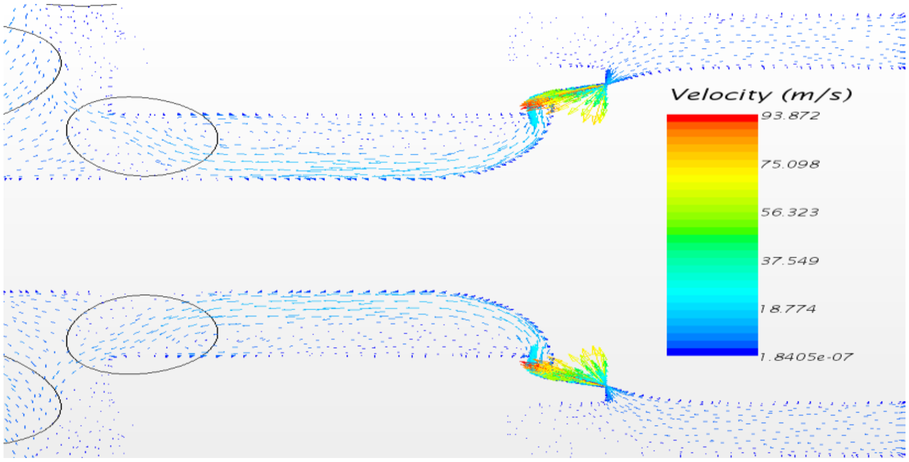

Figure 5.69. Unsteady state velocity vector - type B- gap 0.005in, time-step 0.004S.

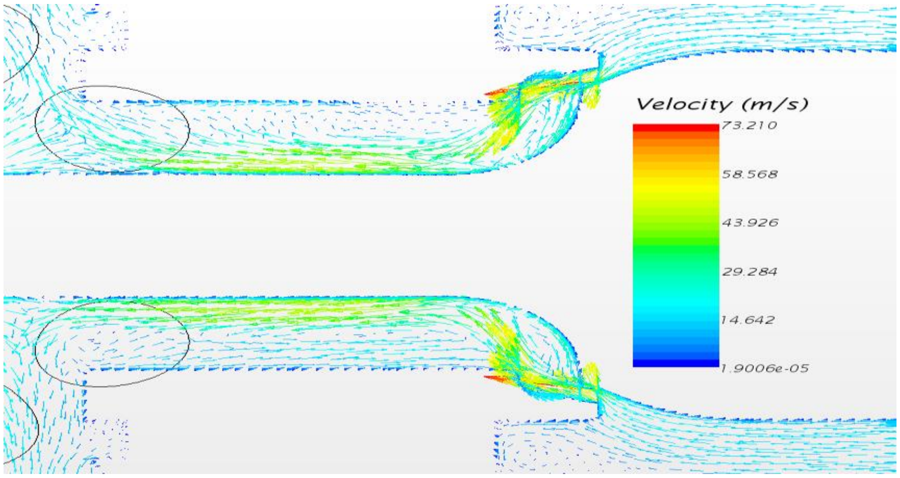

Figure 5.70. Unsteady state velocity vector - type B- gap 0.017in, time-step 0.004S.

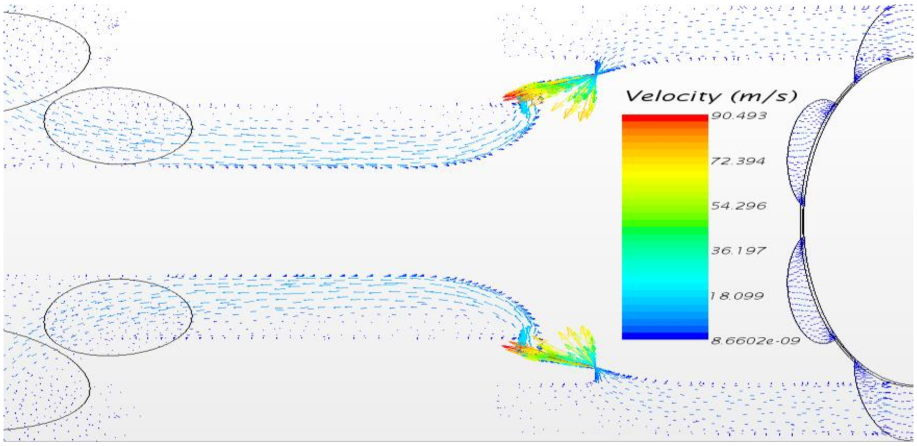

Figure 5.71. Unsteady state velocity vector - type B- gap 0.002in, time-step 0.08S.

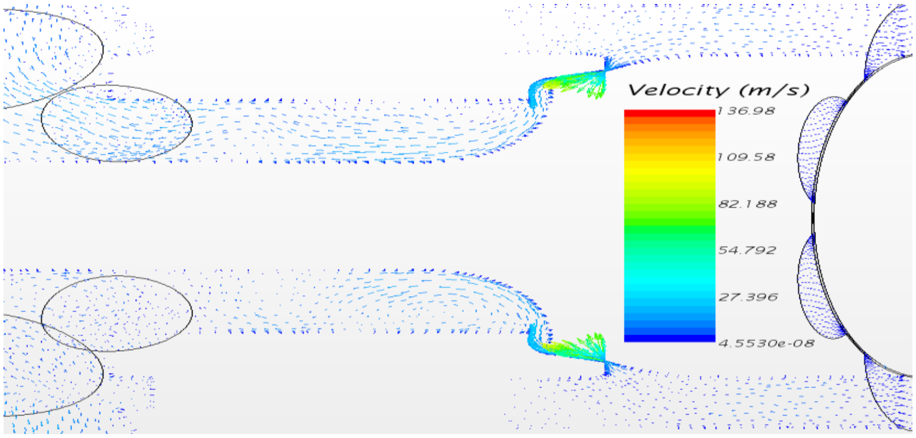

Figure 5.72. Unsteady state velocity vector - type B- gap 0.005in, time-step 0.08S.

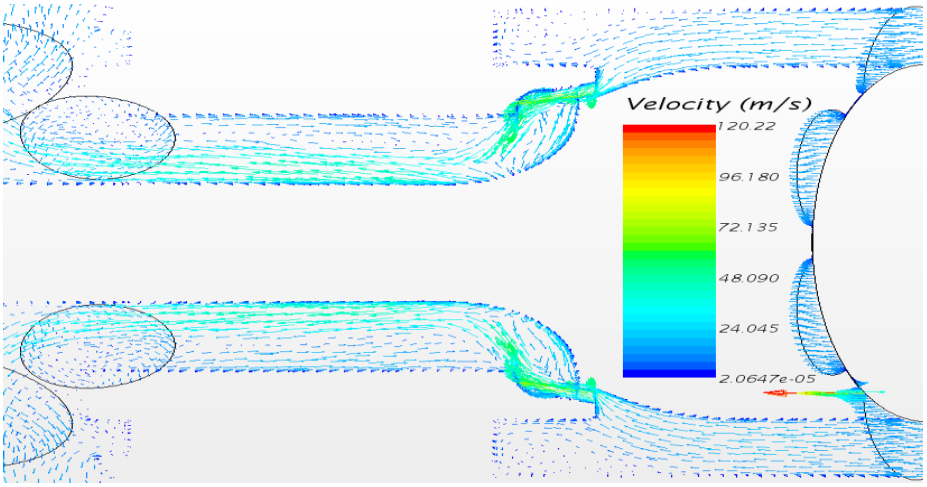

Figure 5.73. Unsteady state velocity vector - type B- gap 0.017in, time-step 0.08S.

The same boundary condition of 700-psi upstream and 300-psi downstream pressure has been used in these simulations. The resulting flow field pressure plots are shown in Figures 5.74 to 5.79. The results are very much the same for the 0.002in and the 0.005in gaps. After the gap entrance, the pressure drops to 350 psi and stays constant through the gap and at the expansion areas. For the larger opening there is a clear pressure decrease before the gap area. The pressure drops to 500 psi and further to 350 psi at the expansion area.

The flow streamlines are shown in Figures 5.80 and 5.93 show similar results in that no recirculation bubbles can be seen close to the poppet wall. Figure 5.88 present the 0.005in gap, the result is different showing 3-D streamline flow. This difference is due to the very large velocity on gap area. The result show the path of the fluid flow is hitting in multiple directions. This 3-D result illustrate the oscillatory nature of the fluid affected by the change in velocities. For the 0.002in and 0.017 gaps, the streamlines confirm the results of the scalar and velocity vector plots showing that the recirculation region increases and elongates from gaps 0.017in to 0.002in as presented in Figures 5.90 to 5.92. Figures 5.85 and 5.91 present 3-D flow streamline at the expansion as in that for figures 5.60 and 5.61. Appearance of the small recirculation bubble at the large opening that can be clearly seen in Figures 5.86 and 5.93 as observed in larger gap in type B valve of steady state case. These plots are in agreement with velocity plots, showing the same recirculation regions.

The volumetric flow rate results was calculated for all gaps. The results show flows of 1.87 gpm, 2.38 gpm and 10.11 gpm, as the type A valve, the volumetric flow rate increases as the gap increases.

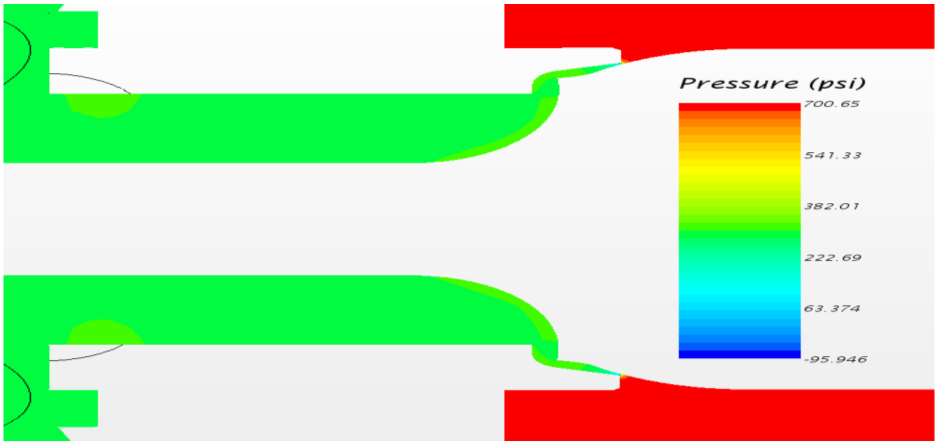

Figure 5.74. Unsteady state pressure scalar - type B- gap 0.002in, time-step 0.004S.

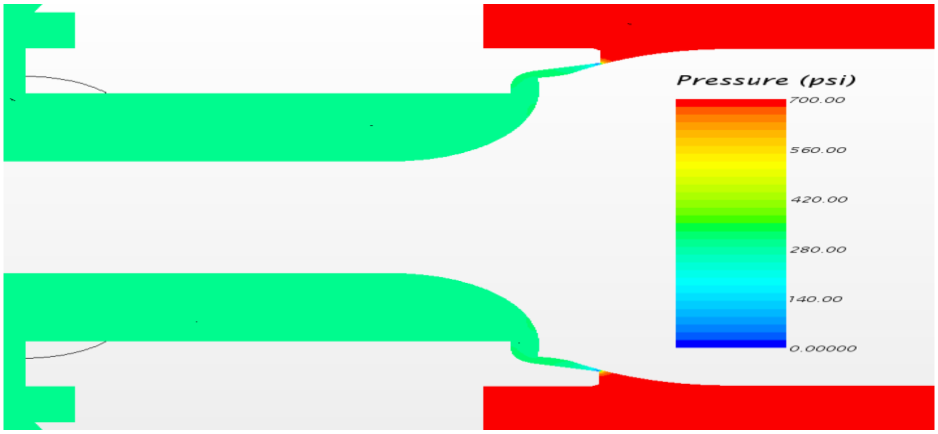

Figure 5.75. Unsteady state pressure scalar - type B- gap 0.005in, time-step 0.004S.

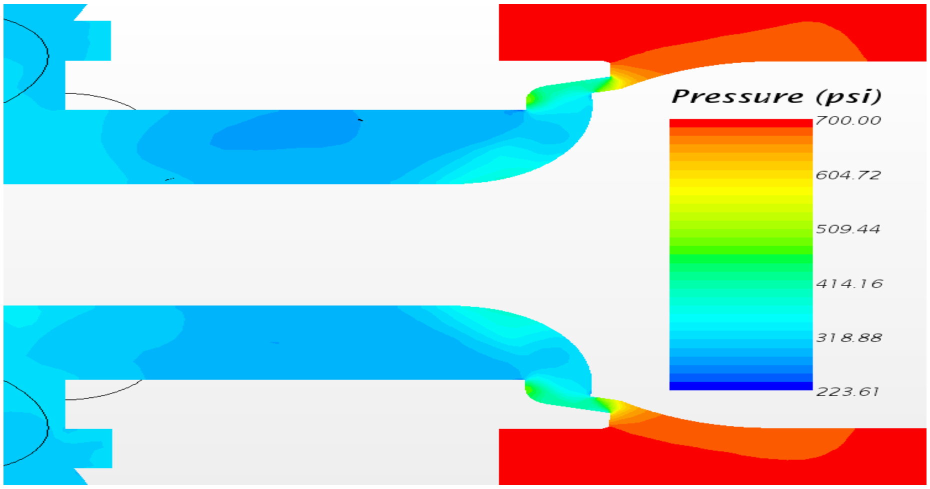

Figure 5.76. Unsteady state pressure scalar - type B- gap 0.017in, time-step 0.004S.

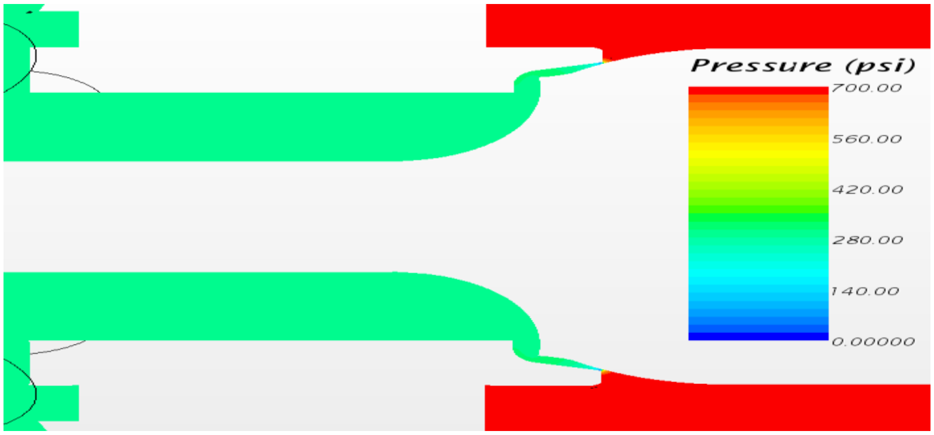

Figure 5.77. Unsteady state pressure scalar - type B- gap 0.002in, time-step 0.08S.

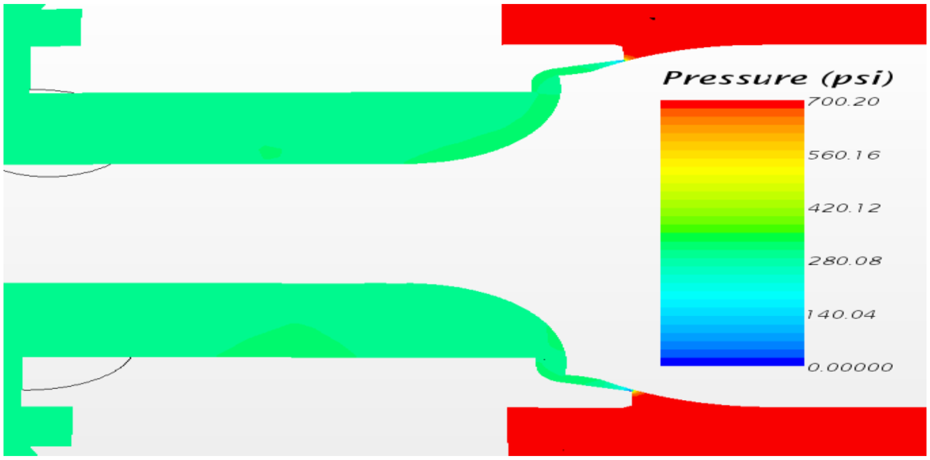

Figure 5.78. Unsteady state pressure scalar - type B- gap 0.005in, time-step 0.08S.

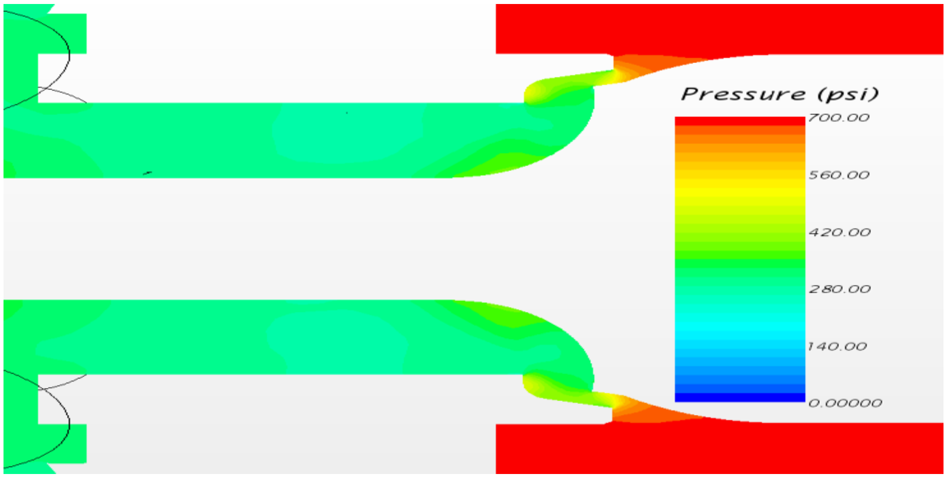

Figure 5.79. Unsteady state pressure scalar - type B- gap 0.017in, time-step 0.08S.

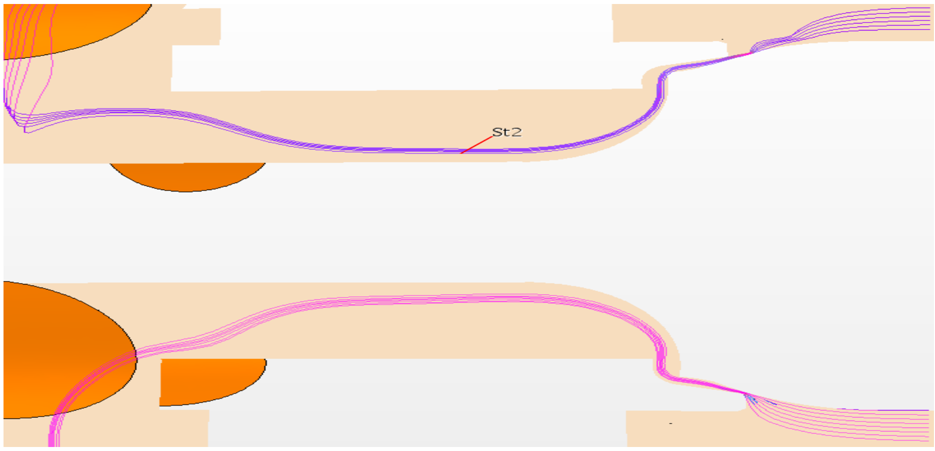

Figure 5.80. Unsteady state streamline plot for gap 0.002in, valve type B, time-step 0.004S.

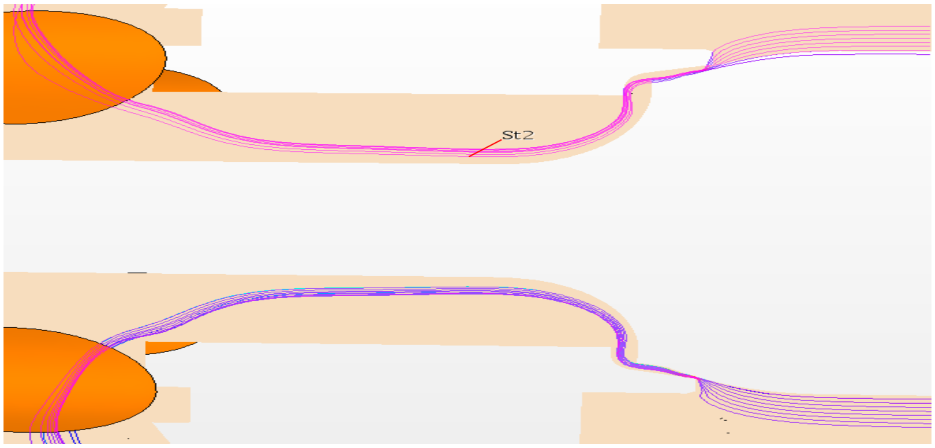

Figure 5.81. Unsteady state streamline plot for gap 0.005in, valve type B, time-step 0.004S.

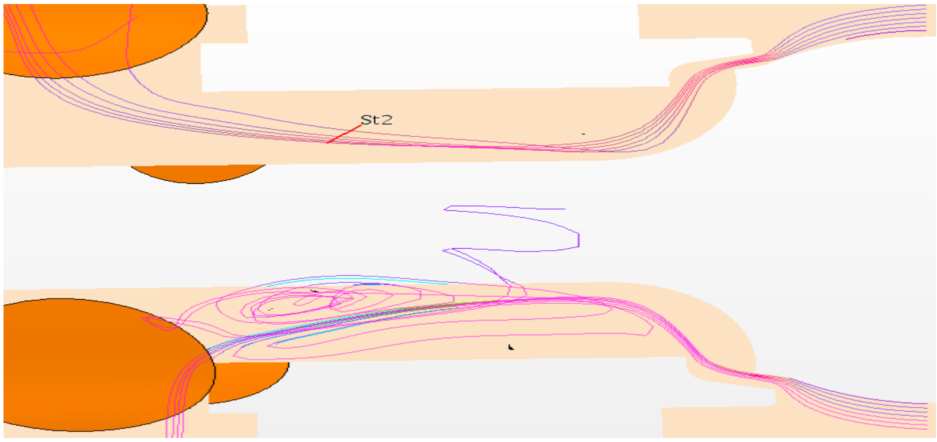

Figure 5.82. Unsteady state streamline plot for gap 0.017in, valve type B, time-step 0.004S.

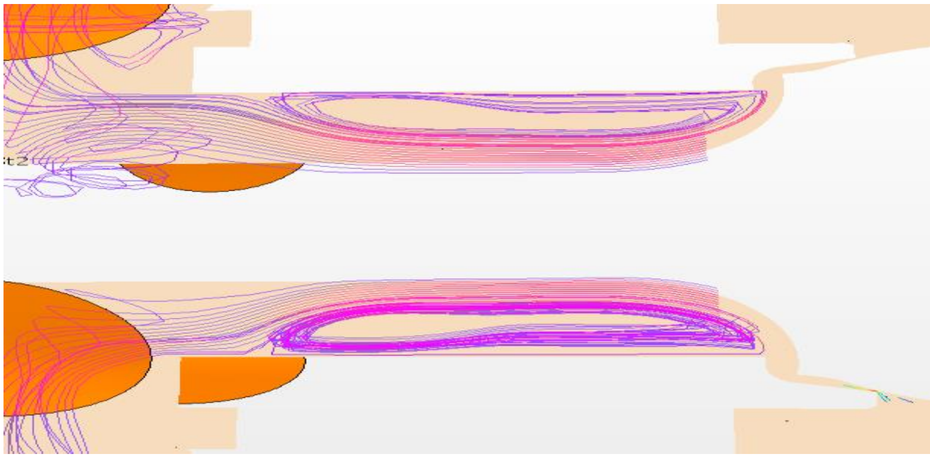

Figure 5.83. Unsteady state streamline plot at the expansion area, gap 0.002in, valve type B, time-step 0.004S.

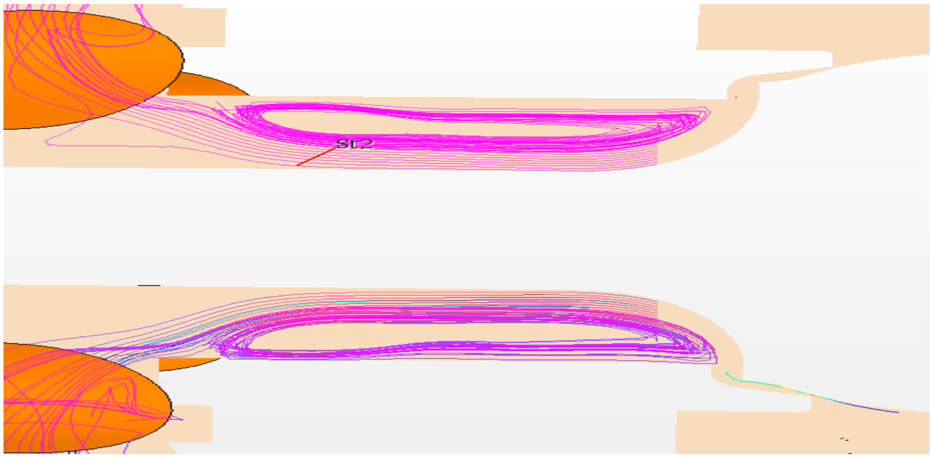

Figure 5.84. Unsteady state streamline plot at the expansion area, gap 0.005in, valve type B, time-step 0.004S.

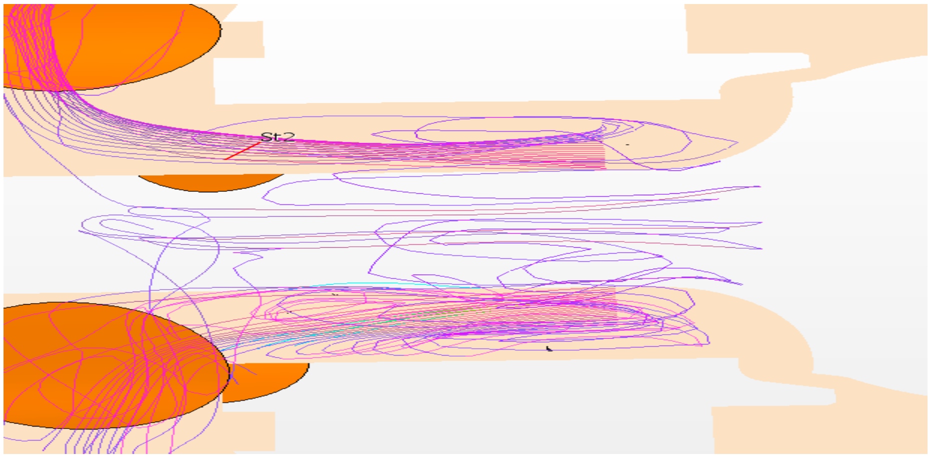

Figure 5.85. Unsteady state streamline plot at the expansion area, gap 0.017in, valve type B, time-step 0.004S.

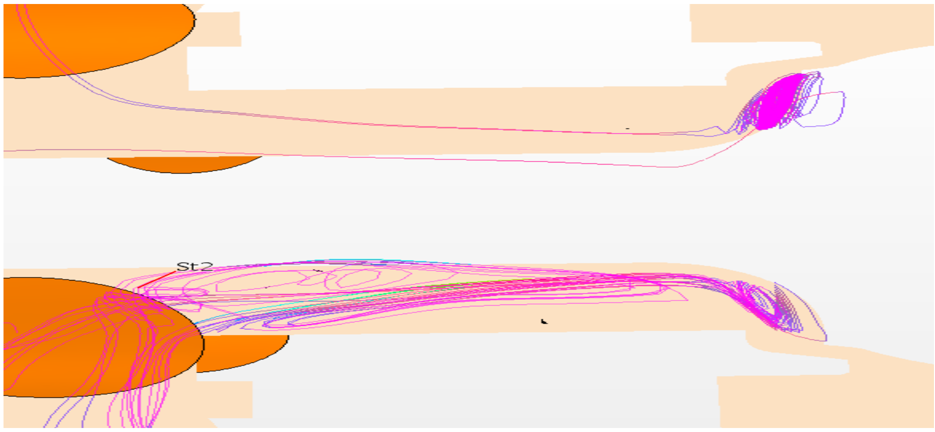

Figure 5.86. Unsteady state streamline plot at the expansion area, gap 0.017in, showing recirculation at the jet exit, valve type B, time-step 0.004S.

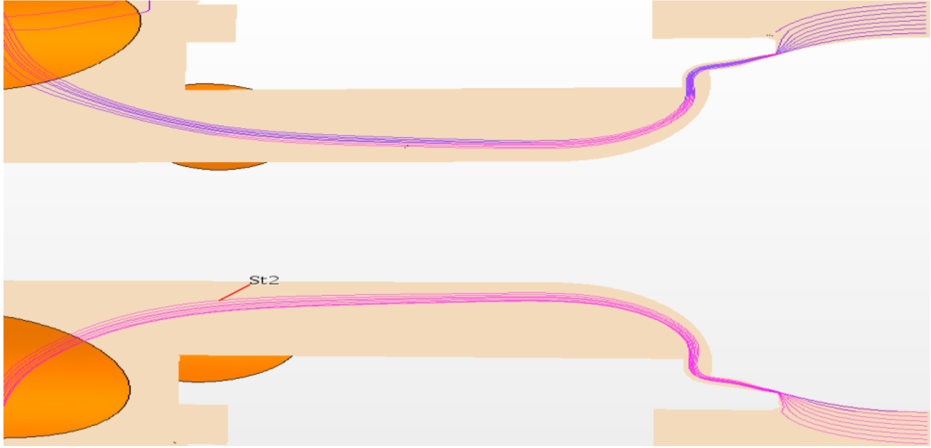

Figure 5.87. Unsteady state streamline plot for gap 0.002in, valve type B, time-step 0.08S.

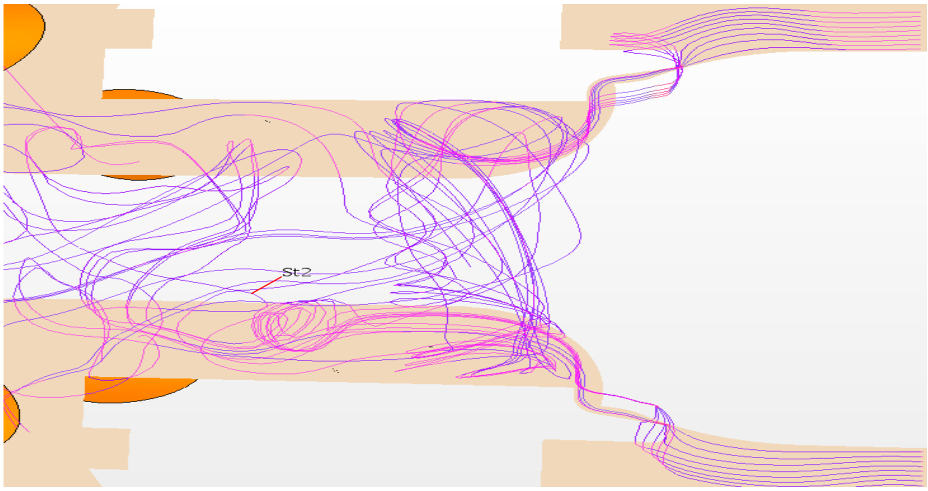

Figure 5.88. Unsteady state streamline plot for gap 0.005in, valve type B, time-step 0.08S.

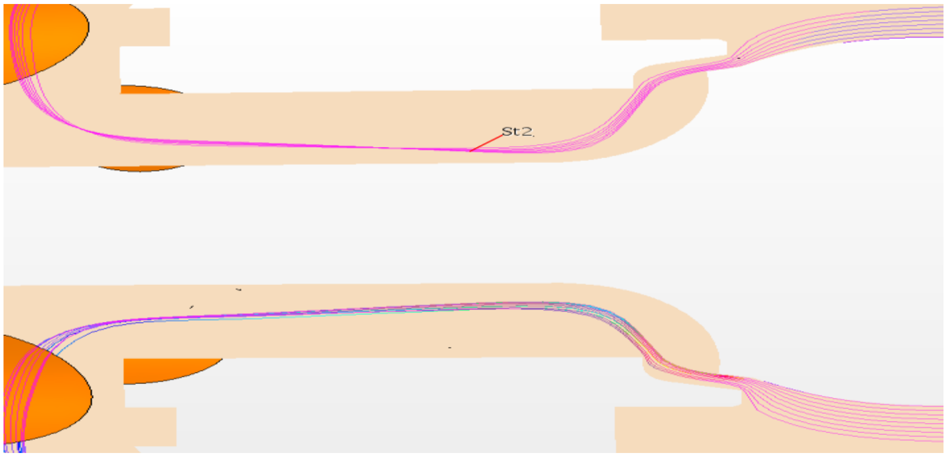

Figure 5.89. Unsteady state streamline plot for gap 0.017in, valve type B, time-step 0.08S.

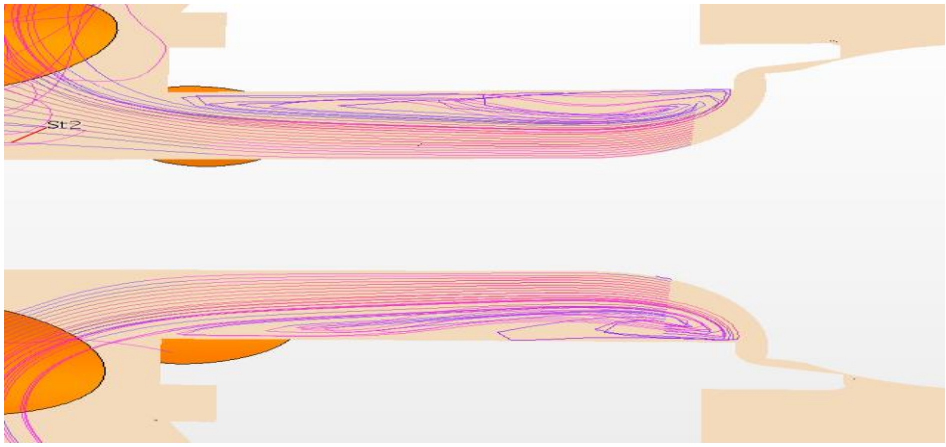

Figure 5.90. Unsteady state streamline plot at the expansion area, gap 0.002in, valve type B, time-step 0.08S.

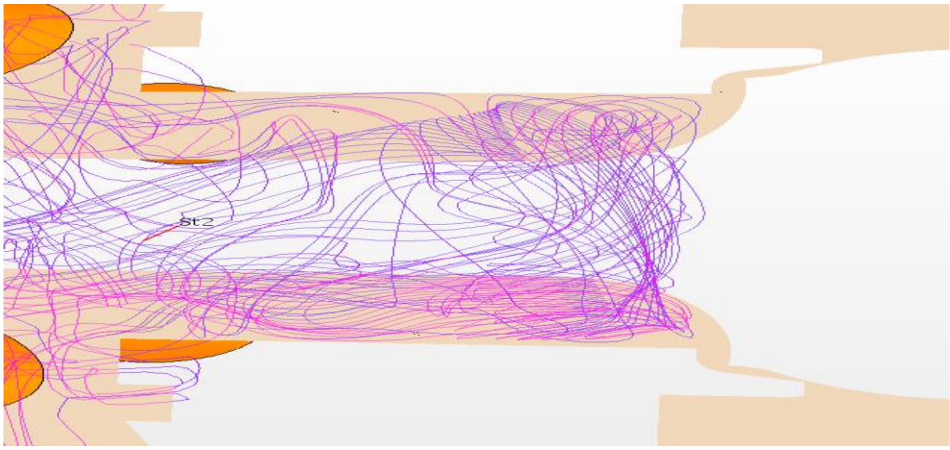

Figure 5.91. Unsteady state streamline plot at the expansion area, gap 0.005in, valve type B, time-step 0.08S.

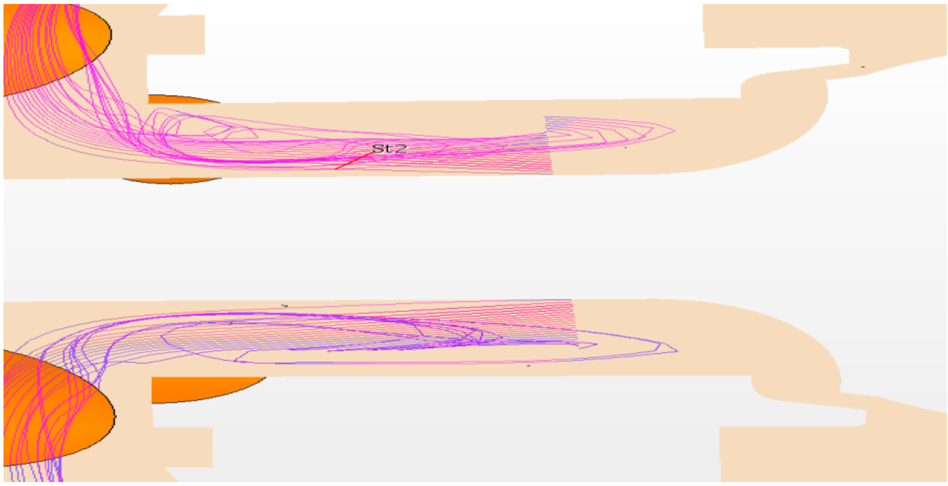

Figure 5.92. Unsteady state streamline plot at the expansion area, gap 0.017in, valve type B, time-step 0.08S.

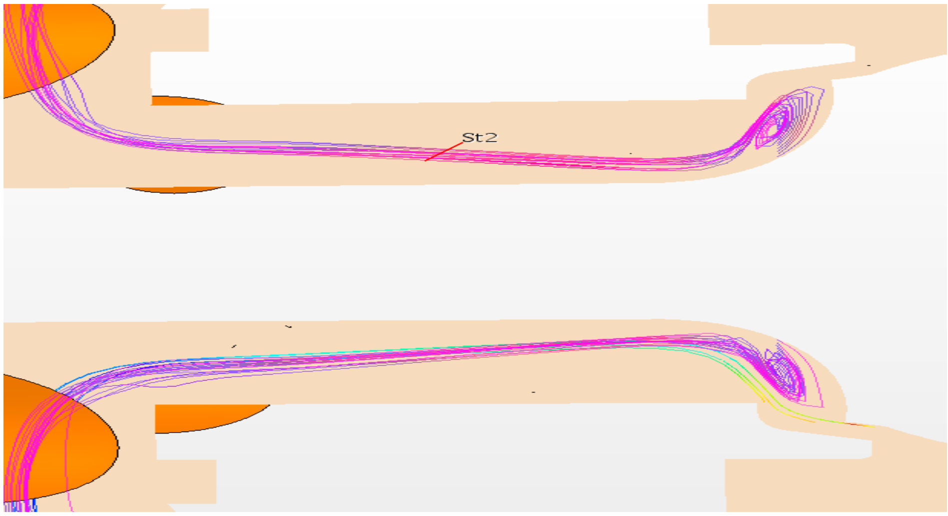

Figure 5.93 Unsteady state streamline plot at the expansion area, gap 0.017in, showing recirculation at the jet exit, valve type B, time-step 0.08S.

5.3.3. Unsteady State Summary

There was great similarity between the steady state and the unsteady state results. The unsteady-state results are very similar for both valves, except for valve type B with a large gap. For both valves, the velocity plots are in agreement in that the velocities are low everywhere except at the gap area. For both the unsteady and steady state simulations, the velocity increases proportionally with the gap from 0.002in to 0.005in and decreases for the 0.017in gap.

The velocity-vector plots show no recirculation bubbles close to the poppet wall in both valves as in the steady-state case. For both valves, recirculation zones can be seen above the gap and the expansion areas, and the recirculation bubble at the expansion area increases and elongates when the gap decreases. A small recirculation bubble can be seen at the area of expansion next to the jet exit for the larger gap of type B valve as appeared in the steady-state case for the same valve and opening. Animation of the oscillatory nature of the fluid flow can be seen on movies for both valves under all opening conditions attached with this dissertation as (DVD).

700-psi upstream and 300-psi downstream flow field pressure plots were analyzed for both valves. In both valves for the 0.002in and 0.005in gaps, high pressure can be seen before the gap. Low pressure can be clearly observed in the area for the two larger gaps. Again, as for steady state the results show that for both valves the pressure drop across the gap decreases as the gap increases.

Slightly differences of flow streamline plots between steady and unsteady state can be observed. For both valves, the volumetric flow rate was calculated. The results confirm the steady-state results in that the volumetric flow rate increases with the gap increases. Table 5.2 present a detailed results for the maximum velocities and the volumetric flow rates for both unsteady and steady state simulations. The results show, for both cases the maximum velocities and the volumetric flow rates are very much the same for the 0.002in and 0.005in gaps of type A valve and 0.002in gap for the type B valve. The 0.005in and the two larger gaps show high the maximum velocities and the volumetric flow rates for the unsteady state than the steady state one.

Table 5.3. Maximum velocities and volumetric flow rates of the unsteady-state solution for both valves (A, and B)

Gap type	**Unsteady state Maximum Velocity ft/s**	**Steady state Maximum Velocity ft/s**	**Unsteady state Volumetric flow rate gpm**	**Steady state Volumetric flow rate gpm**
A-0.002	151	150	0.73	0.73
A-0.005	256	255	2.92	2.39
A-0.017	296	307	14.99	12.98
B-0.002	297	297	1.87	1.60
B-0.005	449	309	2.38	1.99
B-0.017	394	243	10.11	8.60

5.4. Unsteady State Streamline Behavior

In order to verify our hypothesis that the flow induced noise was the result of a shear-layer induced acoustic resonance in the valve cavity, the shear-layer was investigated by plotting the time dependent behavior of the streamlines in the narrow gap between the piston and poppet. Four streamlines, evenly spaced within that gap were chosen, for each of those streamlines four points, also evenly spaced, one each at the inlet and outlet of the gap and the other two inside the gap were analyzed. The location of the four points for both types of valves is shown in Fig. 5.94 to 5.101.

5.4.1. Unsteady State Results for the Type A Valve

Figures 5.102 to 5.113 summarize streamline behavior for the type A valve. The results are presented for all 3 gaps and for running times of 0.04 and 0.8 seconds. Each plots shows the time dependent behavior of one point in the streamline, the x-coordinate being time in seconds and the y-coordinate the radial coordinate in normalized units. The upper points being closer to the poppet and the lower ones closer to the piston. It is quite remarkable to note that in all cases there is a radial displacement for every point at intervals 0.0009 seconds, corresponding to a wave frequency of 1111 Hz. For the smallest gap, 0.002 in., there are no significant differences between the 0.004 and 0.08 plots for any of the locations. For the larger two gaps, 0.005 0.017, there is a significant difference in the streamline behavior between the 0.04 and 0.8 seconds results. It is clear that the larger gaps allow for larger oscillations in the streamline position. These oscillations increase as the gap increases and they are more pronounced as we move downstream. Figures 5.93 and 5.94 corresponding to the two downstream positions for the largest gap clearly demonstrate this behavior. In both cases the 1111 Hz superimposed pulse can be clearly observed. The results of the other points for all 3 gaps are presented in Appendix B Figures 5.126 – 5.137.

5.4.2. Unsteady State Results for the Type B Valve

The results obtained for valve B are presented are presented in Fig.5.114 – Fig. 125. For the largest and smallest gaps (0. 002 and 0.017 in.) the behavior is somewhat similar to the type A valve, showing a radial streamline displacement at 0.0009 second intervals for all locations. For the 0.002 gap, oscillatory behavior could be observed at 0.08 seconds that was absent in the type A valve. For the large gap (0.017 in.) the 1111 Hz signal could be observed for all locations at 0.004 s. but it was very weak or missing at 0.08 s. for the points closest to the piston, at the largest distance from the flow centerline.

Remarkably, the 1111 Hz signal could not be detected at any of the locations for the middle (0.005 in.) gap. For both 0.004 and 0.08 seconds streamline location did not show any regularity or discernable pattern, appearing to be aleatory in nature. Figure 5.89 showing the unsteady flow streamlines for the 0.05 gap at 0.08 seconds shows a very complex tri-dimensional behavior that is consistent with this result. As for the type A the results of the other points for all 3 gaps are presented in Appendix B Figures 5.138 – 5.149.

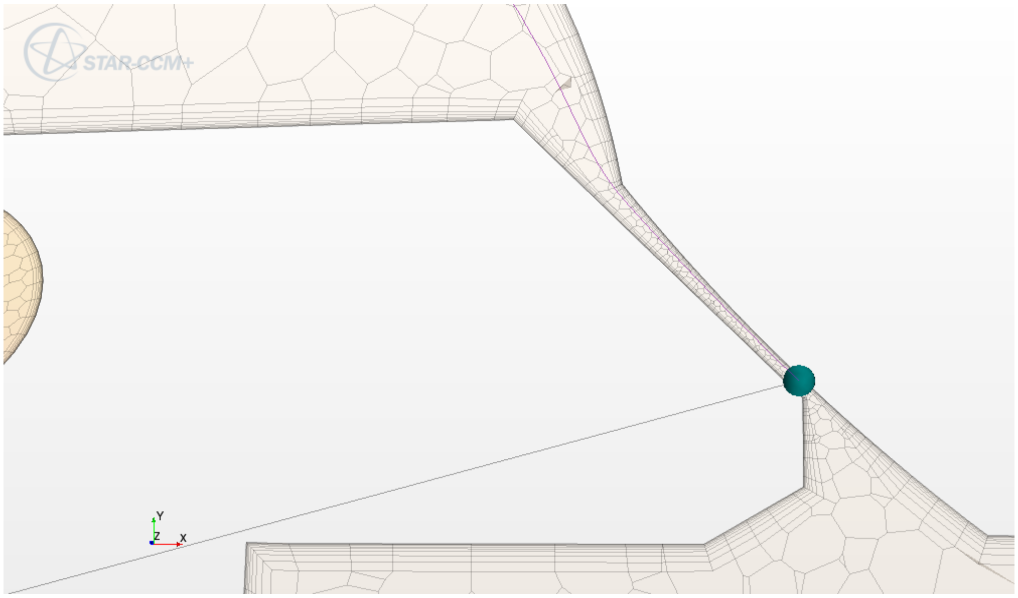

Figure 5.94. Point one counterbalance valve type A.

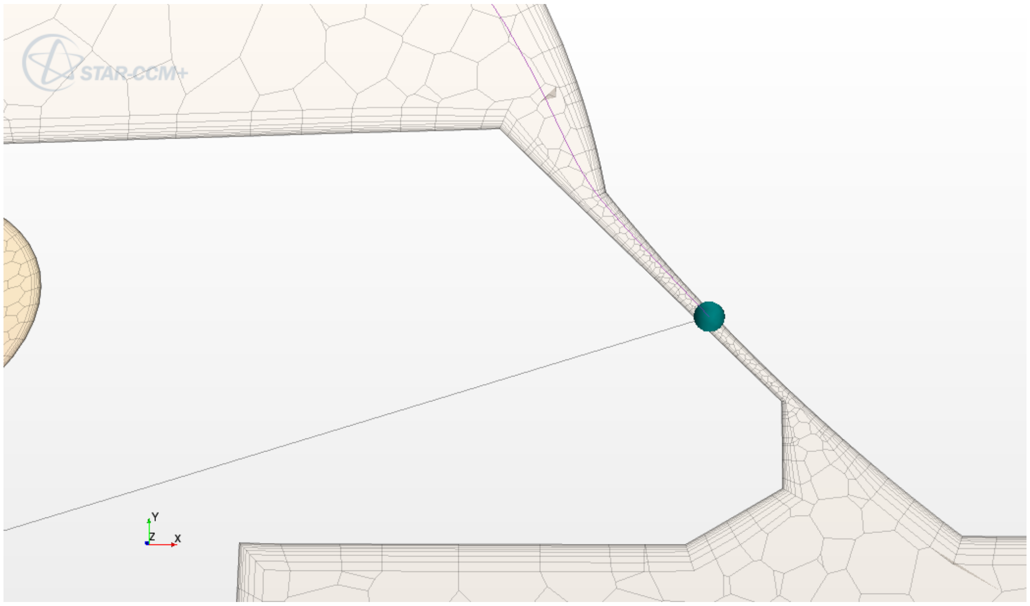

Figure 5.95. Point two counterbalance valve type A.

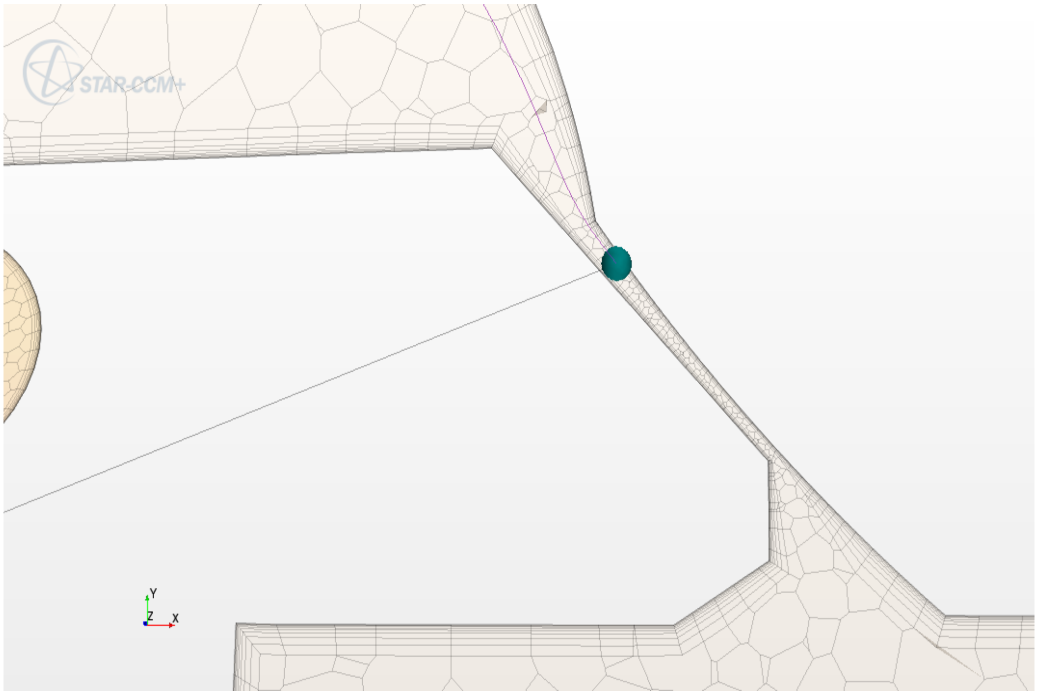

Figure 5.96. Point three counterbalance valve type A.

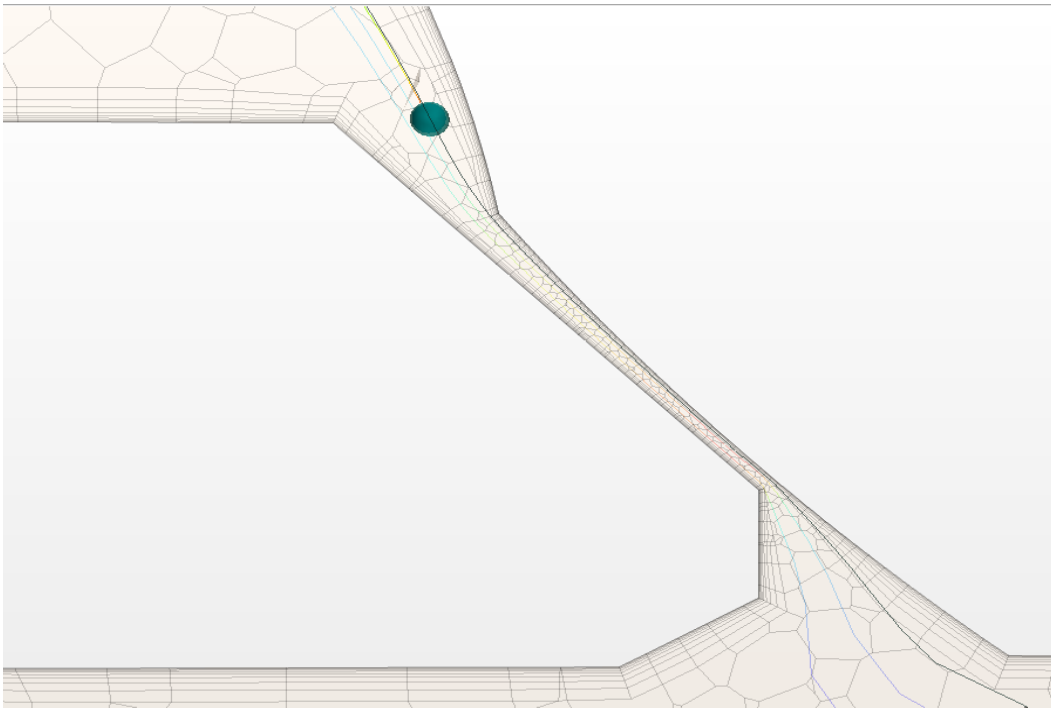

Figure 5.97. Point four counterbalance valve type A.

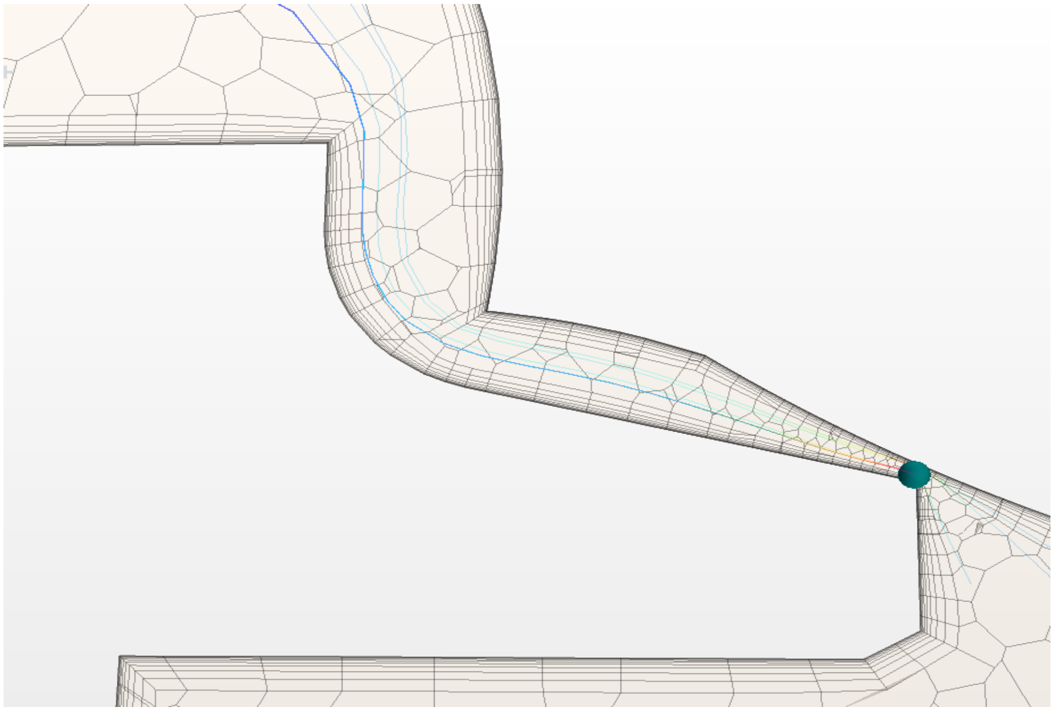

Figure 5.98. Point one counterbalance valve type B.

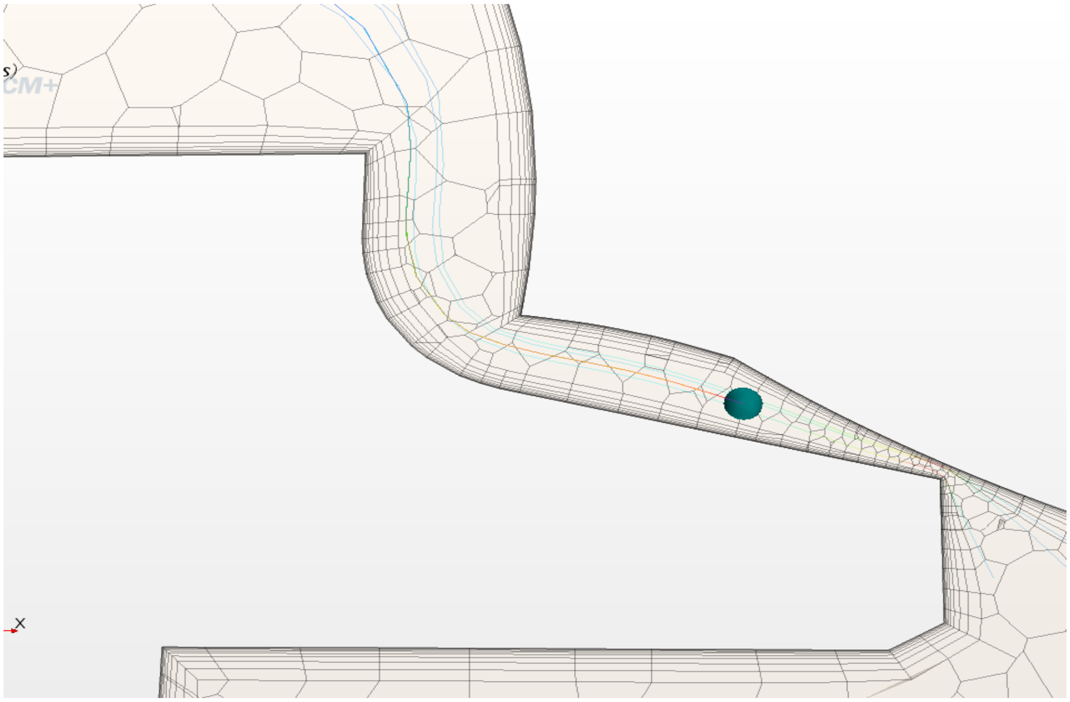

Figure 5.99. Point two counterbalance valve type B.

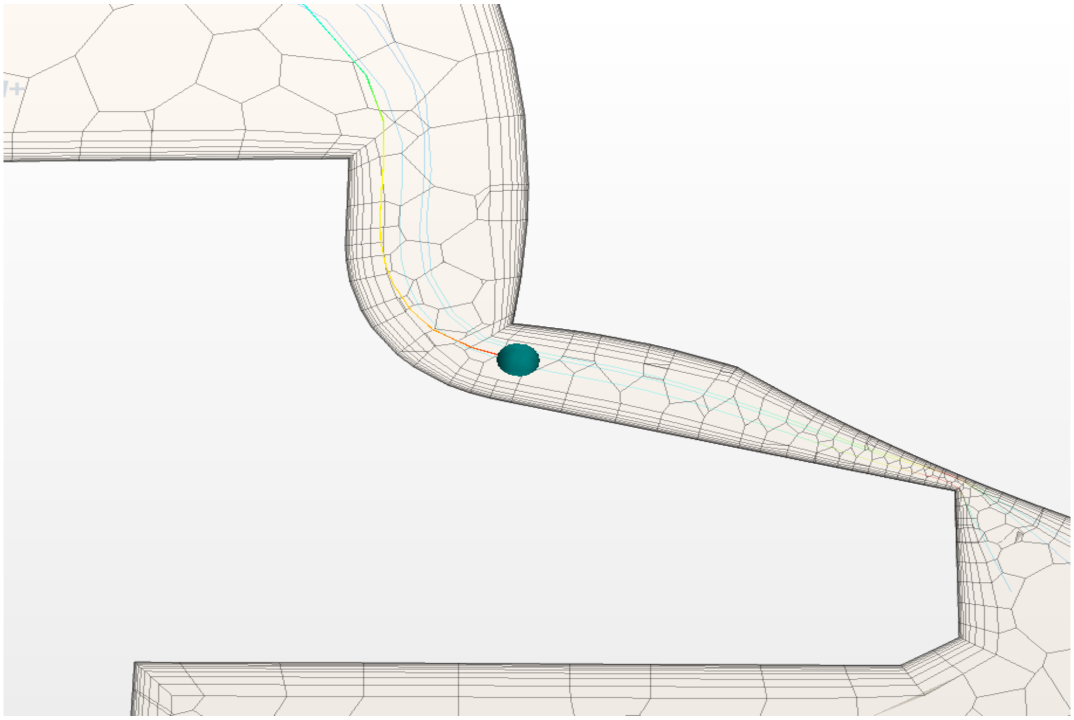

Figure 5.100. Point three counterbalance valve type B.

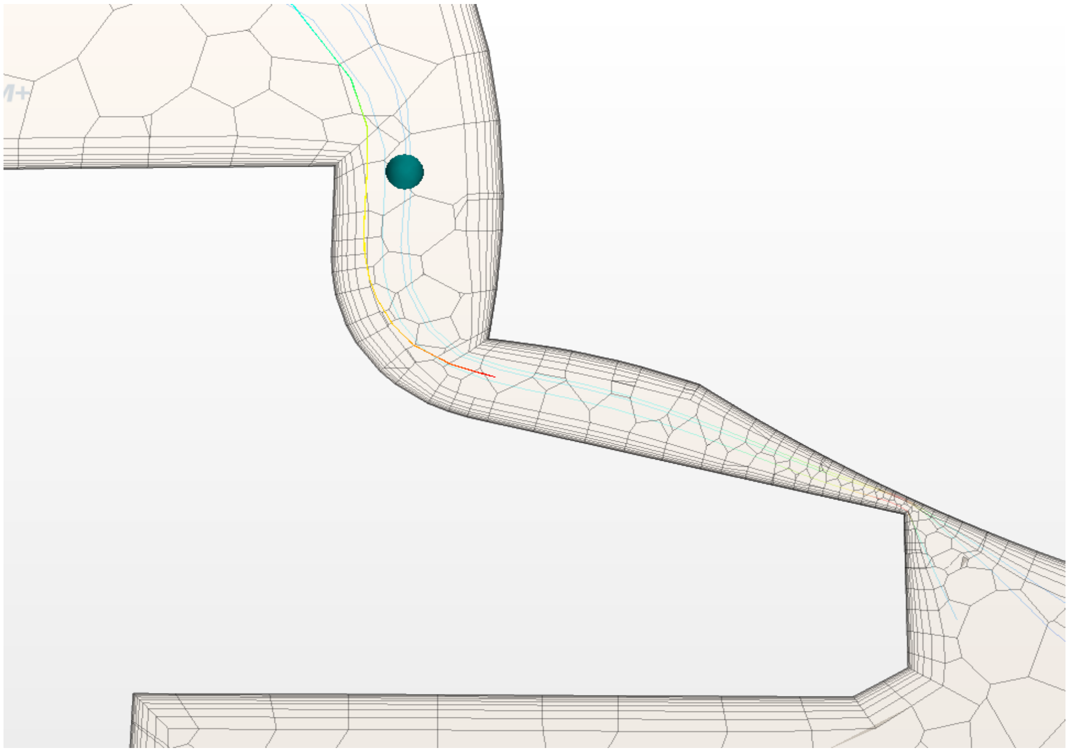

Figure 5.101. Point four counterbalance valve type B.

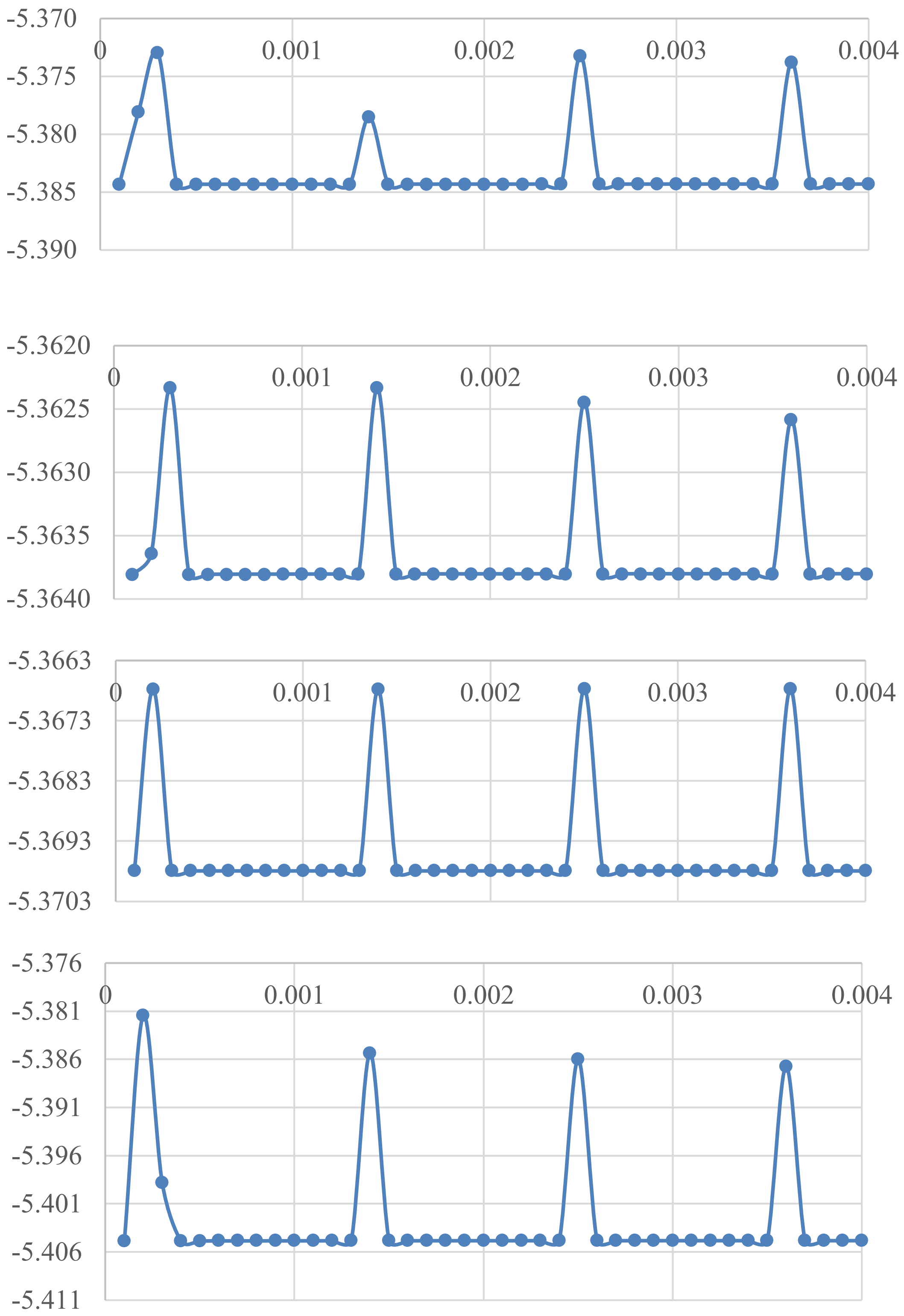

Figure 5.102. Streamlines at point one (x = 0.005mm) for type A-gap 0.002in, maximum physical time 0.004 second, x-axis time in s, y-axis in mm.

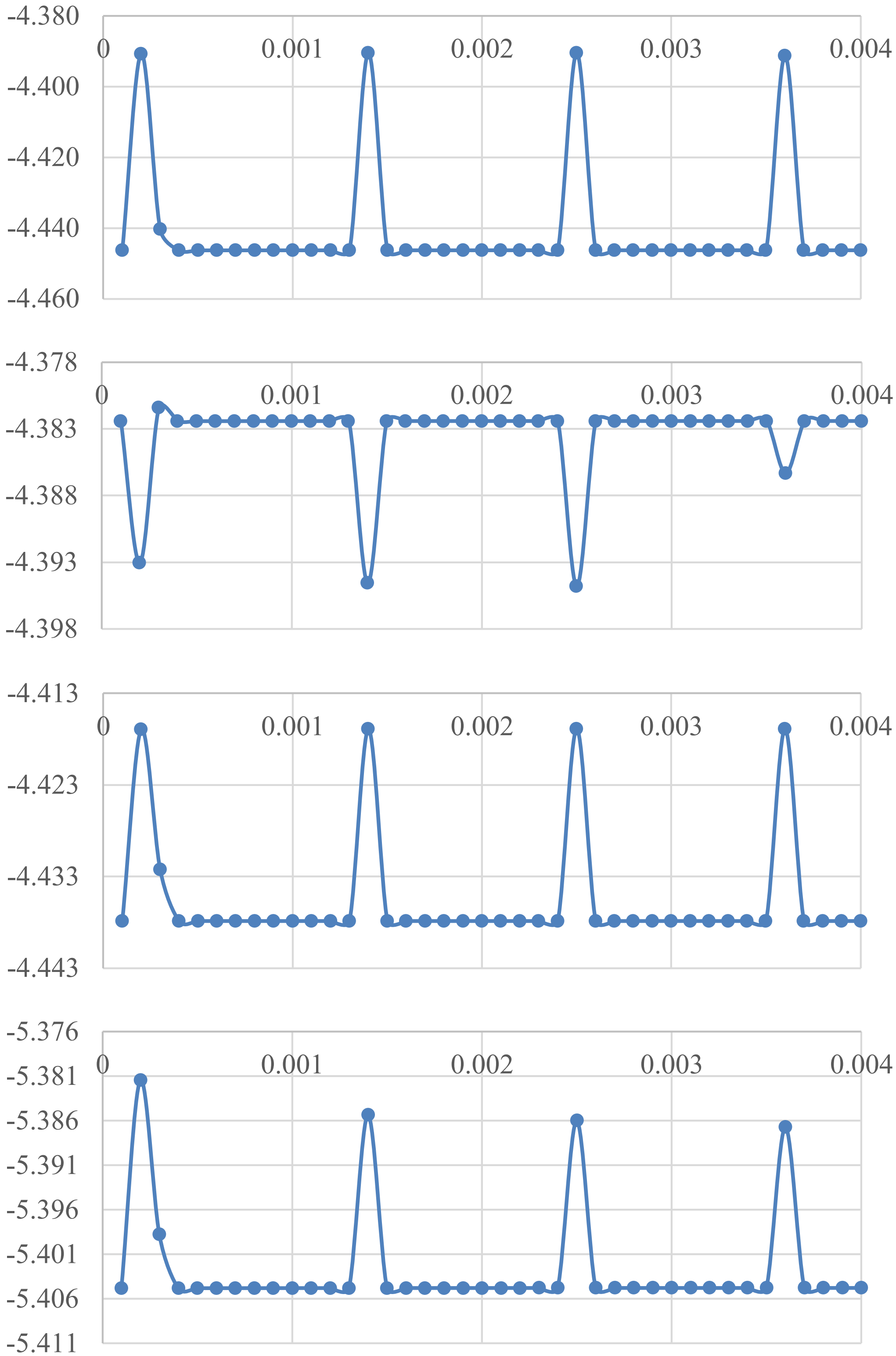

Figure 5.103. Streamlines at point four (x = 0.810mm) for type A-gap 0.002in,maximum physical time 0.004 second, x-axis time in s, y-axis in mm.

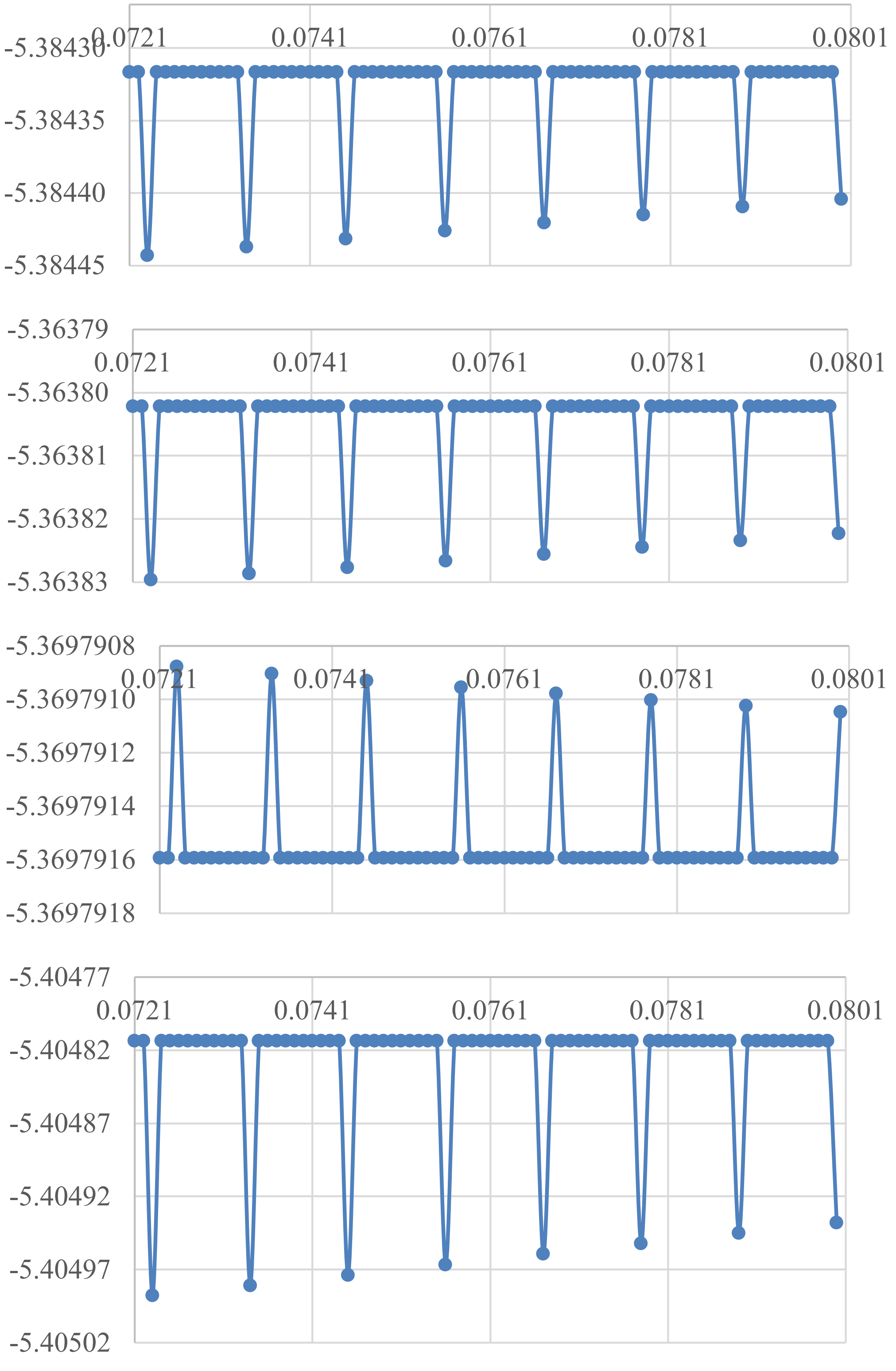

Figure 5.104. Streamlines at point one (x = 0.005mm) type A-gap 0.002in, maximum physical time 0.08 second, x-axis time in s, y-axis in mm.

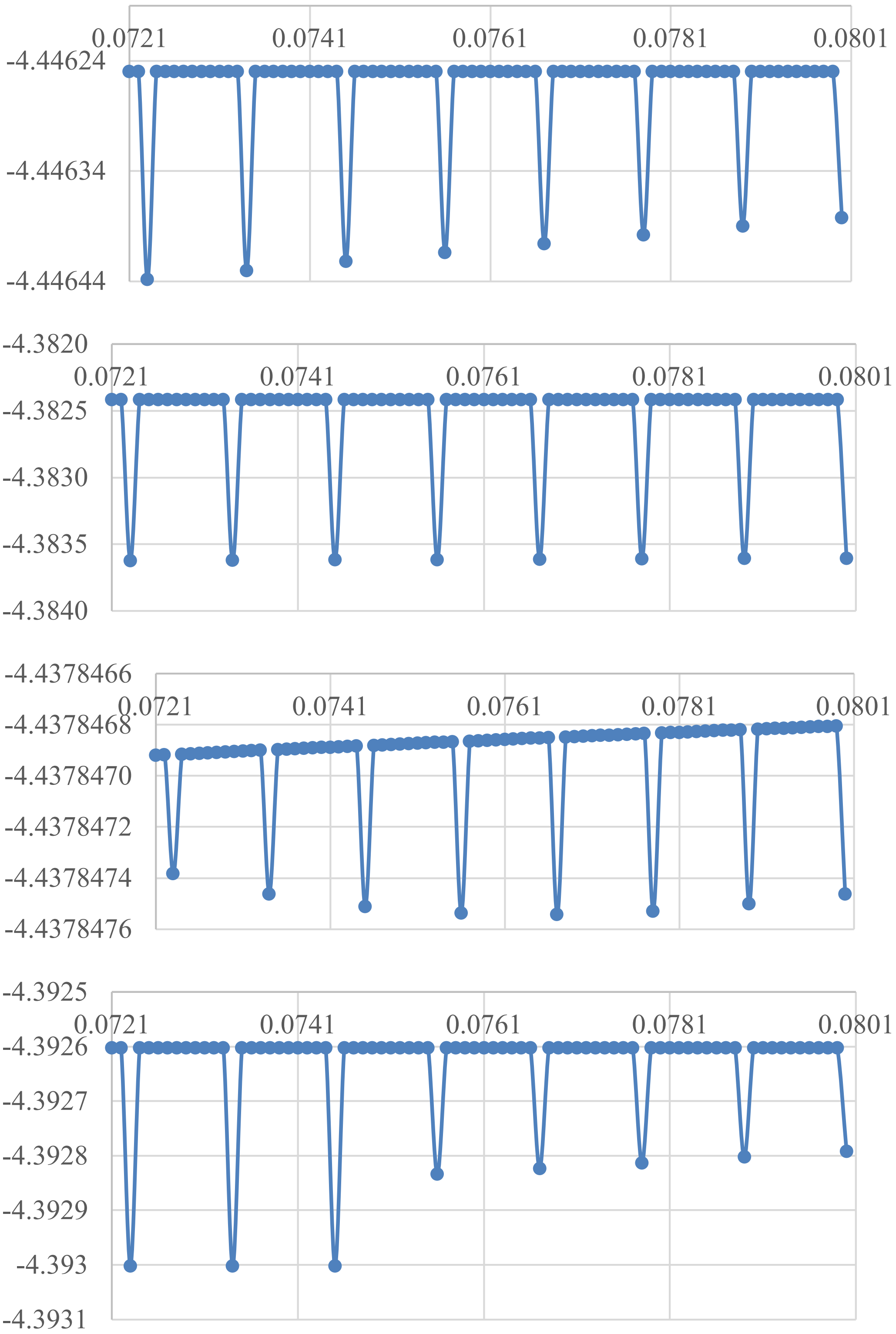

Figure 5.105. Streamlines at point four (x = 0.810mm) for type A-gap 0.002in, maximum physical time 0.08 second, x-axis time in s, y-axis in mm.

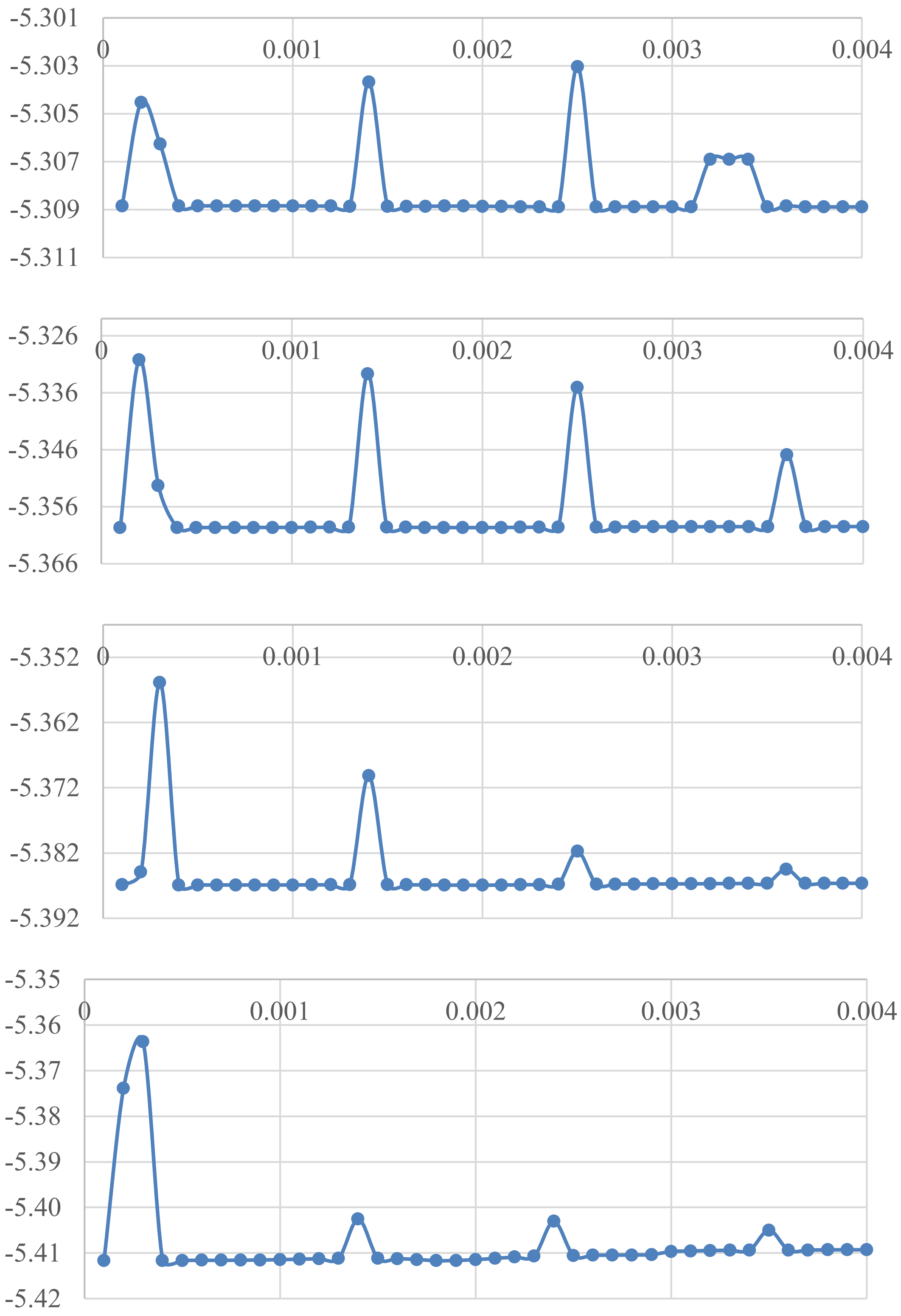

Figure 5.106. Streamlines at point one (x = 0.005mm) for type A-gap 0.005in, maximum physical time 0.004 second, x-axis time in s, y-axis in mm.

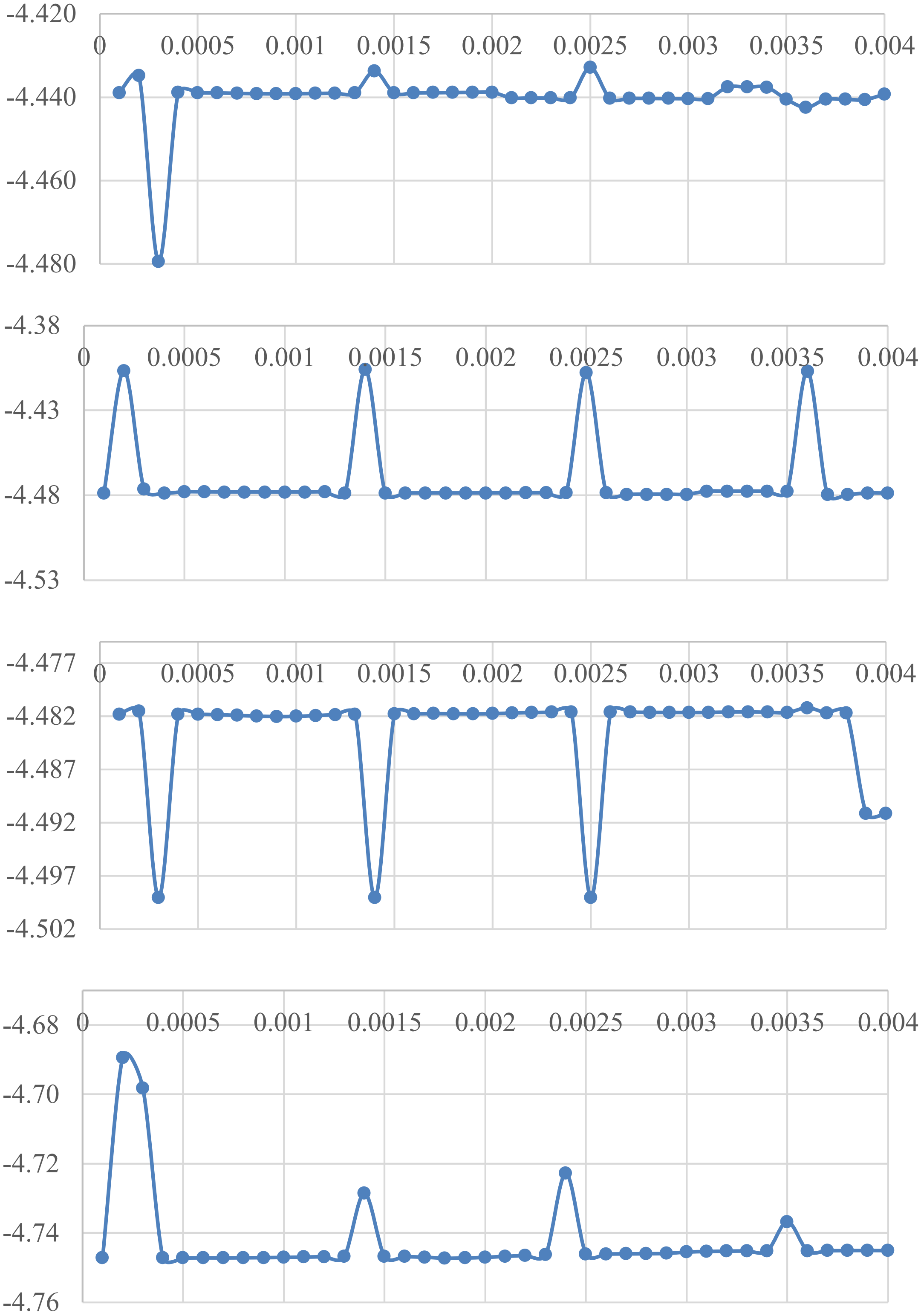

Figure 5.107. Streamlines at point four (x = 0.810mm) for type A-gap 0.005in, maximum physical time 0.004 second, x-axis time in s, y-axis in mm.

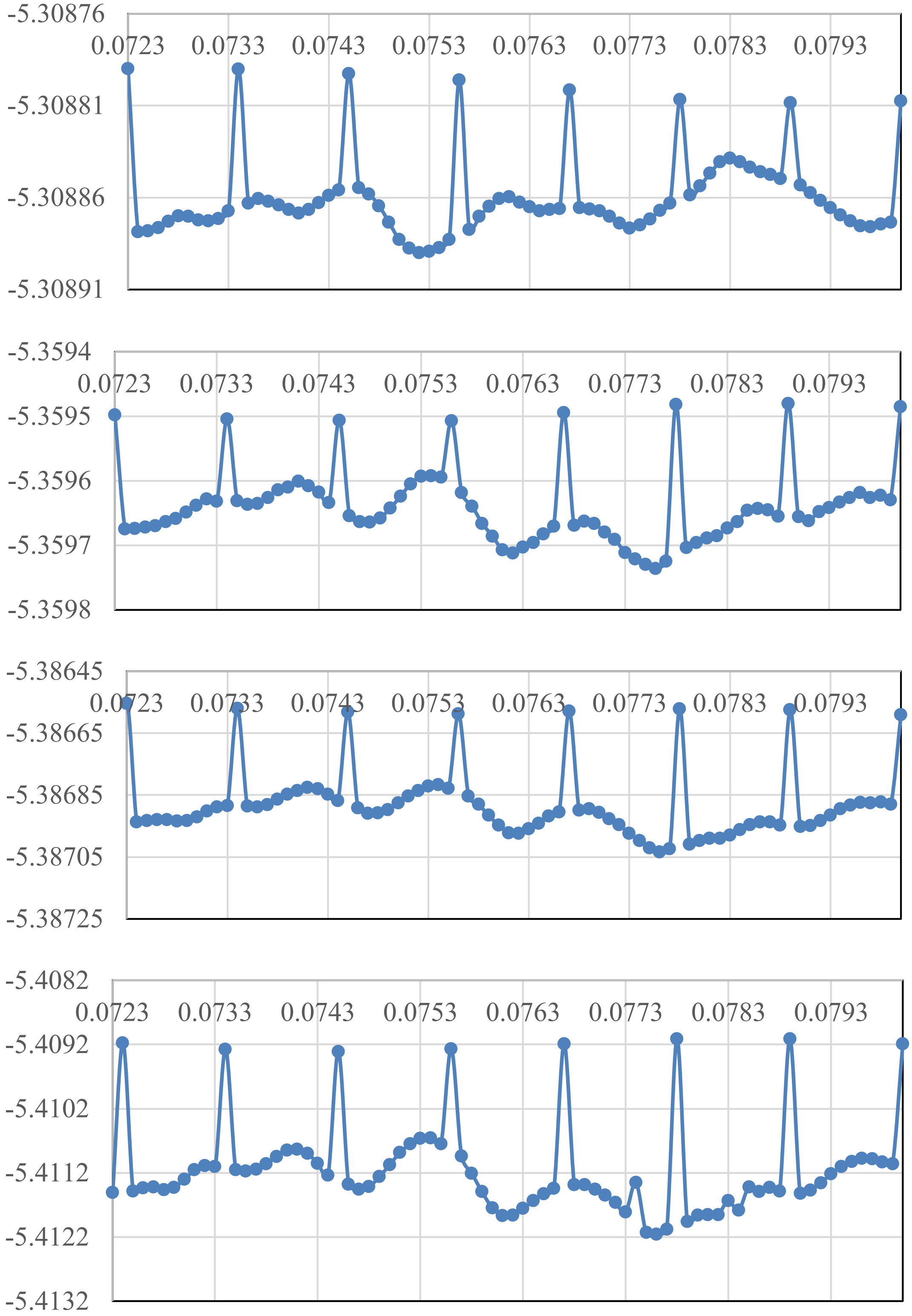

Figure 5.108. Streamlines at point one (x = 0.005mm) for type A-gap 0.005in, maximum physical time 0.08 second, x-axis time in s, y-axis in mm.

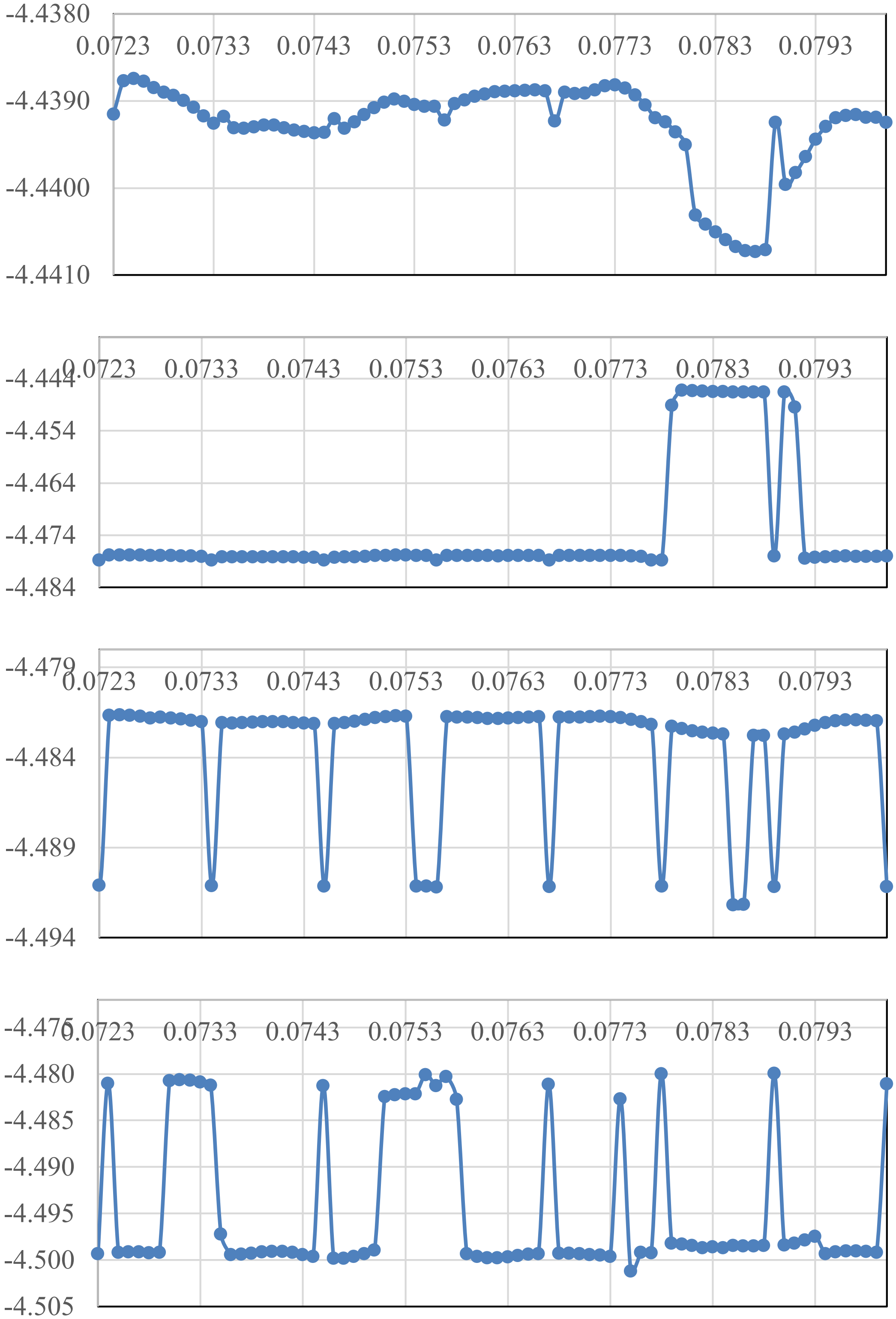

Figure 5.109. Streamlines at point four (x = 0.810mm) for type A-gap 0.005in, maximum physical time 0.08 second, x-axis time in s, y-axis in mm.

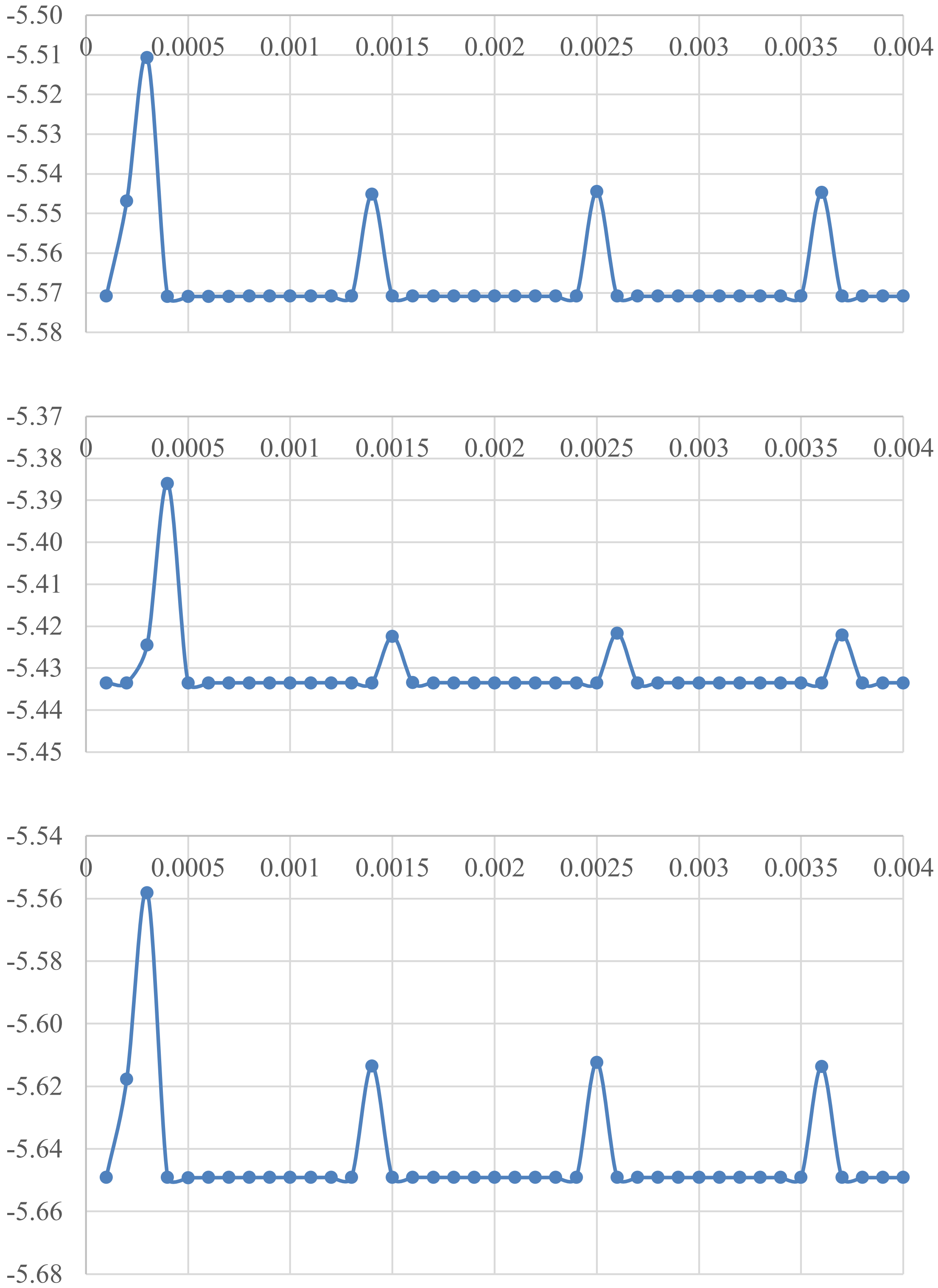

Figure 5.110. Streamlines at point one (x = 0.005mm) for type A-gap 0.017in, maximum physical time 0.004 second, x-axis time in s, y-axis in mm.

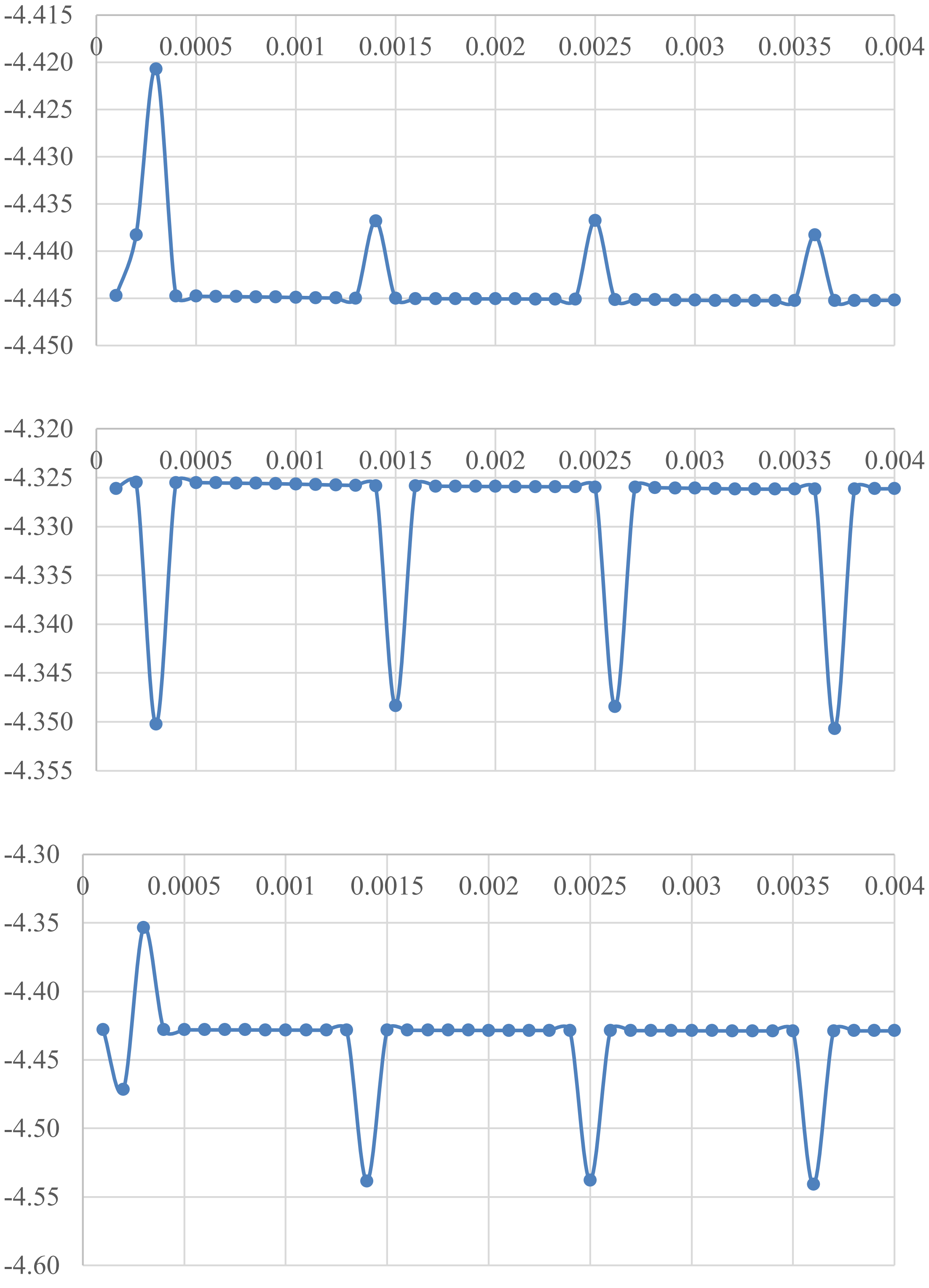

Figure 5.111. Streamlines at point four (x = 0.810mm) for type A-gap 0.017in, maximum physical time 0.004 second, x-axis time in s, y-axis in mm.

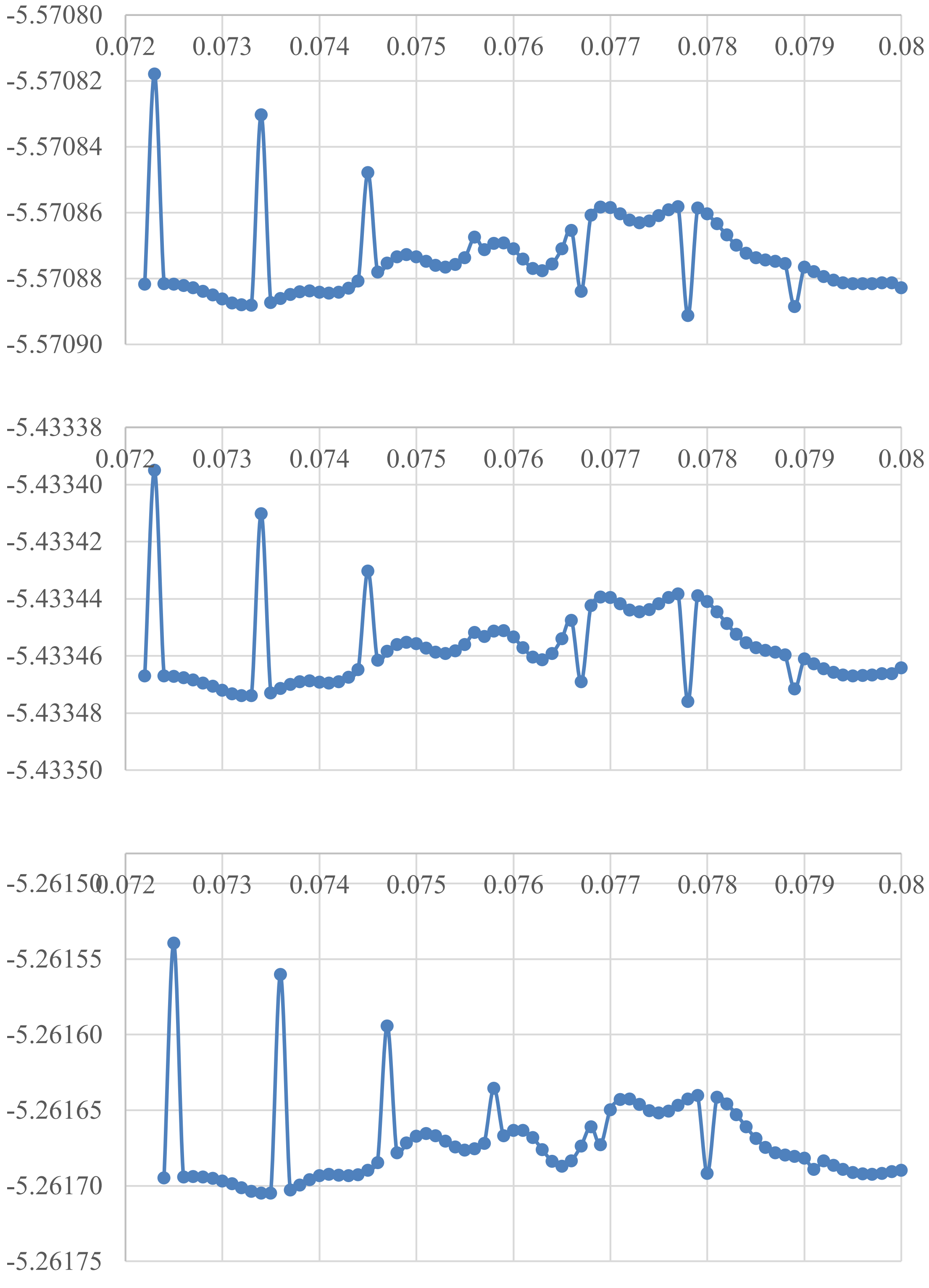

Figure 5.112. Streamlines at point one (x = 0.005mm) for type A-gap 0.017in, maximum physical time 0.08 second, x-axis time in s, y-axis in mm.

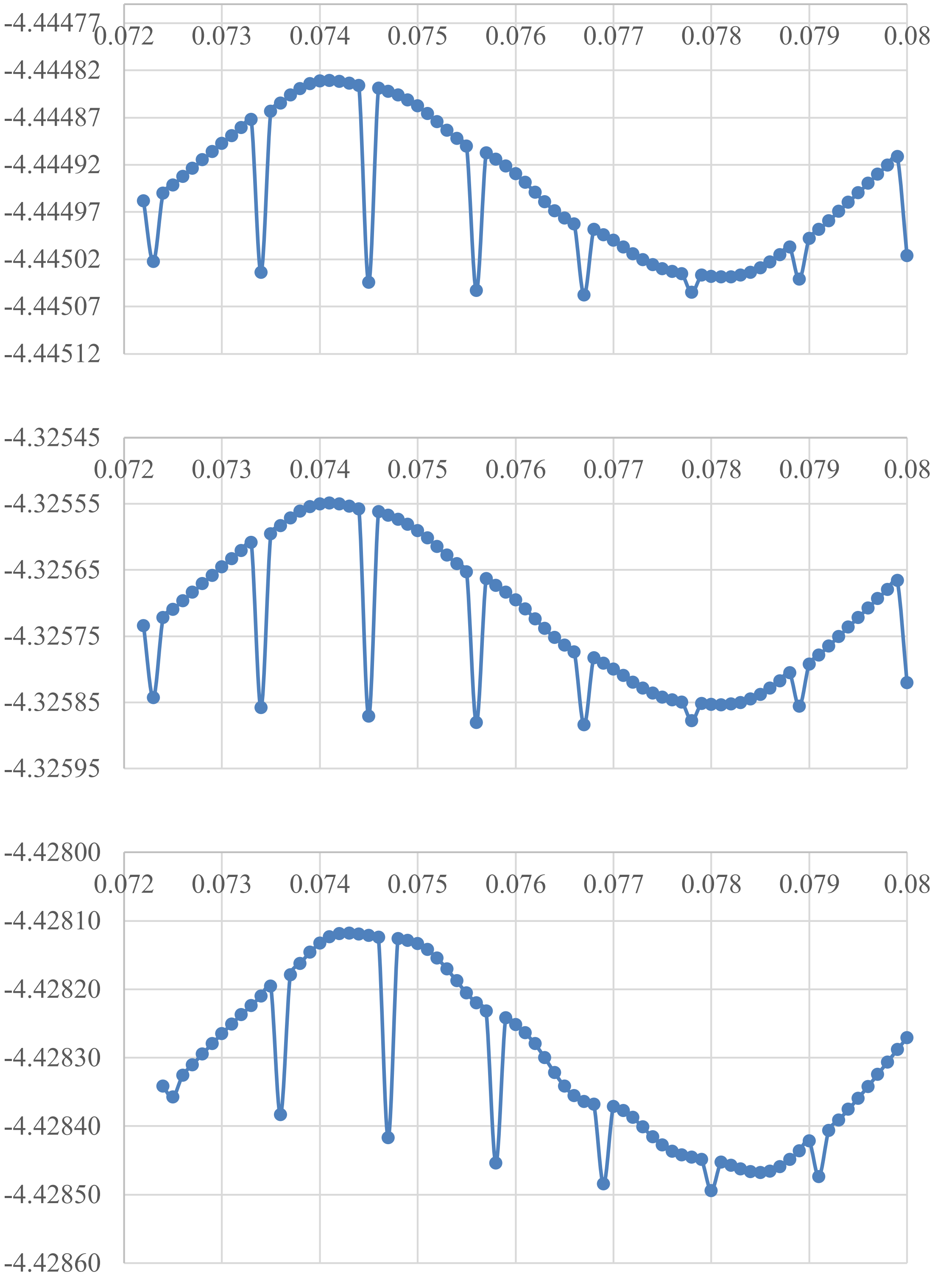

Figure 5.113. Streamlines at point four (x = 0.810mm) for type A-gap 0.017in, maximum physical time 0.08 second, x-axis time in s, y-axis in mm.

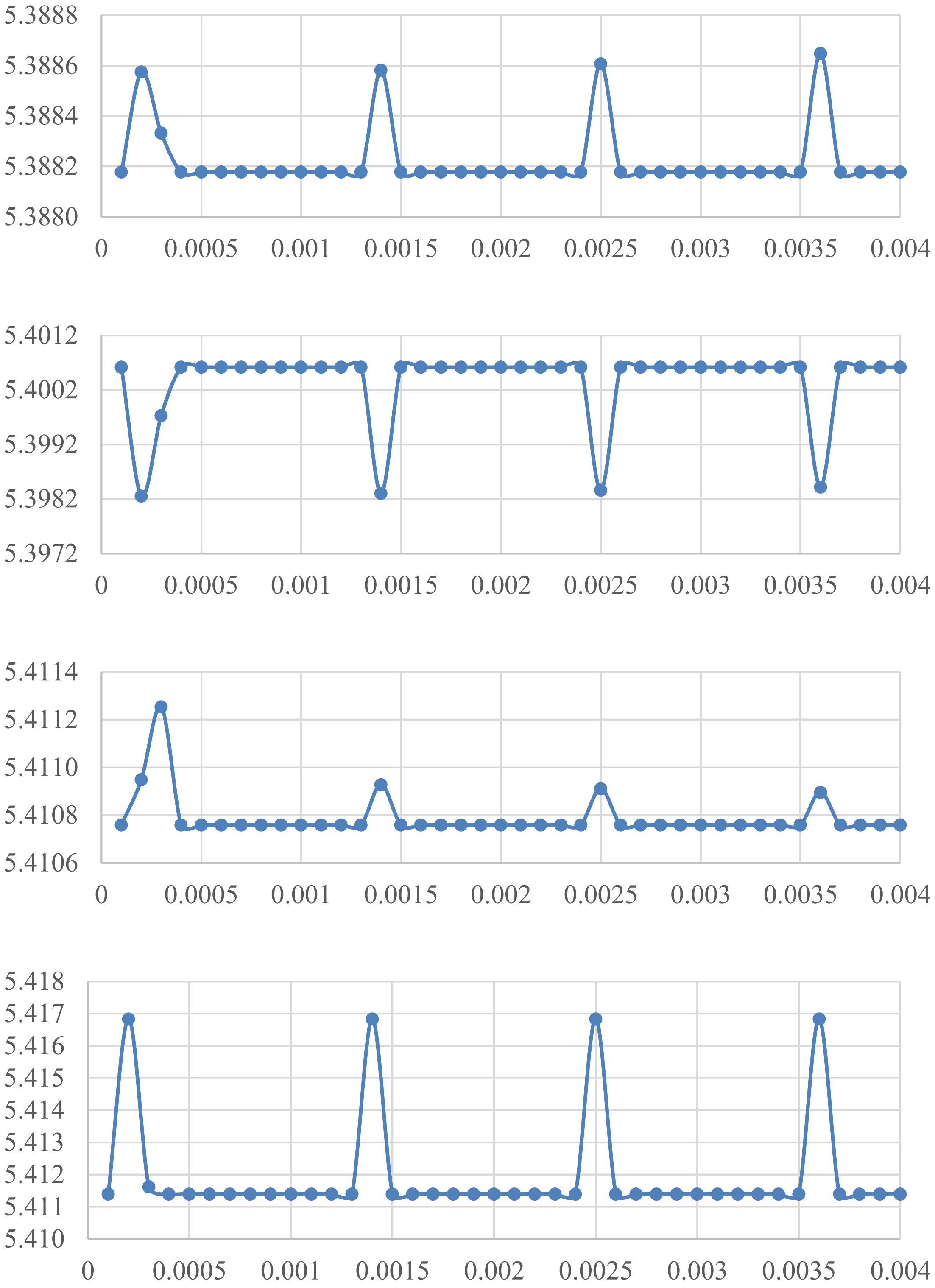

Figure 5.114. Streamlines at point one (x = 0.005mm) for type B-gap 0.002in, maximum physical time 0.004 second, x-axis time in s, y-axis in mm.

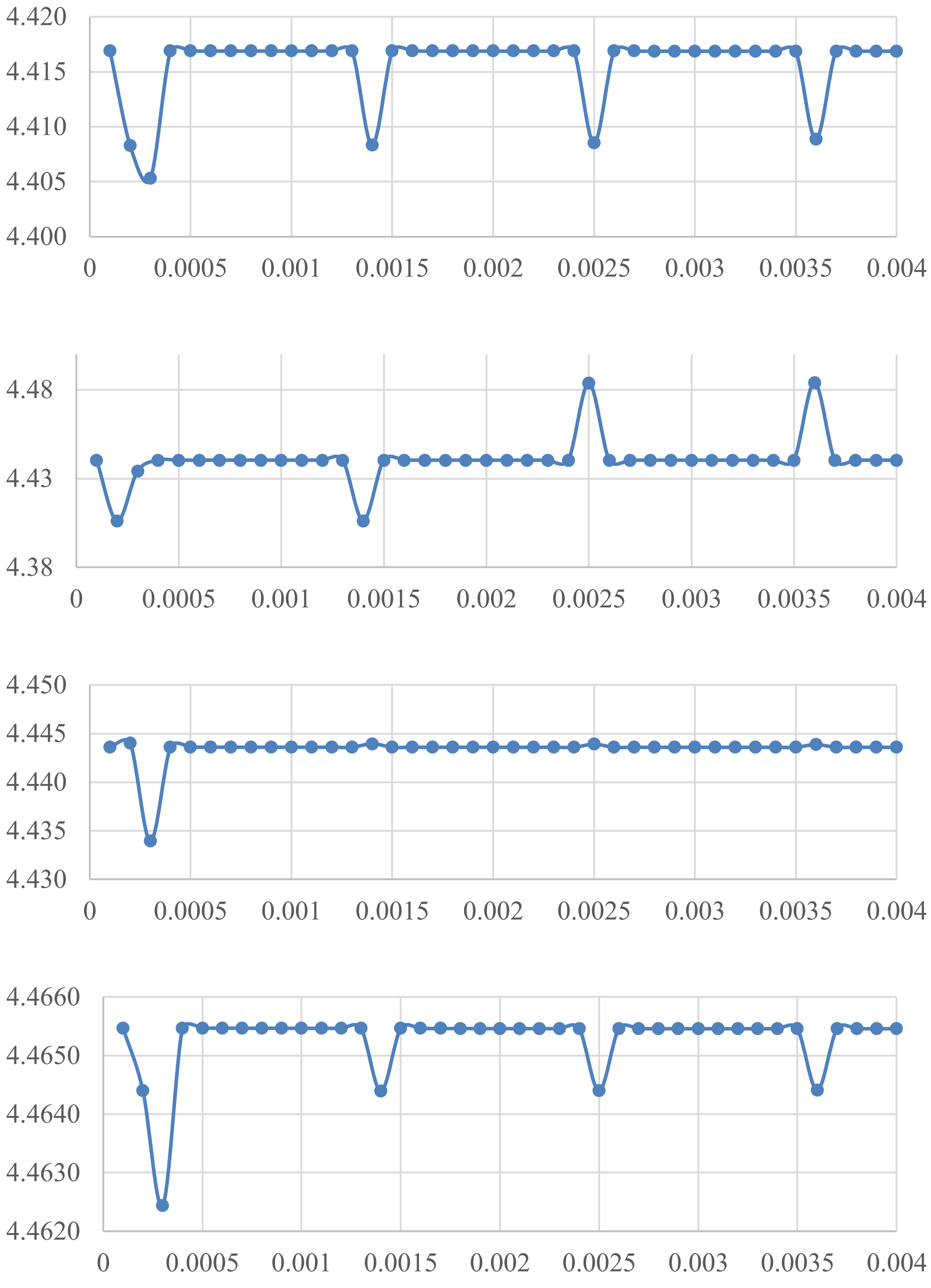

Figure 5.115. Streamlines at point four (x = 0.810mm) for type B-gap 0.002in, maximum physical time 0.004 second, x-axis time in s, y-axis in mm.

Figure 5.116. Streamlines at point one (x = 0.005mm) for type B-gap 0.002in, maximum physical time 0.08 second, x-axis time in s, y-axis in mm.

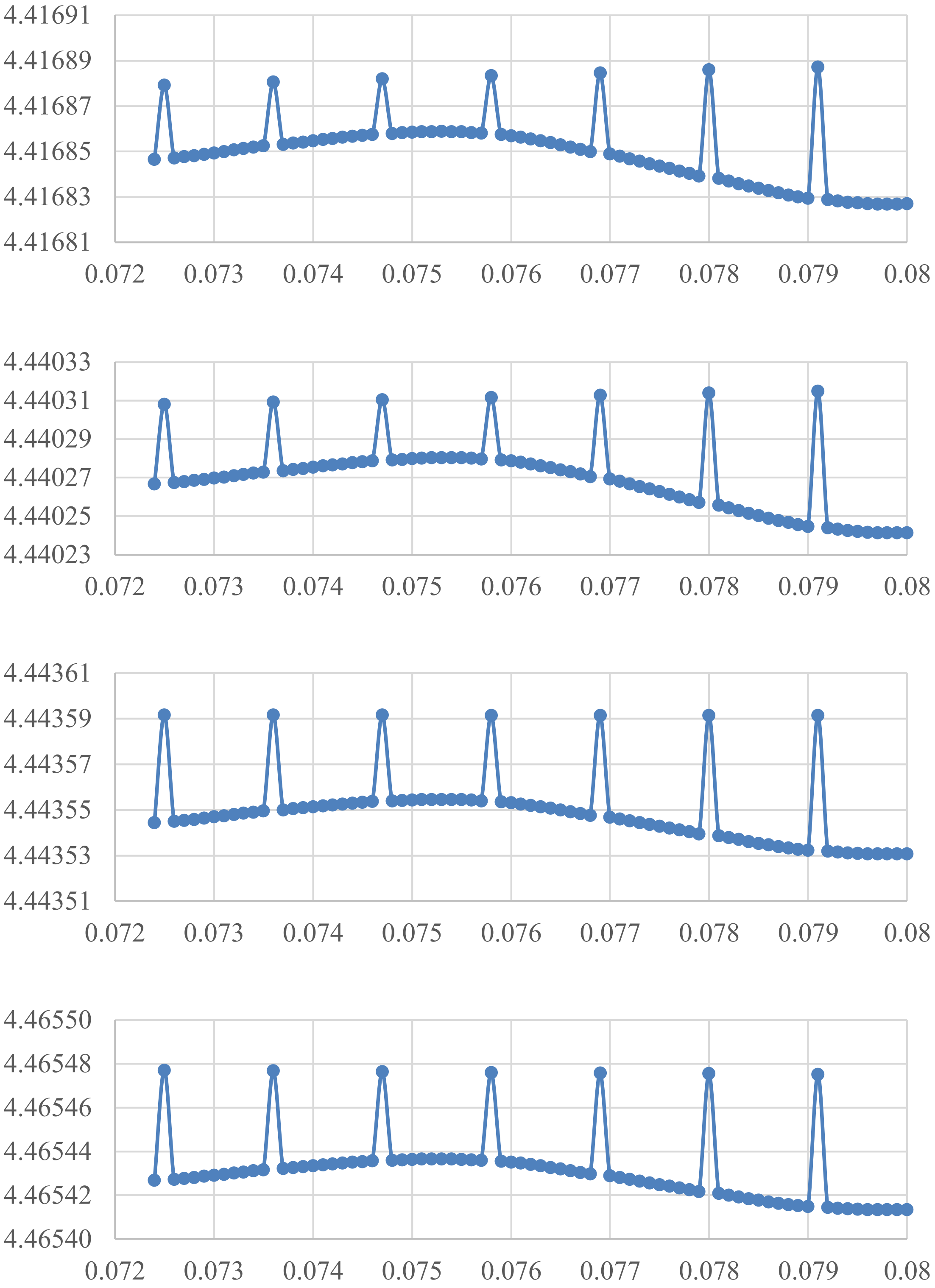

Figure 5.117. Streamlines at point four (x = 0.810mm) for type B-gap 0.002in, maximum physical time 0.08 second, x-axis time in s, y-axis in mm.

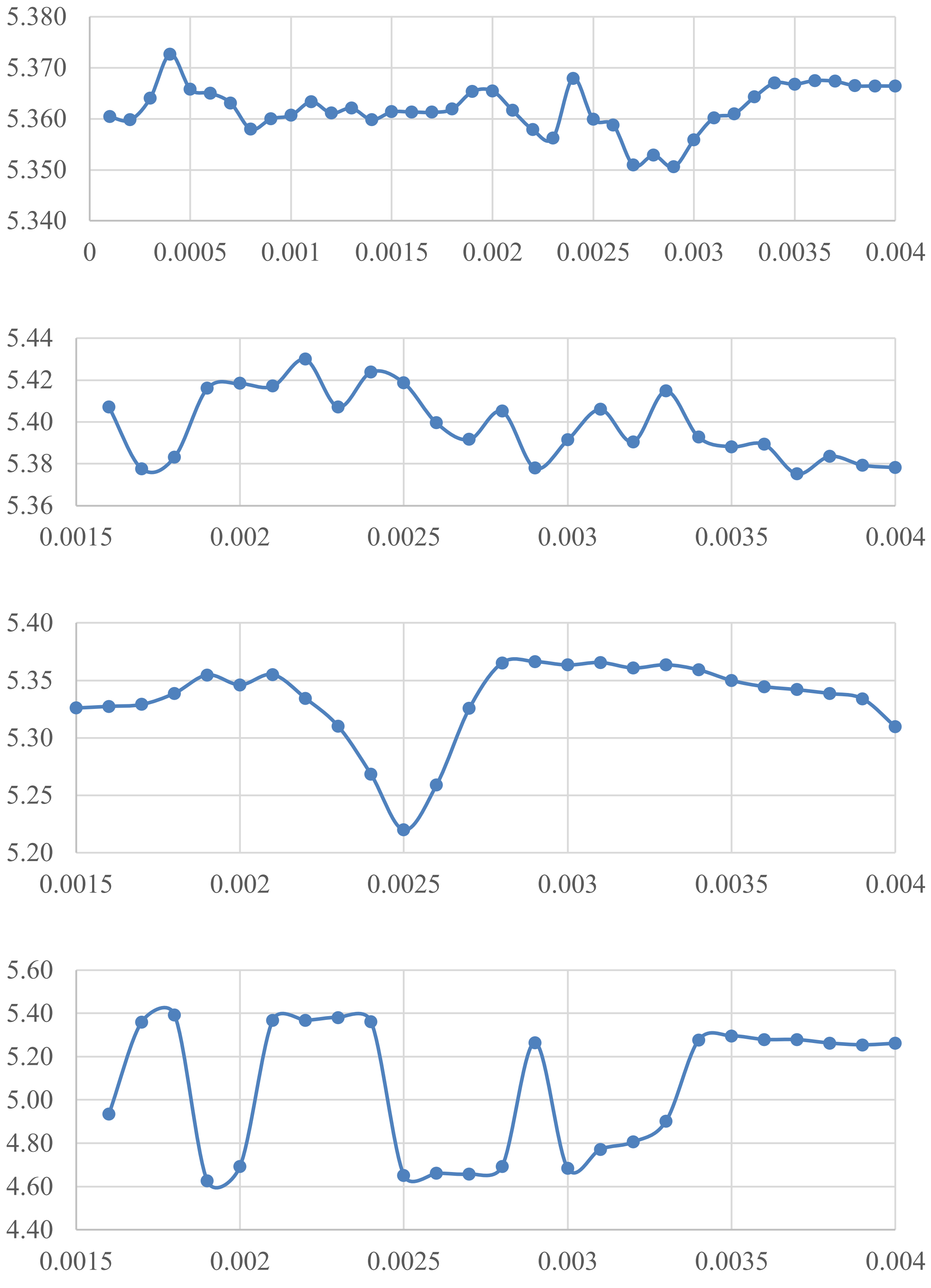

Figure 5.118. Streamlines at point one (x = 0.005mm) for type B-gap 0.005in, maximum physical time 0.004 second, x-axis time in s, y-axis in mm.

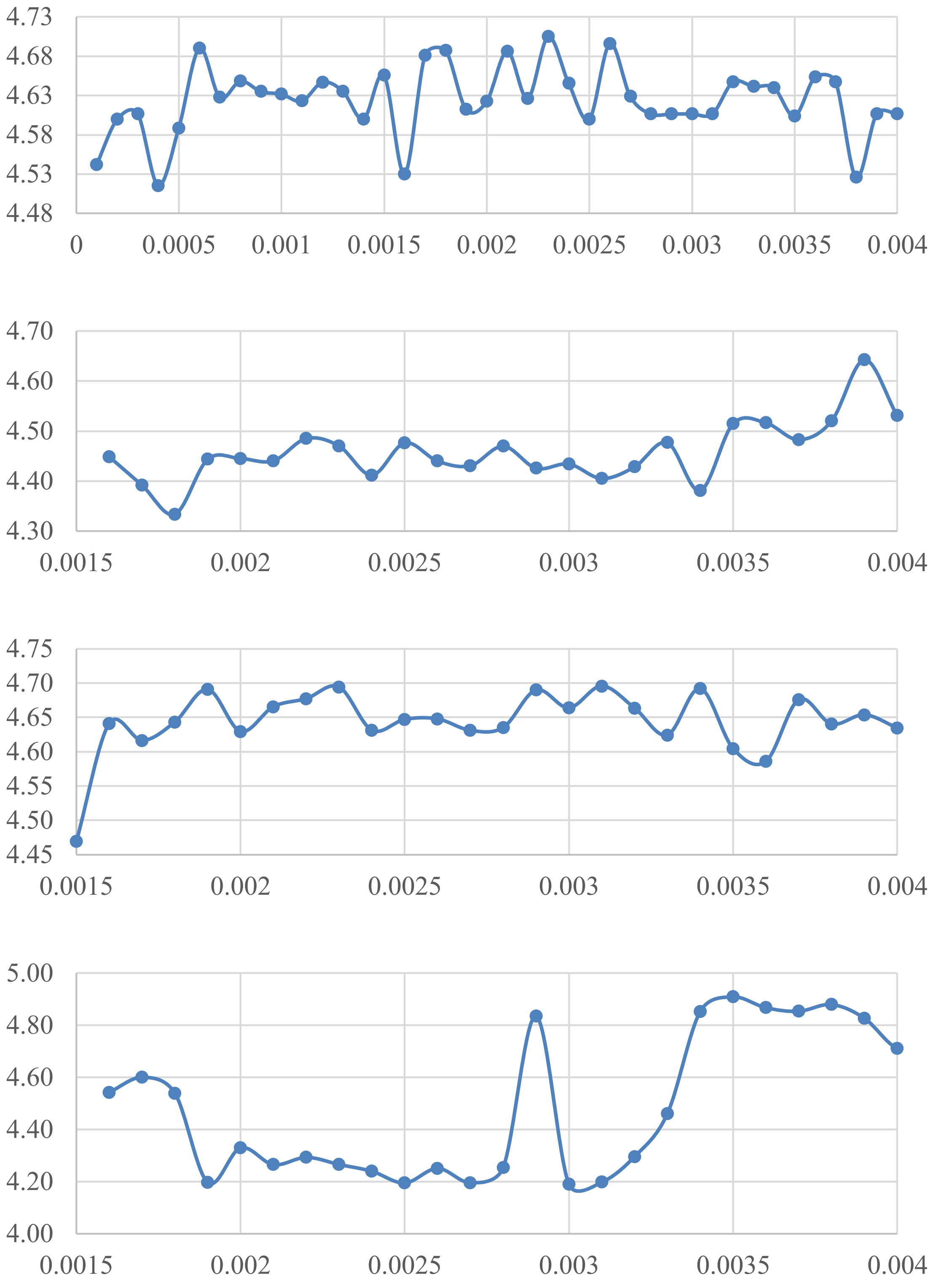

Figure 5.119. Streamlines at point four (x = 0.810mm) for type B-gap 0.005in, maximum physical time 0.004 second, x-axis time in s, y-axis in mm.

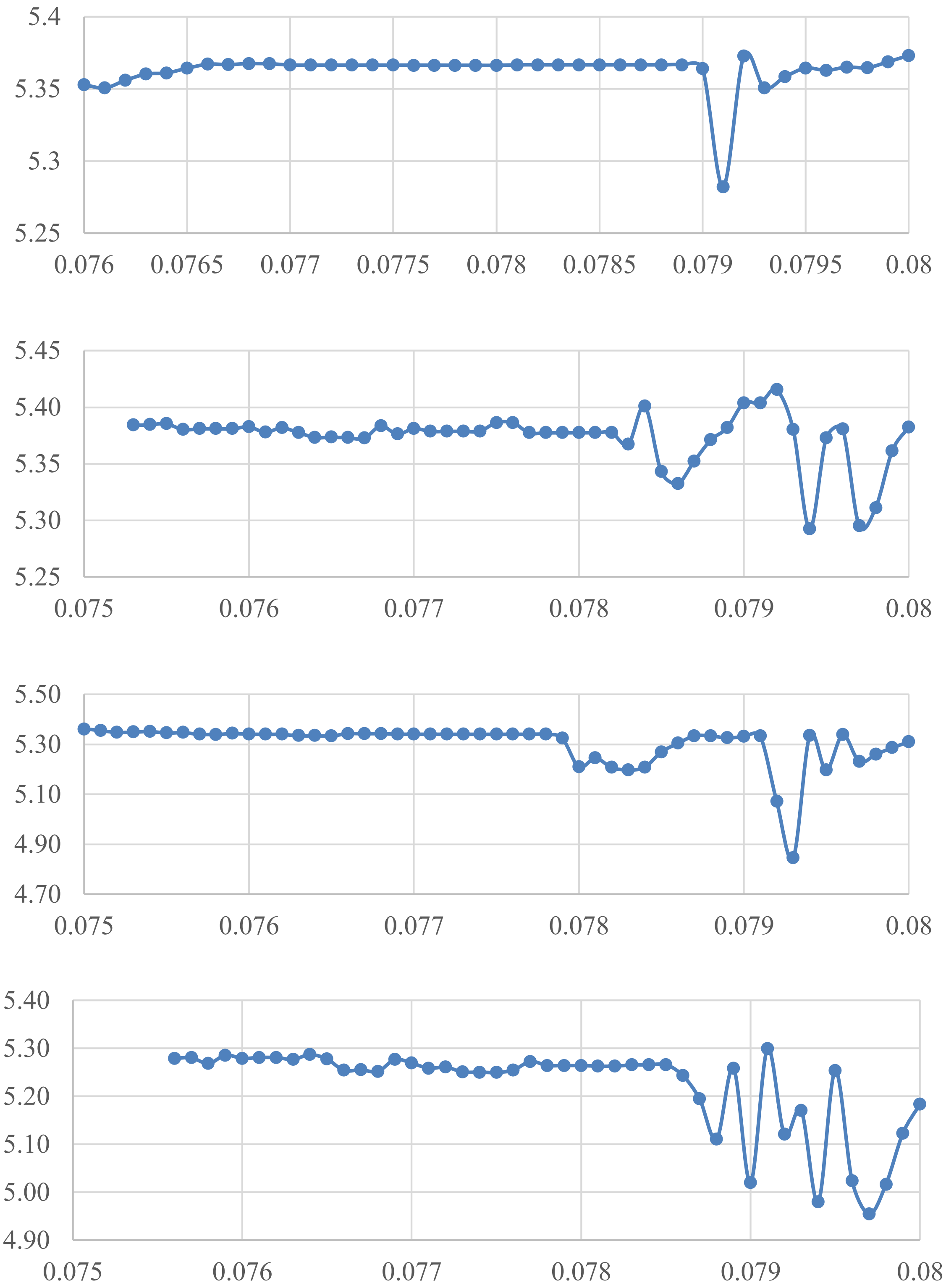

Figure 5.120. Streamlines at point one (x = 0.005mm) for type B-gap 0.005in, maximum physical time 0.08 second, x-axis time in s, y-axis in mm.

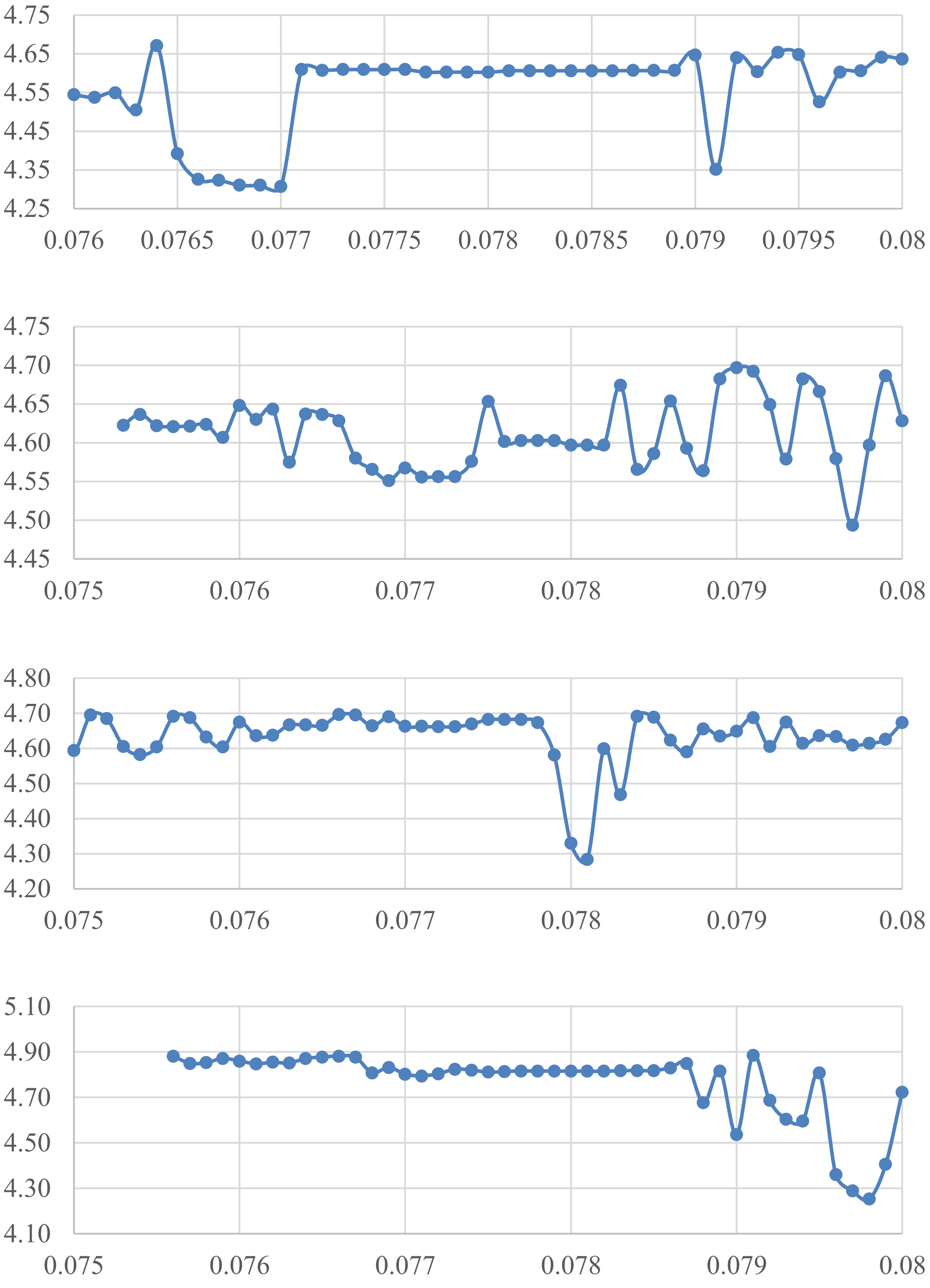

Figure 5.121. Streamlines at point four (x = 0.810mm) for type B-gap 0.005in, maximum physical time 0.08 second, x-axis time in s, y-axis in mm.

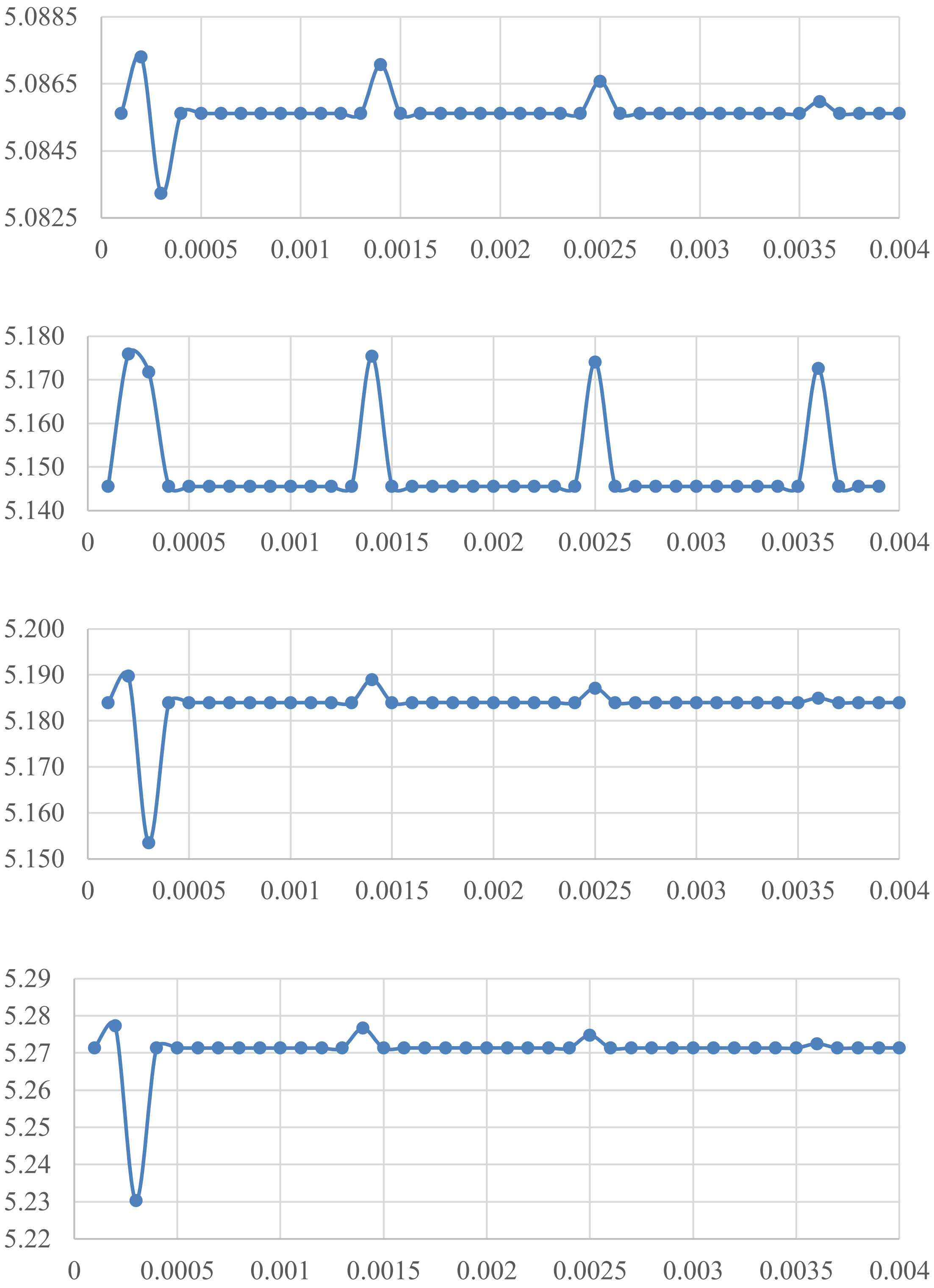

Figure 5.122. Streamlines at point one (x = 0.005mm) for type B-gap 0.017in, maximum physical time 0.004 second, x-axis time in s, y-axis in mm.

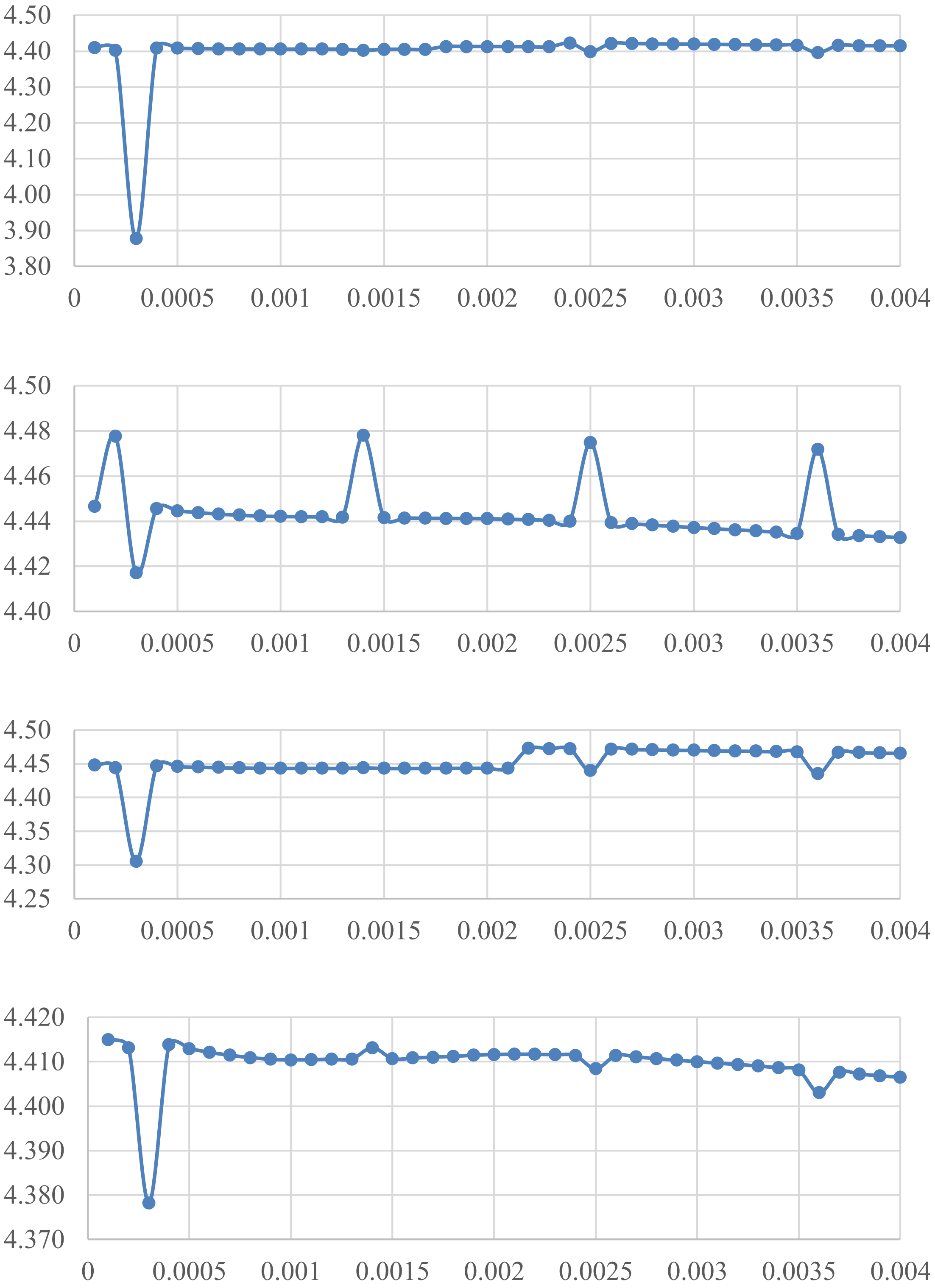

Figure 5.123. Streamlines at point four (x = 0.810mm) for type B-gap 0.017in, maximum physical time 0.004 second, x-axis time in s, y-axis in mm.

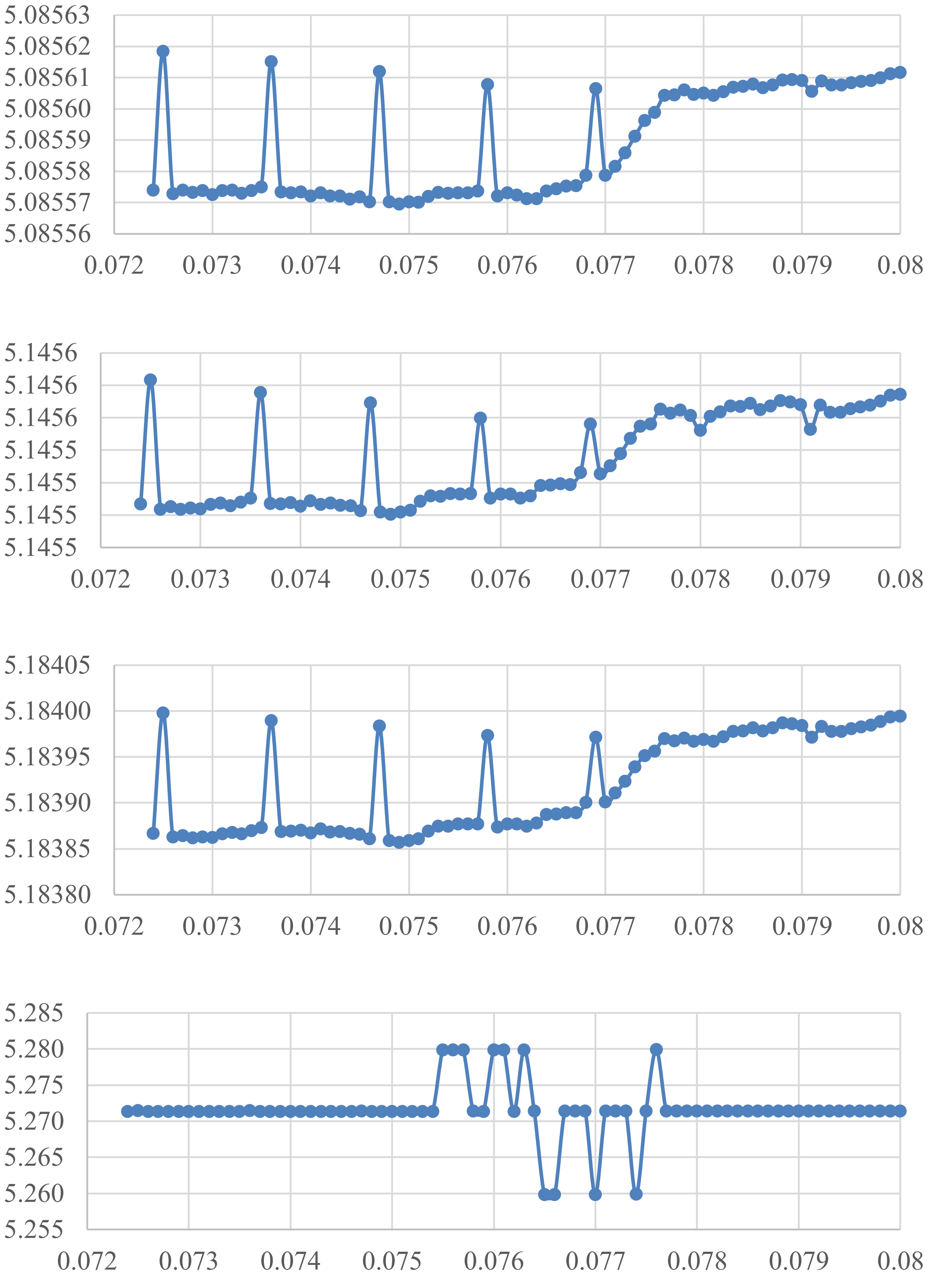

Figure 5.124. Streamlines at point one (x = 0.005mm) for type B-gap 0.017in, maximum physical time 0.08 second, x-axis time in s, y-axis in mm.

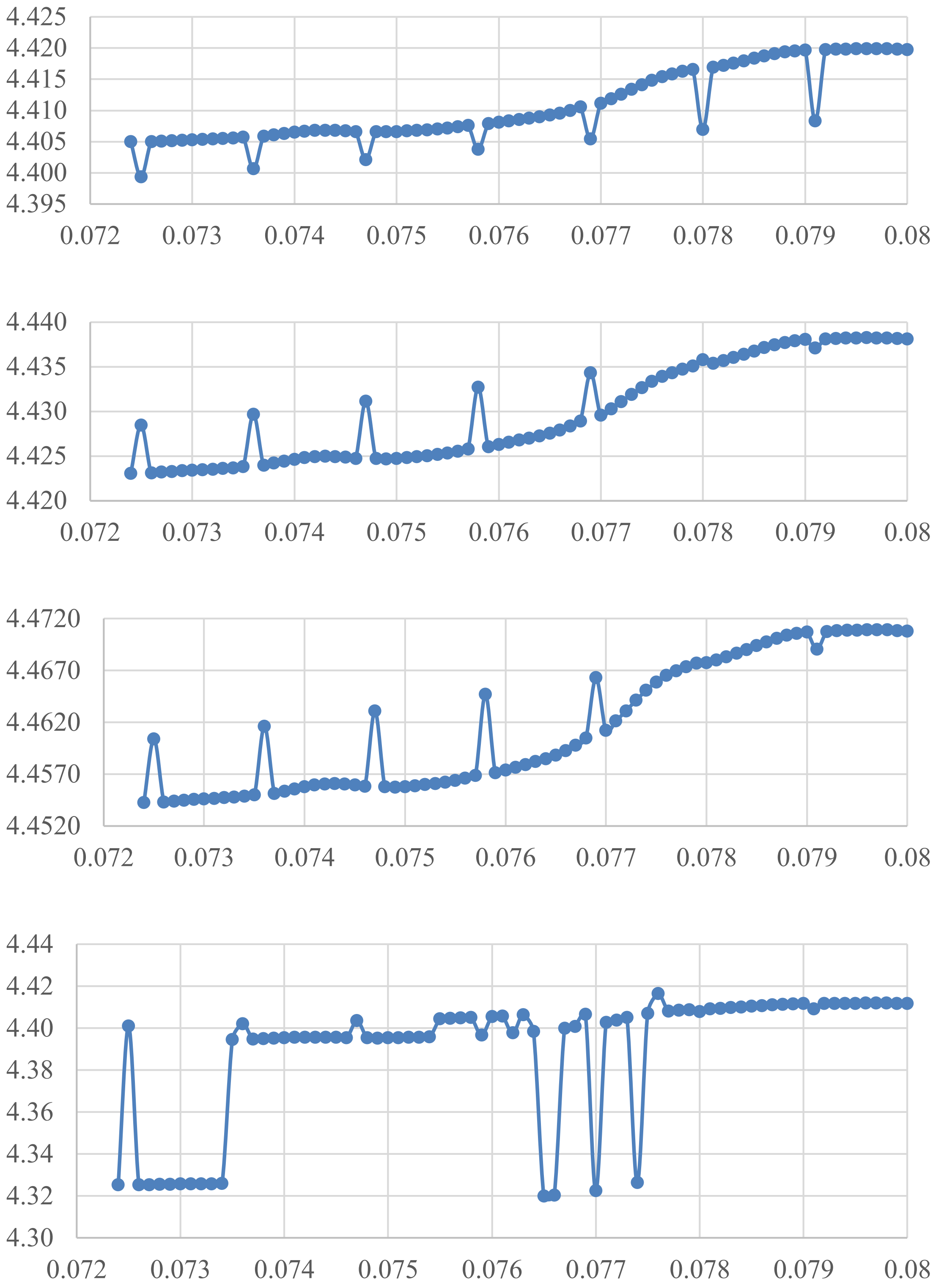

Figure 5.125. Streamlines at point four (x = 0.810mm) for type B-gap 0.017in, maximum physical time 0.08 second, x-axis time in s, y-axis in mm.

CHAPTER 6: CONCLUSIONS AND RECOMMENDATIONS

6.1. Conclusions

Both the experimental and numerical work have provided valuable insights into the flow through the counterbalance valve under operational conditions. While the experimental work has given a detailed information about the main characteristics of the oscillatory flow such as the magnitude and frequency of the pressure oscillations, the numerical work provided a clear picture of the resulting internal flows. Streamline analysis of the unsteady flow reveals the existence of an 1111 Hz. pulse throughout the flow field. The experimental frequency analysis reveals pressure fluctuations with main frequencies ranging from 1113 to 9375 Hz. While the close proximity of the lowest experimental frequency and the numerically obtained frequency (1113 and 1111 Hz) can only be the result of serendipity, a detailed study suggests that the numerical simulation is capturing a feature of the flow and is not the product of a numerical artifact. The absence of higher frequencies in the simulations is a consequence of the nature of the flow and the size of the grid. The maximum frequency resolved by a computational grid is a function of the turbulent kinetic energy, k, and the grid size:

$$f_{\max} = \frac{\sqrt{\frac{2k}{3}}}{2(Vcell)^{1/3}}$$

For this simulation, the cutoff frequency is approximately 2000 Hz, and therefore the absence of higher frequencies is to be expected.

The results obtained with valve type B are encouraging from both the numerical and experimental perspectives. The experimental results showed that the improvement is both quantitative and qualitative and strongly suggest that further improvement is still possible.

Numerically, the tridimensional flow field observed at the 0.005 inches opening is indicative of a poorly organized flow that may be a useful mechanism in suppressing flow oscillations and deserves to be analyzed further.

Overall, the software used for the numerical work proved to be a quite powerful tool for the analysis of a very complex flow bounded by a quite complex geometry. Though by no means a simple tool to use, and requiring significant computational and storage resources, it is a worthy tool to use.

6.2. Recommendations for Future Work

On the experimental side, while the type B valve design was successful in suppressing the strong Mode 2 oscillations and reduced the range of Mode 1, mode 1 failed in eliminating it completely. This may be due to the appearance of a secondary recirculation bubble at large valve openings as shown in the numerical simulations. The possibility of inhibiting the development of this bubble as a way of totally suppressing Mode 1 oscillations should be investigated. Two possible mechanisms are suggested: notching the piston such that the velocity distribution in the gap area is not uniform and altering the diameter of the outlet holes thereby creating an asymmetrical flow field throughout the valve that would achieve the same effect.

On the numerical side, the computational grid should be refined to allow the resolution of higher frequencies. This would require a significant upgrade in computational and storage capabilities.

The present analysis was carried out at quite small valve openings. Flow characteristics at larger openings should be investigated.

Finally, an acoustic analysis should be carried out. The emphasis of such an effort should be in the capture of acoustic resonances rather than in the calculation of flow-field noise generation.

REFERENCES

[1] Vickers. (1992) "*Vickers industrial hydraulic manual. 4d ed.* Eaton Corp. Training, 1992, Pennsylvania State University.

[2] Rayleigh L. (John William Strutt) (1879–1919)"investigations of the densities of the most important gases, Rayleigh's textbook, *The Theory of Sound*, referred to by acoustic engineers.

[3] Lighthill, M. J. (1950). "On sound generated aerodynamically. I. General theory". *Proceedings of the Royal Society A 211* (1107): 564–587. Bibcode: 1952RSPSA.211.564,. doi:10.1098/rspa.1952.0060.

[4] Lighthill, M. J. (1952). "On sound generated aerodynamically. II. Turbulence as a source of sound". *Proceedings of the Royal Society A 222* (1148): 1–32., Bibcode:1f954RSPSA.222....1L. doi:10.1098/rspa.1954.0049.

[5] Curle, N.; (1955). "The influence of solid boundaries upon aerodynamic sound". *Proceedings of the Royal Society of London. Series A, Mathematical and Physical Sciences:* DOI: 0.1098/rspa.1955.0191.

[6] Ffowcs W., and Hawking D. L.,(1969). " Sound Generation by Turbulence and Surfaces in Arbitrary Motion *". Phil. Trans. R. Soc. Lond. A May 8, 1969 264 1151 321-342.*

[7] Flening, J. S.; Tramschek, A. B.; and Abdul-Husain, J. M. H. (1988) "A comparison of flow and pressure distribution in simple valves using different coputational methods", *proceedings 1988 international Compressor Engineering Conference at Purdue July 18-21, pp. 117-120.*

[8] Guo, Mao-Ying., and Nakano, Kazuo. (1989). "Numerical study for the copensation of axil flow force in a spool valve by boundary elemnt method", *Fluid Power Transmission and Control-Proccesding of the 2nd Internatiional Conference March 20-22, Hangzhou, China, International Academic Publishers, pp. 171-176.*

[9] Ito, K.; Takahasi, K.; and Inoue, K. (1992) "Pressure distributions and flow forces on the body of a poppet valve", *Fluid Power systems and control 4th Bath International power workshop 18th–20th September 1991,* Research Studies Press, Somerest, England*, pp. 123–138.*

[10] Johnston, D. N., and Vaughhan, N. D. (199 –1992), " Eperimental investigation of flow and force characteristics of hydraulic poppet and disc valves", *Proceeding of the Institution of Mechanical Engineerings, vol. 205, pp. 161–171.*

[11] Nguyen–Schaefer, H., Sprafke, P., and Mittwollen, N. (1997) "Study on the flow in an Typical Seat Valve of Mobile Hydraulics", *Overview of ABS/TCS and Brake Technology, SP–1229, SAE, Paper Number 970812, pp. 11–22.*

[12] Francis, J., and P. L. Bettes. (1997) "Modelling incompressible flow in a pressure relief valve. In *Proceedings of the Institution of Mechanical Engineers, vol. 211, by IMechE, 83–93.*

[13] Porteiro, J. L. F., Weber, and M. M. Rahman. (1997). "An experimental study of flow inducted noise in counterbalance valves", In *Proceedings ASME 4th International Symposiumon Fluid–Structure Interactions,* Aeroelasticsity, Flow–Induced Vibration and Noise 53–2, *edited by M. P. Paidouss., 557–62. New York: ASME.*

[14] Weber T. S., and M. M. Rahman. (1998). "An investigation of flow inducted noise in hydraulic counterbalance valves", *MSME thesis*. Department of Mechanical Engineering, *University of South Florida,* Accession Number: *usflc.035434923.*

[15] Borghi, M., Cantore, G., Milani, M., and R. Paoluzzi. (1998). "Transient flow force estimation on the pilot stage of a hydraulic valve", In *Proceedings of the (1998) International Mechanical Engineers Congress and Exposition* (Fluid Power Systems and Technology) 5, *by ASME, 149–56, New York: ASME.*

[16] Wang, L., Chen, Y., and Lu, Y.(1998) "Numerical study on the axial flow force of a spool valve", ASME Fluid Power Systems and Technology *5, 177–83.*

[17] Pennington, R. E., and Porteiro, J. L. F., (2002) "A numerical and experimental investigation of direct acting, differential area relief valves", *PhD dissertation*, Department of Mechanical Engineering, *University of South Florida,* Accession Number: *usflc.028880982.*

[18] Weerachai, C., Jean, C., Mahmoud, H., and Chawalit, K., (2011) "An Investigation of the Water Flow Past the Butterfly Valve. *AIP Conference Proceedings. 6/28/2010, Vol. 1225 Issue 1, p249-262. 14p. 5.*

[19] Zhang, Sh., and Manring, D. N., (2011) " Testing the Pressure Transient Flow-Force for Spool-Type Two-Way Valves ", *PhD dissertation*, Department of Mechanical, and Aerospace Engineering*;* By University of Missouri-Columbia.

[20] Lisowski, E., Czyzycki,. Rajda, J. (2013) "Three dimensional CFD analysis and experimental test of flow force acting on the spool of solenoid operated directional control valve", In *Proceedings of the Energy Conversion and Management. June, 2013, Vol. 70, p220, 10 p.*

[21] Tidor, M. (1954) “ A study of pressure and flow in a poppet valve model”, *B. S. Thesis,* Department of Mechanical Engineering, Massachusetts Institute of Technology (MIT), Cambridge, Massachusetts, USA.

[22] Stone, j. A. (1954) “ Design and development and apparatus to study the flow-induced forces in a poppet-type flow valve*”. B. S Thesis, Department of Mechanical Engineering,* Massachusetts Institute of Technology (MIT), Cambridge, Massachusetts, USA.

[23] Stone, j. A. (1957) “An investigation of discharge coefficient and steady atate flow forces for poppet type valves”, *M. S Thesis, Department of Mechanical Engineering*, Massachusetts Institute of Technology (MIT), Cambridge, Massachusetts, USA.

[24] Stone, j. A. (1960) “ Discharge coefficients and steady–state flow forces for hydrualic poppet valves”. *Transactions of the ASME Journal of Basic Engineering*, ASME, *vol. 82, no. 1, March, pp. 144–54*.

[25] Kawakami, k., Oki, Iwao. (1961) “Experimental research on disc valve (7th report, experimental formula for discharge and lifting–force)”, *Bulletin of JSME, vol. 4, no, 13, pp 87–93.*

[26] Kawakami, k., and Oki, I., (1961) “Characteristics of flat–seated valve with broader seat–face (8th report, experimental research on disc valve)”, *Bulletin of JSME, vol. 4, no, 14, pp 278–286.*

[27] Takenaka, T., Yamane, R., and Iwamizo, T., (1964) “Thrust of a disc valve”, *Bulletin of JSME, vol. 7, no. 27, pp 558–566.*

[28] McCloy, D., and McGuigan, R. H. (1964) “Some static and dynamic charateristics of poppet valves” Proceedings of the institution of Mechanical Engineers, *vol. 179, part 3H, pp. 199–213.*

[29] Takenaka, T., and Urata, E., (1968) “Static and dynamic charateristics of oil – hydrualic control valves”, *In The 1968 Fluid Power International Conference67–74.*

[30] Takenaka, T., and Urata, E., (1969) “The dynamic charateristics of oil hydrualic control valves”, *Bulleetin of the JSME, Volume 12, No. 52, p. 765-773.*

[31] Urata, E. 1969. Thrust of poppet valve. JSME 12, NO, 1099–109.

[32] Feigel, H. J. (1990) “Stromungskraftkompensation in Hydraulik–Schieberventilen”, 9. Aachener Fluidtechnisches Kolloquim *20–22 Marz, Band 2: 79–98.* (in German, English trans. Univ. Bath, UK).

[33] Ishii, Y., Yonezawa, Y., Tsukiji, T., Suzuki, R., and Ishii, S. (1994). “Flow in a Three-Dimensional Poppet Valve for Oil Hydraulic Power Applications”, Flucome 94 Toulouse (France) 29 August – 1 September Fourth Triennial International Symposium on Fluid Control, Fluid measurement, Fluid Mechanics, Visualization, and Fluidics, *Volume 2, Ensae, Toulouse, France, app. 1095 – 1099.*

[34] Tsukiji, Tetsuhiro, Takahashi, Koji, Hori, and Hiroyuki. (1989). “A study on the axial flow forces on a spool valve using flow visulization and imge processing techiques”, Fluid Power Transportation and Control-Proceedings of the 2nd International Conference, *March 20-22, Hangzhou, China, International Acadimic Publisher, pp. 177-182.*

[35] Tsukiji, Tetsuhiro, Sumikawa, Sumita, Sato, Takashi, Koji, Hori, and Takehio. (1996). “ cavitation in hydraulic holding valve”, *Proceeding of the ASME* Fluids Engineering Division Summer Meeting *July 7-11, san Diego, California, USA, Volume 236, Part 1, pp. 373-378.*

[36] Tsukiji Tetsuhiro, Sumikawa, Sumita, Sato, Takashi, Koji, Hori, and Takehio. (1996b). “ Flow visulazation in hydraulic holing valves”, Fluid Power-Proceeding of the Third JHPS International Symposium on Fluid Power, Yokahma, *November 4-6, Japan Hydraulics and Pneumatics Society, Tokyo, pp. 437-441.*

[37] Guivier, C., Deplano, V., and Bertrand, E., (2009) “Validation of a numerical 3-D fluid–structure interaction model for a prosthetic valve based on experimental PIV measurements” In *Medical Engineering and Physics,* University of South Florida, *31(8):986-993, ISSN: 1350–4533.*

[38] Wang, C., Chen, H., and Hsiao, Y., (2011) “Experimental study of the flow rectification performance of conical diffuser valves”, *Acta Mechanica. June, 2011, Vol. 219 Issue 1-2, 15.*

[39] Herakovic, N., (2007) “Flow force analysis in a hydrulaic sliding spool-valve,”. Strojarstvo; 49(3), pp-117-126.

[40] Haroutunian, V., (1996) “Course Notes on Simualtion Turbulent Flows With FIDAP,”, *Fluid dynamics International, Evanston, IL.*

[41] Fletcher, C. A. J., (1984) “Computaional Galerkin Methoeds”, *Springer-Verlag,* New York, NY.

[42] Logan, D. L., (1993) “A first Course in the Finite Elements Methoed,”. PWS Publishing, Boston, MA, pp.30, 281, and 238.

[43] WWW.STARCCM.COM.

APPENDICES

Appendix A. Symbols and Their Meaning

A.1. List of Symbols

A	Gap Area [m^2]
C_v	Specific heat [J/kg ^oC]
d	Gap spacing [m]
f	Frequency of oscillation [Hz]
k	Turbulent Kinematic Energy [J/Kg]
p	Pressure [Psi]
P	Aspect ratio, (t/p)
r	Poppet radius [m]
t	Time [S]
T	Temperature [^oC]
TQ	turbulence quantity
u	Friction velocity [m/s]
u_j	Local mean velocity [m/s]
v	Velocity [m/s]
v	local kinematic viscosity [m/s]
x_j	Coordinate axis [m/s]
y	Normal distance from the wall [m]

A.2. Greek Letters

Ɛ	Turbulent kinematic energy dissipation rate [$N/m^2.s$]

ρ	Density [kg/m^3]
μ_j	Turbulent Viscosity [kg/m.s]
σ	Cauchy stress tensor [kg/m^2]
ω	Turbulent frequency [kg/m^3.s]

A.3. Subscripts

x	Coordinate direction, is also r in cylindrical coordinate
y	Coordinate direction, is also z in cylindrical coordinate
z	Coordinate direction, is also ϕ in cylindrical coordinate

A.4. Units

cSt	Centistokes [mm^2/s]
gpm	Gallon per minutes
kg	Kilogram
m	Meter
ms	Milliseoncd
psi	Pound per square inches
psid	Pound per square inches differential
psig	Pound per square inches gauge
s	Second distance from the wall [m]
vdc	Volt direct current
ampt	Amplitude

Appendix B. Time-dependent Behavior of Streamline

B.1. Time-dependent Behavior of Streamline for Type A Valve

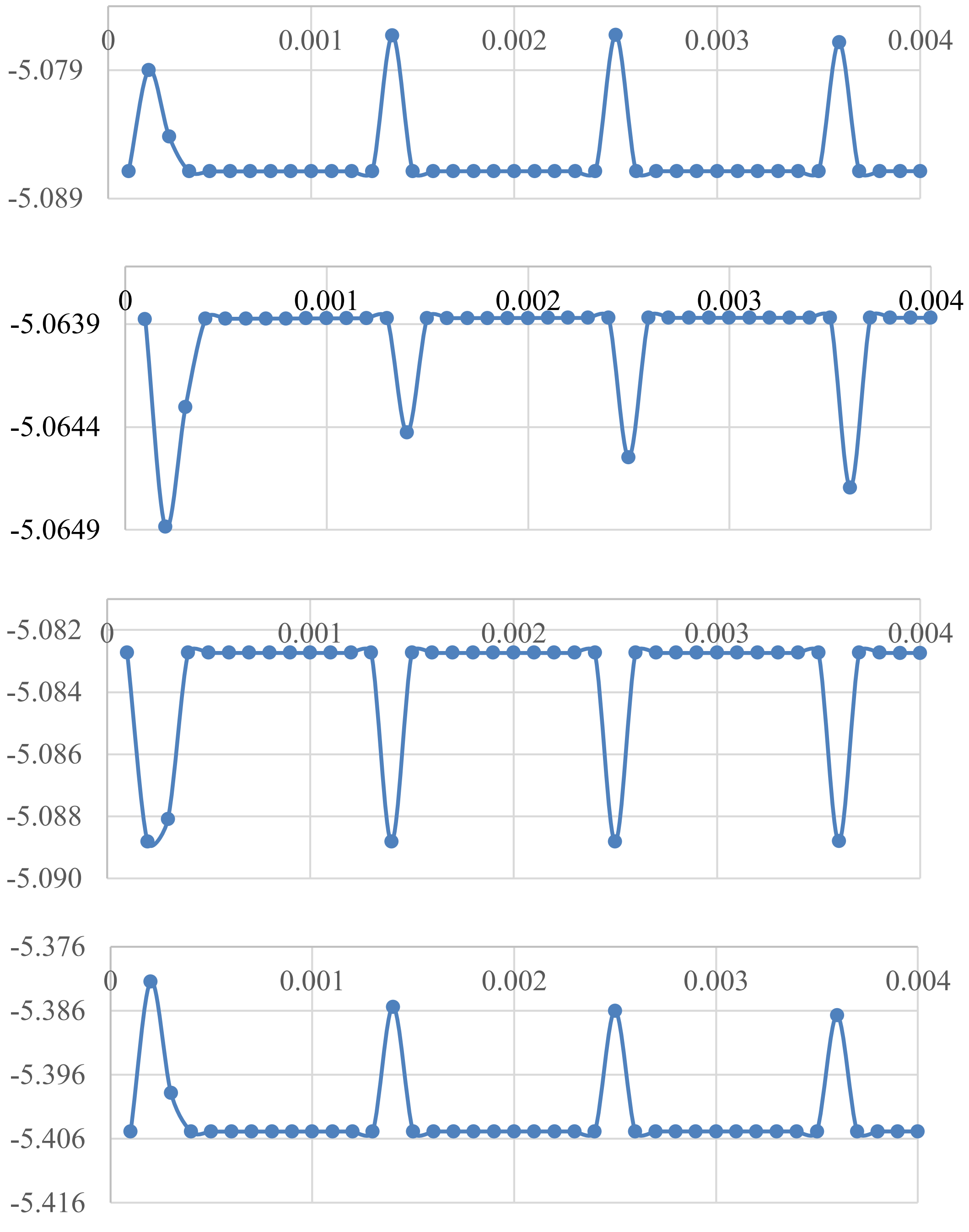

Figure B.1. Streamlines at point two (x = 0.290mm) for type A-gap 0.002in, maximum physical time 0.004 second, x-axis time in s, y-axis mm.

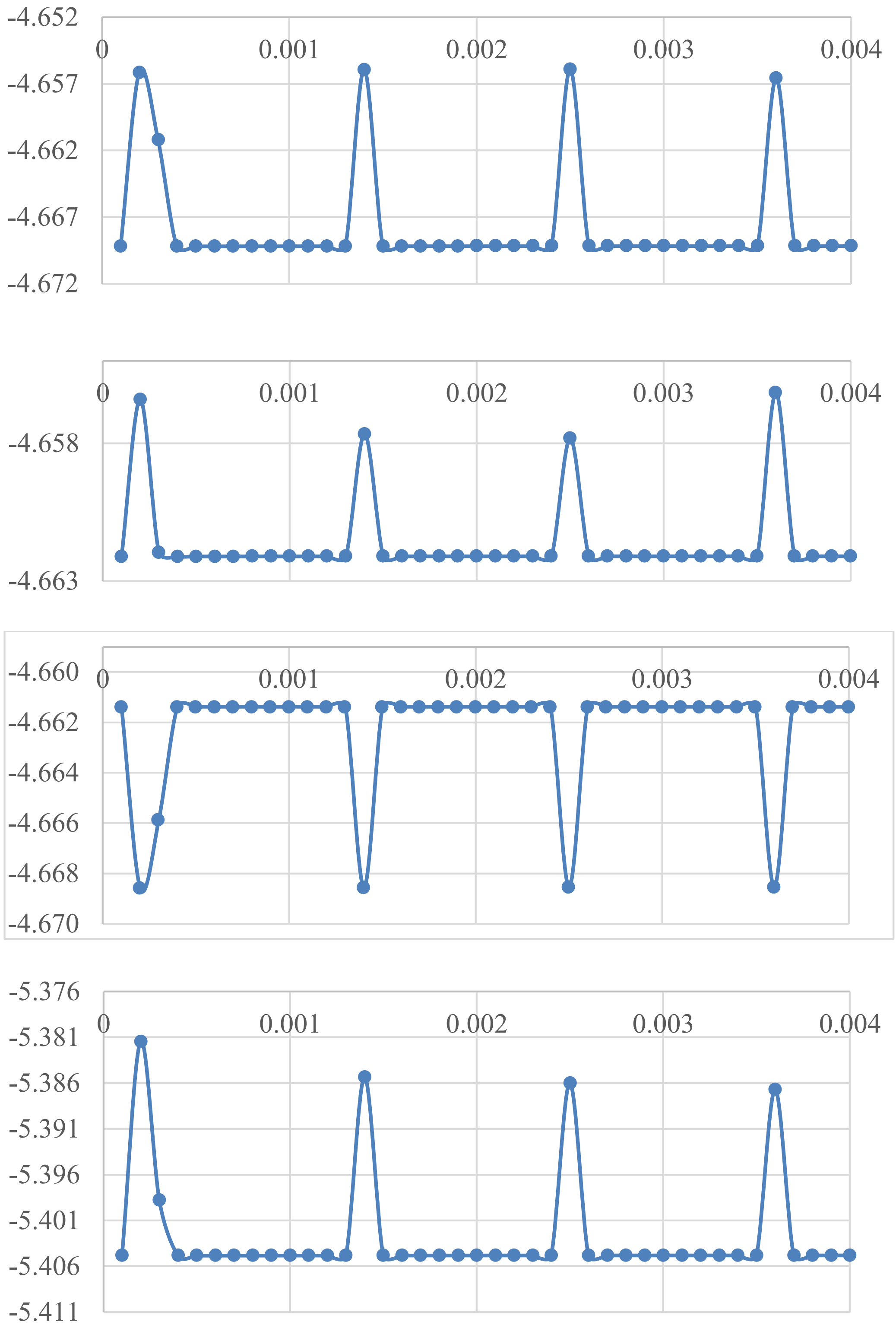

Figure B.2. Streamlines at point three (x = 0.660mm) for type A-gap 0.002in, maximum physical time 0.004 second, x-axis time in s, y-axis mm.

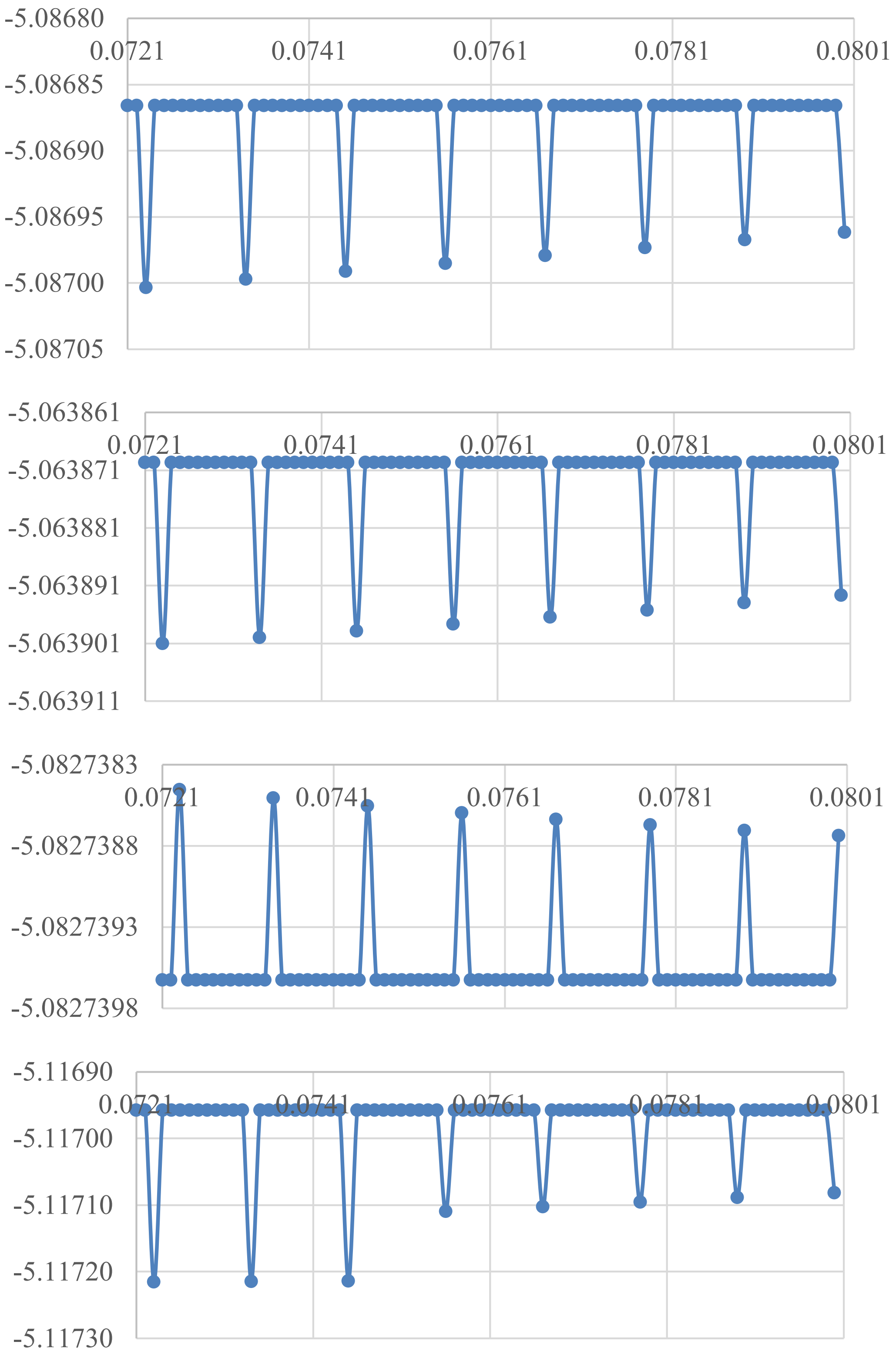

Figure B.3. Streamlines at point two (x = 0.290mm) for type A-gap 0.002in, maximum physical time 0.08 second, x-axis time in s, y-axis in mm.

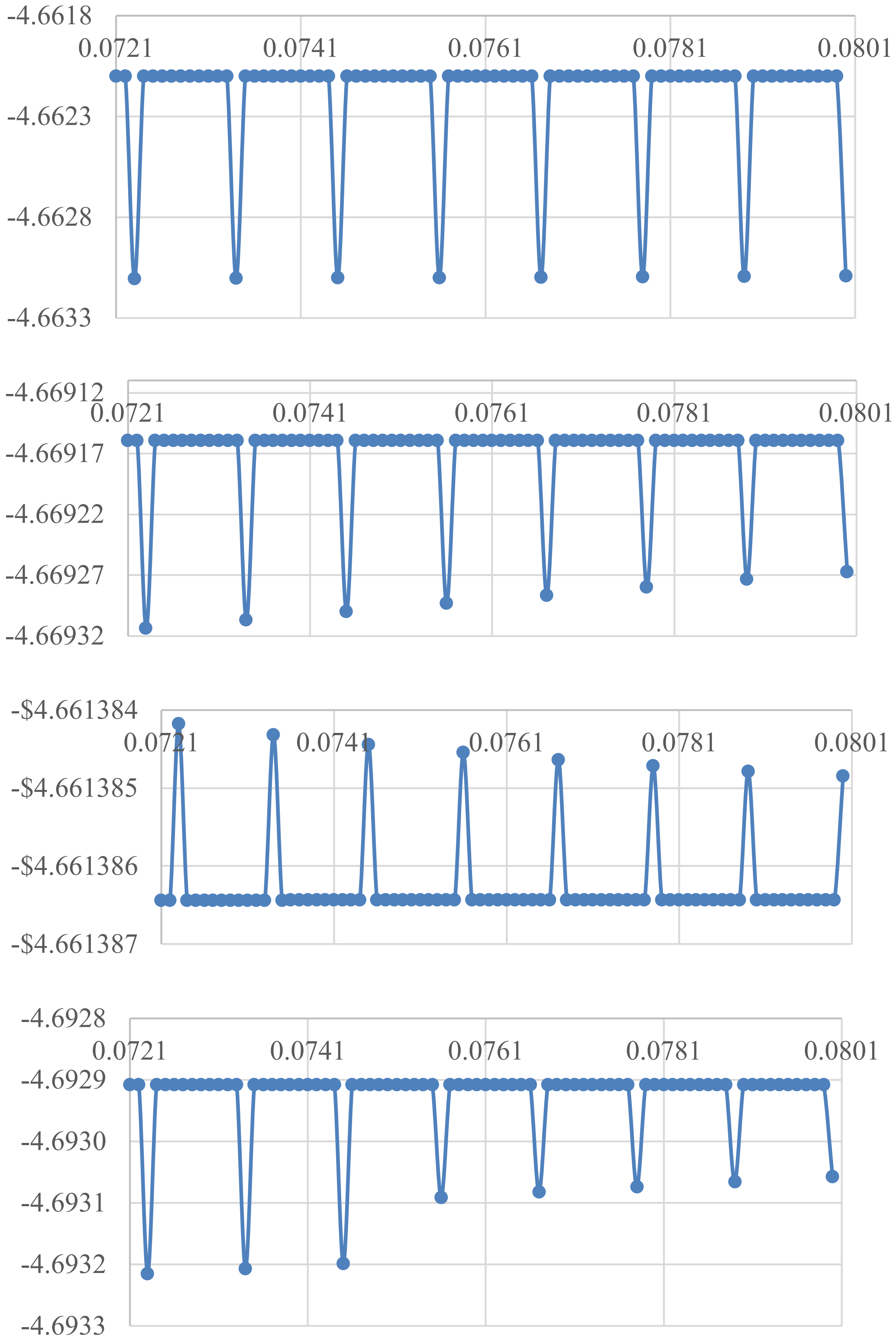

Figure B.4. Streamlines at point three (x = 0.660mm) for type A-gap 0.002in, maximum physical time 0.08 second, x-axis time in s, y-axis in mm.

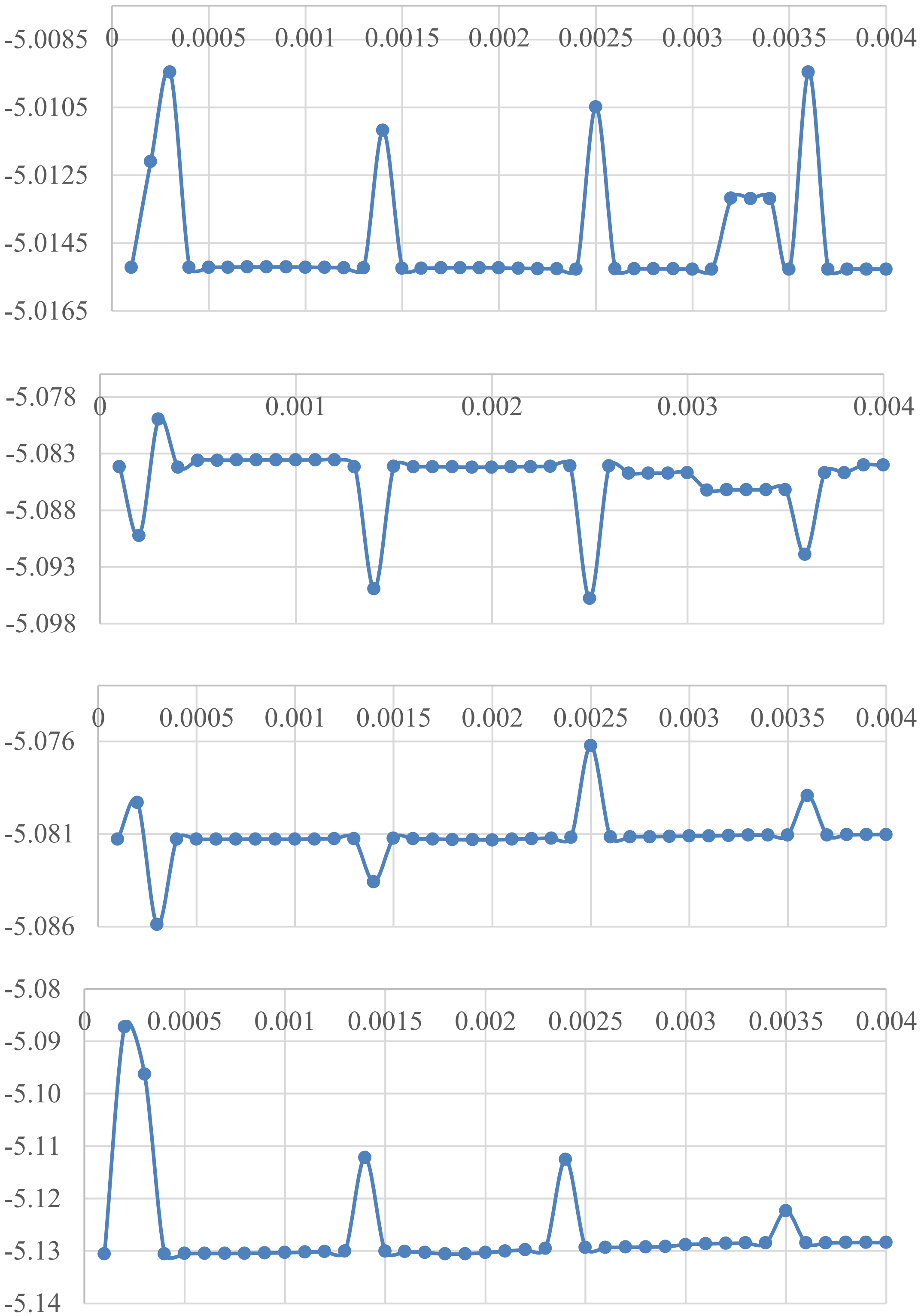

Figure B.5. Streamlines at point two (x = 0.290mm) for type A-gap 0.005in, maximum physical time 0.004 second, x-axis time in s, y-axis in mm.

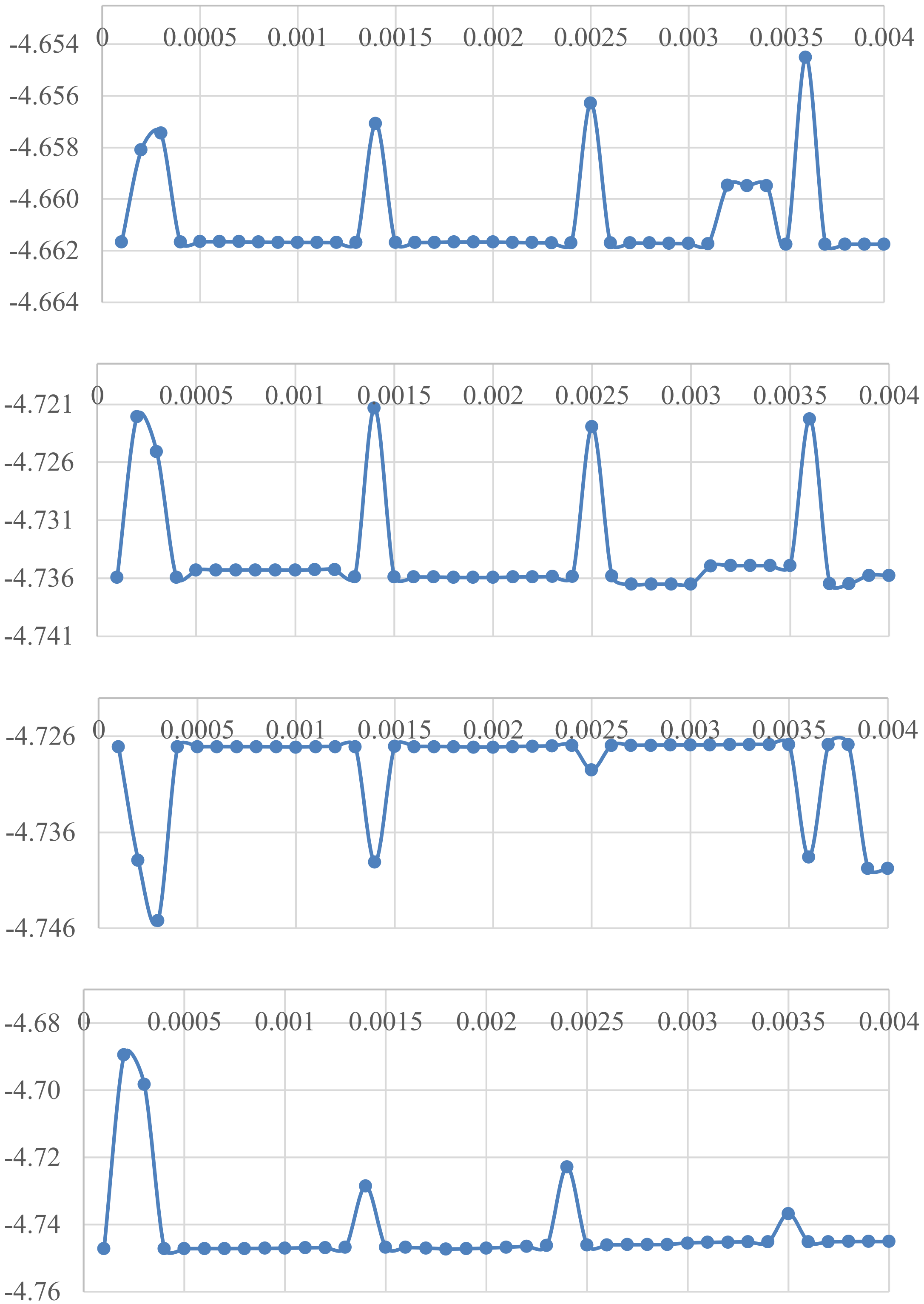

Figure B.6. Streamlines at point three (x = 0.660mm) for type A-gap 0.005in, maximum physical time 0.004 second, x-axis time in s, y-axis in mm.

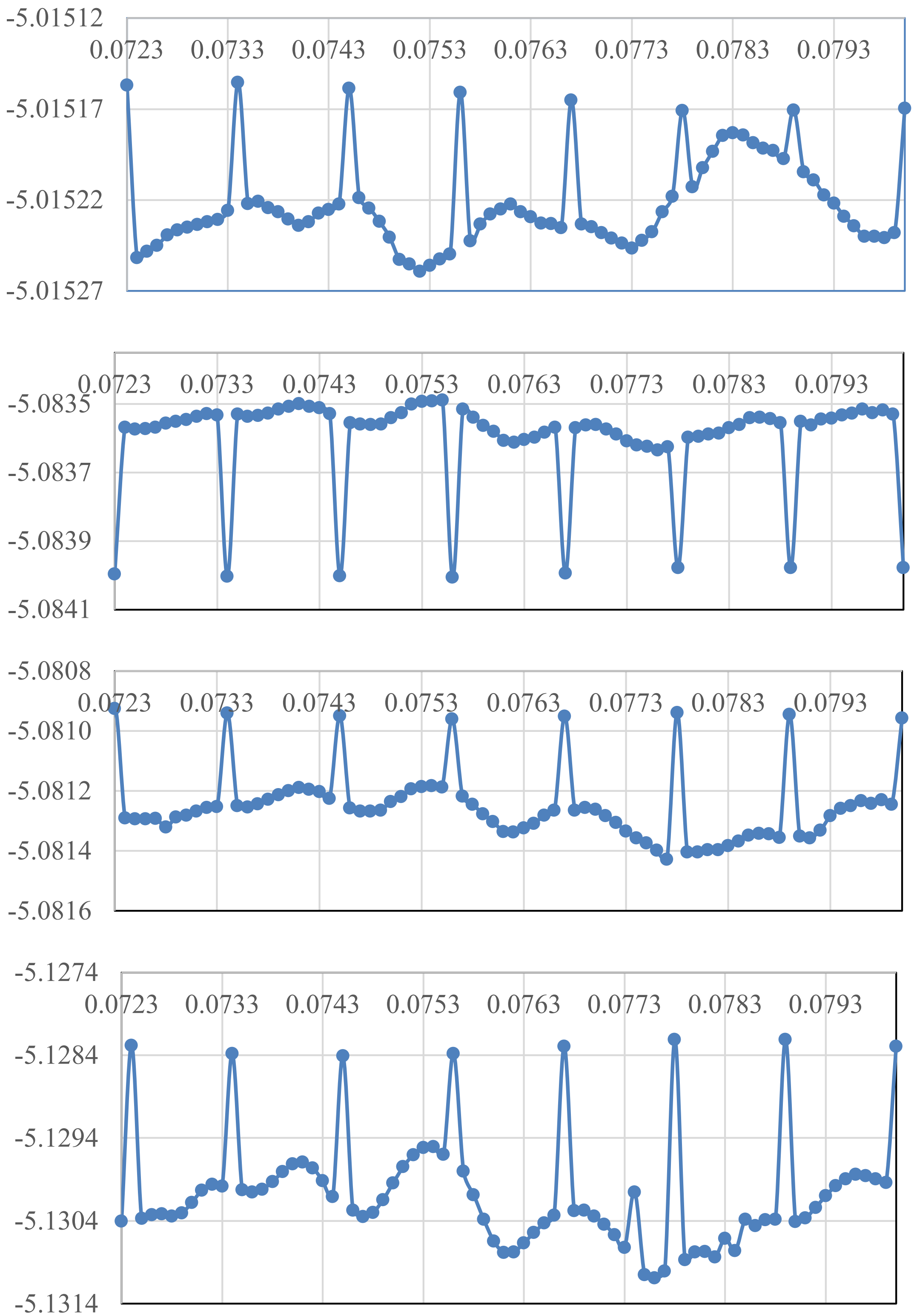

Figure B.7. Streamlines at point two (x = 0.290mm) for type A-gap 0.005in, maximum physical time 0.08 second, x-axis time in s, y-axis in mm.

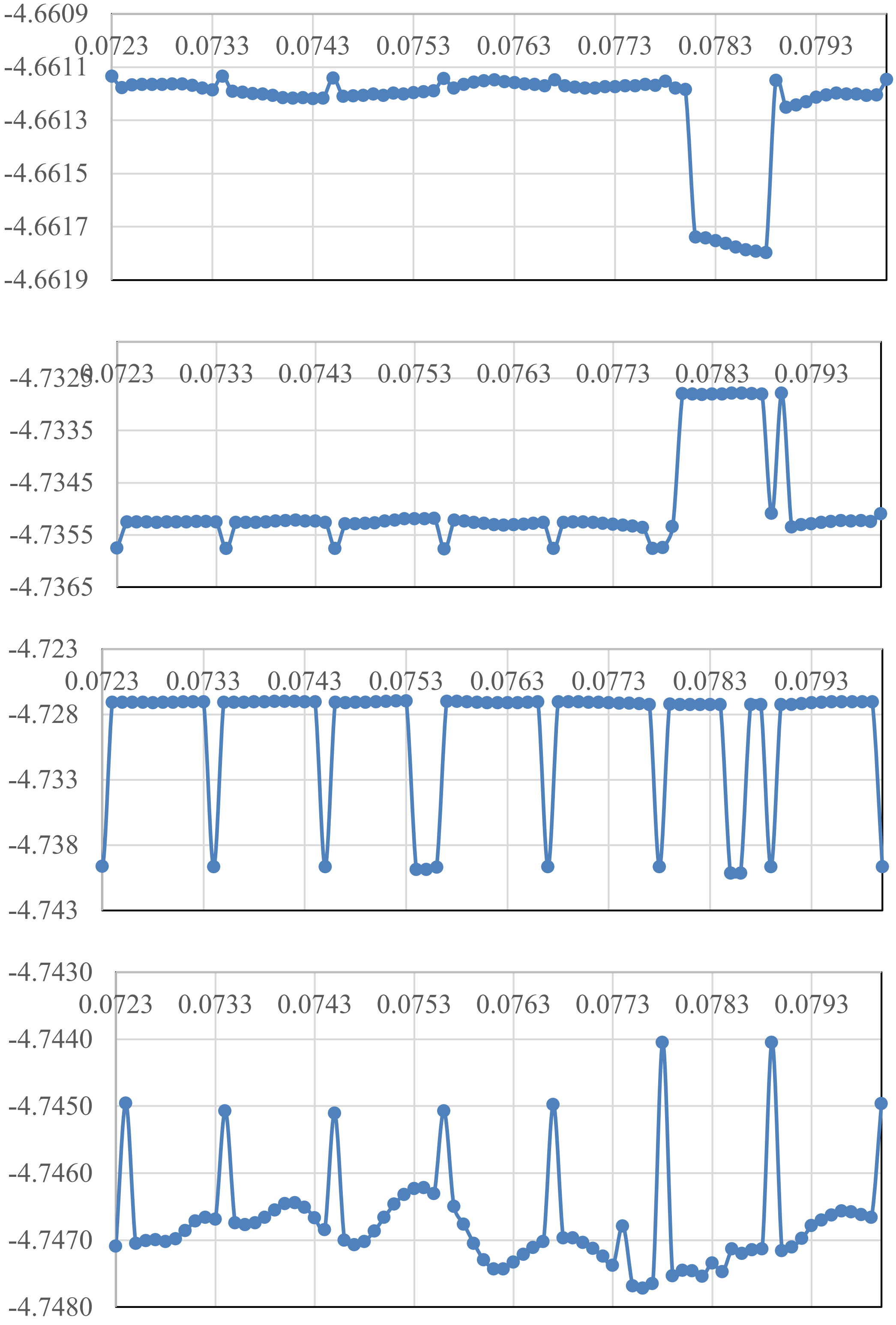

Figure B.8. Streamlines at point three (x = 0.660mm) for type A-gap 0.005in, maximum physical time 0.08 second, x-axis time in s, y-axis in mm.

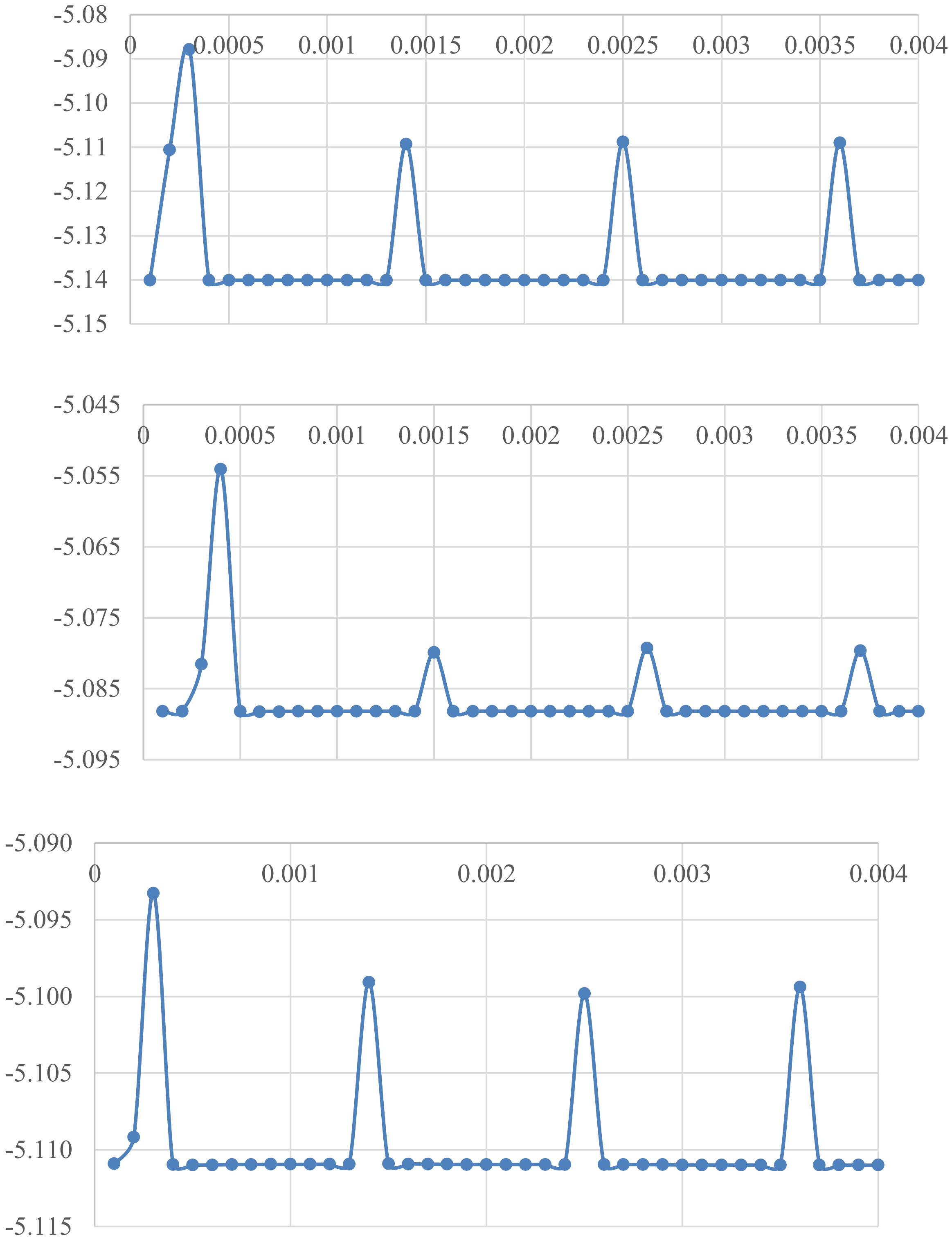

Figure B.9. Streamlines at point two (x = 0.290mm) for type A-gap 0.017in, maximum physical time 0.004 second, x-axis time in s, y-axis in mm.

Figure B.10. Streamlines at point three (x = 0.660mm) for type A-gap 0.017in, maximum physical time 0.004 second, x-axis time in s, y-axis in mm.

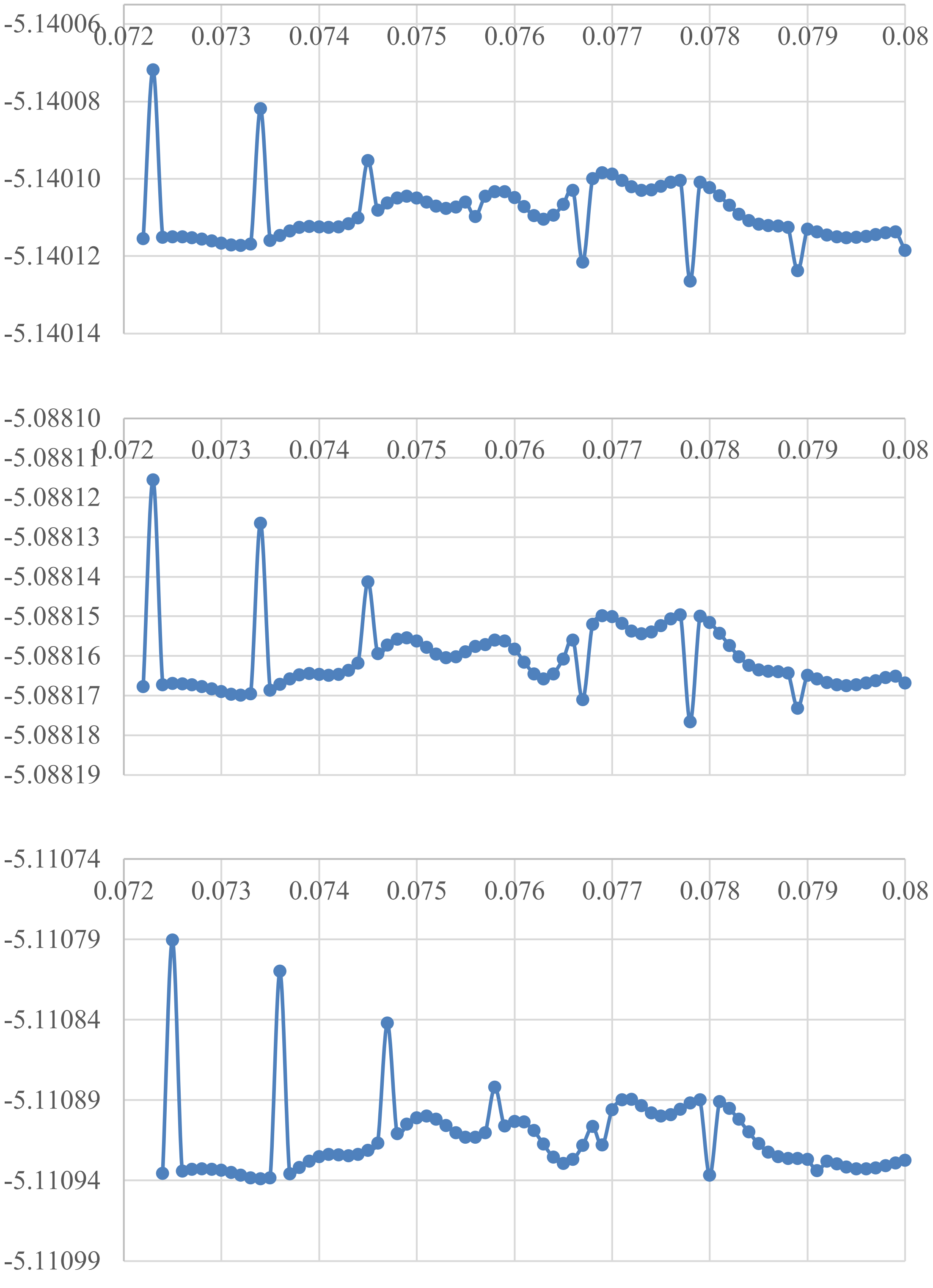

Figure B.11. Streamlines at point two (x = 0.290mm) for type A-gap 0.017in, maximum physical time 0.08 second, x-axis time in s, y-axis in mm.

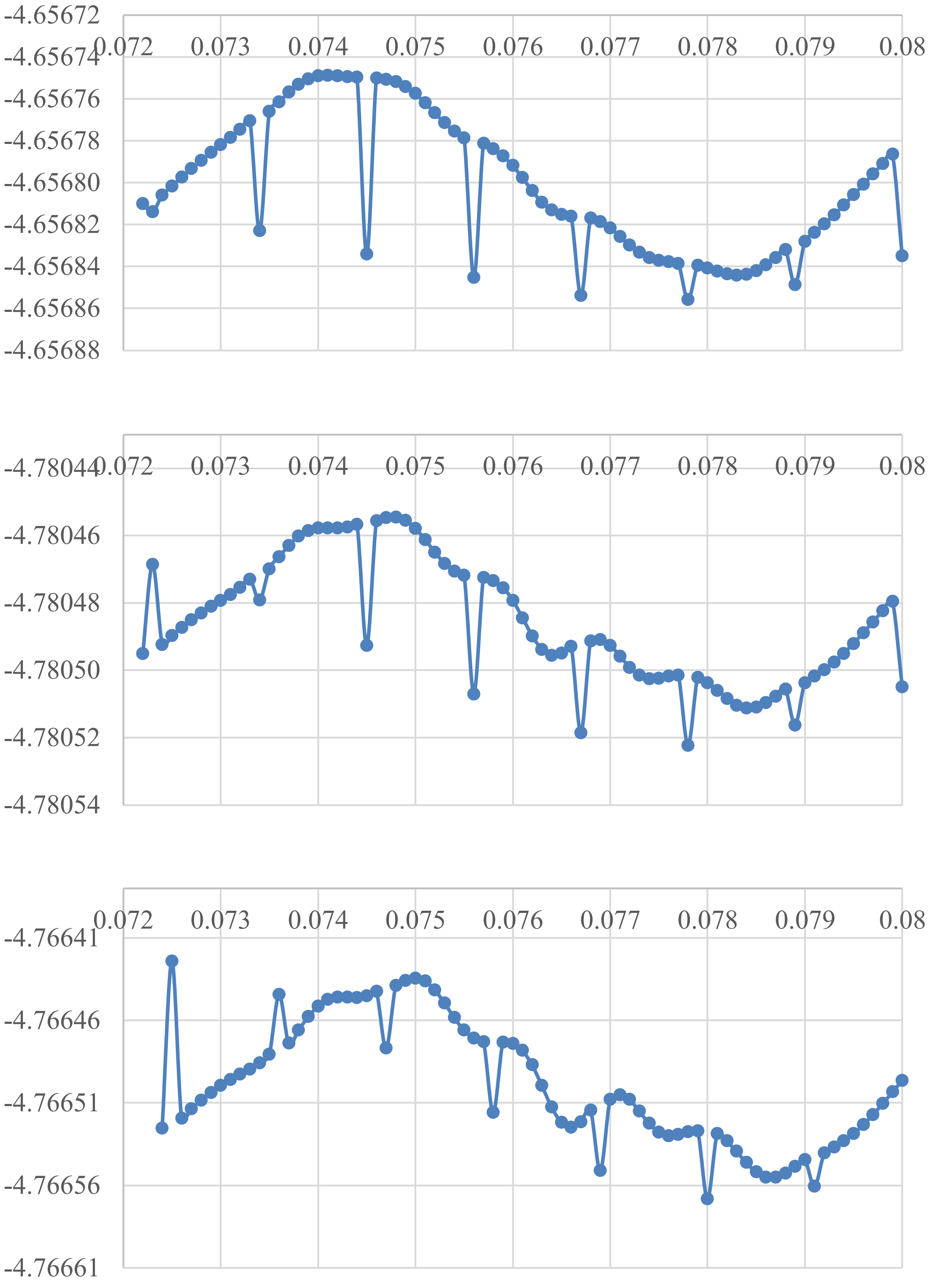

Figure B.12. Streamlines at point three (x = 0.660mm) for type A-gap 0.017in, maximum physical time 0.08 second, x-axis time in s, y-axis in mm.

B.2. Time-dependent Behavior of Streamline for the Type B Valve

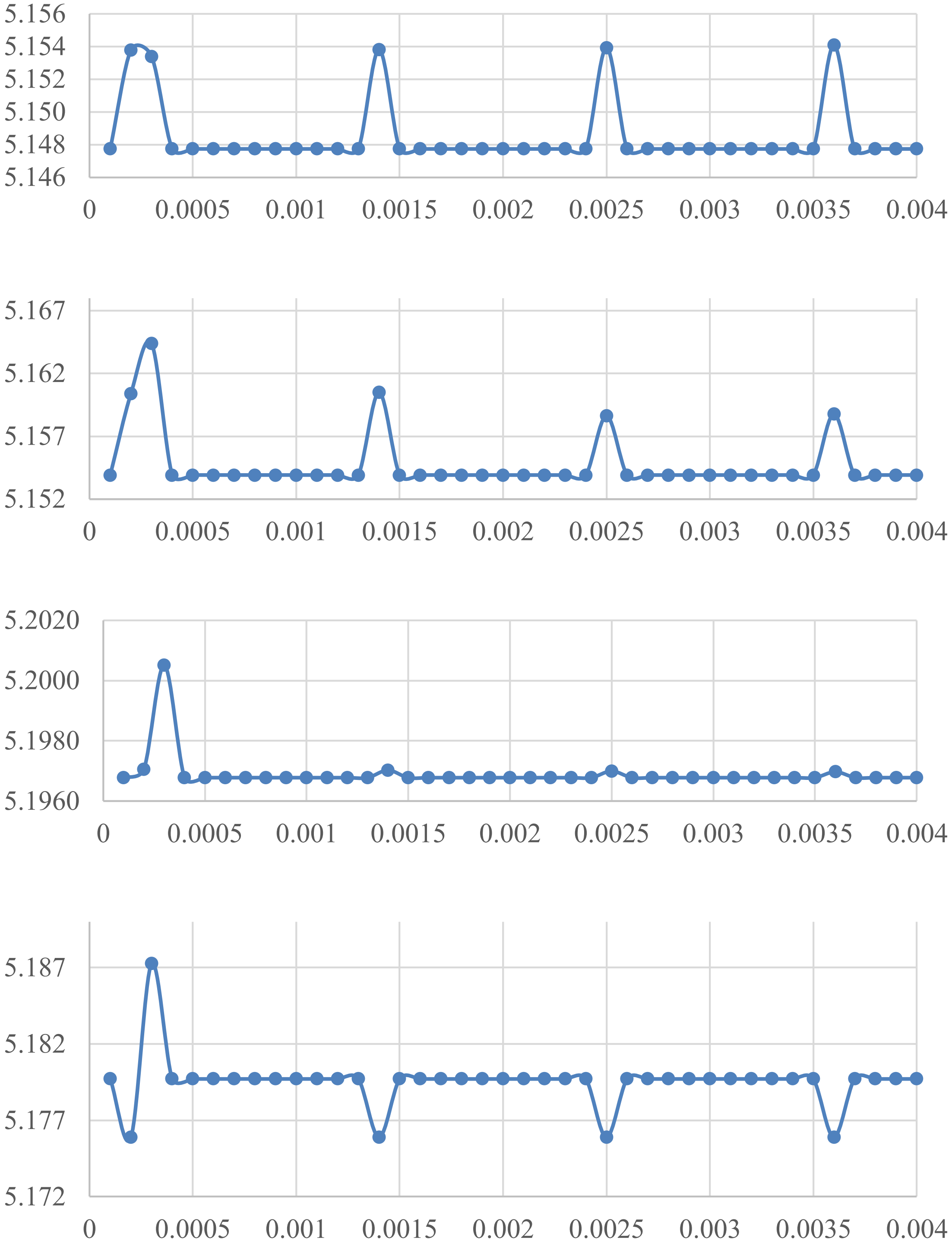

Figure B.13. Streamlines at point two (x = 0.290mm) for type B-gap 0.002in, maximum physical time 0.004 second, x-axis time in s, y-axis in mm.

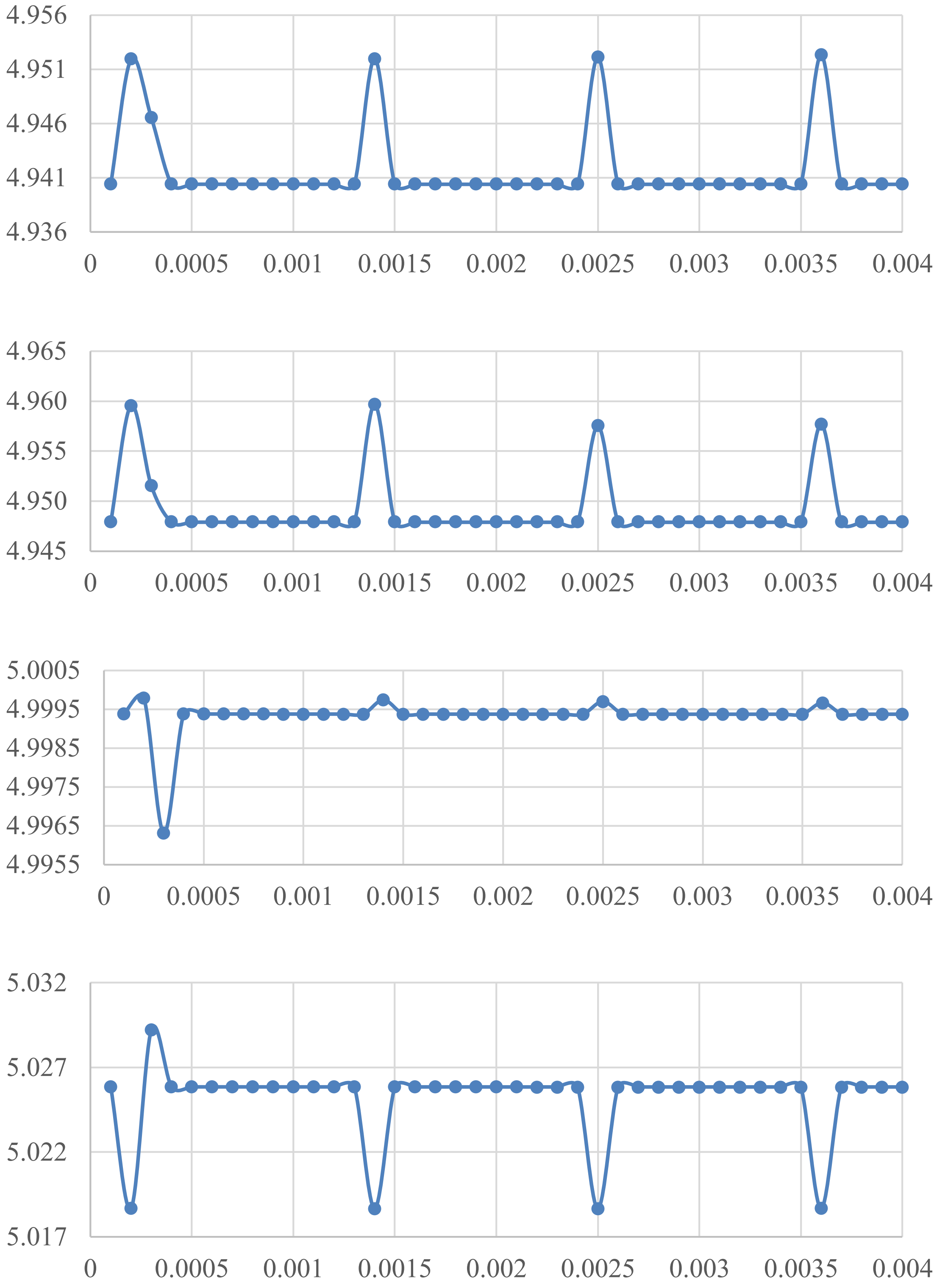

Figure B.14. Streamlines at point three (x = 0.660mm) for type B-gap 0.002in, maximum physical time 0.004 second, x-axis time in s, y-axis in mm.

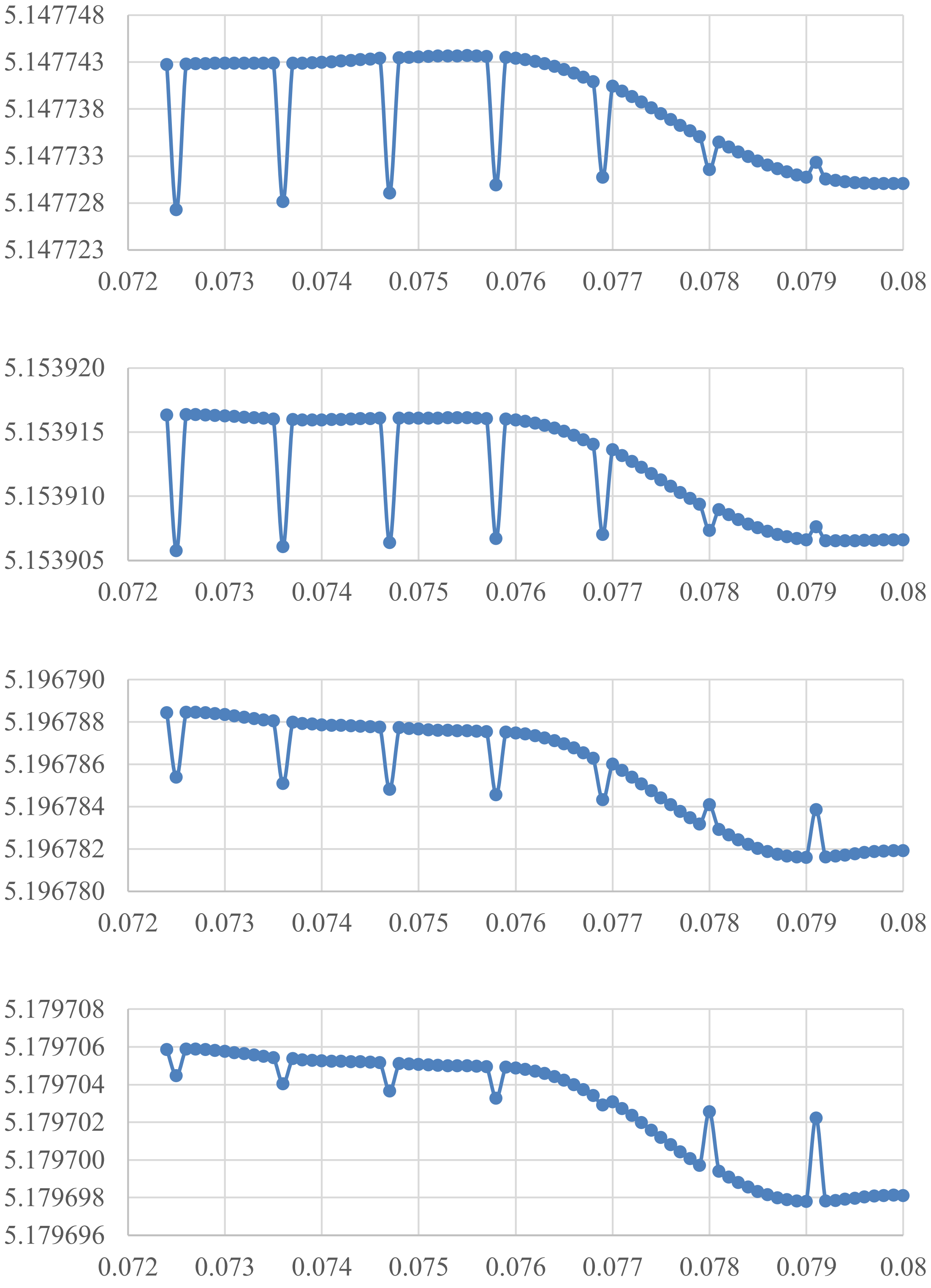

Figure B.15. Streamlines at point two (x = 0.290mm) for type B-gap 0.002in, maximum physical time 0.08 second, x-axis time in s, y-axis in mm.

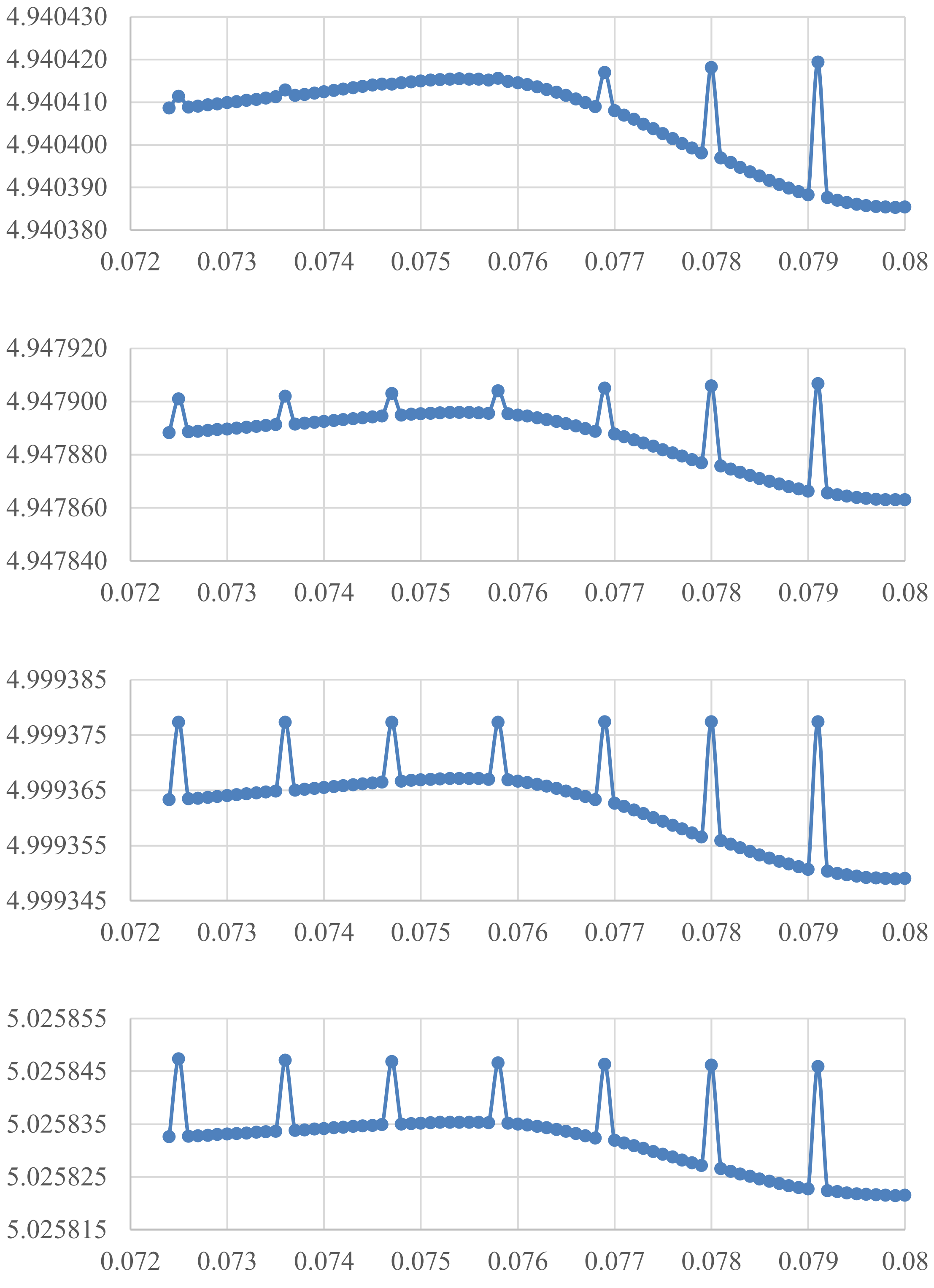

Figure B.16. Streamlines at point three (x = 0.660mm) for type B-gap 0.002in, maximum physical time 0.08 second, x-axis time in s, y-axis in mm.

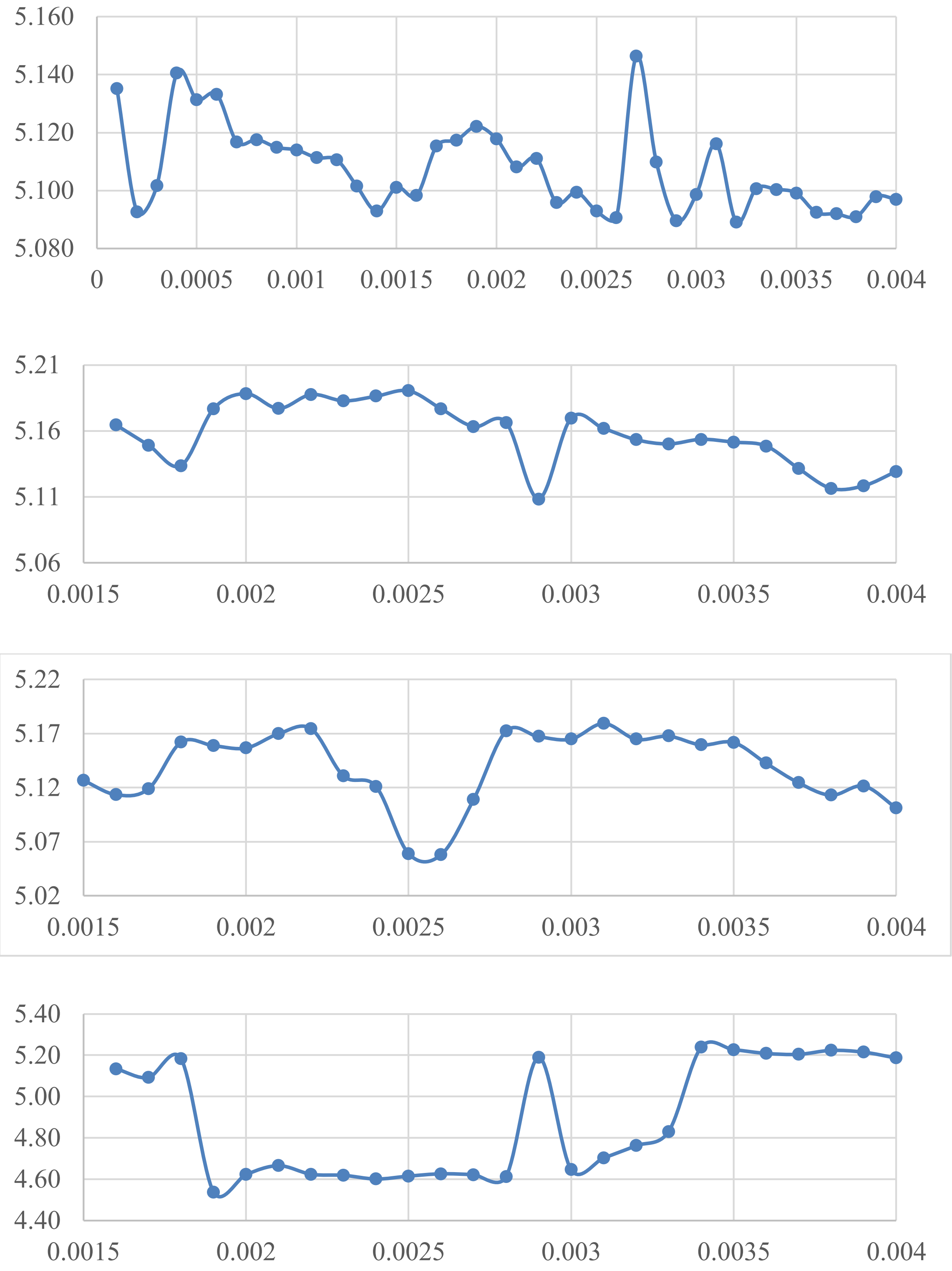

Figure B.17. Streamlines at point two (x = 0.290mm) for type B-gap 0.005in, maximum physical time 0.004 second, x-axis time in s, y-axis in mm.

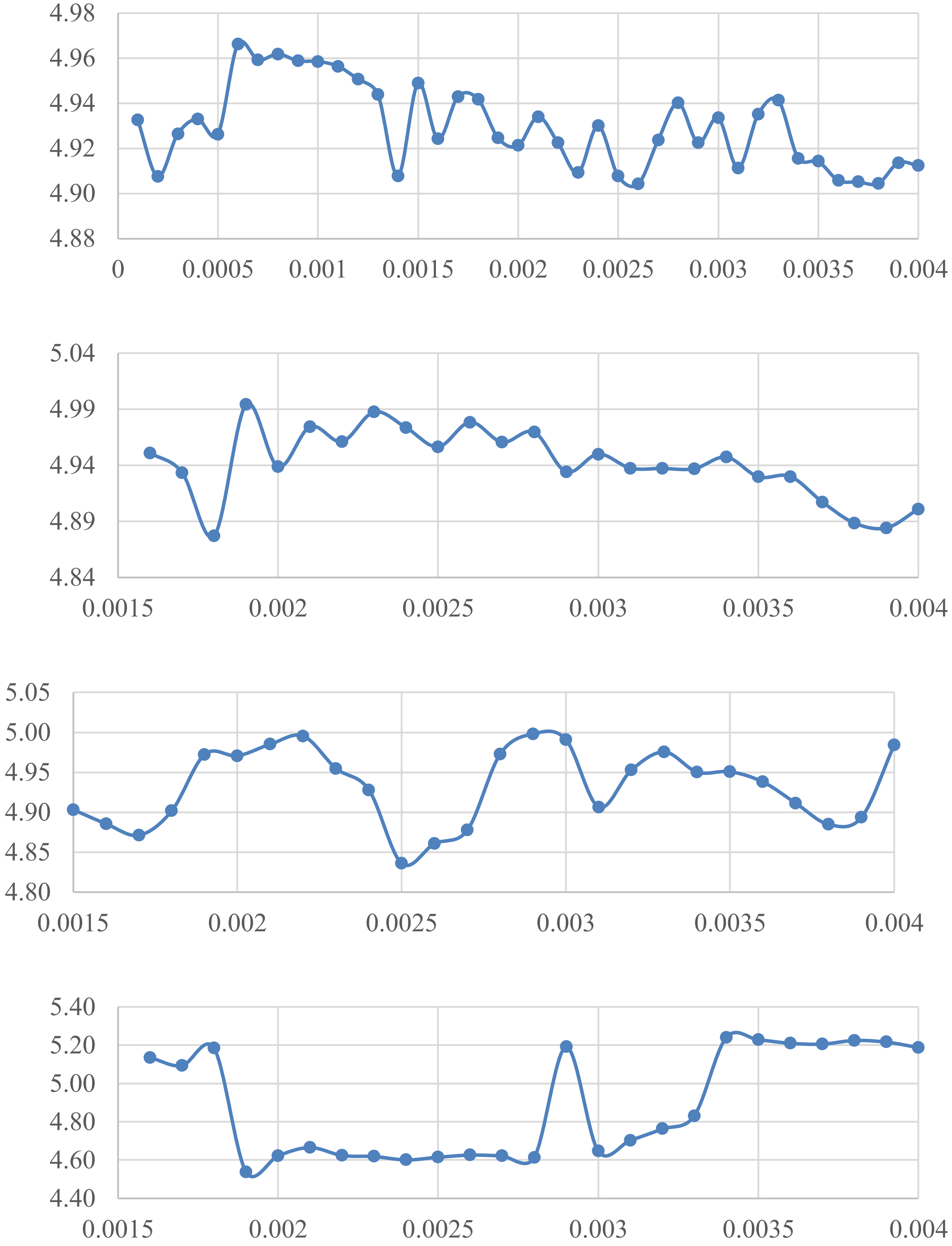

Figure B.18. Streamlines at point three (x = 0.660mm) for type B-gap 0.005in, maximum physical time 0.004 second, x-axis time in s, y-axis in mm.

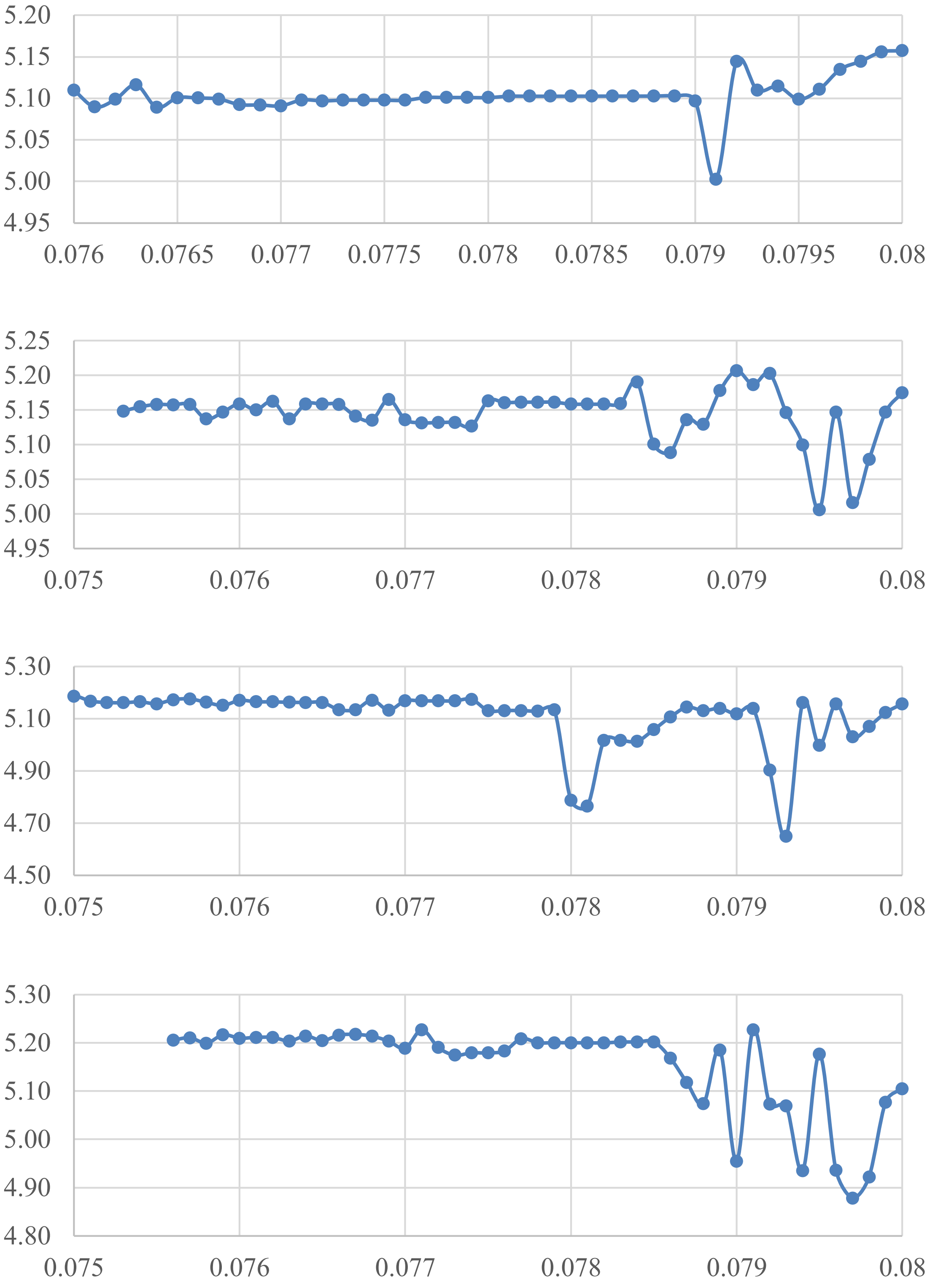

Figure B.19. Streamlines at point two (x = 0.290mm) for type B-gap 0.005in, maximum physical time 0.08 second, x-axis time in s, y-axis in mm.

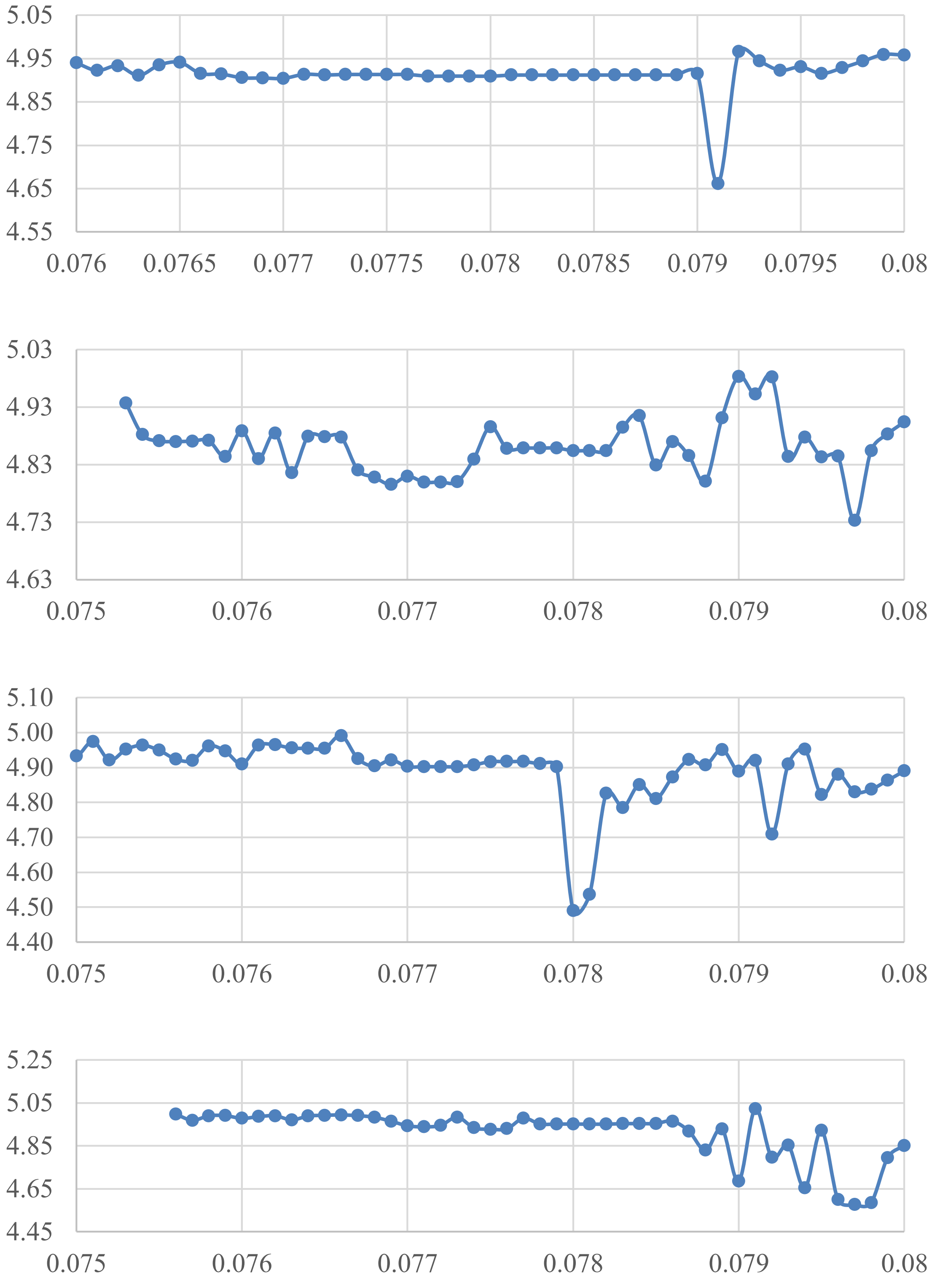

Figure B.20. Streamlines at point three (x = 0.660mm) for type B-gap 0.005in, maximum physical time 0.08 second, x-axis time in s, y-axis in mm.

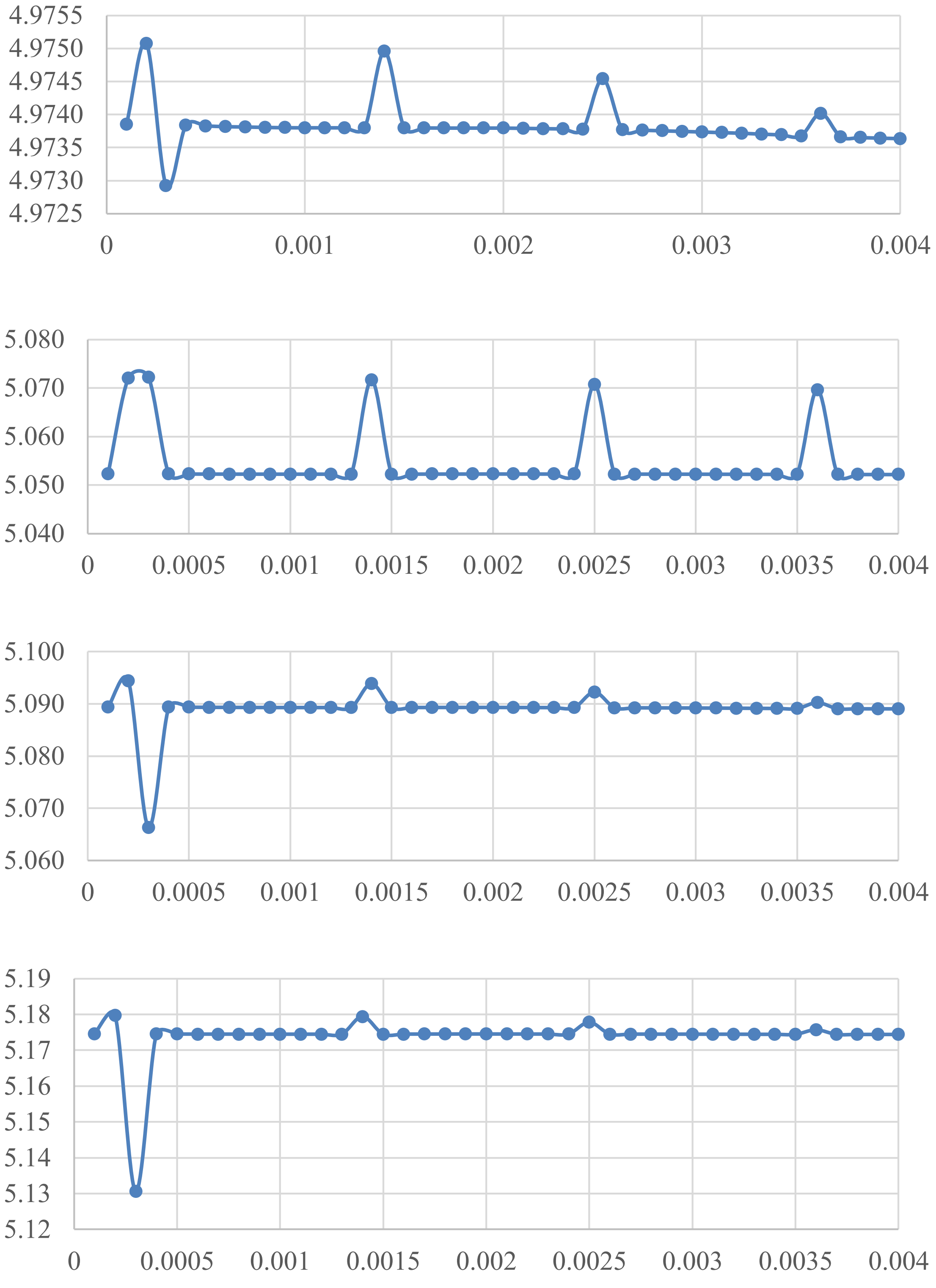

Figure B.21. Streamlines at point two (x = 0.290mm) for type B-gap 0.017in, maximum physical time 0.004 second, x-axis time in s, y-axis in mm.

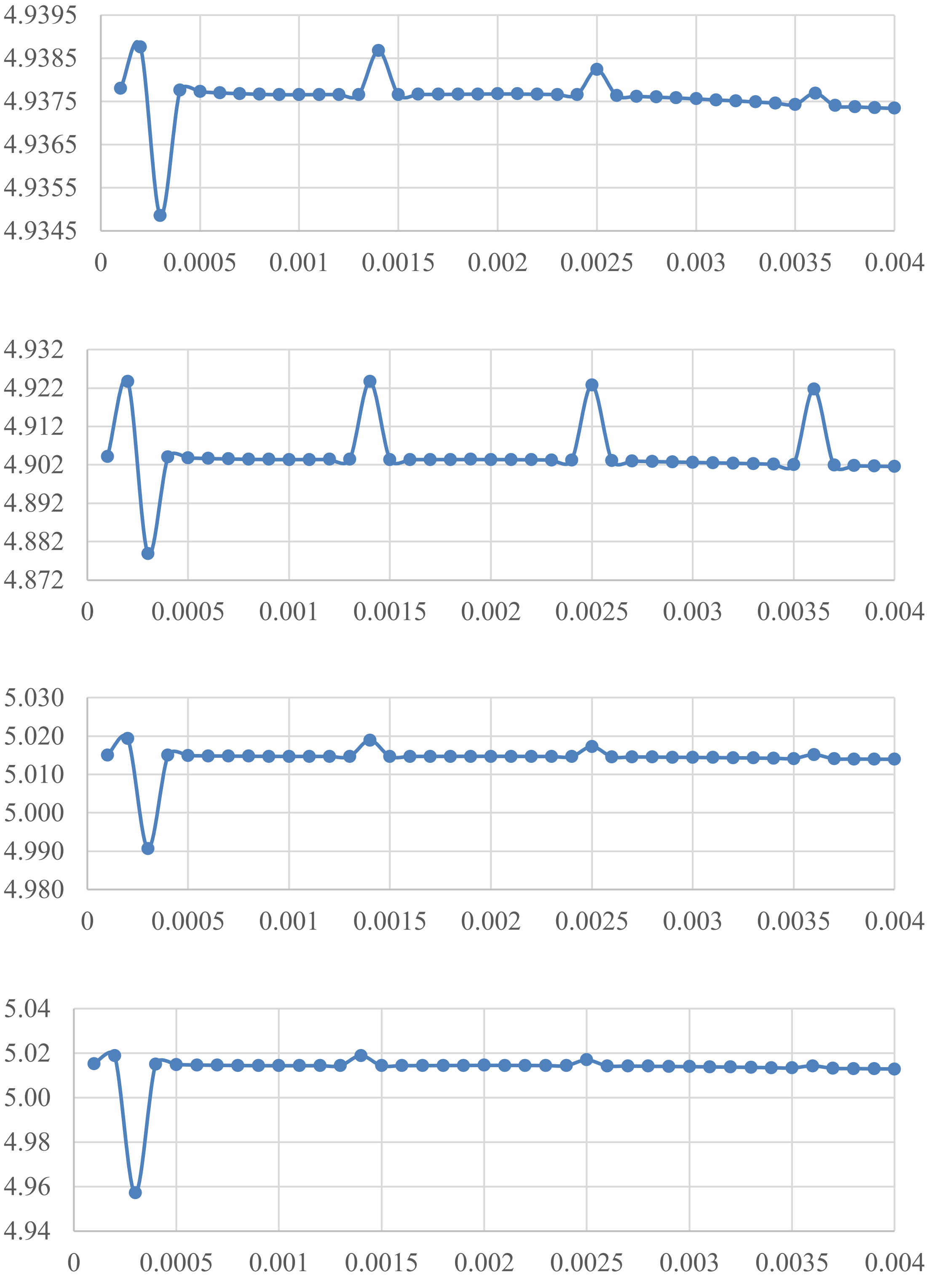

Figure B.22. Streamlines at point three (x = 0.660mm) for type B-gap 0.017in, maximum physical time 0.004 second, x-axis time in s, y-axis in mm.

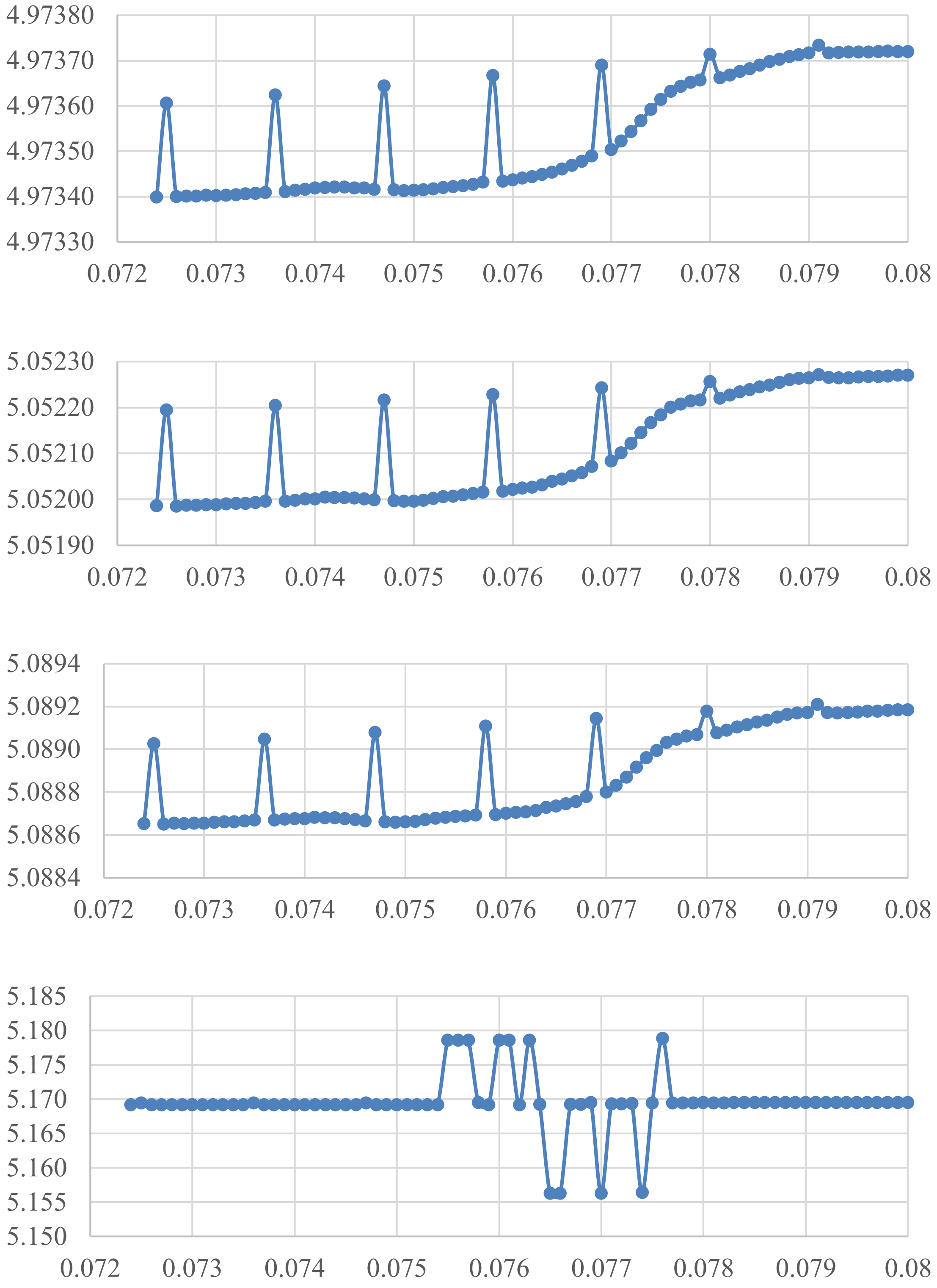

Figure B.23. Streamlines at point two (x = 0.290mm) for type B-gap 0.017in, maximum physical time 0.08 second, x-axis time in s, y-axis in mm.

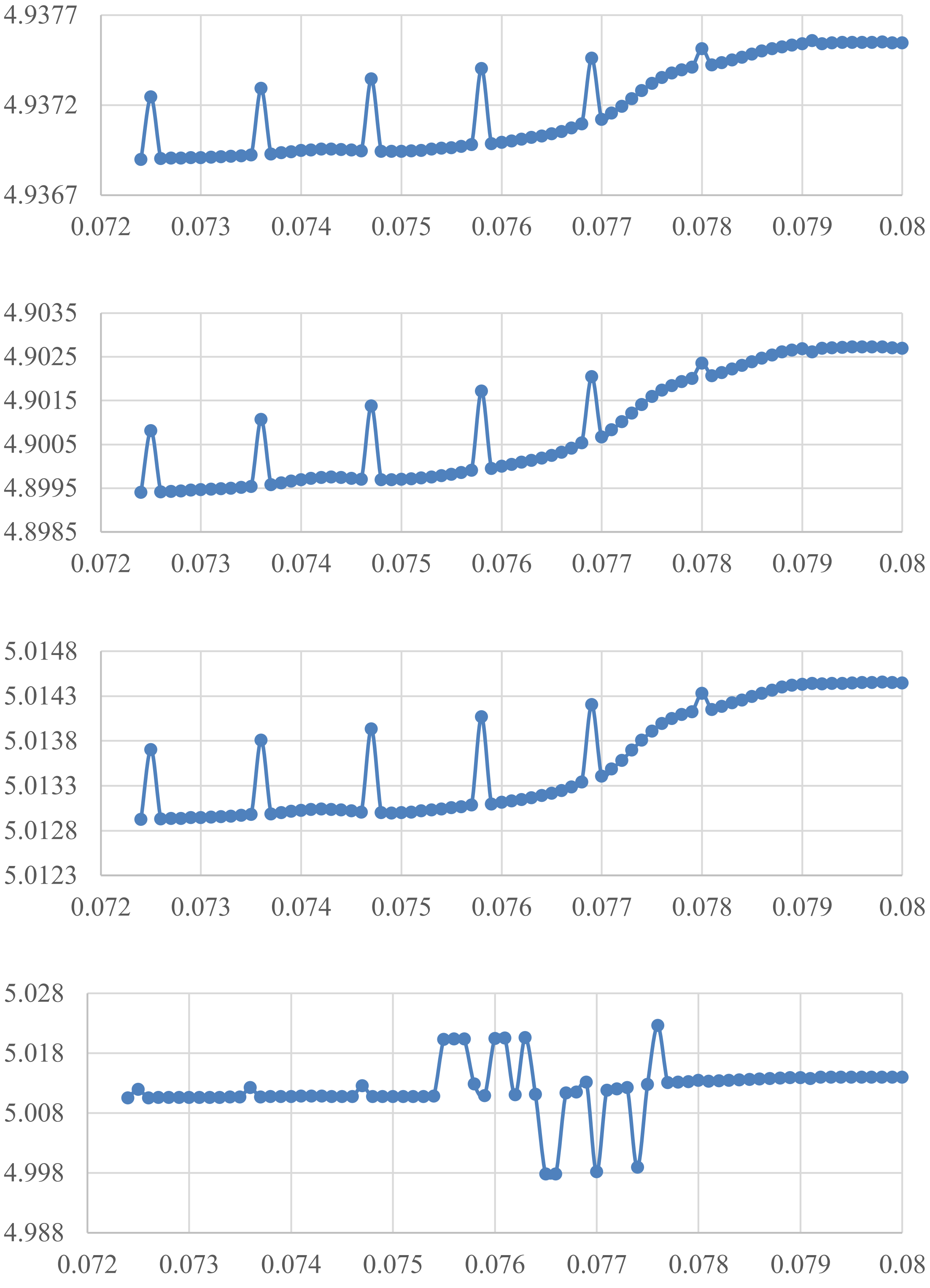

Figure B.24. Streamlines at point three (x = 0.660mm) for type B-gap 0.017in, maximum physical time 0.08 second, x-axis time in s, y-axis in mm.

ABOUT THE AUTHOR

Mutasim Elsheikh was born in Sudan-Africa. He graduated from the University of Khartoum with a Bachelor of Engineering degree in Mechanical. He previously worked for Petro-Gabs Corporation for three years in Sudan. He migrated to USA in 2005. He worked at Cox-target Media 2006 to 2007 in Largo USA.

Mr. Elsheikh joined USF 2008 as a Master degree student. He got his degree in MSME 2011. He started his PhD. 2011. He is married and have three kids and they are all live in Florida.